P241

NASA Conference Publication 3020—Vol. II

Transonic Symposium: Theory, Application, and Experiment

Date for general release April 30, 1991

Proceedings of a symposium held at
NASA Langley Research Center
Hampton, Virginia
April 19-21, 1988

NASA

(NASA-CP-3020-Vol-2) TRANSONIC SYMPOSIUM: THEORY, APPLICATION AND EXPERIMENT, VOLUME 2 (NASA) 241 p CSCL 01A

N91-24132
--THRU--
N91-24136
Unclas
H1/02 0019647

NASA Conference Publication 3020—Vol. II

Transonic Symposium: Theory, Application, and Experiment

Jerome T. Foughner, Jr., *Compiler*
Langley Research Center
Hampton, Virginia

Proceedings of a symposium sponsored by the
National Aeronautics and Space Administration,
Washington, D.C., and held at
NASA Langley Research Center
Hampton, Virginia
April 19-21, 1988

National Aeronautics and
Space Administration
Office of Management
Scientific and Technical
Information Division

1989

PREFACE

The last major Transonic Symposium was held at NASA Ames Research Center in February 1981. Since then, significant advances have been made in computer hardware, theoretical and computational methods, applications, experimental facilities, and testing techniques. Although much research remains to be done, these advances now provide us with capabilities in the transonic regime which we hardly envisioned at that time. In order to assess the state of the art in transonic flow disciplines and to glimpse at future directions, the NASA Langley Research Center held a Transonic Symposium on April 19-21, 1988. Emphasis was placed on steady, three-dimensional external, transonic flow and its simulation, both numerically and experimentally.

Papers were presented by researchers from NASA, industry, and universities. The symposium included technical sessions on wind tunnel and flight experiments; computational fluid dynamics applications (industry overviews and configuration analysis design); inviscid methods and grid generation; viscous methods and boundary-layer stability; and wind tunnel techniques and wall interference.

The proceedings are published in two volumes as follows because of the range of classifications:

Volume I, Unclassified (Parts 1 and 2)
Volume II, Unclassified, [redacted]

A list of attendees is included in this document.

General Chairman:	P. J. Bobbitt
Organizing Committee:	M. D. Salas
	L. E. Putnam
	J. T. Foughner
Technical Committee Chairmen:	
Theory and Computational	J. L. Thomas
Applications	E. G. Waggoner
Experiments	L. W. McKinney

PRECEDING PAGE BLANK NOT FILMED

PRECEDING PAGE BLANK NOT FILMED

CONTENTS

PREFACE iii

ATTENDEES ix

Volume I - Part 1*

SESSION 1: WIND TUNNEL AND FLIGHT EXPERIMENTS
Chairman: P. J. Bobbitt

AIRFRAME/PROPULSION INTEGRATION CHARACTERISTICS AT TRANSONIC SPEEDS 1
William P. Henderson and Bobby L. Berrier

FLIGHT RESEARCH AND TESTING 33
Terrill W. Putnam and Theodore G. Ayers

SHOCK-BOUNDARY-LAYER INTERACTION IN FLIGHT 61
Arild Bertelrud

SESSION 2: CFD APPLICATIONS, INDUSTRY OVERVIEWS
Chairman: E. G. Waggoner

TRANSONIC CFD APPLICATIONS AT BOEING 79
E. N. Tinoco

THE APPLICATION OF CFD FOR MILITARY AIRCRAFT DESIGN AT TRANSONIC SPEEDS 109
C. W. Smith, W. W. Braymen, J. C. Bhateley, and W. K. Londenberg

APPLIED TRANSONICS AT GRUMMAN 133
W. H. Davis

TRANSONIC AND FIGHTER AIRCRAFT: CHALLENGES AND OPPORTUNITIES FOR CFD 153
Luis R. Miranda

COMPUTATION OF AIRCRAFT COMPONENT FLOW FIELDS AT TRANSONIC MACH NUMBERS USING A THREE-DIMENSIONAL NAVIER-STOKES ALGORITHM 175
George D. Shrewsbury, Joseph Vadyak, David M. Schuster, and Marilyn J. Smith

TRANSONIC AERODYNAMIC DESIGN EXPERIENCE 195
E. Bonner

SESSION 3: INVISCID METHODS AND GRID GENERATION
Chairman: J. L. Thomas

EULER SOLVERS FOR TRANSONIC APPLICATIONS 217
Bram van Leer

*Volume I, Part 1 is presented under separate cover.

PRECEDING PAGE BLANK NOT FILMED

AN EMBEDDED MESH PROCEDURE FOR LEADING-EDGE VORTEX FLOWS 231
Kenneth G. Powell and Earll M. Murman

ASYMPTOTIC METHODS FOR INTERNAL TRANSONIC FLOWS 261
T. C. Adamson, Jr. and A. F. Messiter

WAVE DRAG DUE TO LIFT FOR TRANSONIC AIRPLANES 293
Julian D. Cole and Norman D. Malmuth

VECTOR POTENTIAL METHODS 309
M. Hafez

DEVELOPMENTS AND TRENDS IN THREE-DIMENSIONAL MESH GENERATION 341
Timothy J. Baker

GENERATION OF UNSTRUCTURED GRIDS AND EULER SOLUTIONS FOR COMPLEX GEOMETRIES 377
Rainald Lohner, Paresh Parikh, and Manuel D. Salas

Volume I - Part 2*

SESSION 4: CFD APPLICATIONS, CONFIGURATION ANALYSIS AND DESIGN
Chairman: L. E. Putnam

TRANSONIC PROPULSION SYSTEM INTEGRATION ANALYSIS AT MCDONNELL AIRCRAFT COMPANY 409
Raymond R. Cosner

AERODYNAMIC ANALYSIS OF THREE ADVANCED CONFIGURATIONS USING THE TRANAIR FULL-POTENTIAL CODE 437
M. D. Madson, R. L. Carmichael, and J. P. Mendoza

METHOD TO PREDICT EXTERNAL STORE CARRIAGE LOADS AT TRANSONIC SPEEDS 453
Bruce S. Rosen

STEADY AND UNSTEADY TRANSONIC SMALL DISTURBANCE ANALYSIS OF REALISTIC AIRCRAFT CONFIGURATIONS 467
John T. Batina, David A. Seidel, Robert M. Bennett, Herbert J. Cunningham, and Samuel R. Bland

INVERSE WING DESIGN IN TRANSONIC FLOW INCLUDING VISCOUS INTERACTION 497
Leland A. Carlson, Robert R. Ratcliff, and Thomas A. Gally

EULER/NAVIER-STOKES CALCULATIONS OF TRANSONIC FLOW PAST FIXED- AND ROTARY-WING AIRCRAFT CONFIGURATIONS 521
J. E. Deese and R. K. Agarwal

SESSION 5: VISCOUS METHODS AND BOUNDARY-LAYER STABILITY
Chairman: M. D. Salas

NAVIER-STOKES AND VISCOUS-INVISCID INTERACTION 547
Joseph L. Steger and William R. Van Dalsem

*Volume I, Part 2 is presented under separate cover.

3-D EULER AND NAVIER-STOKES CALCULATIONS FOR AIRCRAFT COMPONENTS 571
Veer N. Vatsa, Bruce W. Wedan, and Eli Turkel

TURBULENCE AND MODELING IN TRANSONIC FLOW 581
Morris W. Rubesin and John R. Viegas

TURBULENT EDDY VISCOSITY MODELING IN TRANSONIC SHOCK/BOUNDARY-LAYER INTERACTIONS 611
G. R. Inger

STABILITY OF COMPRESSIBLE BOUNDARY LAYERS 629
Ali H. Nayfeh

SECONDARY THREE-DIMENSIONAL INSTABILITY IN COMPRESSIBLE BOUNDARY LAYERS 691
Nabil M. El-Hady

SESSION 6: WIND TUNNEL TECHNIQUES AND WALL INTERFERENCE
Chairman: L. W. McKinney

TEST TECHNIQUES - A SURVEY PAPER ON CRYOGENIC TUNNELS, ADAPTIVE WALL TEST SECTIONS, AND MAGNETIC SUSPENSION AND BALANCE SYSTEMS 705
Robert A. Kilgore, David A. Dress, Stephen W. D. Wolf, and Colin P. Britcher

AN LDA INVESTIGATION OF THREE-DIMENSIONAL NORMAL SHOCK WAVE BOUNDARY-LAYER INTERACTIONS 741
R. M. Chriss, W. R. Hingst, A. J. Strazisar, and T. G. Keith, Jr.

INSTRUMENTATION ADVANCES FOR TRANSONIC TESTING 765
Percy J. Bobbitt

WALL INTERFERENCE ASSESSMENT AND CORRECTIONS 817
P. A. Newman, W. B. Kemp, Jr., and J. A. Garriz

TWO-MEASURED VARIABLE METHOD FOR WALL INTERFERENCE ASSESSMENT/CORRECTION 853
C. F. Lo and W. L. Sickles

COMPARISON OF AIRFOIL RESULTS FROM AN ADAPTIVE WALL TEST SECTION AND A POROUS WALL TEST SECTION 867
Raymond E. Mineck

CAPABILITIES OF WIND TUNNELS WITH TWO ADAPTIVE WALLS TO MINIMIZE BOUNDARY INTERFERENCE IN 3-D MODEL TESTING 891
Rainer Rebstock and Edwin E. Lee, Jr.

Volume II

NATIONAL TRANSONIC FACILITY STATUS
L. W. McKinney, W. E. Bruce, Jr., and B. B. Gloss 1

REYNOLDS NUMBER EFFECTS ON THE TRANSONIC AERODYNAMICS OF A SLENDER WING-BODY CONFIGURATION 41
James M. Luckring, Charles H. Fox, Jr., and Jeffrey S. Cundiff

LAMINAR-FLOW FLIGHT EXPERIMENTS 59
R. D. Wagner, D. V. Maddalon, D. W. Bartlett, F. S. Collier, Jr., and A. L. Braslow

LAMINAR-FLOW WIND TUNNEL EXPERIMENTS 105
William D. Harvey, Charles D. Harris, William G. Sewall, and John P. Stack

COMPUTATIONAL SUPPORT OF THE X-29A ADVANCED TECHNOLOGY DEMONSTRATOR FLIGHT EXPERIMENT 147
E. G. Waggoner and B. L. Bates

RESULTS OF CORRELATIONS FOR TRANSITION LOCATION ON A CLEAN-UP GLOVE INSTALLED ON AN F-14 AIRCRAFT AND DESIGN STUDIES FOR A LAMINAR GLOVE FOR THE X-29 AIRCRAFT ACCOUNTING FOR SPANWISE PRESSURE GRADIENT 167
S. H. Goradia, P. J. Bobbitt, H. L. Morgan, J. C. Ferris, and W. D. Harvey

ATTENDEES

NASA LANGLEY

ABEYOUNIS, W. K.
Mail Stop 280

ABDUL-HAMID, K
Analytical Services & Materials, Inc.
Mail Stop 280

ADCOCK, J.
Mail Stop 267

AL-SAADI, J.
N. C. State University
Mail Stop 267

ALLISON, D. O.
Mail Stop 294

ANDERSON, C.
Mail Stop 159

ATKINS, H.
Mail Stop 159

BANGERT, L.
Mail Stop 280

BARE, E. A.
Mail Stop 280

BARNWELL, R.
Mail Stop 105A

BARTLETT, D.
Mail Stop 261

BATES, B. L.
Vigyan Research Associates, Inc.
Mail Stop 294

BATINA, J. T.
Mail Stop 173

BENNETT, B. B.
Mail Stop 280

BERRIER, B. L.
Mail Stop 280

BERTELRUD, A.
High Technology Corporation
Mail Stop 163

BIEDRON, R. T.
Mail Stop 128

BLAND, S. R.
Mail Stop 173

BOBBITT, P. J.
Mail Stop 285

BOYDEN, R.
Mail Stop 267

BOYLES, G.
Mail Stop 267

BRASLOW, A.
Analytical Services & Materials, Inc.
Mail Stop 261

BROOKS, C. W., Jr.
Mail Stop 359

BRUCE, W. E.
Mail Stop 267

CAMPBELL, D.
Mail Stop 294

CANNIZZARO, F. E.
Old Dominion University
Mail Stop 159

CARLSON, J. R.
Mail Stop 280

CARPENTER, M. H.
Mail Stop 156

CARRAWAY, D. L.
Mail Stop 238

CARSON, G. T., Jr.
Mail Stop 280

CHU, Julio
Mail Stop 267

CLUKEY, P.
Mail Stop 359

CLUKEY, S.
Mail Stop 359

COMPTON, W. B.,
Mail Stop 280

COVELL, P.
Mail Stop 413

CUNDIFF, J. S.
Mail Stop 294

DAGENHART, J. R.
Mail Stop 339

DAVIS, R. E.
Mail Stop 474

DESMARAIS, R.
Planning Research Corporation
Mail Stop 246

DODBELE, S.
Vigyan Research Associates, Inc.
Mail Stop 247

DRESS, D. A.
Mail Stop 267

EL-HADY, N. M.
Old Dominion University
Mail Stop 359

EVANGELISTA, R.
Analytical Services & Materials, Inc.
Mail Stop 359

FAULKNER, J.
Mail Stop 390

FERRIS, J.
Mail Stop 294

FLECHNER, S.
Mail Stop 267

FOSS, W.
Mail Stop 431

FOSTER, J.
Mail Stop 294

FOUGHNER, J. T., Jr.
Mail Stop 285

FOX, C. H., Jr.
Mail Stop 295

FULLER, D.
Mail Stop 267

GAINER, T.
Mail Stop 359

GARRIZ, J.
Vigyan Research Associates, Inc.
Mail Stop 159

GATLIN, G. M.
Mail Stop 286

GHAFFARI, F.
Vigyan Research Associates, Inc.
Mail Stop 294

GLOSS, B. B.
Mail Stop 267

GORADIA, S. H.
Vigyan Research Associates, Inc.
Mail Stop 359

GREEN, L. L.
Mail Stop 159

GUMBERT, C. R.
Mail Stop 159

HALL, R. M.
Mail Stop 294

HALLISSY, J. B.
Mail Stop 294

HARRIS, C. D.
Mail Stop 359

HARRIS, R. V., Jr.
Mail Stop 116

HARVEY, W. D.
Mail Stop 359

HEMSCH, M. J.
Planning Research Corporation
Mail Stop 294

HENDERSON, W. P.
Mail Stop 280

HODGE, S.
Mail Stop 159

JONES, G.
Mail Stop 359

KALBURGI, V.
Analytical Services & Materials, Inc.
Mail Stop 359

KAMEMOTO, D.
Mail Stop 359

KEMP, W. B.
LRC
Mail Stop 267

KURUVILLA, G.
Vigyan Research Associates, Inc.
Mail Stop 159

LEE, E.
Mail Stop 173

IGOE, W.
Mail Stop 267

INGRALDI, A.
Mail Stop 280

JACOBS, P.
Mail Stop 294

JENKINS, R. V.
Mail Stop 359

JOHNSON, C. B.
Mail Stop 359

JOHNSON, T.
Planning Research Corporation
Mail Stop 294

JOHNSON, W. G., Jr.
Mail Stop 267

LADSON, C. L.
Mail Stop 285

LAMAR, J.
Mail Stop 294

LEAVITT, L.
Mail Stop 280

LUCKRING, J. M.
Mail Stop 294

MADDALON, D
Mail Stop 261

MANGALAM, S.
Analytical Services & Materials, Inc.
Mail Stop 915

MANN, M
Mail Stop 411

MAVRIPLIS, D.
ICASE
Mail Stop 132C

MCKINNEY, L. W.
Mail Stop 285

MCGHEE, R.
Mail Stop 339

MEHROTRA, S. C.
Vigyan Research Associates, Inc.
Mail Stop 912

MELSON, D.
Mail Stop 159

MERCER, C.
Mail Stop 280

MINECK, R.
Mail Stop 294

MOLLOY, J. K.
Mail Stop 11b

MORGAN, H. L.
Mail Stop 359

MURTHY, A.
Vigyan Research Associates, Inc.
Mail Stop 287

NAIK, D.
Vigyan Research Associates, Inc.
Mail Stop 280

NEELY, R. W.
Mail Stop 173

NEWMAN, P. A.
Mail Stop 159

PARIKH, P.
Vigyan Research Associates, Inc.
Mail Stop 159

PASCHAL, K.
Mail Stop 359

PATTERSON, J. C., Jr.
Mail Stop 246A

PENDERGRAFT, O. C.
Mail Stop 280

PETERSON, J. B.
Mail Stop 267

PFENNINGER, W.
Analytical Services & Materials, Inc.
Mail Stop 261

PHILLIPS, P.
Mail Stop 294

POPERNACK, T. G., Jr.
Mail Stop 267

PUTNAM, L. E.
Mail Stop 294

RADESPIEL, R.
Mail Stop 267

RE, R.
Mail Stop 280

REBSTOCK, R.
National Research Council
Mail Stop 287

ROSE, L. J.
Mail Stop 139A

RUMSEY, C
Mail Stop 128

SALAS, M. D.
Mail Stop 159

SCHOONOVER, E.
Mail Stop 294

SEIDEL, D. A.
Mail Stop 173

SEKAR, B.
Vigyan Research Associates, Inc.
Mail Stop 156

SEWALL, W. G.
Mail Stop 339

SMITH, L. A
Mail Stop 294

SONERS, D. M.
Mail Stop 294

SOUTH, J. C.
Mail Stop 128

STACK, J. P.
Mail Stop 359

STAINBACK, P. C.
Mail Stop 359

STRGANAC, T.
Mail Stop 431

SWANSON, R. C.
Mail Stop 159

SWITZER, G.
Analytical Services & Materials, Inc.
Mail Stop 156

TAYLOR, J.
Mail Stop 280

THAMES, F.
Mail Stop 159

THIBODEAUX, J. J.
Mail Stop 267

THOMAS, J. L.
Mail Stop 128

TURKEL, E.
ICASE
Mail Stop 132C

VATSA, V. N.
Mail Stop 159

VEMURU, C. S.
Mail Stop 159

VENKATAKRISHNAN, V.
Analytical Services & Materials, Inc.
Mail Stop 159

VIJGEN, P.
High Technology Corporation
Mail Stop 247

VRETAKIS, N. G.
AFSCLO
Mail Stop 221

WAGGONER, E. G.
Mail Stop 294

WAGNER, R. D.
Mail Stop 261

WAHLS, R. A.
N. C. State University
Mail Stop 156

WALKER, B.
Mail Stop 359

WARREN, G. P
Mail Stop 128

WATSON, R.
Mail Stop 163

WHITCOMB, R. T.
Mail Stop 188E

WHITESIDES, J.
George Washington University
Mail Stop 269

WIESEMAN, C. D.
Mail Stop 243

WILLIAMS, M. S.
Mail Stop 267

WOLF, S.
Vigyan Research Associates, Inc.
Mail Stop 287

WOODSON, S.
Mail Stop 294

WORNOM, S. F.
Mail Stop 159

YAKOS, S. F.
Mail Stop 280

YATES, C.
Mail Stop 246

NON-LANGLEY

ADAMSON, Thomas C., Jr.
The University of Michigan

AGARWAL, Ramesh K.
McDonnell Douglas Research Labs.

AYERS, Theodore G.
NASA Ames Research Center

BAKER, T. J.
Princeton University

BENGELINK, Ronald L.
Boeing Commercial Airplane Company

BHARADVAJ, Bala K.
Douglas Aircraft Company

BONNER, Ellwood
Rockwell International Corporation

BRAYMEN, William
General Dynamics

CARLSON, Leland A.
Texas A&M University

CHAN, Y. Y.
National Aeronautical Establishment

CHEN, Lee T.
McDonnell Douglas Corporation

CHRISS, Randall
NASA Lewis Research Center

COLE, Julian D.
Rensselaer Polytechnic

COLEHOUR, Jeffery L.
Boeing Commercial Airplane Company

CONNELL, Stuart
General Electric

COSNER, Ray R.
McDonnell Aircraft Co.

DA COSTA, A. L.
Boeing Advanced Systems

DANG, Thong
Douglas Aircraft Company

DAVIS, Warren H., Jr.
Grumman Corporation

DEESE, E. Jerry
McDonnell Douglas Research Labs.

DIRLIK, Steven P.
David Taylor Research Center

DOUGHERTY, F. Carroll
University of Colorado

DRIVER, Cornelius
Eagle Engineering, Incorporated

DUQUE, Earl P. N.
NASA Ames Research Center

GEORGE, Mike
Northrop Corporation

GOLDHAMMER, Mark I.
Boeing Commercial Airplane Div.

GORDNIER, Raymond E.
University of Cincinnati

GREGOREK, Gerald M.
Ohio State University

GROSSMAN, B.
Virginia Polytechnic Institute
and State University

GRUBER, Glenn J.
Pratt & Whitney

HAFEZ, D. D.
University of California-Davis

HASSAN, H. A.
North Carolina State University

IDE, Hiroshi
Rockwell International

INGER, George R.
Iowa State University

ISHIMITSU, K. K.
Boeing Advanced Systems

JAMESON, Antony
Princeton University

KHOSLA, Prem K.
University of Cincinnati

LAN, C. Edward
University of Kansas

LEVINE, Mark
Rockwell International

LO, Ching F.
Calspan Corporation

LOFTIN, Laurence K., Jr.
Self Employed

LORD, Wesley
Pratt & Whitney

LYNCH, Frank T.
Douglas Aircraft Company

MACWILKINSON, Derek G.
Douglas Aircraft Co.

MADSON, Mike
NASA Ames Research Center

MAGUIRE, William B.
David Taylor Research Center

MALMUTH, Norman D.
Rockwell International Science Center

MASIELLO, Matthew
Grumman Aerospace Corporation

MAYER, David
Boeing Military Airplane Company

MIDDLETON, Wilbur D.
Boeing Company

MIRANDA, L. R.
Lockheed-California Company

MUELLER, Thomas J.
University of Notre Dame

NACHMAN, Arje
U. S. Air Force

NAYFEH, Ali H.
Virginia Polytechnic Institute
and State University

NIETUBILZ, Charles J.
Ballistic Research Laboratory

POWELL, Ken
University of Michigan

PUTNAM, Terry
NASA Dryden Flight Research Facility

RATCLIFF, Robert
Texas A&M University

ROSEN, Bruce S.
Grumman Corporation

RUBESIN, M. W.
NASA Ames Research Center

RUBIN, Stanley G.
University of Cincinnati

SCHLEINIGER, Gilberto
University of Delaware

SHREWSBURY, G. D.
Lockheed-Georgia Company

SMITH, Charles
General Dynamics

SMITH, Norbert F.
McDonnell Douglas Corporation

SNYDER, James
Wright Patterson Air Force Base

SORRELLS, Russell B.
U. S. Air Force

STEGER, J. L.
NASA Ames Research Center

TINOCO, E. N.
Boeing Commercial Airplane Company

TSENG, Wei W.
Naval Air Development Center

VAN LEER, Bram
University of Michigan

VERHOFF, August Dr.
McDonnell Aircraft Company

VOLPE, Giuseepe
Grumman Aerospace Corporation

WEBBER, Geoff W.
Lockheed Aeronautical Systems Company

WIGTON, Larry
Boeing Aerospace Corporation

WILCOX, Peter
Douglas Aircraft Company

WYCKOFF, John C.
AMETEK

ZICKUHR, Tom
Beech Aircraft Corporation

N91-24133

NATIONAL TRANSONIC FACILITY STATUS

5,-09
19848

L. W. McKinney, W. E. Bruce, Jr., and B. B. Gloss
Langley Research Center
Hampton, Virginia

ABSTRACT

The National Transonic Facility (NTF) has been operational in a combined checkout and test mode for about 3 years. During this time there have been many challenges associated with movement of mechanical components, operation of instrumentation systems, and drying of insulation in the cryogenic environment. Most of these challenges have been met to date along with completion of a basic flow calibration and aerodynamic tests of a number of configurations. This paper reviews some of the major challenges resulting from the cryogenic environment with regard to hardware systems and data quality. Reynolds number effects on several configurations are also discussed.

INTRODUCTION

The National Transonic Facility (NTF), which was constructed by NASA with a goal of meeting the national needs for High Reynolds Number Testing, has been operational in a checkout and test mode for about 3 years. The order of magnitude increase in Reynolds number over existing transonic wind tunnels provided by the NTF, figure 1, is the result of operating at cryogenic temperature and stagnation pressures to 8.8 atmospheres. Although the cryogenic temperatures provide some significant and well documented benefits from a Reynolds number standpoint, the harsh environment also provides equally significant challenges for reliable operation of large mechanical systems and instrumentation.

The approach followed during the 3 years of operating in a combined checkout and test mode had some obvious advantages for a facility like the NTF where there is not a significant experience base. Known problems can be solved while identifying and solving those problems that will only show up by using the tunnel in a testing mode. The end result is a fully operational facility at an earlier date. However, there are also some disadvantages. Most significant among them is that testing during this time period is at a much reduced level of efficiency. For a facility like NTF where a very high level of efficiency is important, it is difficult for both operators and observers to maintain perspective during this test period.

Over the past 3 years a host of operating problems resulting from the cryogenic environment have been identified and solved. These ranged from making mechanical/electrical systems functional to eliminating temperature-induced vibration, to minimizing the effect of moisture outgassing from the thermal insulation. Additionally, a preliminary flow calibration has been completed, and a series of aerodynamic tests has demonstrated data quality and provided Reynolds number effects on several configurations. Currently, a major effort is under way, through the summer of 1988, which is devoted to improving operating efficiency with a goal of being ready to efficiently support both research and development testing requirements by the fall.

This paper will review some of the more significant efforts during this time period and summarize the NTF status concerning hardware and instrumentation systems, operating constraints imposed by the cryogenic environment, data quality, and some Reynolds number data.

SYMBOLS

c	wing chord, ft.
C_L	lift coefficient
C_l	rolling moment coefficient
C_{l_β}	rolling moment coefficient due to sideslip
C_N	normal force coefficient
C_n	yawing moment coefficient
C_{n_β}	yawing moment coefficient due to sideslip
C_p	pressure coefficient
°F	degrees Fahrenheit
GPM	gallons per minute
HP	horsepower
LN_2	liquid nitrogen
M	Mach number
mv	milivolts
P_T	total pressure
P_∞	free-stream static pressure
$\tilde{p}$	root mean square (rms) value of fluctuating component of static pressure
q	dynamic pressure
RN	Reynolds number
T	stagnation temperature
U	mean velocity streamwise
$\tilde{U}$	rms value of mean velocity streamwise
$\frac{x}{c}$	fraction of chord
$\frac{dM}{dx}$	partial derivative of Mach number with respect to test section length
α	model angle of attack

β model sideslip angle

ΔW test section floor and ceiling angle relative to the horizontal

TESTING AND CHECKOUT EXPERIENCE

The testing and checkout experience is summarized in figure 2. The initial start-up experience (prior to 1985) is reported in references 1 to 3. As stated previously, the testing that has been accomplished to date has a two-fold purpose of providing aerodynamic data and exposing testing problems associated with the tunnel and instrumentation systems. Nine of the configurations tested are shown in figure 3 which collectively utilized the maximum capability of the NTF at both ambient and cryogenic conditions over the Mach number range. Two other aircraft configurations have also been tested but will not be discussed here. The primary model used for checkout of both tunnel and instrumentation systems was the Pathfinder I which has a high aspect ratio wing with a supercritical airfoil (reference 4). This model was first installed in the tunnel during the first quarter of 1985.

The major areas receiving attention during the checkout are listed at the bottom of figure 2 and include model access, process controls, moisture in the tunnel, model vibration, and tunnel/test instrumentation. All of these problems were worked simultaneously as indicated by the figure and were phased in with the testing schedule as appropriate. The tunnel was unavailable for cryogenic operation during most of the first half of 1987 due to a failure of an expansion joint in the liquid nitrogen supply system.

Model Access. - Access to the model requires the movement of large components within the tunnel, (figures 4, 5, and 6), over the temperature range from ambient to fully cryogenic. The details of this system are defined in references 3 and 5. The test section plenum is isolated from the rest of the tunnel circuit by large isolation valves. The process of putting these valves in place involves unlocking and translating a large section of the contraction cone and the high speed diffuser away from the plenum; this process uses dual electrical driven actuators with a seven-foot stroke which must operate in phase on each component. Additionally, the ability to make up limit switches or components to fairly close tolerance where the components may be exposed to large temperature excursions is required. With the plenum vented to atmospheric pressure, the 9- by 12-foot doors in the pressure shell are opened and the test section sidewalls are dropped so that access housings may be inserted to encapsulate the model as shown in figures 5 and 6. The reliable movement of these large components at cryogenic temperatures has required several modifications to the basic actuation concept. These modifications have resulted from operational experience and were implemented over the past 3 years. A final series of modifications to these components is being made during the current enhancement period which should make it a fully operational system.

Process Controls. - The primary controls for the tunnel are closed loop and provide fast response interactive control of pressure, temperature, and Mach number and control of model attitude (see figure 7). The controls for the test section variables (tunnel walls and re-entry flaps) are also closed loop but have slower response requirements.

A detailed description of the process controls is provided in reference 6 and only a brief summary will be presented here. The approach used in design of the pressure, temperature, and Mach number controls involved using a mathematical model of the process to determine circuit response characteristics in order to establish the design criteria for the control hardware and the initial control laws. This approach as indicated in figure 8 required measurement of actual tunnel response characteristics for verification of the control laws and update of the math model. This effort was a first priority in the early tunnel operation and indicated that the accuracy required could not be obtained due to insufficient system resolution and excessive instrumentation noise. To correct this problem the microprocessors, servo control valves, and instrumention were upgraded. The upgraded stagnation pressure and Mach number control systems were completed in the first half of last year. The Mach number system provides a rapid response and will control around set point to within ±0.001. The last system to become fully operational was the temperature control. Initially, this system was based on a measurement of the liquid nitrogen flow rate entering the tunnel. Minimal success was obtained in making this measurement and an alternative approach which calculates the flow rate has been recently implemented and provides adequate performance.

Moisture Contamination. - During the early operation of the NTF at Cryogenic temperatures, a coating was observed on several models that had a frost-like appearance. Quantifiable measurements of the extent of the coating were not obtainable. However, it was clear that frost-like crystals were forming and that reflected light was making it visible with a television system. An extensive study was undertaken to determine the contaminating substance and its source as well as its possible effect on the aerodynamic data. This study identified the contaminant to be water.

Further evaluation of the incoming liquid nitrogen, various tunnel purge technique, and samples of the thermal insulation system identified the insulation as the water source. The closed-cell polyisocyanhrate foam used for the thermal insulation has been shown to have approximately 1.5 percent water by weight. (As a reference, dry wood has approximately 6-percent water by weight.) The problem, as shown in figure 9, is that at the cryogenic temperatures only a very small quantity of water is required to saturate the free-stream gas. For example, at -70°F only about 0.2 pounds of water is required to saturate all of the gas in the tunnel at atmospheric pressure, while at +70°F about 200 lbs of water is required. Two questions naturally arise at this point. How to eliminate the moisture, and what is its effect on the aerodynamic data measurements? Extensive investigations have been conducted in both areas. With regard to the question of eliminating the moisture, the studies have indicated that the simplest solution appears to be drying the tunnel and then maintaining a dry environment. Drying has been accomplished in the past by maintaining the tunnel at the maximum warm temperature (approximately 150°F) for several hours in dry nitrogen gas with a periodic purge. The diffusion of water from the insulation in the NTF is a maximum at this condition as indicated in figure 10. The figure also illustrates the reduction in diffusion with decreasing temperature which is, of course, a favorable effect. Since in the nitrogen operating mode the tunnel is continuously vented, i.e., purged to maintain constant stagnation pressure, test conditions with very small amounts of condensation can be obtained. Aerodynamic studies conducted under these conditions, which will be discussed later, have indicated that the resulting effects on the aerodynamic data are not measurable.

Therefore, the plannned approach when the tunnel is brought back into operation at the conclusion of the current enhancement period will be to dry it for several days and keep it closed to atmospheric air. It should be pointed out that the drying process takes place in static as well as operating conditions; therefore, it continues to dry over weekends and nonworking shifts.

The two cryogenic tunnels in Europe with internal insulation, KKK at Köln and T2 at Toulouse, have experienced similar moisture concerns and have also reached the conclusion that they can achieve conditions of dryness where effects on the aerodynamic data are not measurable. We are convinced from experience to date, with the NTF and other studies, that procedures can be followed that will eliminate moisture contamination as a concern regarding aerodynamic data quality.

Model Vibration. - Significant vibration of the model/balance combination in the lateral plane has been encountered at some conditions since the initial operation of the NTF. After some period of operation the vibration was found to be more severe when the structure was cold. The model pitch system is illustrated in figure 11 and is composed of an arc sector driven by a hydraulic cylinder. Restraint is provided by a series of bearing pads located at both the top and bottom of the sector. The loads are transmitted through the pads to the internal tunnel structure. There is also a fairing on the downstream part of the sector that is fixed to the tunnel structure and provides a cavity for instrumentation leads. The attachment of the fixed fairing to the arc sector is a slip joint which allows the sector to move independently of the fairing. The bearing pads, while providing restraint, also have clearance to allow for thermally induced movement of the internal structure.

The vibration problem has been investigated both experimentally and analytically. In the experimental investigation, the Pathfinder model was used as a test vehicle. Both it and the model support system were extensively instrumented as follows:

a. Six component force balance and 3-axis accelerometer package in the Pathfinder model

b. Pressure tranducers in the fixed fairing and test section walls

c. Accelerometers on the fixed fairing, bearing pads, and the surrounding tunnel support structure

d. Strain gages and thermocouples on the tunnel support structure

The analytical investigation involved detailed calculations of the dynamic structural respose and of the unsteady aerodynamic characteristics of the model support system.

Experimental observations were made of the dynamic structural response characteristics, Mach number, dynamic pressure, test temperature, and coldsoak time. The installation of vortex generators and splitter plate on the fixed fairing afterbody helped to identify unsteady flow at the rear of the arc sector as one of the sources of dynamic excitation. Eventually, the primary factor governing the dynamic response of the model was found to be the clearance tolerance between the bearing pads and the surface of the arc sector. A

procedure was evolved for setting the clearance adjustment which reduced the model dynamic response to acceptably low levels independent of temperature cycling. Some of the test results are illustrated in figure 12 which shows the dynamic yawing moment as a function of stagnation temperature for several of the test configurations of the arc sector. Although the low level shown in the figure for the last case is completely satisfactory, it may be sensitive to adjustment with time due to temperature cycling.

Instrumentation. - For several years prior to initial operation of the NTF an extensive research and development program was undertaken by the Instrument Research Division at Langley to develop instrumentation systems for basic measurements of forces and moments, pressures, and angle of attack that would function with both reliability and accuracy in the cryogenic environment. The results of this program were the development of strain gage balances that were not temperature controlled and heated instrument packages for pressure and angle of attack measurements. These instrument systems were developed in cryogenic chambers and verified to the extent possible, in the 0.3-Meter Transonic Cryogenic Tunnel and indicated good performance and soundness of the basic concepts. Upon application of these instruments to models in the NTF, there were several system problems that had to be resolved. The most significant of these were the effect of leads required to support the pressure instrumentation system on the balance axial force component, and the calibration system for the electronic scanning pressure (ESP) system. Recent tests, both in the NTF and in the cryogenic checkout chamber, have indicated satisfactory resoultion of both of these problems.

As will be discussed in a later section, a strong concern from the outset has been data quality. In this regard, an extensive effort has been carried out to eliminate data scatter due to electrical noise and extraneous signals. Care was taken from the beginning to provide a "clean" instrumentation ground, but as is often the case, extraneous signals can creep into the system. A significant effort has been made over the past year to track down and eliminate noise sources that were infiltrating the data system. The results of this effort are indicated in figure 13. The figure illustrates a reduction in data scatter by a factor of 5 to a level less than 10 microvolts. This level corresponds to a balance error of less than 0.1 percent of full scale.

OPERATING CONSTRAINTS

The NTF has the general appearance of, and is often talked about, as a typical continuous operating fan driven wind tunnel that has the potential to mass produce data on a continuous basis. Although in principle the potential exists, it is somewhat misleading to think about a large cryogenic tunnel in this context. In reality the operation must be viewed much as a blow-down tunnel with efforts directed toward minimizing run time and maximizing data gathering rates. The two main constraints with regard to run time are liquid nitrogen logistics and costs, and model access. It was shown in the early 1970's that the application of cryogenics to wind tunnel testing provided the most cost effective approach to high Reynolds number testing. This does not mean, however, that testing at high Reynolds numbers will carry the same cost and degree of complexity as testing in the many ambient temperature and pressure tunnels around the country. This is illustrated in figure 14 where the energy cost ratio (liquid nitrogen is a form of energy) is shown as a function

of Reynolds number ratio for the NTF compared to the Langley 16-Foot Transonic Tunnel. An order of magnitude increase in Reynolds number has an energy cost ratio of approximatley 44. In the cases where high Reynolds number is required for research or development testing, the cost is cheap compared to flight test. But because of this cost difference, test programs and objectives must be carefully defined and supported by adequate precursor studies at low Reynolds numbers. Therefore, it is not well suited for researchers to exercise broad freedom or for indiscriminate development programs.

LN_2 Supply System. - Liquid nitrogen is supplied to the NTF by a commercial air separation plant located adjacent to the Langley property and connected to the NTF site by a pipeline. The capability of this system is shown in figure 15. The challenge is to optimize the interface of the plant which operates continuously 24 hours per day at a 300 ton per day rate with the intermittent operation of the NTF, which can use LN_2 to a maximum rate of 30 tons per minute. This requires, of course, storage tanks to serve as a buffer. The current system has a 2100 ton storage tank at the plant and a 700 ton tank located at the NTF with capability to transfer approximately one tank per 24 hour day. The system can sustain a use rate of 2100 tons per week and if the tunnel has not been using nitrogen for a while, can build up to a maximum quantity available of 4800 tons for a week. This tends to optimize on two week test programs using liquid nitrogen assuming all tanks are full at the start. The maximum transfer rate of the pipeline is 656 tons or approximately one NTF tankful per day; therefore, the maximum use rate is one tankful per day. As shown in figure 16, if operation is started on Monday morning with the equivalent of four NTF tankfuls available and used at a rate of 1 tank per day, with 0.5 tanks being resupplied by the plant, and no use over the weekend, the total supply is exhausted by the end of the second week. The options at that point are either to operate on one-half tank per day (the plant output) which is not practical, or to allow 8 days for the nitrogen supply to be replenished and use the tunnel in the air mode or some other capacity during this period. This use scenario can be changed, of course, by increasing the plant capacity and/or storage and transfer rate. A decision to increase the plant capacity must take into consideration long term use rates. The most immediate benefit will be provided by an increase in storage capacity and associated transfer rates. Current plans are to triple the NTF onsite storage capacity in FY 1990. This will tend to optimize at about a three week test program in nitrogen.

The most important aspect of the tunnel operation from cost considerations is the speed of changing test conditions and data acquisition. This is driven primarily by the degree and quality of automation. Figure 17 illustrates the impact of time per data point for a typical test condition of $M = 0.8$ and temperature = -250°F. This illustration includes time to change angle of attack and Mach number and adjust temperature and pressure. When the NTF was first brought on-line and manual control was used, times averaged greater than 45 seconds per point. After the current enhancement period it is expected to be under 30 seconds per point with a goal of 7 to 10 seconds per point with further refinements in the control and operating system. The reduction in electrical signal noise discussed earlier has a direct impact on this in that it reduces the number of data samples required to be averaged to obtain high quality data.

DATA QUALITY

In this section the status of flow calibrations and efforts to assess data quality will be discussed. The discussion will include both steady and dynamic aspects of the flow calibration, the ability to measure Mach numbers and angle of attack, importance of wall boundary effects, and the effect of moisture contamination or "frost" on the data.

Flow Calibration. - As reported previously, references 3 to 10, the NTF has been operated throughout the operating envelope as shown in the upper left of figure 18. The initial calibration looked at the distributions of temperature, pressure, Mach number, and flow angularity on the tunnel centerline as measured by the model upright and inverted. More recent efforts concerned the details of the Mach number calibration and the effect of temperature on flow angle.

The ability to vary the test section wall angle provides the capability to maintain zero Mach number gradient through the test section, thus eliminating model buoyancy effects in the empty tunnel for all test conditions. A typical variation of wall angle with Mach number is shown in the left of figure 19. This particular case is for a warm temperature of 100°F and varies from approximately 0.2° convergence at M = 0.2 to 0.4° divergence at M = 1.15. A typical correction to Mach number as calculated from the plenum static or reference pressure is also shown. In general the quality of the steady flow appears to be excellent and sufficient adjustments are available on the test section geometry, i.e., wall angle and re-entry flap settings, to eliminate the existence of any Mach number gradients in the empty tunnel.

In order to investigate the effect of tunnel structural deformation due to temperature gradients in the structure on flow angle with temperature, frequent measurements of flow angle have been made during the last several test programs. The data presented in figure 20 are typical of results obtained from these measurements. With the exception of one point the effective flow angle is always equal to or less than 0.02° which is approaching the measurement accuracy. This effect will continue to be monitored until sufficient history is developed to have a firm basis for determining the required frequency of flow angle measurements.

NTF Dynamic Flow Quality. - In 1980 while the NTF was still under construction, the plans for flow quality measurement were described extensively in reference 11. The measurements were to consist primarily of fluctuating pressure and velocity measurements. Since that time, hot-film probes and fluctuating pressure gages have been operated in the test section at the locations indicated in figure 21, and further tests are planned as also shown.

Some results of the measurements made to date are shown in figures 22 and 23. These results have been excerpted from work by W. B. Igoe on a proposed doctoral dissertation to be submitted to the George Washington University. Figure 22 shows the root-mean-square fluctuating static pressure measured in the NTF as a function of Mach number for a unit Reynolds number of 6 million per foot. The fluctuating pressures were measured in air on the test section sidewall and have been divided by free-stream static pressure. Fluctuating static pressures have been measured in the free stream in a number of other large transonic wind tunnels using a 10° cone on the centerline (see

reference 12 for example). Some of these results have been included for comparison in figure 22 for a Reynolds number range of 1.3 to 5 million per foot.

The results of hot-film probe measurements at low Mach number in the test section are shown in figure 23. These measurements were made in the free stream in air with the slots closed. Results are shown for the streamwise measurements at total pressures of 1 and 8 atm. Although there is considerable scatter at a pressure of 1 atm, the measurement levels are about 0.1 percent, which was the target level for the NTF. Streamwise hot-wire probe measurements made in the Langley Low Turbulence Pressure Tunnel (LTPT) at total pressures of 1 and 10 atm (reference 13) are shown for comparison.

Further measurements in the NTF are planned using fluctuating static pressure probes in the test section free stream, and hot-film probes in the test section, settling chamber, and in the vicinity of the cooling coil and screens. The measurements will be made over the full operating range of the NTF. By the time the measurements are completed, the dynamic flow quality of the NTF will have been fully documented.

Mach Number and Angle of Attack Sensitivities. - Prior to looking at either Reynolds number effects or the effects of frost on data quality, it was desirable to obtain an assessment of the sensitivity of the model to the basic test parameters, Mach number and angle of attack, and some qualitative assessment of our ability to measure them. As stated in the introduction, the primary model used for assessing data quality was the Pathfinder I Model. This model was built early in the program for the purpose of developing model design and fabrication technology as well as providing a research model. It has an aspect ratio 10 wing with a supercritical airfoil section typical of supercritical airfoil design technology of the mid 1970's. As a result, shock movement is very sensitive to small changes around the design point in Mach number and angle of attack. This made it a good model for use in assessing our ability to measure Mach number and angle of attack in the NTF. Figures 24 to 26 illustrate the results obtained from this assessment. The figures show pressure distributions for an inboard and an outboard wing station at a Mach number around 0.82 with transition fixed at 10 percent of chord. The data of figure 24 shows that a Mach number increment of 0.0038 results in a shock movement of about 6 percent of chord for the outboard wing station. In light of the high degree of sensitivity to Mach number, a series of runs were compared where all variables except Mach number were held constant and Mach number varied in very small increments of 0.0001 to 0.0006. Wing pressure distributions for these cases are shown in figure 25. The data show an orderly progression of shock movement and the well defined curves suggest that both wing pressures and Mach number are being measured with a high degree of accuracy.

The sensitivity of this model to angle of attack is illustrated in figure 26. In this case, the angle of attack increment was 0.054° with a Mach number difference of 0.0013. Again, the shock movement is about 5 to 6 percent. However, about one half of the movement can be attributed to Mach number effects. These data support the point that the highest quality instrumentation is an absolute requirement for using the NTF to understand incremental effects of Reynolds number and compressibility. Further they support the conclusion that a high degree of accuracy is currently available in the Mach

number, angle of attack, and model pressure measuring systems. The data also underscore the importance of being able to accurately assess wall boundary effects. Recent research on this subject by W. B. Kemp (ref. 14), P. A. Newman and associates (ref. 15), is described by Dr. Newman in a separate session of this symposium. Sophisticated techniques have been developed which utilize measured tunnel wall static pressures to calculate model induced variations of Mach number and upwash through the test section. Figure 27 shows typical contours, in the region of the model, of wall induced Mach number corrections. For this size model at the conditions illustrated the corrections are relatively small, $\Delta M = 0.001$, but as illustrated in the previous figures, corrections of this magnitude are significant if high quality data are to be obtained.

Moisture Contamination "Frost" Effects. - Having established confidence that small incremental effects of the basic test parameters, Mach number, and angle of attack could be both controlled and measured, an investigation to assess the possible effects of frost on the data was undertaken. Care was also taken to insure that comparable test parameters were obtained where the only significant variable was that in one case frost was visible on the model and in the other case it was not visible. Wing pressure distributions from these two cases are compared in figure 28. Although care was exercised in setting the test parameters it should be noted that the Mach number is different by 0.0004 and the angle of attack by 0.01°. These differences are believed, based on previous discussion, to account for the small difference in shock location shown in the data of figure 28 for the outboard wing station. After accounting for the difference in shock location, there is a small difference in pressure level ahead of the shock that may be a small effect of frost. In general the two cases are in very close agreement and provide confidence that when planned tunnel drying procedures are used and the inside of the tunnel kept closed to atmospheric air, frost on the models will not be a problem with regard to data quality.

REYNOLDS NUMBER EFFECTS

During this initial checkout and testing phase several Reynolds number sensitivity studies have been conducted using both the conventional air mode and the cryogenic capability

Air Operation. - The operating envelope in air is shown in figure 29. It is restricted above a Mach number of 0.4 by the drive power in the variable speed motors. A maximum Reynolds number capability of about 20 million per foot at a Mach number of 0.38 is available. This Reynolds number is the maximum available in this speed range and tunnel size in the United States. One of the attractive features of this capability is that a constant dynamic pressure line tends to be close to the maximum drive power boundary. Therefore, models designed for testing at high subsonic or transonic speeds at 1 to 2 atmospheres can also be tested at high Reynolds numbers at the lower Mach numbers at the same dynamic pressure and model loads. One case where this was done was the EA-6B wing modification program. The objectives and overall results from this program are described in reference 16. In summary, it involved modifying the wing leading-edge slat and trailing-edge flap airfoil sections with a major goal of improving maximum lift at loiter and maneuver conditions. A photograph of the EA-6B configuration mounted in the NTF is

shown in figure 30. The effect of Reynolds number on the lift characteristics at a Mach number of 0.30 for the basic and modified configuration are shown in figure 31. The 1.4 million Reynolds number case corresponds to testing at 1 atmosphere stagnation pressure. Two points are significant. First, as would be expected, Reynolds number effects on C_{Lmax} are large for all configurations. Second, modifications to the leading-edge slat showed no benefit at the low Reynolds number condition; however, at the higher Reynolds number the slat benefit was approximately equal to that of the flap. These data are an example of the potential pitfalls of relying on low Reynolds number data for configuration refinement. The effect of Reynolds number on lateral and directional stability as measured by C_{l_β} and C_{n_β} are shown in figures 32 and 33. The effects are not as dramatic as those shown for C_{Lmax}, but in general a stabilizing increment in lateral stability was obtained with increasing Reynolds number. The exception to this was the basic configuration above $\alpha = 16°$ and the modified wing configuration with glove and vertical tail extension above α equal about 14°. A more stabilizing effect in C_{n_β} was obtained for all configurations with increasing Reynolds number.

Cryogenic Operations. - Results from three of the configurations tested during this period will be briefly discussed here. They include the Pathfinder I, a Lockheed high-wing transport which was a Lockheed wing tested on the Pathfinder I fuselage, and a rather large submarine model.

The Pathfinder I (figure 34) was tested over a range of conditions; however, most of the test was aimed at evaluating instrumentation and moisture concerns. Most of the high Reynolds number data was obtained in the early test program and in retrospect may have been contaminated with moisture effects and instrumentation errors. Therefore, the data shown in figure 35 are for more intermediate Reynolds numbers (RN = 5 and 18 million) which were known to be free of instrumentation errors. These data are for a Mach number of 0.82, a constant angle of attack and essentially constant lift coefficient with transition fixed at approximately 10-percent chord. These conditions are the design point for the wing. The natural transition point of the 18 million Reynolds number case was estimated to be essentially at the trip location. The effects of Reynolds number are relatively small with only a slight aft movement of the shock indicated at the outboard wing station.

The data for the Lockheed configuration shown in figure 36 show a much more pronounced effect of Reynolds number. A photograph of the model is presented in figure 37. For the case with transition fixed, the strip was located at a constant 1-inch aft of the wing leading edge. The difference in shock location between transition fixed and free at a Reynolds number of 5 million is about 18 percent of chord. A significant difference was obtained by increasing the Reynolds number to 30 million. A further increase to 40 million produced a negligible effect. These data clearly support the well-known need to be able to monitor transition location as a function of Reynolds number if effects at Reynolds numbers less than full scale are to be interpreted.

The submarine test in NTF was unique in that full scale Reynolds number was obtained in a wind tunnel for the first time. A photograph of the model and Reynolds number velocity envelope is presentd in figure 38. Details of the test and data have been omitted for classified security reasons. In the

test both static and dynamic measurements of pressures were obtained through the boundary layer in the plane of the propeller for evaluation and development of scaling laws. As can be seen on the right of figure 38, data in the past using a 6 percent scale model have been obtained at Reynolds numbers about an order of magnitude below full scale. The test in the NTF extended these data well into the region of full-scale submarine operation.

SUMMARY

The National Transonic Facility has been operational in a checkout and test mode for the past 3 years. During this time there have been many challenges associated with testing in a large cryogenic wind tunnel. For the most part they centered around the effect of large temperature excursions on the mechanical movement of large components, the reliable performance of instrumentation systems, and an unexpected moisture problem with dry insulation. Most of these challenges have been met, and it is expected that the rest of them will be met during a major effort that is ongoing through the summer of 1988 to improve operational efficiency. Also, during the past 3 years a preliminary flow calibration has been completed and a data quality evaluation conducted along with high Reynolds number aerodynamic tests of several configurations. Tests were also conducted that provided major inputs to several programs that were not discussed for classification reasons. There is still a requirement for a major effort to develop and implement flow visualization and diagnostic techniques for maximum utilization of the facility. The current NASA facility revitalization program includes funding for these activities in FY'89 and 90. However, from a basic facility standpoint, we believe that it will be ready to efficiently support research and development requirements by the fall of 1988.

REFERENCES

1. McKinney, Linwood W.: Operational Experience with the National Transonic Facility. AGARD-CP-348, 184, 1983.

2. Bruce, Walter E., Jr.; Fuller, Dennis E.; and Igoe, William B.: National Transonic Facility Shakedown Test Results and Calibration Plans. AIAA Paper 84-0584CP, 1985.

3. Bruce, Walter E., Jr.: The U.S. National Transonic Facility - Parts I and II. AGARD Report No. 722, 1985.

4. McKinney, Linwood W.: Considerations in the Selection of the Pathfinder Model Configurations. NASA CP-2111, Part II, 1980.

5. Igoe, William B.: Characteristics and Status of the U.S. National Transonic Facility. Lecture No. 17 of AGARD Lecture Series No. 111, May 1980.

6. Osborn, James A.: A Description of the National Transonic Facility Process Control System. NAA CP-2122, Part I, 1980.

7. Young, Clarence P., Jr.; and Gloss, Blair B. (editors): Cryogenic Wind Tunnel Models. NASA CP-2262, May 1982, pp. 215-256.

8. Kern, Fredrick A.; Knight, Charles W.; and Zasimowich, Richard F.: National Transonic Facility Mach Number System. ISA Paper No. 85-0174, 1985.

9. Ferris, Alice T.: Cryogenic Strain Gage Techniques Used in Force Balance Design for the National Transonic Facility, NASA TM 87712, 1986.

10. Fuller, Dennis E.; and Williams, M. Susan: Testing Experience with the National Transonic Facility. AIAA Paper No. 86-0748CP, 1986.

11. Stainback, P. Calvin; and Fuller, Dennis E.: Flow Quality Measurements in Transonic Wind Tunnel and Planned Calibration of the National Transonic Facility. NASA CP-2183, 1980, pp. 105-121.

12. Doughtery, N. S., Jr.; and Steinle, Frank W., Jr.: Transition Reynolds Number Comparisons in Several Major Transonic Tunnels. AIAA Paper 74-627, 1974.

13. McGhee, Robert J.; Beasley, William D.; and Foster, Jean M.: Recent Modifications and Calibration of th Langley Low Turbulence Pressure Tunnel. NASA TP 2328, July 1984.

14. Kemp, William B., Jr.: A Panel Method Procedure for Interference as Assessment in Slotted-Wall Wind Tunnels. AIAA 88-2537, 1988.

15. Newman, P. A.; Kemp, W. B., Jr.; and Garriz, J. A.: Wall Interference Assessment Corrections. Presented at the Transonic Symposim, NASA Langley Research Center, Hampton, Virginia, April 19-21, 1988.

16. Waggoner, E. G.; and Allison, D. O.: EA-6B High Lift Wing Modifications. AIAA Paper 87-2360-CP, 1987.

ORIGINAL PAGE IS
OF POOR QUALITY

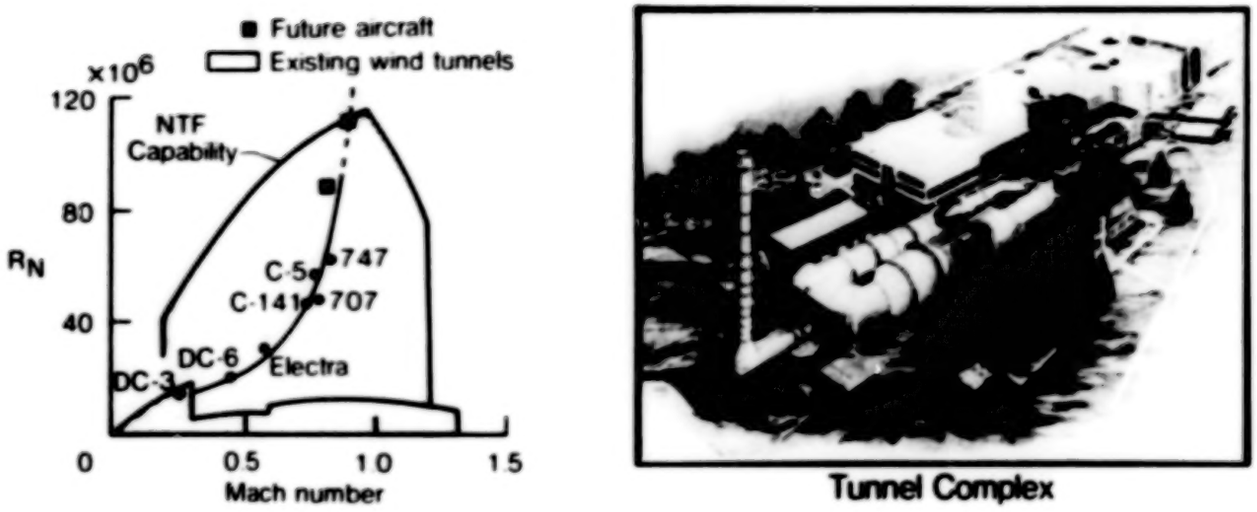

Figure 1. National Transonic Facility perspective and Reynolds number operating envelope.

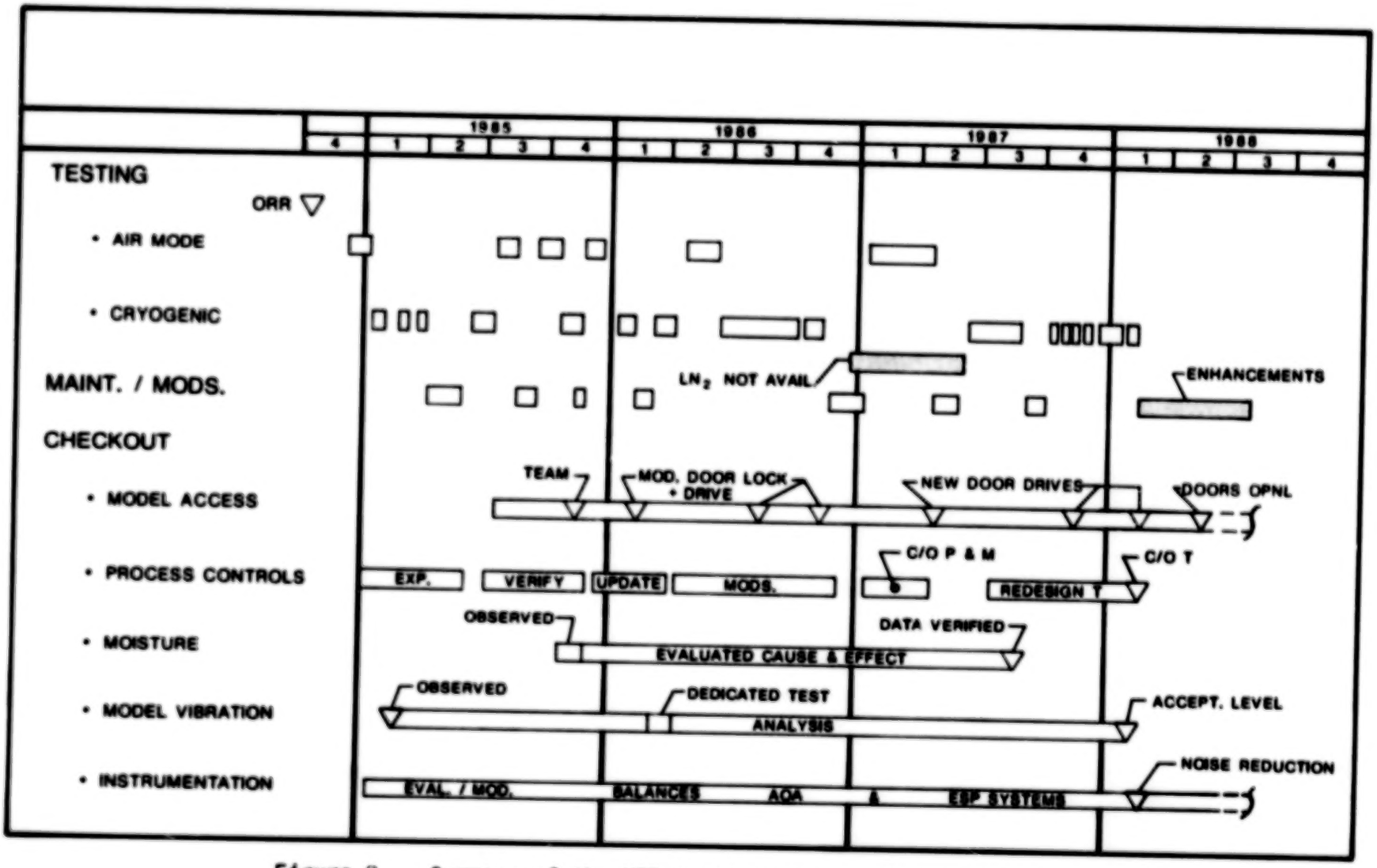

Figure 2. Summary of the NTF testing and checkout experience.

NTF TESTING EXPERIENCE

Figure 3. Photographs of models tested in the NTF.

ORIGINAL PAGE IS
OF POOR QUALITY

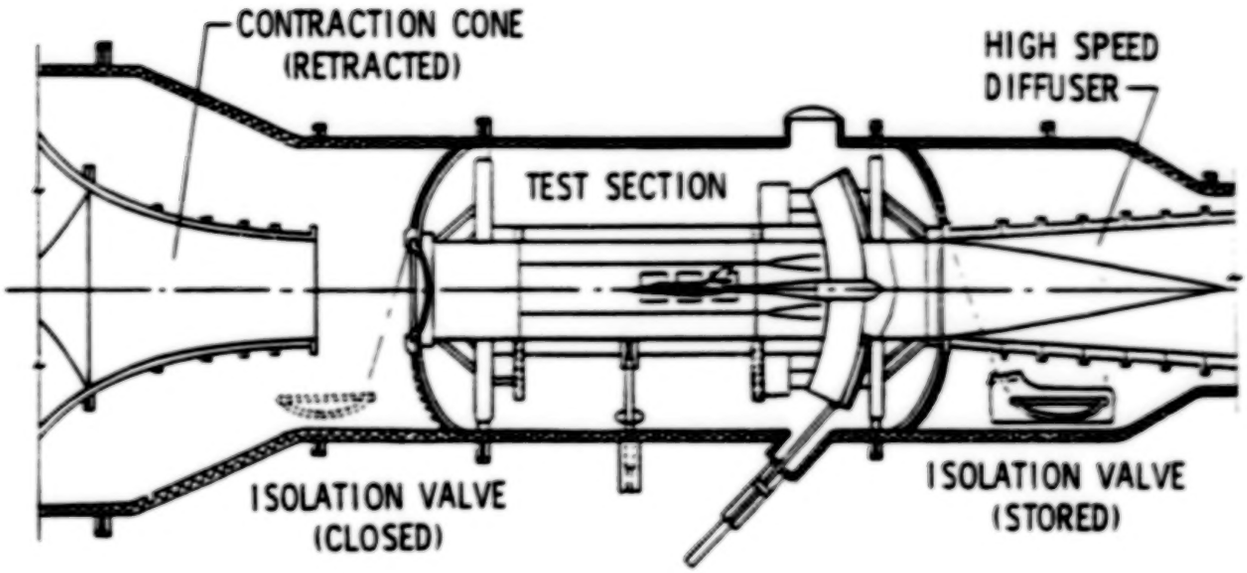

Figure 4. Test section and plenum isolation system.

NATIONAL TRANSONIC FACILITY

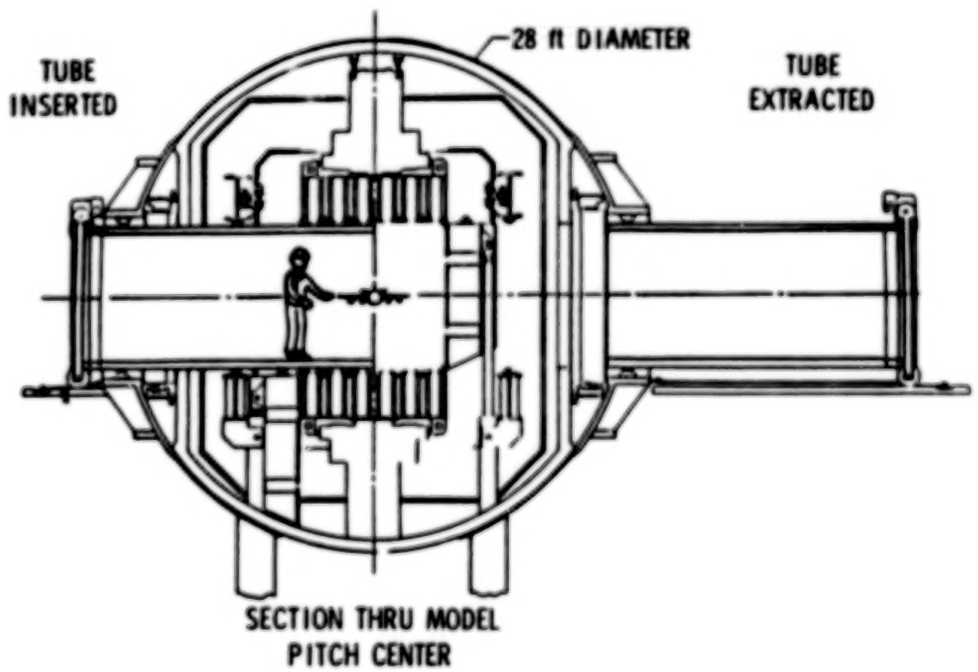

Figure 5. Schematic of model access system illustrating access tubes in the inserted and retracted positions.

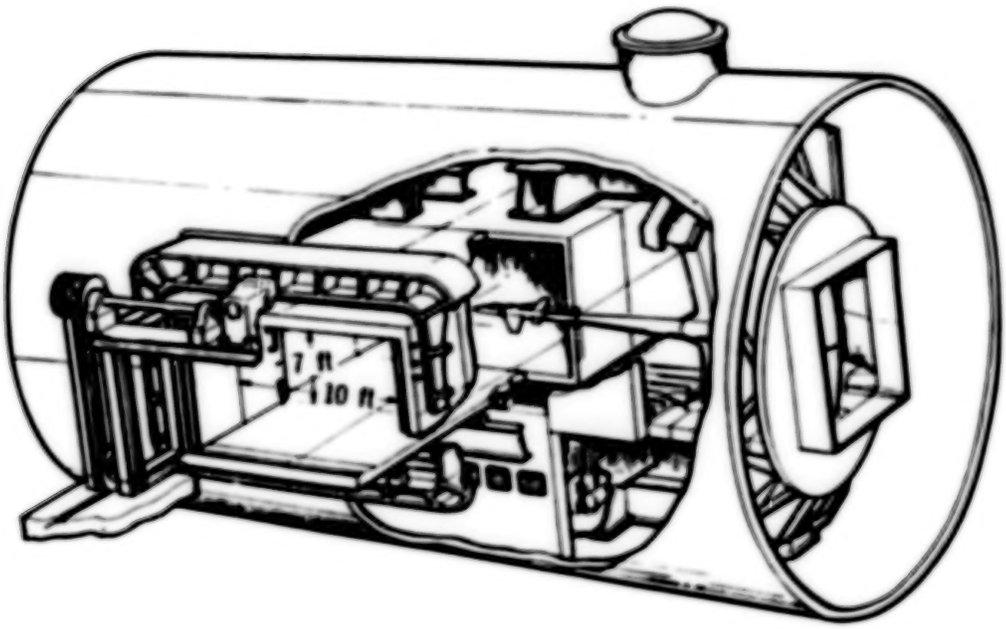

Figure 6. Model access system concept with tubes installed for model entry.

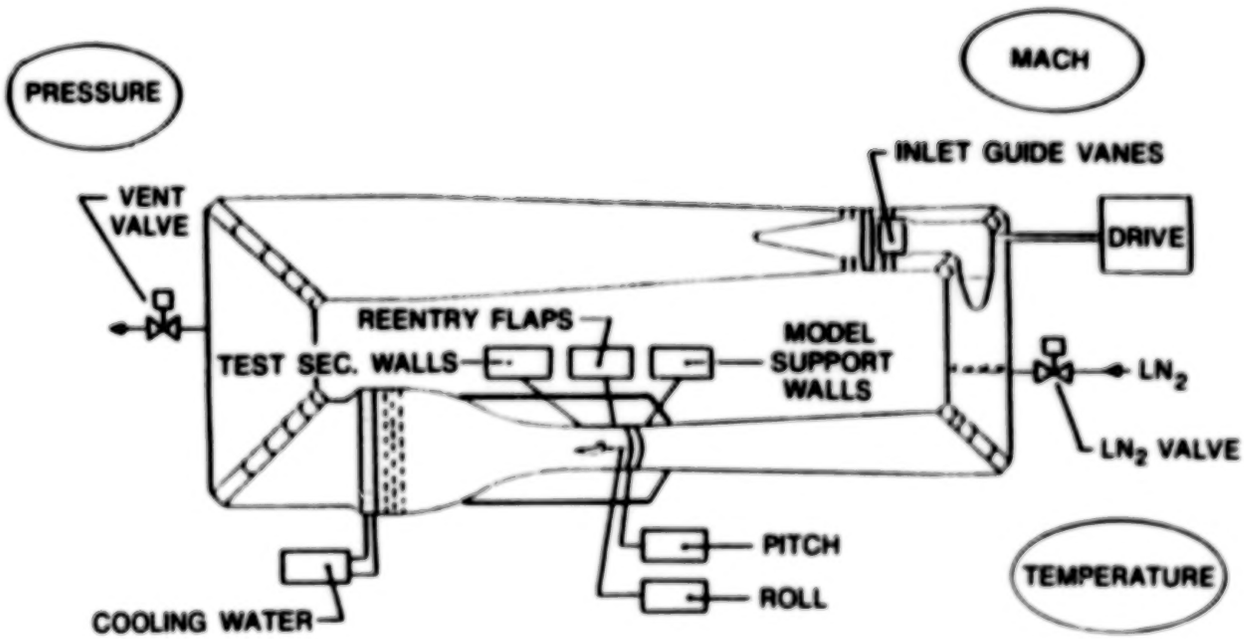

Figure 7. Schematic of NTF process controls.

PRESSURE, MACH NO. & TEMPERATURE CONTROL SYSTEMS

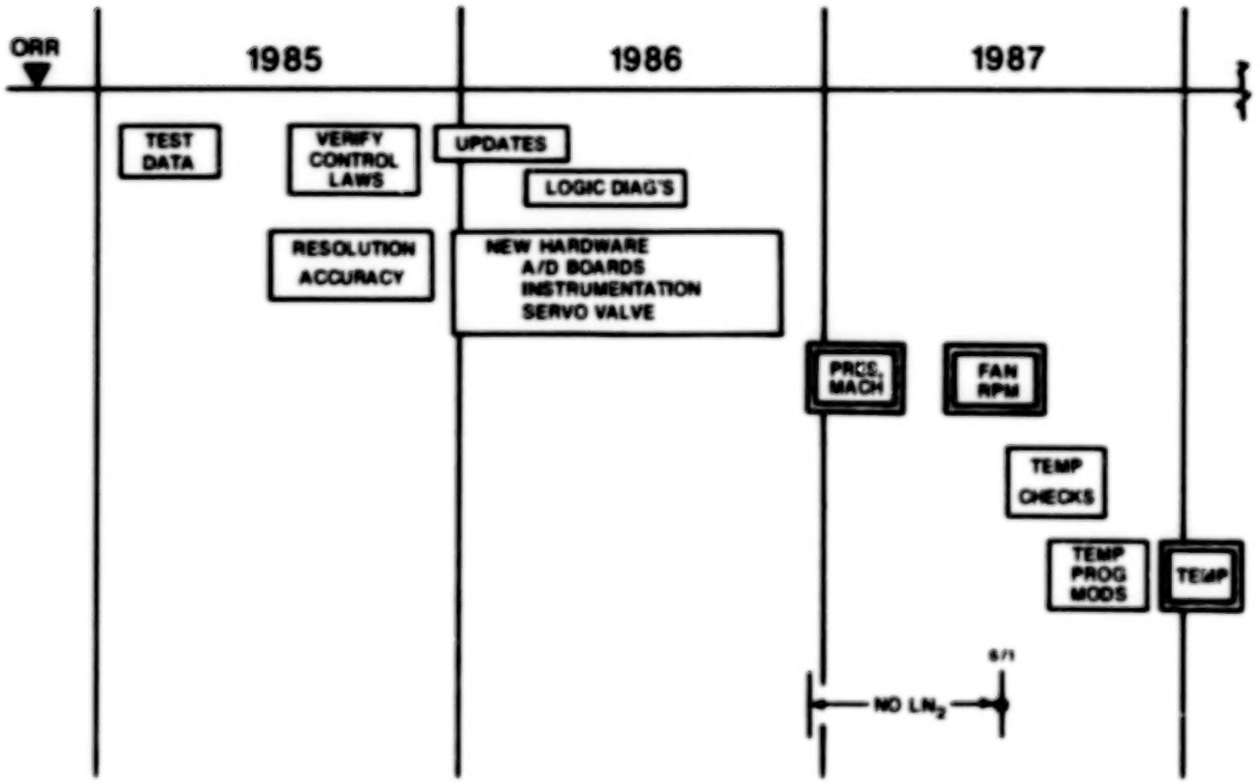

Figure 8. Chronology of events for control system checkout and upgrade.

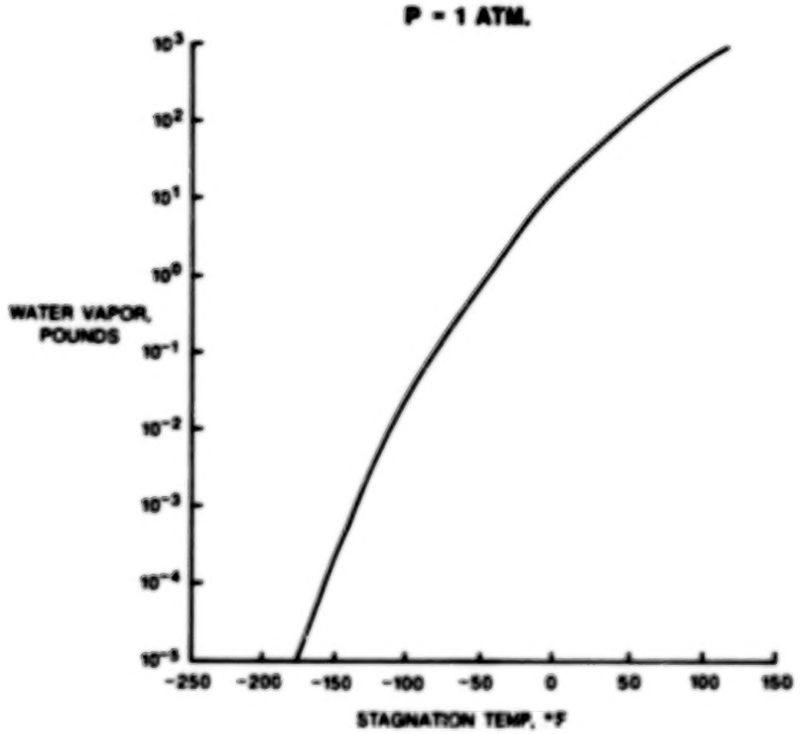

Figure 9. Water vapor required to saturate free-stream gas as a function of stagnation temperature.

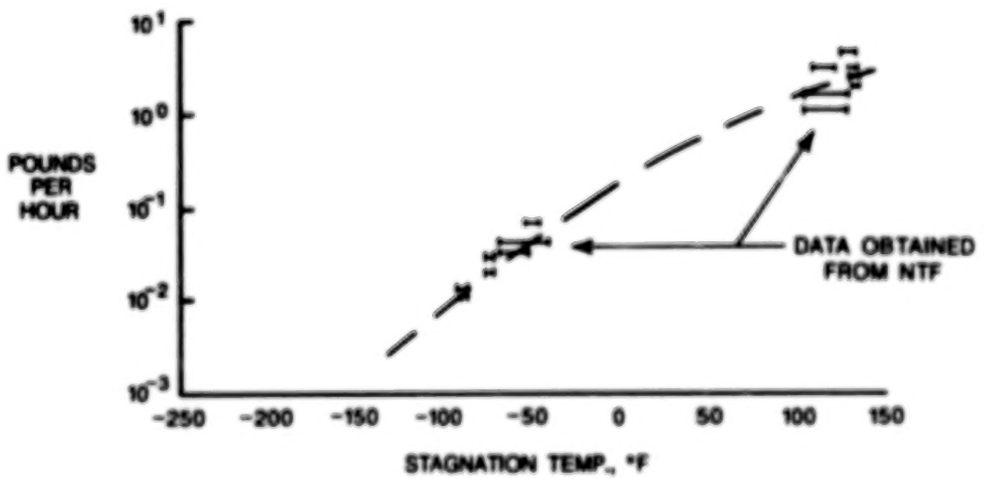

Figure 10. Rate of water transfer from insulation to free-stream gas as a function of stagnation temperature.

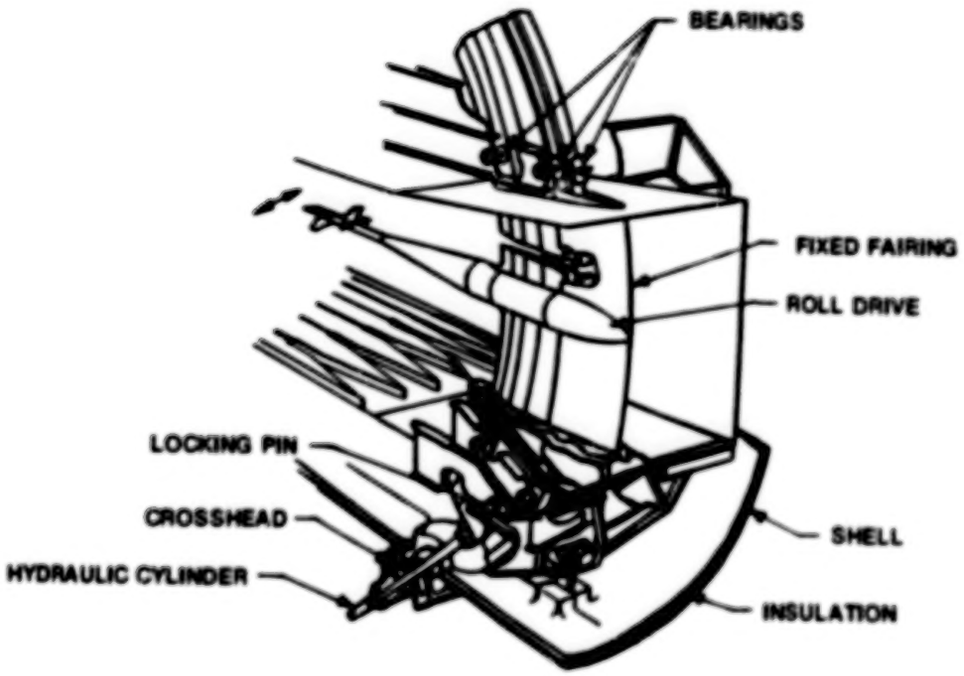

Figure 11. Model sting-support and arc-sector system.

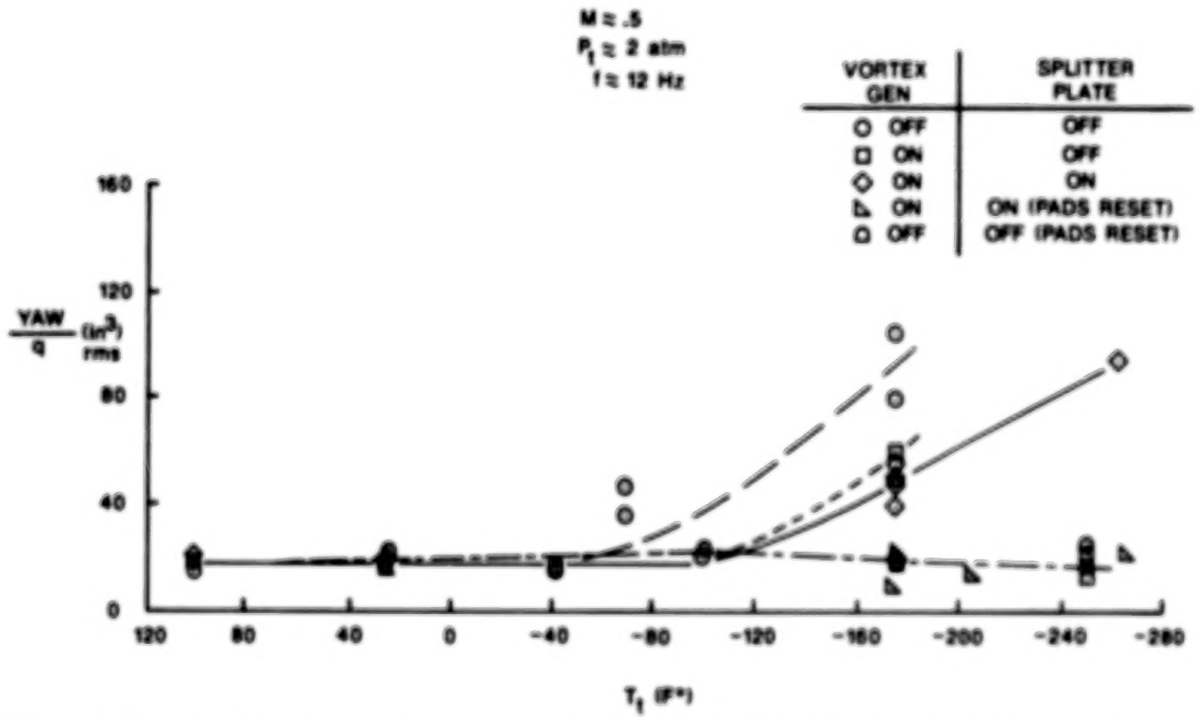

Figure 12. Yawing moment response of the NTF-104 balance with the Pathfinder I Model installed to sting and arc sector dynamics. M = 0.50; P_T = 2 atmos.; f = 12 hz.

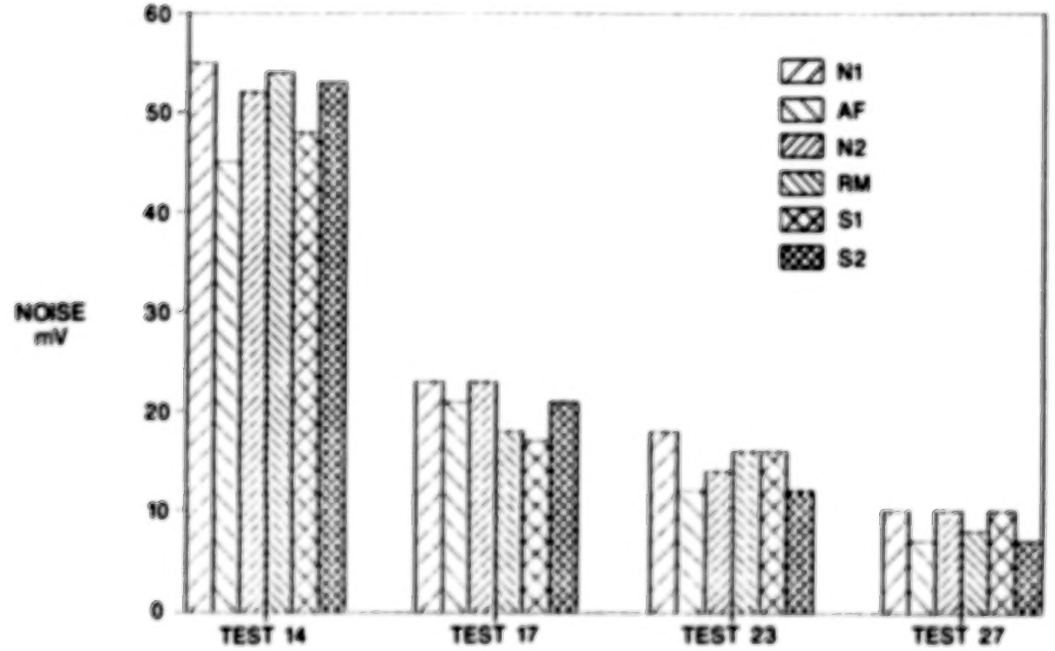

Figure 13. Reduction in electrical noise in the strain gage balance data channels.

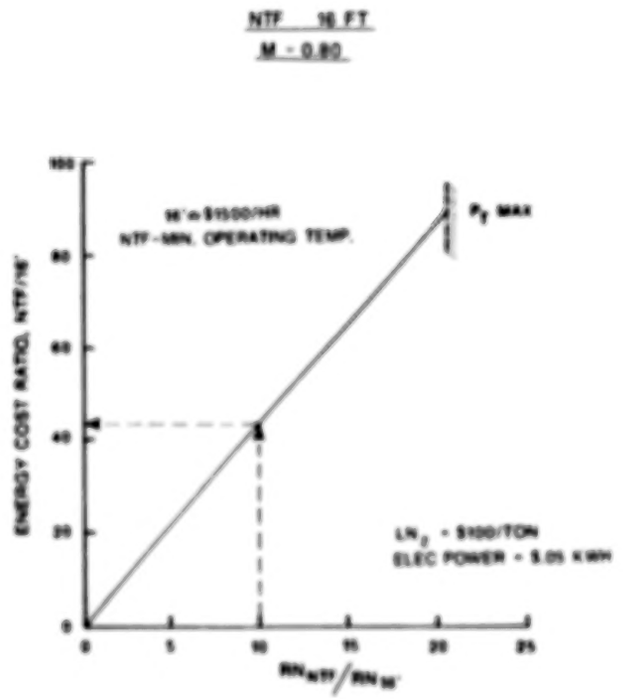

Figure 14. Comparison of operating energy cost between the NTF and the Langley 16-Foot Transonic Tunnel.

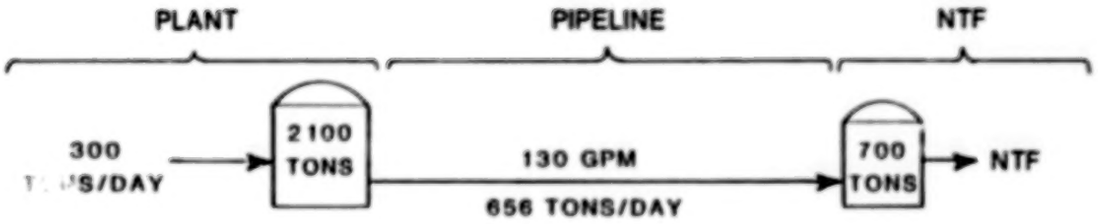

MAX SUSTAINED RATE = 2100 TONS/WK

MAX AVAIL. FOR A WK = 4800 TONS

40 WKS/YEAR = 84,000 TONS

Figure 15. Characteristics of the liquid nitrogen supply system.

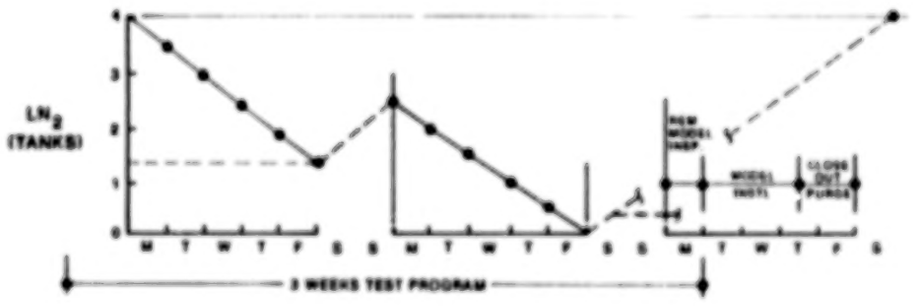

FOR TWO WEEKS OF TESTING

	TONS LN_2
LN_2 AVAILABLE (MAX.)	
BULK STORAGE = 2900 TONS PLANT OUTPUT = 3360 TONS	6300
COOLDOWNS	
2 LARGE ΔT's (300 TO 350°F) 8 SMALLER ΔT's (150°F)	945
PRESSURIZATIONS - 1 PER DAY (AVE)	86
AVAILABLE FOR TESTING	5269

Figure 16. NTF maximum utilization based on LN_2 supply system.

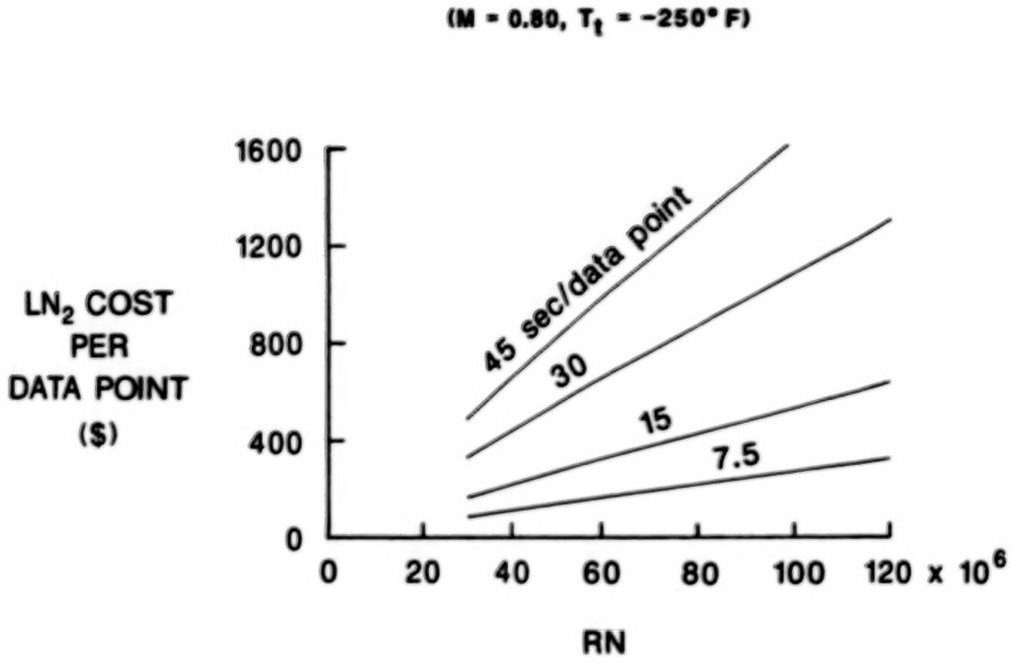

Figure 17. The effect of data sampling rate on liquid nitrogen costs.

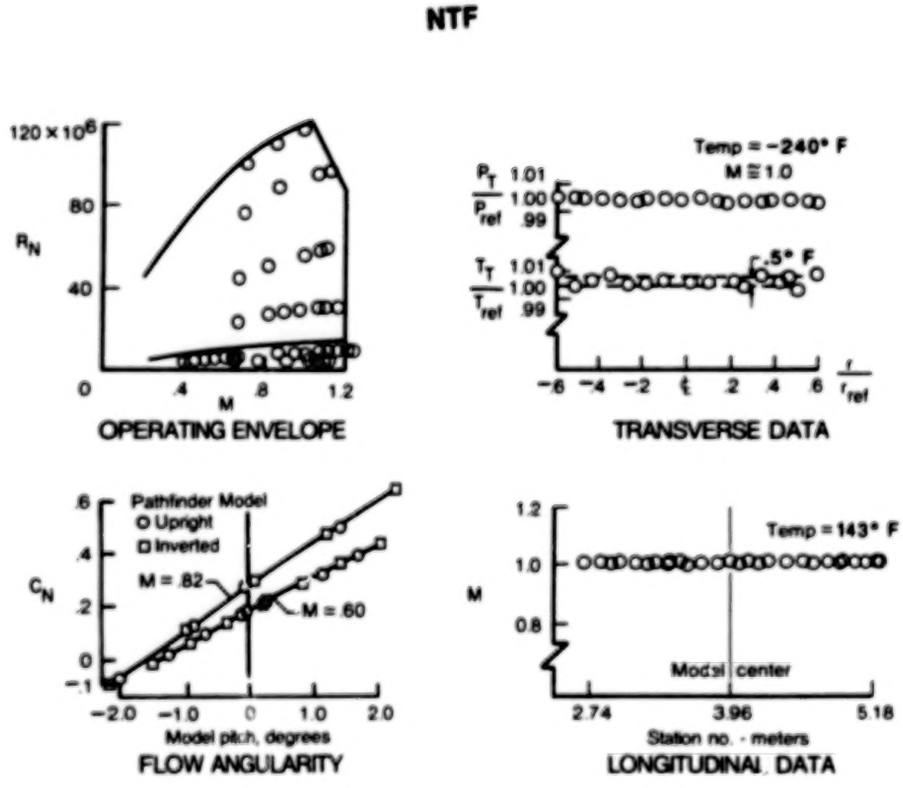

Figure 18. Typical calibration results.

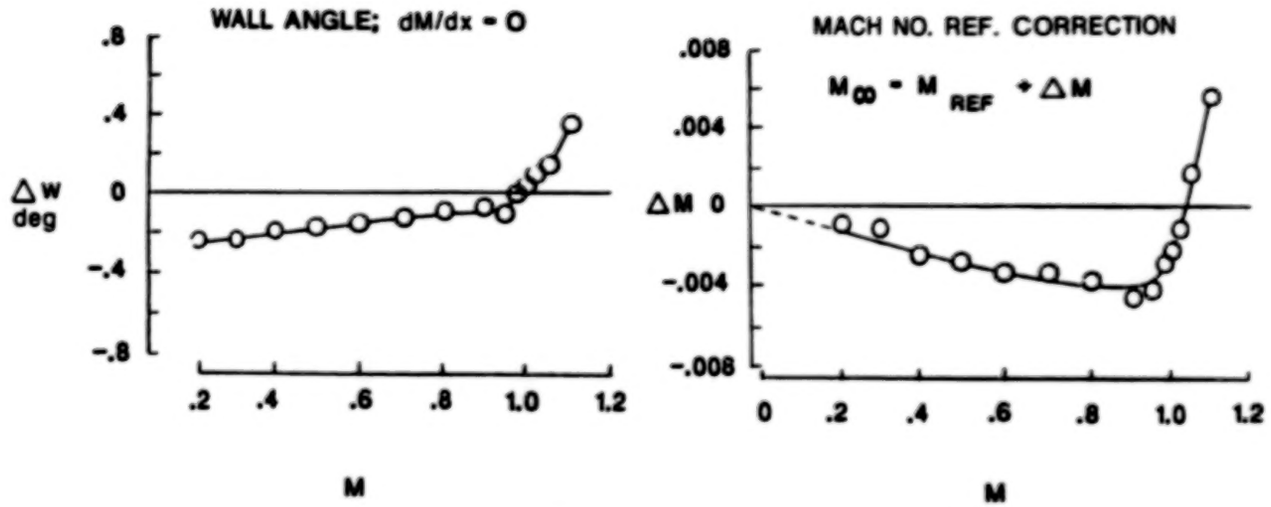

Figure 19. Variations of test section wall angle required for zero Mach number gradient at the model location and correction to reference Mach number with Mach number. Stagnation temperature = 100°F.

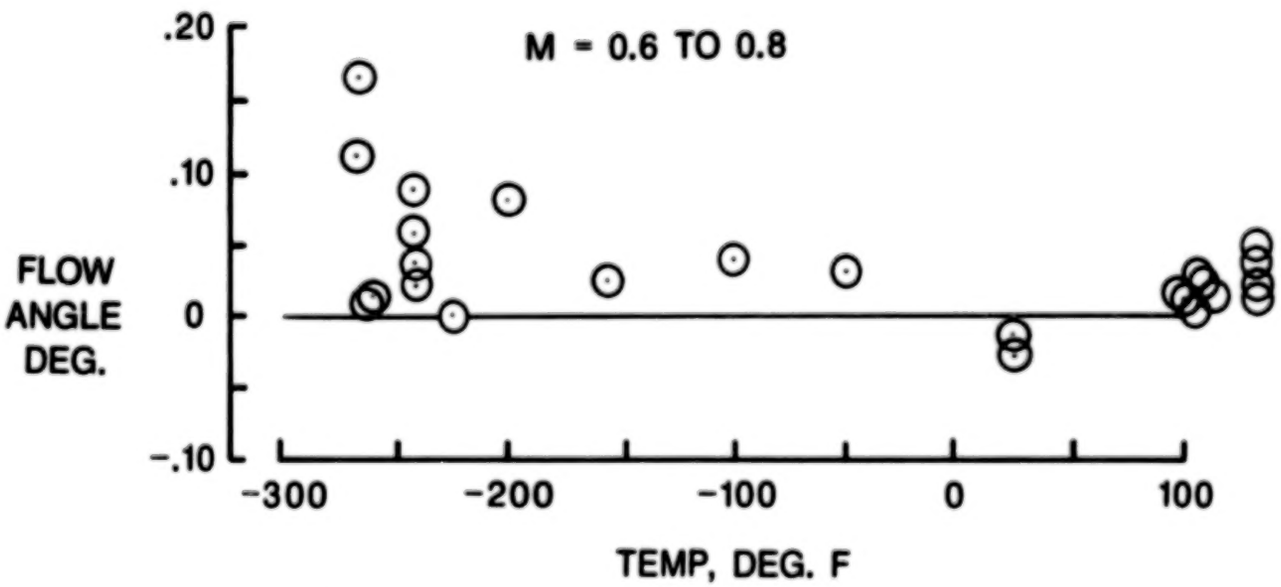

Figure 20. Typical variation of tunnel flow angle with temperature as measured by model upright and inverted. M = 0.82.

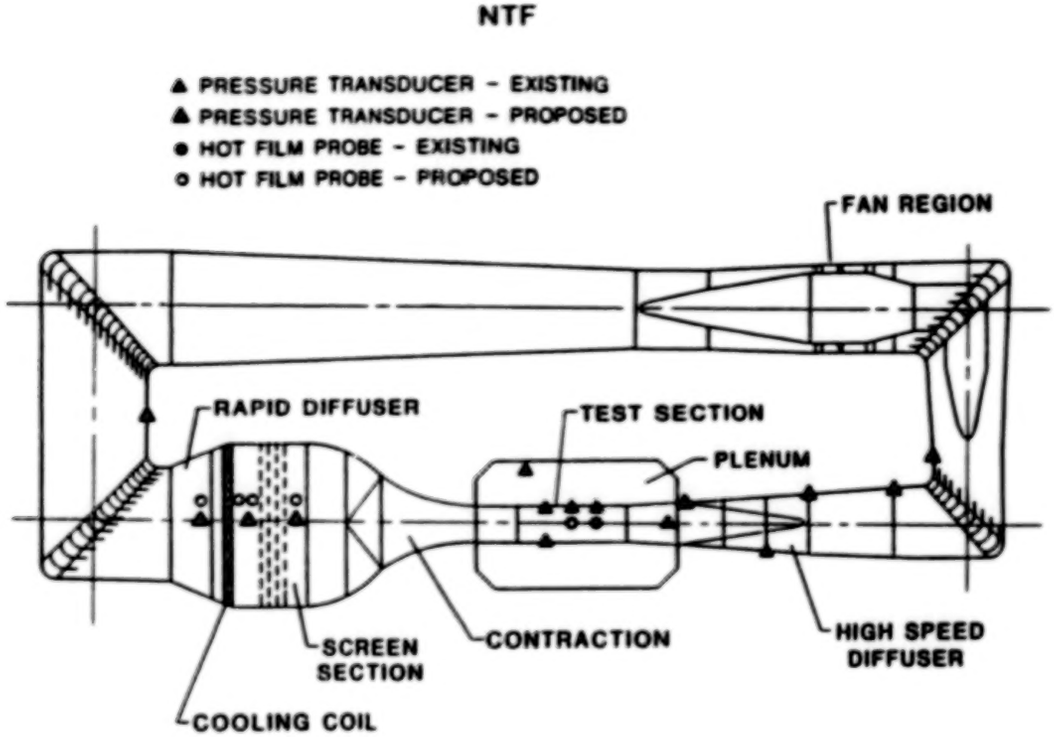

Figure 21. Location of dynamic flow quality measurements.

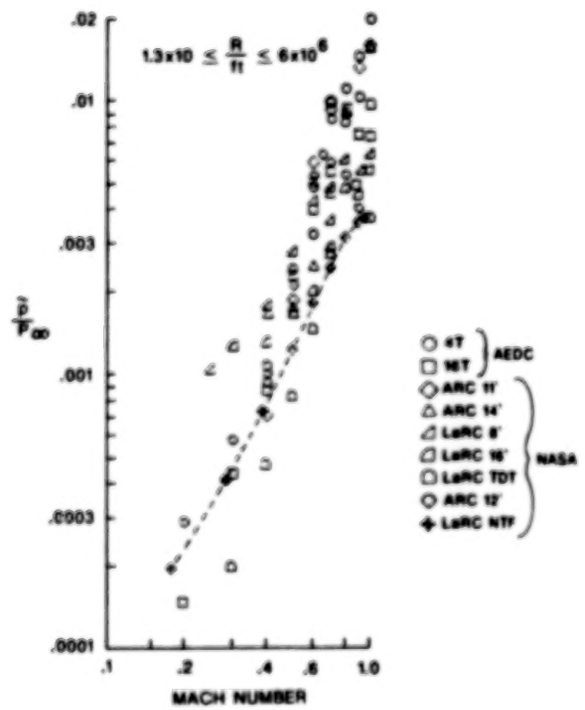

Figure 22. Variation of fluctuating static pressure in the test section with Mach number for several major wind tunnels.

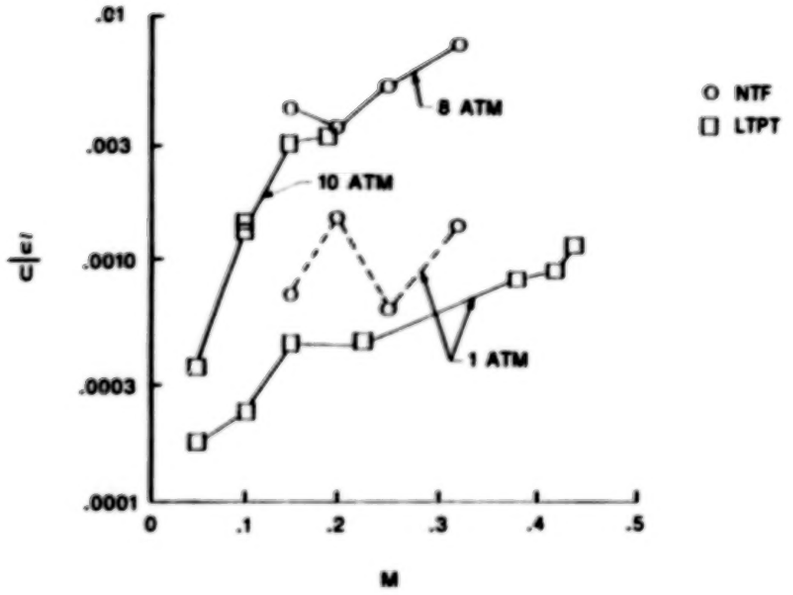

Figure 23. Comparison of turbulence measurements in the test section for the NTF and LTPT.

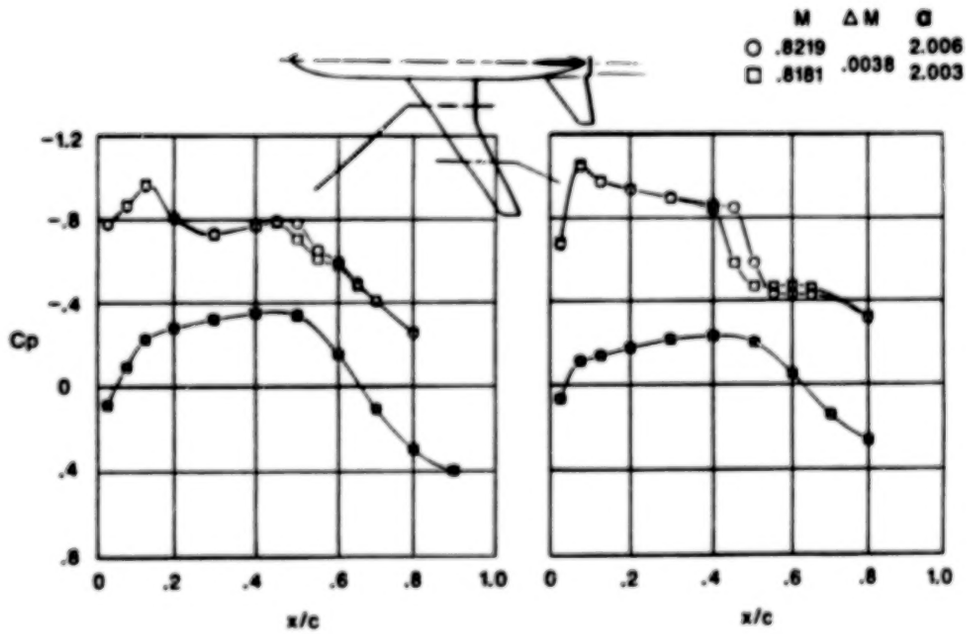

Figure 24. The effect of Mach number on wing pressure distributions for the Pathfinder I model. RN = 6.5 x 10^6; transition fixed at 0.10c.

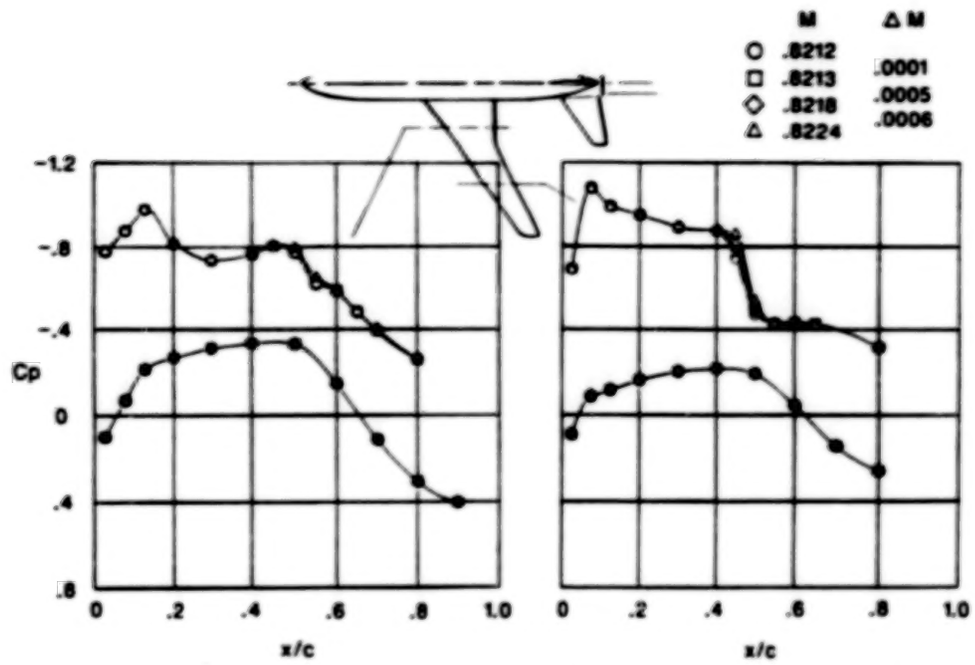

Figure 25. The effect of Mach number on wing pressure distributions for the Pathfinder I model. RN = 8.9 x 10^6; transition fixed at 0.10c.

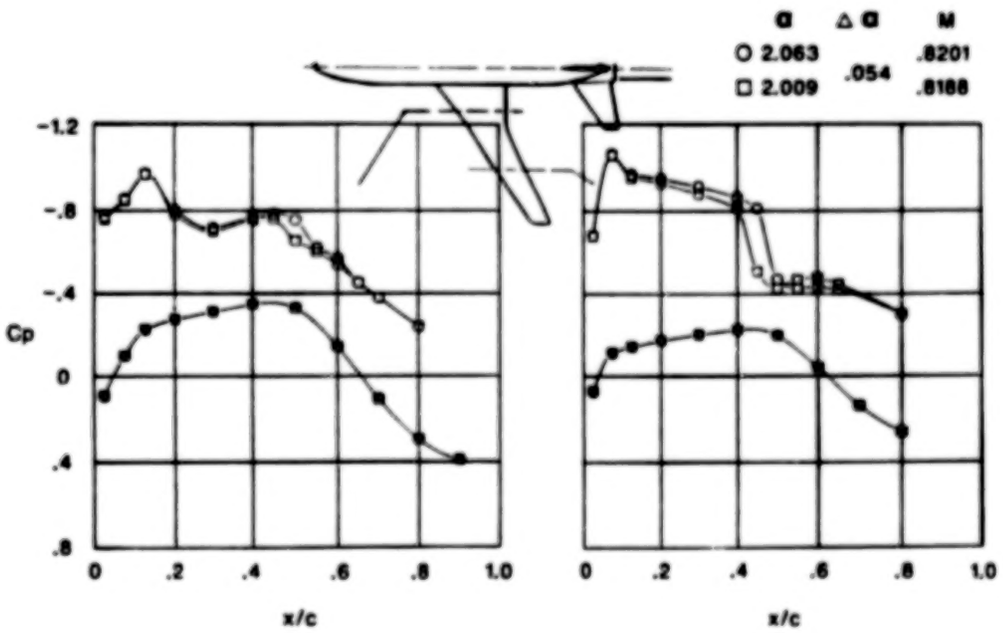

Figure 26. The effect of angle of attack on wing pressure distributions for the Pathfinder I model. RN = 6.0 x 10^6; transition fixed at 0.10c.

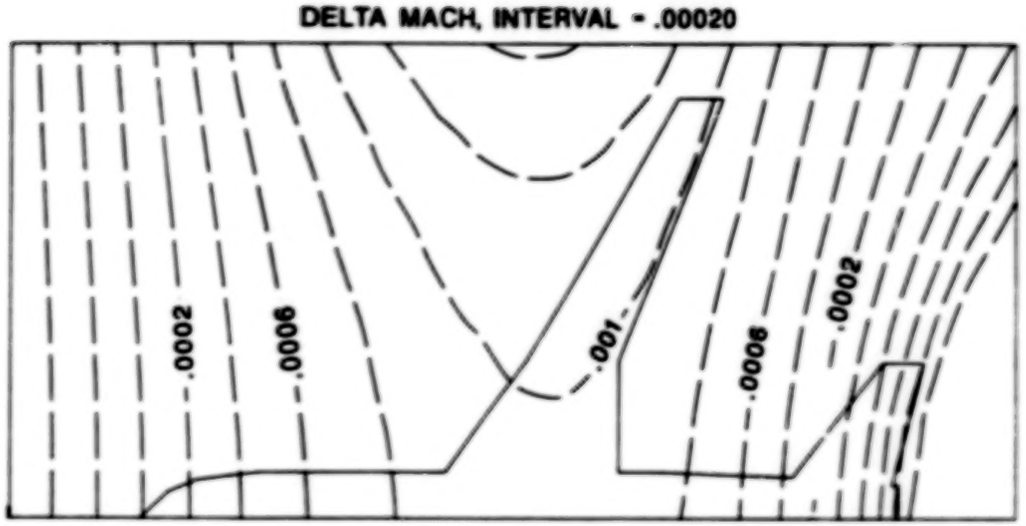

Figure 27. Typical example of calculated wall boundary induced Mach number contours.

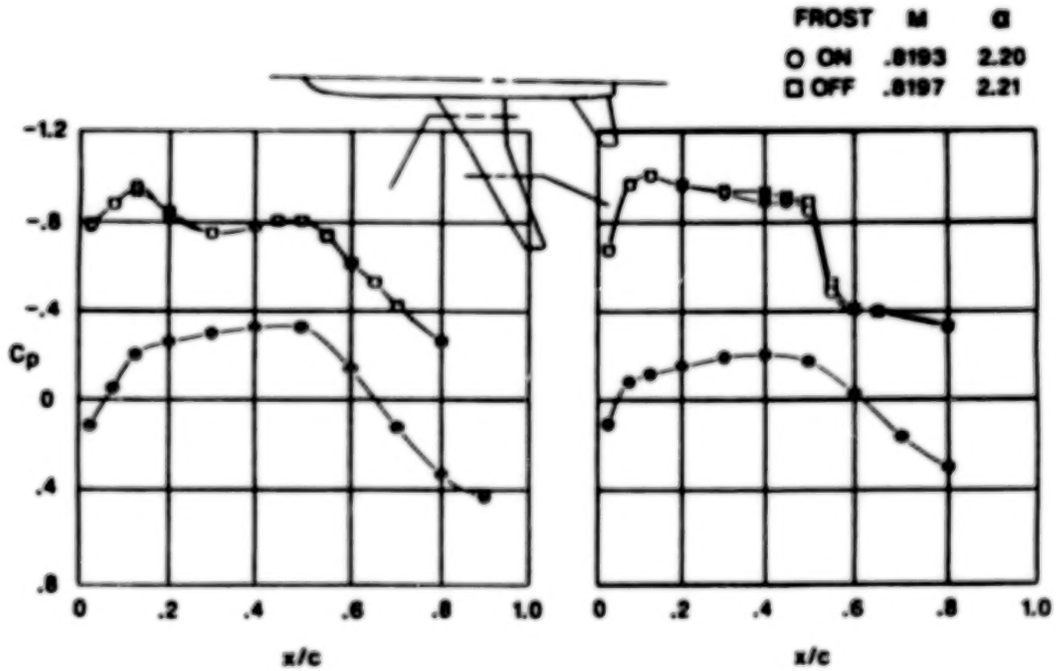

Figure 28. Comparison of pressure distribution for the Pathfinder I model with and without frost on the wing. RN = 23.0 x 10^6.

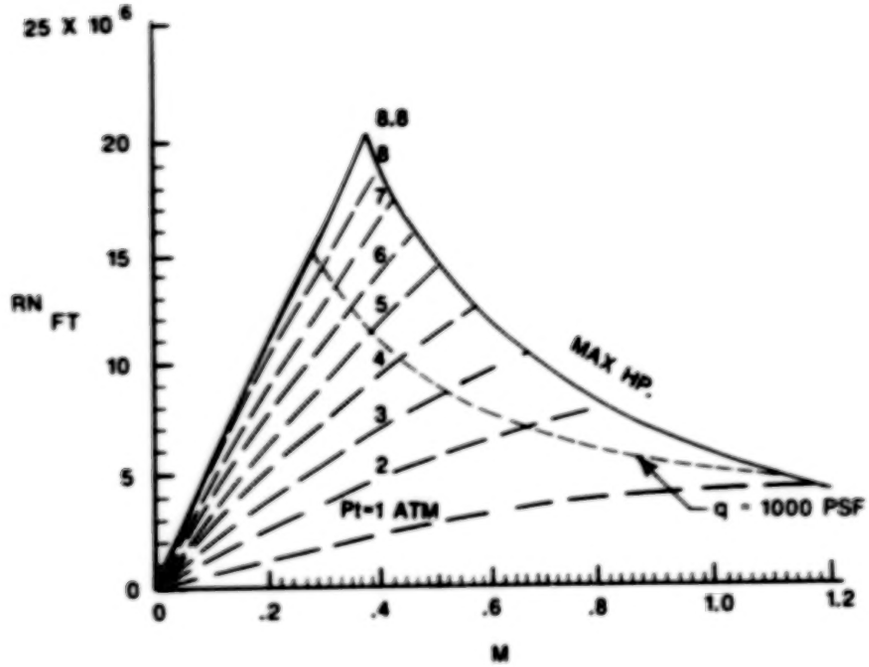

Figure 29. NTF operating envelope at ambient temperature.

ORIGINAL PAGE IS
OF POOR QUALITY

Figure 30. EA-6B model mounted in NTF.

ORIGINAL PAGE
BLACK AND WHITE PHOTOGRAPH

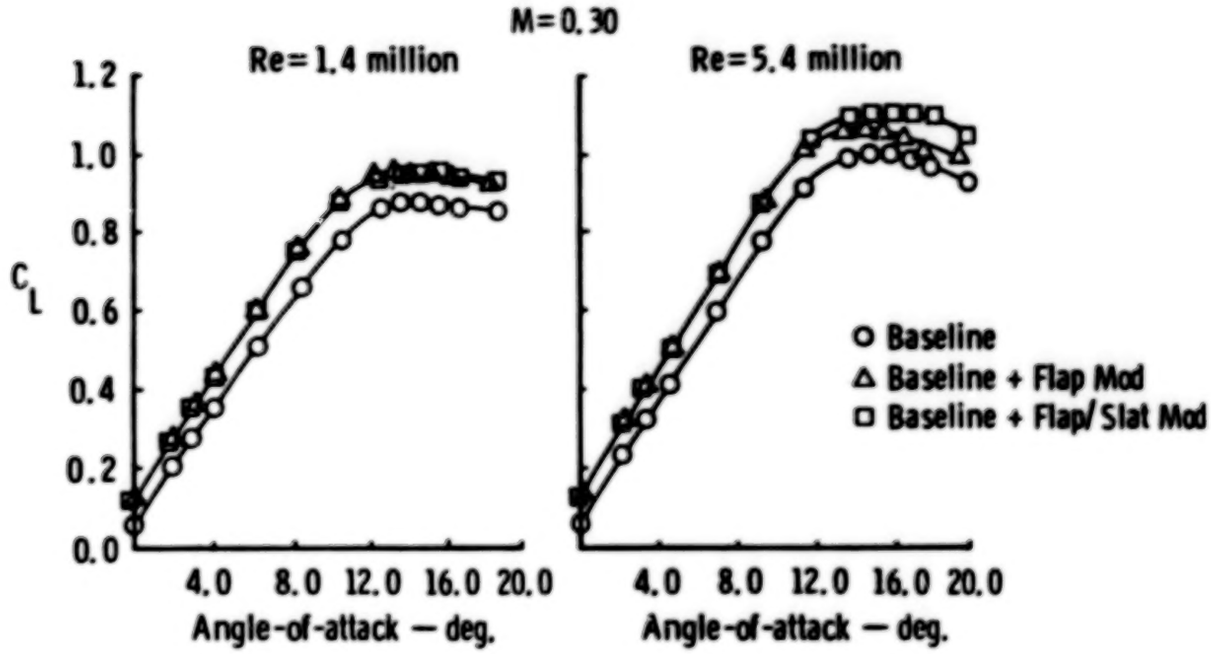

Figure 31. The effect of flap/slat modifications on the low speed lift characteristics for the EA-6B aircraft model. M = 0.30.

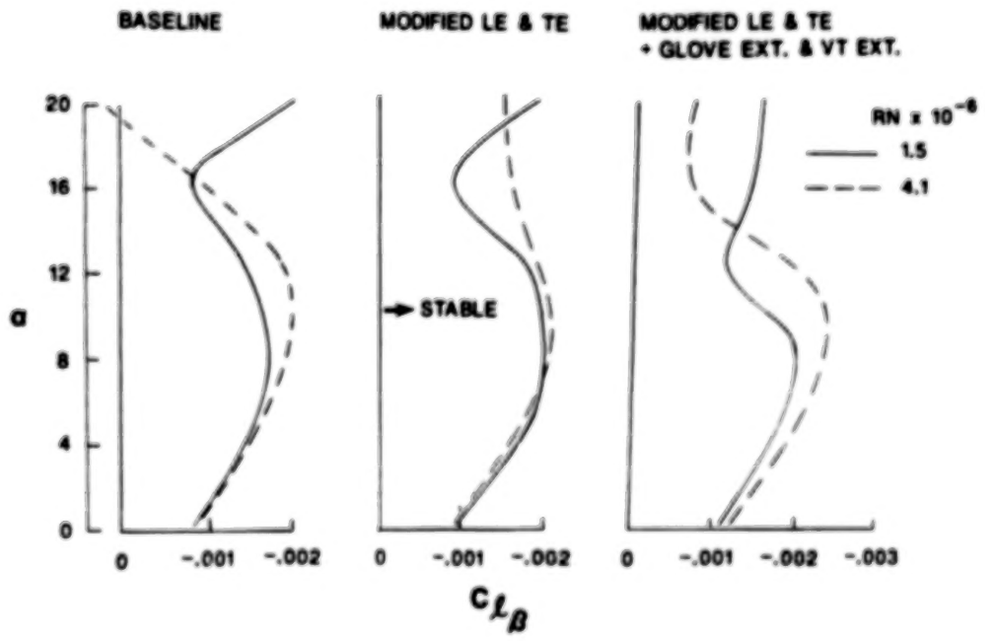

Figure 32. The effect of Reynolds number on rolling moment due to sideslip for the EA-6B. M = 0.30.

ORIGINAL PAGE IS
OF POOR QUALITY

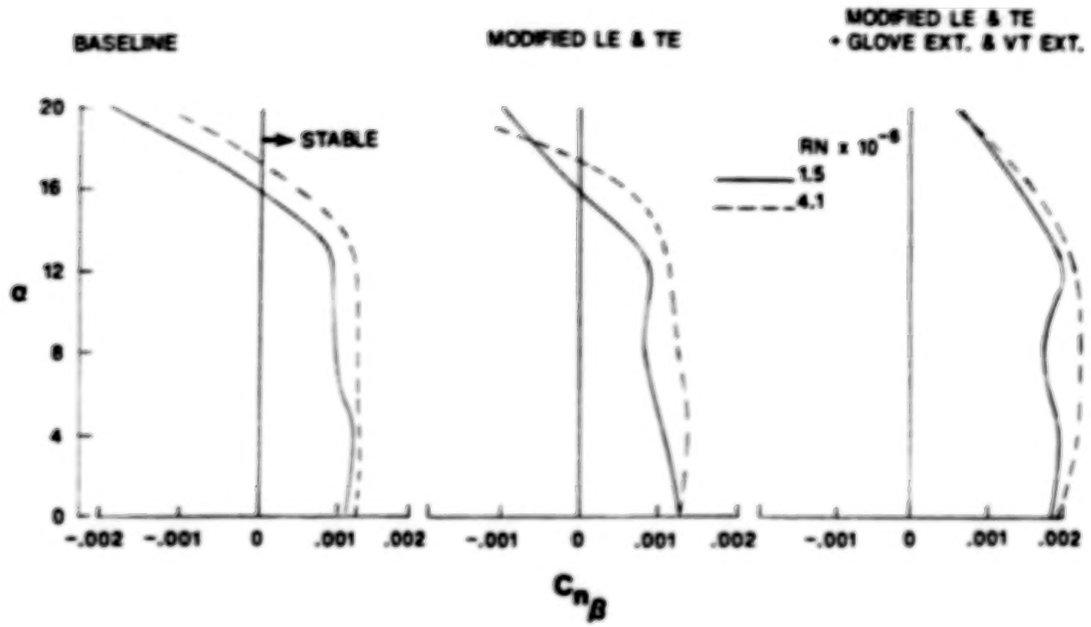

Figure 33. The effect of Reynolds number on yawing moment due to sideslip for the EA-6B. M = 0.30.

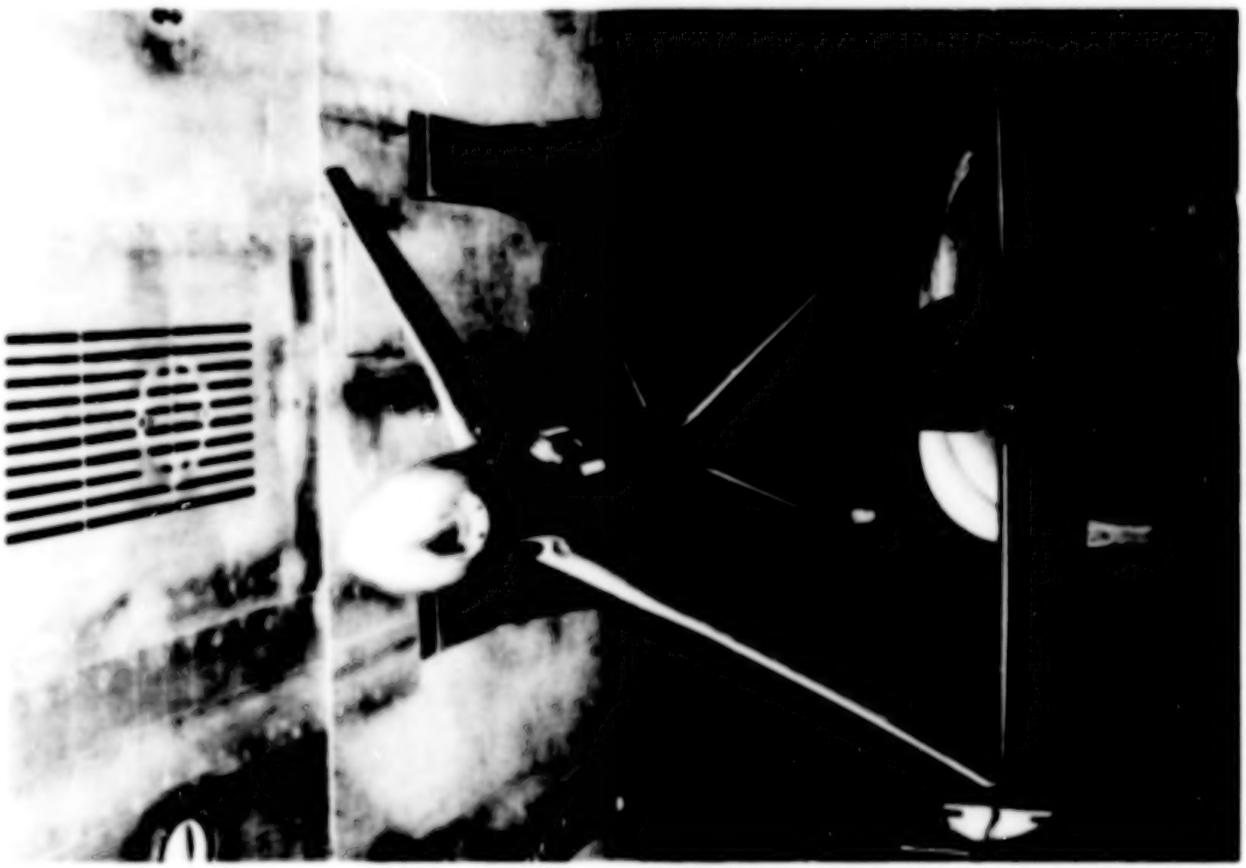

Figure 34. Photograph of the Pathfinder I model mounted in the NTF.

ORIGINAL PAGE
BLACK AND WHITE PHOTOGRAPH

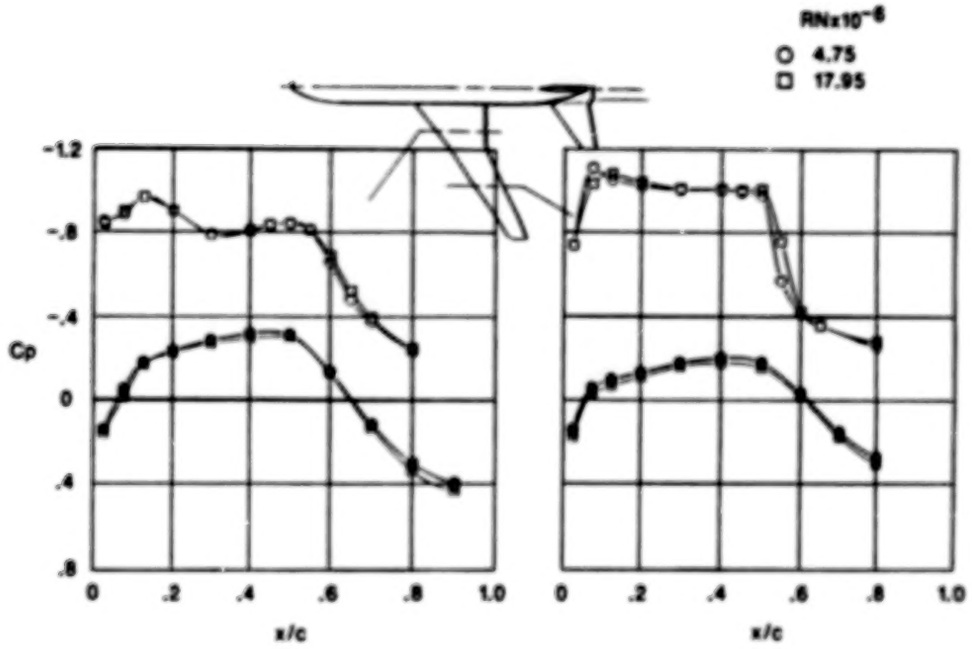

Figure 35. Effect of Reynolds number on wing pressure distributions for the Pathfinder I model. M = 0.82; α = 2.57°; transition fixed at 0.10c.

LOCKHEED HIGH WING TRANSPORT CONFIGURATION

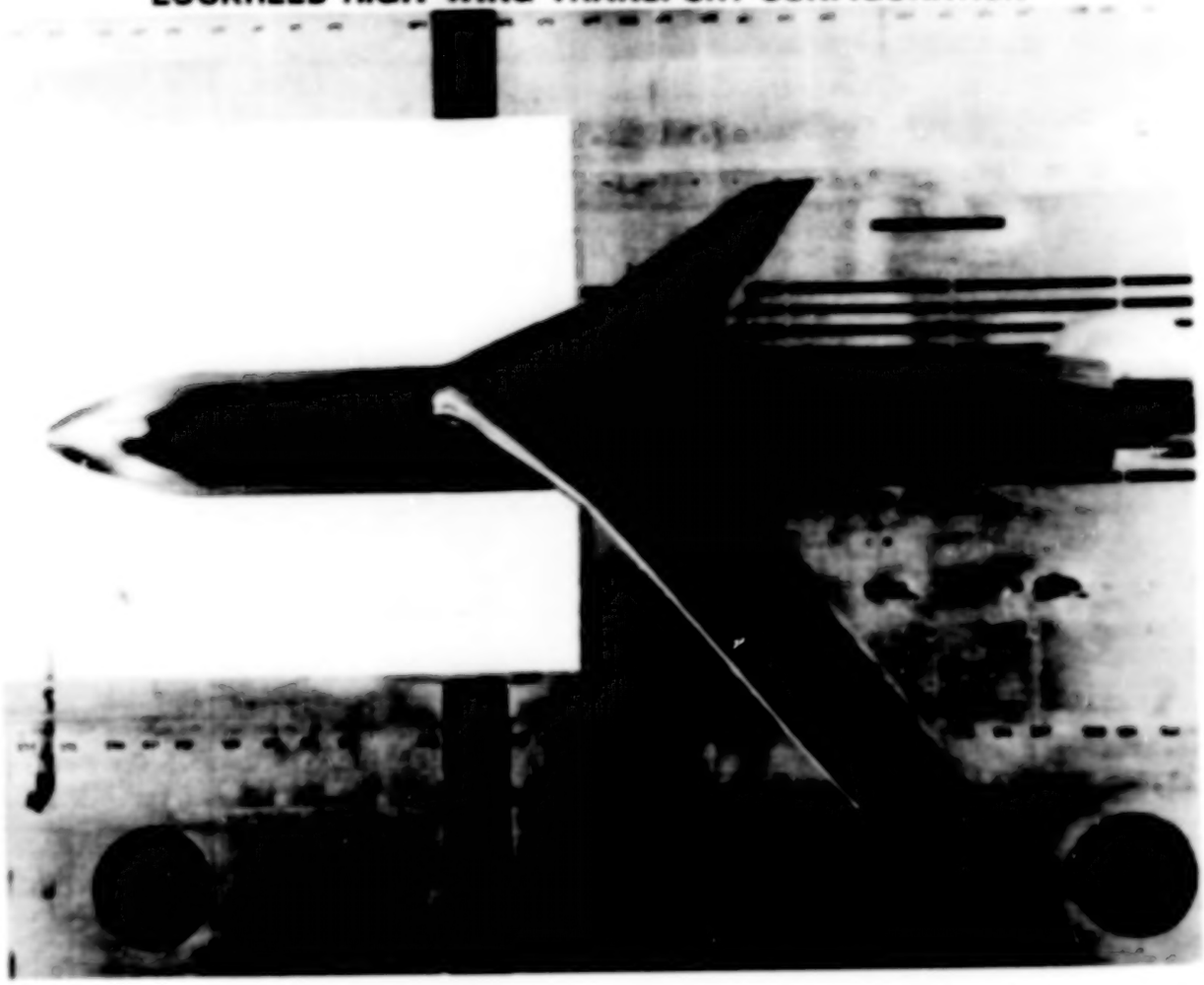

Figure 36. Photograph of Pathfinder I fuselage with the Lockheed transport wind installed in the NTF.

ORIGINAL PAGE
BLACK AND WHITE PHOTOGRAPH

ORIGINAL PAGE IS
OF POOR QUALITY

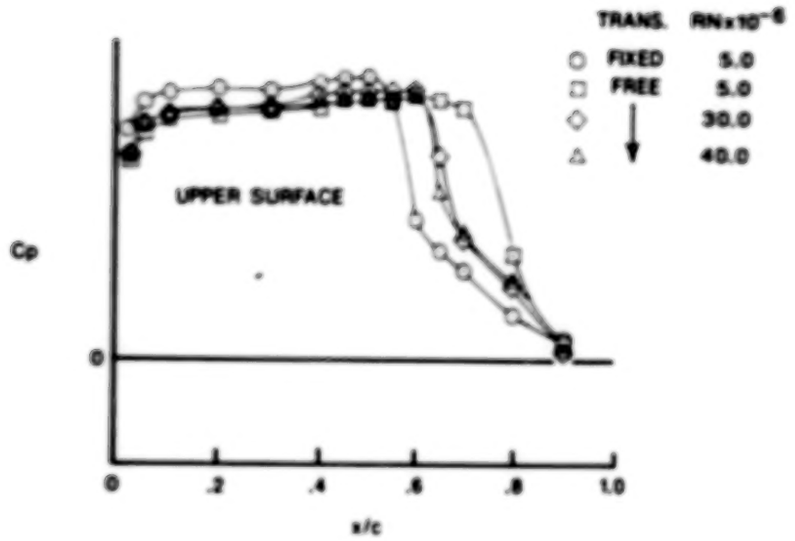

Figure 37. Effect of Reynolds number on wing pressure distributions for the Lockheed high wing transport configuration. M = 0.80; C_N = Constant.

ORIGINAL PAGE IS
OF POOR QUALITY

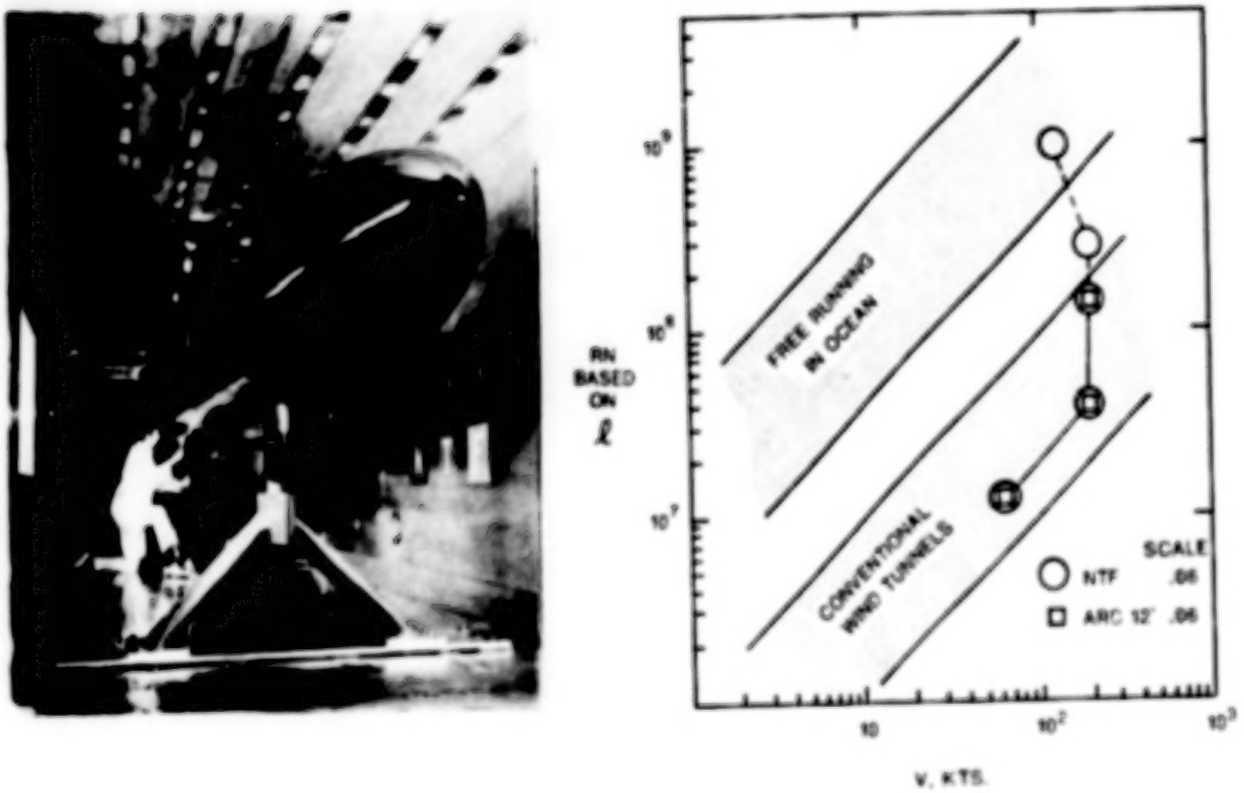

Figure 38. Photograph of submarine model mounted in the NTF and Reynolds number envelope.

ORIGINAL PAGE
BLACK AND WHITE PHOTOGRAPH

N91-24134

Reynolds Number Effects on the Transonic Aerodynamics of a Slender Wing-Body Configuration

52-02
19849

James M. Luckring
NASA-Langley Research Center

Charles H. Fox, Jr.
NASA-Langley Research Center

Jeffrey S. Cundiff
George Washington University / USAF
Hampton, Virginia

Summary

Aerodynamic forces and moments for a slender wing-body configuration are summarised from an investigation in the Langley National Transonic Facility (NTF). The results include both longitudinal and lateral-directional aerodynamic properties as well as sideslip derivatives. Results have been selected to emphasise Reynolds number effects at transonic speeds although some lower speed results are also presented for context. The data indicate nominal Reynolds number effects on the longitudinal aerodynamic coefficients and more pronounced effects for the lateral-directional aerodynamic coefficients. The Reynolds number sensitivities for the lateral-directional aerodynamic coefficients were limited to high angles of attack.

Introduction

Recent interest has developed in advanced aerospace vehicles which are capable of very high speed flight. Examples of such vehicles include a variety of advanced transport concepts designed for supersonic cruise as well as transatmospheric vehicles such as the proposed X-30. These vehicles all tend to be slender due to high speed considerations, although they still embrace a wide range of configurational concepts (i.e., wing-bodies, waveriders, accelerators, etc.). The aerodynamic challenges for such vehicles are by no means limited to high speed concerns such as cruise design or aerothermal heating. Most aerodynamic subdisciplines (e.g., stability and control, propulsion integration, transonic flow, high angle of attack, etc.) present unique and often conflicting challenges for these vehicles. Extending the current aerodynamic data base for such a broad range of concepts and issues would constitute a vast research endeavor and possibly require more time than is practical. However, focused investigations for selected configurations could provide insight to certain fundamental aerodynamic issues in a timely manner.

The present investigation is directed toward transonic Reynolds number effects for a slender wing-body configuration of the accelerator class. Some discussion of lower speed and lower Reynolds number data is also provided for perspective. The accelerator class of configuration tends toward body-dominant conical geometries with slender wings. As a consequence, the wing and body related aerodynamics are very closely coupled. Some prominent aerodynamic features for this class of configuration include conical-like shock structures and boundary layer flows and, at high angles of attack, forebody separated flows along with wing (leading edge) vortex flows.

This research is part of a broader experimental program at NASA Langley. The purpose of this program is to (i) design a force-and-moment wind-tunnel model with suitable configuration parametrics which is based upon one of the configurational concepts and (ii) examine selected aerodynamic phenomena over an appreciable range of Reynolds numbers and Mach numbers. The status of this program will be briefly addressed.

PRECEDING PAGE BLANK NOT FILMED

Symbols

b	wing span
C_D	drag coefficient, Drag/ $q_\infty S_{ref}$
$C_{D,o}$	drag coefficient at zero lift
C_L	lift coefficient, Lift/ $q_\infty S_{ref}$
C_l	body-axis rolling-moment coefficient, Rolling Moment/ $q_\infty S_{ref} b$
C_{l_β}	beta derivative of body-axis rolling-moment coefficient
C_m	pitching-moment coefficient, Pitching Moment/ $q_\infty S_{ref} \bar{c}$
C_N	normal-force coefficient, Normal Force/ $q_\infty S_{ref}$
C_n	body-axis yawing-moment coefficient, Yawing Moment/ $q_\infty S_{ref} b$
C_{n_β}	beta derivative of body-axis yawing-moment coefficient
$\bar{c}$	mean aerodynamic chord of reference wing planform
ℓ	total body length
M_∞	freestream Mach number
q_∞	freestream dynamic pressure
R	Reynolds number based on ℓ
r_n	nose radius
S_{ref}	area of reference wing planform, extended to model centerline
α	angle of attack, degrees
β	angle of sideslip, degrees
θ_b	frustum angle, degrees
θ_c	cone angle, degrees
Λ	leading-edge sweep angle, degrees

Abbreviations

LTPT	Low Turbulence Pressure Tunnel
NTF	National Transonic Facility
UPWT	Unitary Plan Wind Tunnel

Configuration and Test Program

Basic geometric features of the configuration are presented in figure 1. The fuselage was comprised of a cone/cylinder/frustum with a cone half angle of 5 degrees, a boattail angle of 9 degrees, and an overall length of three feet. The maximum fuselage diameter was 12.87 percent of the body length and the sharp nose radius was approximately 0.014 percent of the body length. The delta wing was of unit aspect ratio (75.96 degrees leading-edge sweep) with a symmetric 4 percent thick diamond airfoil section and a span of 30 percent body length. The leading and trailing edges were sharp. The wing was mounted with zero incidence such that the trailing edge fell at 92 percent of the body length. Moments were referenced about the quarter chord point of the mean aerodynamic chord for the wing planform extended to the plane of symmetry; this occurred at 62 percent of the body length. The vertical tail had a leading-edge sweep of 70 degrees, a trailing-edge sweep of approximately -2 degrees, and a symmetric 4 percent thick diamond airfoil section. Additional details of the model geometry have been reported by Fox et al. (reference 1). A photograph of the model mounted in NTF is presented in figure 2.

The overall range of test conditions for the NTF experiment are summarized in figure 3. Reynolds numbers are based upon the reference body length of 3 feet. The tests were conducted for Mach numbers ranging from 0.3 to 1.15 and Reynolds numbers ranging from 18 million to 180 million. The maximum Reynolds number data were obtained at $M_\infty = 0.6$. Test conditions were accomplished with total pressures nominally ranging from 2.0 to 7.3 atmospheres and total temperatures nominally ranging from 120 down to -225 degrees Fahrenheit. The model was sting mounted on an internal six-component force balance. The support mechanism included a roll coupling so that pitch and roll could be combined to

achieve angle of attack and sideslip.

A more detailed description of the test program is presented in figure 4 along with the NTF tunnel envelope as reported by Fuller (reference 2). The test was structured such that (i) Reynolds number effects could be studied at a subsonic and a transonic freestream Mach number and (ii) Mach number effects could be studied at a low and a high Reynolds number. Both longitudinal and lateral-directional aerodynamic properties were investigated up to an angle of attack of approximately 20 degrees. Sideslip derivatives were computed from data taken at +4 and -4 degrees of sideslip. These data were only obtained at freestream conditions corresponding to the "corners" of the test matrix shown in figure 4. Results for the present paper are focused on the Reynolds number data taken at a freestream Mach number of 0.9.

The data were obtained in NTF with the test section floor and ceiling slotted and the side walls solid. The measurements have been compensated for temperature effects, and conventional corrections have been applied to the data for the effects of deflection due to load, flow angularity, and base pressure. These corrections were, in general, small. No buoyancy corrections have been applied to the data. However, these effects were also found to be small. Tests in NTF occurred in early February, 1988.

The test program for this wind-tunnel model encompasses additional facilities to NTF as shown in figure 5. In particular, the model design permits supersonic testing in the Langley Unitary Plan Wind Tunnel (UPWT) as well as low-speed Reynolds-number testing in the Langley Low Turbulence Pressure Tunnel (LTPT). Included in figure 5 is the tunnel envelope for UPWT as reported by Jackson et al. (reference 3), the tunnel envelope for LTPT as reported by McGhee et al. (reference 4), and an indication of the freestream conditions at which testing has been completed. Thus far, data have been obtained for Mach numbers ranging from 0.2 to 4.5 and Reynolds numbers ranging from 1 million to 180 million; these results have been obtained with the same wind-tunnel model. Preliminary supersonic results from the UPWT investigation may be found in the paper by Covell et al. (reference 5). Results from the LTPT experiment have been reported by Fox et al. (reference 1) as well as by Luckring et al. (reference 6).

Both the UPWT and the LTPT tests addressed a substantially broader range of configuration parametrics than was investigated in NTF. The configuration variables for the LTPT investigation included fuselage nose bluntness, vertical tails, and canards. The UPWT investigation included these same variables as well as wing incidence, longitudinal wing position, and wingtip-mounted vertical fins.

The current test program includes plans for further testing in the UPWT to obtain data at low supersonic speeds. In addition, a set of nominally half-scale models have been fabricated for testing at hypersonic speeds.

Results and Discussion

The general effects of Reynolds number on longitudinal aerodynamic properties are summarised in figure 6 for a freestream Mach number of 0.9. As would be expected, Reynolds number had minimal effects on the lift and pitching moment data. The lift-curve slope evidences a break at approximately 4 degrees angle of attack beyond which nonlinear lift effects are observed. The pitching moment data show a nose-down break at a comparable angle of attack. These effects are primarily associated with the separation-induced leading-edge vortex flow from the wing. The data of figure 6c show a reduction in the zero-lift drag coefficient of approximately 25 counts due to an increase in Reynolds number from 24 to 45 million. The shape of the drag polar was unaffected by this increase in Reynolds number. Further increases in Reynolds number had little effect on the drag.

The results of figure 6c include wave drag increments as indicated by the data presented in figure 7. Here the drag coefficient is presented for several freestream Mach numbers ranging from 0.6 to 1.15 at a fixed Reynolds number of 90 million. At a freestream Mach number of 0.9, the zero-lift drag coefficient has roughly doubled as compared to the results for a freestream Mach number of 0.6; this increment is primarily associated with wave drag. Additional discussion of the zero-lift drag rise will be included in the section regarding theoretical estimates. In general, the Reynolds number effects for the longitudinal forces and moments were nominal.

Contrary to the longitudinal results, Reynolds number has a more pronounced effect on the lateral-directional aerodynamic properties; this effect occurs at high angles of attack. An example is presented in figure 8 for the variation of yawing moment with angle of attack at zero sideslip. These data were obtained at a freestream Mach number of 0.3 over a range of Reynolds numbers in the LTPT investigation reported by Fox et al. (reference 1). All lateral-directional properties in this paper are presented in the body axis coordinate system.

The yawing moment is essentially zero up to a critical angle of attack of approximately 12 degrees. Beyond this angle of attack, nonzero values of the yawing moment develop due to asymmetric forebody separation and demonstrate a strong sensitivity to Reynolds number. However, the onset angle of attack for the asymmetric loads shows little effect of Reynolds number. The initial buildup of yawing moment (2 to 3 degrees beyond the onset angle) also shows little effect of Reynolds number. The critical angle of 12 degrees is on the order of twice the cone semiapex angle, as would be expected from previous forebody research such as has been reported by Keener and Chapman (reference 7). These yawing moment trends are representative of the other lateral-directional aerodynamic coefficients. These data, along with the other results reported by Fox et al. (reference 1), served as precursor information for the high Reynolds number investigation in NTF.

The model configuration for the data of figure 8 differs from the configuration for the NTF tests in two respects. First, the sharp nose used for the NTF experiments was a replacement for the one utilised for the LTPT test which had become damaged. The second difference is that the vertical tail was removed for the data presented in figure 8.

Reynolds number effects for the current investigation are first addressed by presenting results over a range of freestream Mach numbers at both a low and a high Reynolds number test condition, figure 9. Before addressing the Reynolds and Mach number effects, it should be noted that the yawing moment has the opposite sign at high angles of attack as compared to the results from the LTPT investigation (cf, figure 8). This indicates that the flow asymmetry has occurred in the opposite sense. This can be caused by either (i) minor differences in the geometry of the nose or (ii) minor differences in flow angularity between the tunnels. However, for each test the asymmetry tended to occur either with one sense or the other throughout the test; it was very repeatable.

At a Reynolds number of 24 million (figure 9a) the data show minimal Mach number effects for the angle-of-attack range investigated. A lack of sensitivity to Mach number was also observed by Fox et al. (reference 1) at a Reynolds number of 9 million for Mach numbers ranging from 0.2 to 0.375. However, at a Reynolds number of 90 million (figure 9b) the data do evidence compressibility effects for angles of attack in excess of approximately 16 degrees.

The results presented in figure 9 also demonstrate significant Reynolds number effects at high angles of attack. The nonlinear reversal in yawing moment which occurred at a Reynolds number of 24 million did not occur at a Reynolds number of 90 million within the angle of attack range investigated. The data presented in figure 10 indicate that this change in the high angle of attack yawing moment is generally associated with high Reynolds number flow. At a freestream Mach number of 0.6 (figure 10a) the data for the two lower Reynolds numbers both show the yawing moment reversal whereas the data for the two higher Reynolds numbers do not evidence this effect. The transonic case (figure 10b) shows a similar trend. In addition, the high Reynolds number yawing moments do not appreciably change beyond 16 degrees angle of attack. This effect was not observed at $M_\infty = 0.6$. It is difficult to determine from the data specific Reynolds numbers at which the changes occur.

The data of figure 10 show limited Reynolds number effects in the 10 to 16 degree angle of attack range. This differs from the results presented in figure 8 where Reynolds number sensitivities were manifested at only 2 to 3 degrees angle of attack beyond the onset angle of attack for flow asymmetry. Therefore, it appears that the angle of attack at which Reynolds number effects become evident in the lateral directional coefficients increases as the Reynolds number itself increases. Confirmation of this observation will require further testing.

Sideslip derivative data were obtained at nominally the limiting freestream conditions of the test matrix shown in figure 4. The results presented in figure 11 show compressibility effects on the lateral-directional stability derivatives at a low and a high Reynolds number. As was observed for the yawing moment data of figure 9, the low Reynolds number data (figure 11a) show virtually no compressibility

effect whereas at the high Reynolds number condition (figure 11b) significant compressibility effects are indicated for high angles of attack. The results presented in figure 12 indicate that Reynolds number effects were limited to high angles of attack and were most prevalent at low speeds. The data of figures 11 and 12 show that neither Mach number nor Reynolds number had any significant effects on the lateral-directional stability derivatives below approximately 14 degrees angle of attack.

Theoretical Estimates

A preliminary theoretical analysis of the longitudinal forces and moments was conducted to provide design loads as well as to provide some insight to the longitudinal aerodynamic phenomena. Calculations were performed with the vortex lattice program of Margason and Lamar (reference 8) as extended by Lamar and Gloss (reference 9) to account for separation-induced vortex lift effects by the leading-edge suction analogy of Polhamus (reference 10). This method was selected because it has proved over many years to provide reasonable estimates of longitudinal forces and moments for a wide range of applications as reported by Lamar and Luckring (reference 11), for example. The method was also chosen because (i) it tends to provide conservative load estimates (i.e., errors result in over predictions of the loads) and (ii) it is a very rapid method to utilise. These attributes are principally due to Polhamus' suction analogy concept which allows nonlinear integral properties associated with leading-edge vortex flows to be extracted from a simple linear theory computation.

Theoretical estimates for the effects of compressibility are presented in figure 13. The normal force results are for a fixed angle of attack of 10 degrees whereas the pitching moment results are for a fixed lift coefficient of 0.3. Differences between the attached flow theory and the vortex flow theory are due to the vortex lift increment predicted for the wing by the suction analogy. Although the trend with Mach number is reasonably well predicted by the theory, the magnitudes of normal force and pitching moment are not. The differences between the vortex-flow theory and the experiment are larger than would be expected from prior experience; they are primarily due to a poor representation of the fuselage in the computation as a flat plate. This approach neglects the nonlinear interaction of the leading-edge vortex with the thick body.

A surface grid representation of the configuration (without tail) is presented in figure 14 which illustrates the relative size of the body to the wing. Near the forward portion of the wing the body thickness will tend to crowd the leading-edge vortex off of the wing. This effect reduces the vortex lift increment which also results in a negative pitching moment increment for the assumed moment reference point. Methods which properly account for the vortex-body interaction have been shown to accurately predict force and moment properties for configurations similar to the one of the present investigation. An example has been given by Luckring and Thomas (reference 12) for the wing-body configuration tested by Stahl et al. (reference 13).

Computations for the zero-lift drag rise have also been performed using the analysis system reported by Middleton et al. (reference 14). Calculations are presented in figure 15 along with experimental results at a Reynolds number of 90 million. The theoretical drag is comprised of a skin friction increment based upon the method of Sommer and Short (reference 15) along with a standard supersonic wave drag increment; form drag effects were not included in these estimates.

The computed friction drag provides a reasonable estimate from which the transonic drag rise is evident. The experimental drag coefficient at a freestream Mach number of 0.3 is less accurate than the other data shown on the figure due to the reduced loads at this freestream condition. This relative difference in accuracy is conjectured to be a leading cause for the seemingly high experimental value of $C_{D,o}$ at this Mach number. The supersonic drag estimate is higher than the experimental value by approximately 60 counts. A comparable drag increment between theory and experiment was found by Compton (reference 16) for the boattail drag of a geometrically similar afterbody when suitably normalised.

Concluding Remarks

Selected results have been presented from an experimental investigation in the Langley National Transonic Facility (NTF) of a slender wing-body configuration. The tests were conducted at Reynolds numbers ranging from 18 million to 180 million based on total model length and at Mach numbers ranging from 0.3 to 1.15. The configuration is similar to the accelerator class of vehicles which have been considered (along with other configurational concepts) for future high-speed aerospace vehicles.

Experimental results for the effects of Mach number and Reynolds number on the longitudinal forces and moments were found to be nominal. However, the effects of Mach number and Reynolds number on the lateral-directional forces and moments were more pronounced. These effects only occurred at high angles of attack. Yawing moments became less nonlinear at the high Reynolds number test conditions. Compressibility was found to have a larger effect at high Reynolds numbers than was observed at low Reynolds numbers. In addition, the angle of attack at which Reynolds number effects became evident seems to have increased as Reynolds number itself increases.

Simple theoretical methods based upon linear theory were found to provide less accurate estimates of the longitudinal forces and moments than is usually achievd. This was due to the lack of representing the nonlinear wing-fuselage interaction effects as regards the leading edge vortex flow. Approximate estimates of the zero-lift drag coefficient were obtained at subcritical and supersonic conditions using conventional methodology.

References

1. Fox, C. H., Jr.; Luckring, J. M.; Morgan, H. L., Jr.; and Huffman, J. K. (1988): Subsonic Longitudinal and Lateral-Directional Static Aerodynamic Characteristics of a Slender Wing-Body Configuration. NASP TM-1011.
2. Fuller, D. E. (1981): Guide for Users of the National Transonic Facility. NASA TM 83124.
3. Jackson, C. M., Jr.; Corlett, W. A.; and Monta, W. J. (1981): Description and Calibration of the Langley Unitary Plan Wind Tunnel. NASA TP-1905.
4. McGhee, R. J.; Beasley, W. D.; and Foster, J. M. (1984): Recent Modifications and Calibration of the Langley Low-Turbulence Pressure Tunnel. NASA TP-2328.
5. Covell, P. F.; Wood, R. M.; Bauer, S. X. S.; and Walker, I. J. (1988): Experimental and Theoretical Evaluation of a Generic Wing Cone Hypersonic Configuration at Supersonic Speeds. Fourth National Aerospace Plane Symposium, Paper No. 83.
6. Luckring, J. M.; Fox, C. H., Jr.; and Cundiff, J. S. (1988): Reynolds Number Effects on the Subsonic Aerodynamics of a Generic Accelerator Configuration. Fourth National Aero-Space Plane Technology Symposium, Paper No. 82.
7. Keener, E. R.; and Chapman, G. T. (1974): Onset of Aerodynamic Sideforces at Zero Sideslip on Symmetric Forebodies at High Angles of Attack. AIAA Paper No. 74-770.
8. Margason, R. J.; and Lamar, J. E. (1971): Vortex-Lattice Fortran Program for Estimating Subsonic Aerodynamic Characteristics of Complex Planforms. NASA TN D-6142.
9. Lamar, J. E.; and Gloss, B. B. (1975): Subsonic Aerodynamic Characteristics of Interacting Lifting Surfaces with Sharp Edges Predicted by a Vortex-Lattice Method. NASA TN D-7921.
10. Polhamus, E. C. (1966): A Concept of the Vortex Lift of Sharp-Edged Delta Wings Based on a Leading-Edge-Suction Analogy. NASA TN D-3767.
11. Lamar, J. E.; and Luckring, J. M. (1979): Recent Theoretical Developments and Experimental Studies Pertinent to Vortex Flow Aerodynamics - With a View Towards Design. AGARD CP-247, Paper No. 24.
12. Luckring, J. M.; and Thomas, J. L. (1986): Separation Induced Vortex Flow Effects - Some Capabilities and Challenges. First National Aerospace Plane Technology Symposium.

13. Stahl, W.; Hartmann, K.; and Schneider, W. (1971): Kraft- und Druckverteilungsmessungen an einer Flugel-Rumpf-Kombination mit Flugel kleiner Streckung in kompressibler Stromung. DGLR / AVA-FB 7129.

14. Middleton, W. D.; Lundry, J. L.; and Coleman, R. G. (1980): A System for Aerodynamic Design and Analysis of Supersonic Aircraft. Part 1 - General Description and Theoretical Development. NASA CR-3351.

15. Sommer, S. C.; and Short, B. J. (1955): Free-Flight Measurements of Turbulent-Boundary-Layer Skin Friction in the Presence of Severe Aerodynamic Heating at Mach Numbers From 2.8 to 7.0. NACA TN 3391.

16. Compton, W. B., III (1972): Jet Effects on the Drag of Conical Afterbodies at Supersonic Speeds. NASA TN D-6789.

ORIGINAL PAGE IS
OF POOR QUALITY

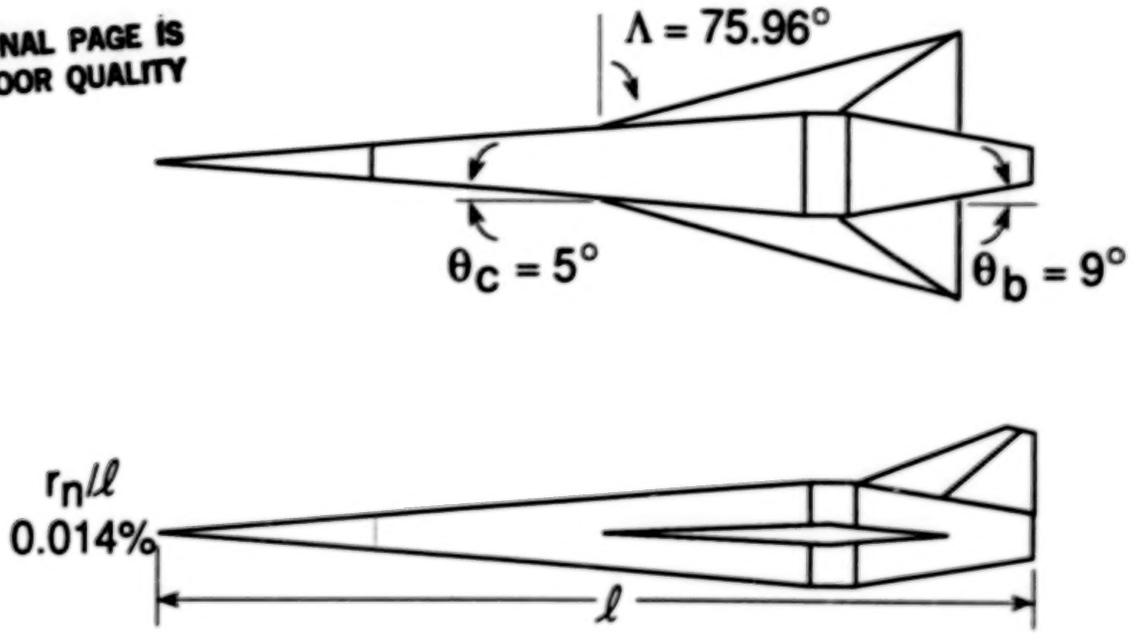

Figure 1.- Geometric features.

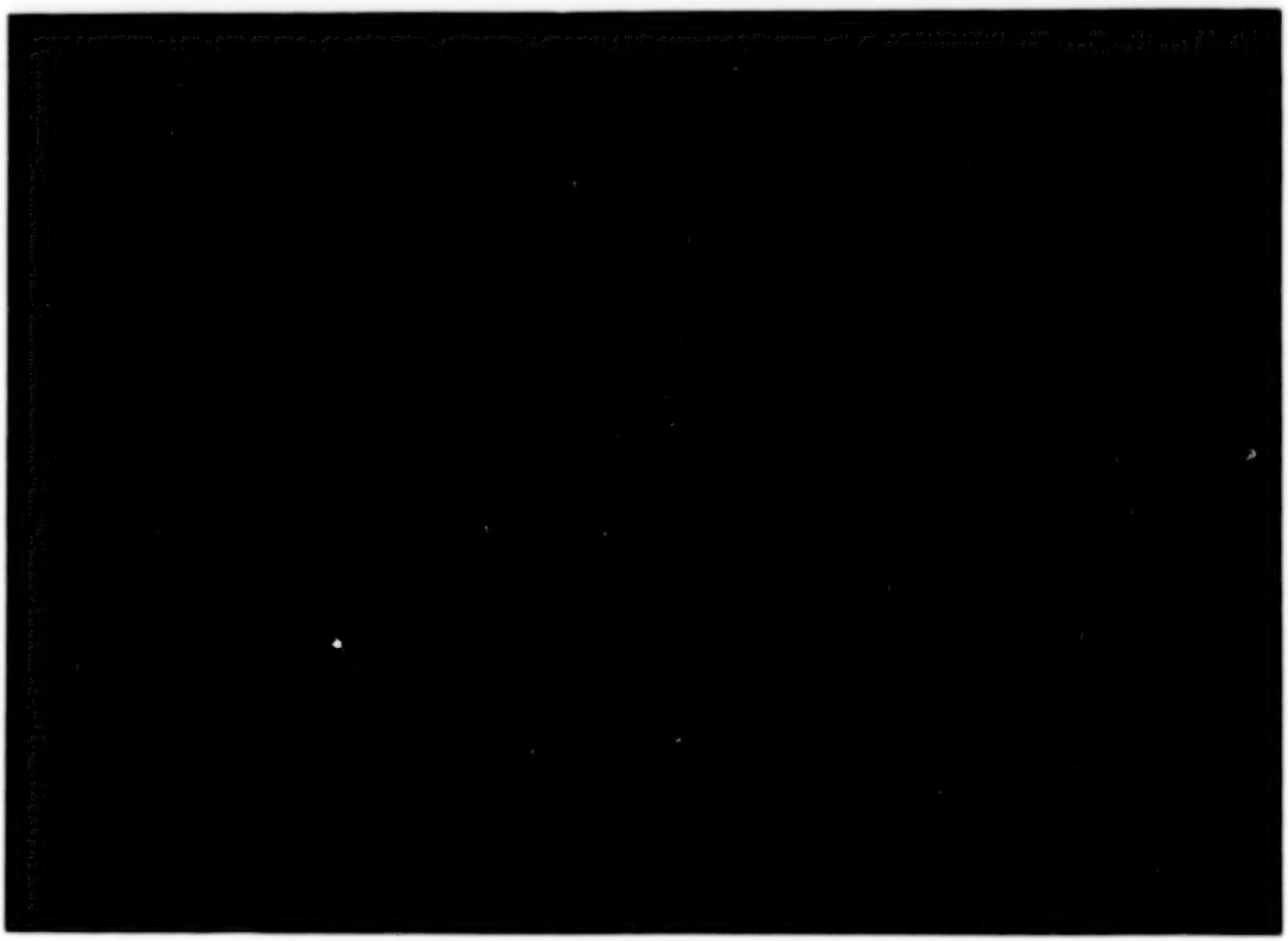

Figure 2.- Model mounted in NTF.

ORIGINAL PAGE
BLACK AND WHITE PHOTOGRAPH

ORIGINAL PAGE IS

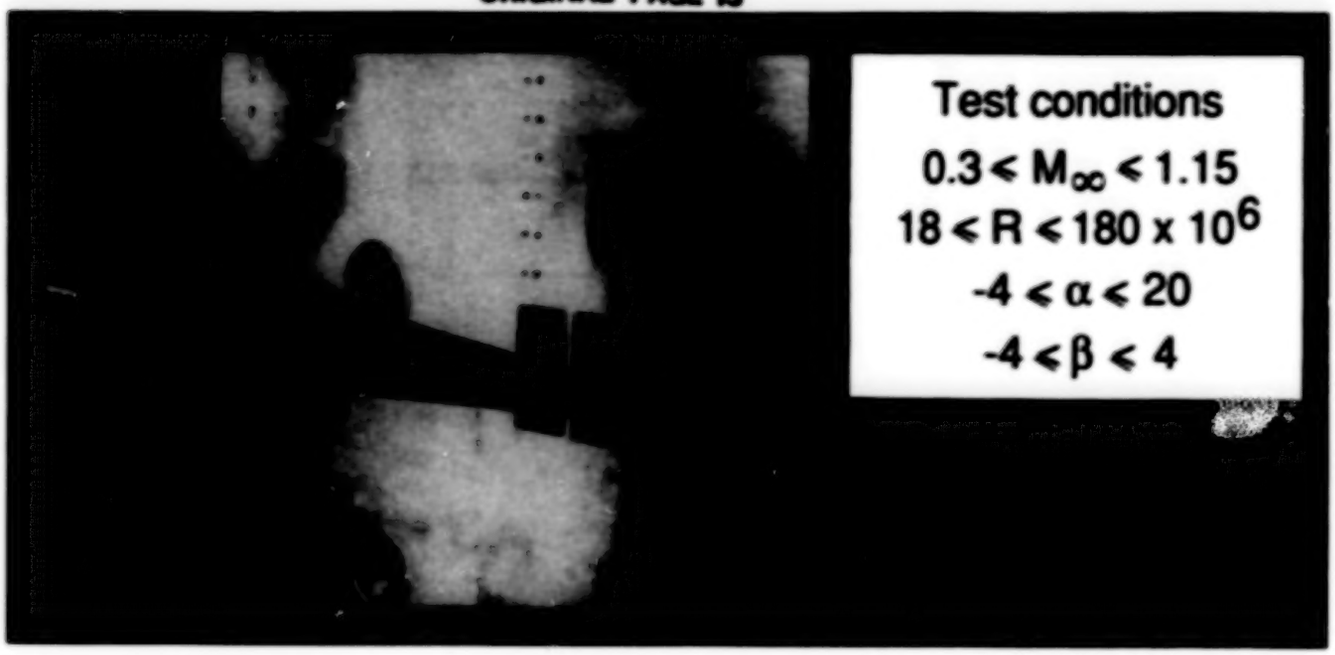

Figure 3.- Range of test conditions.

ORIGINAL PAGE
BLACK AND WHITE PHOTOGRAPH

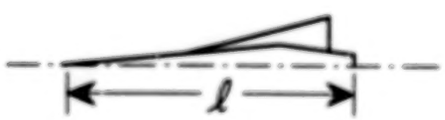

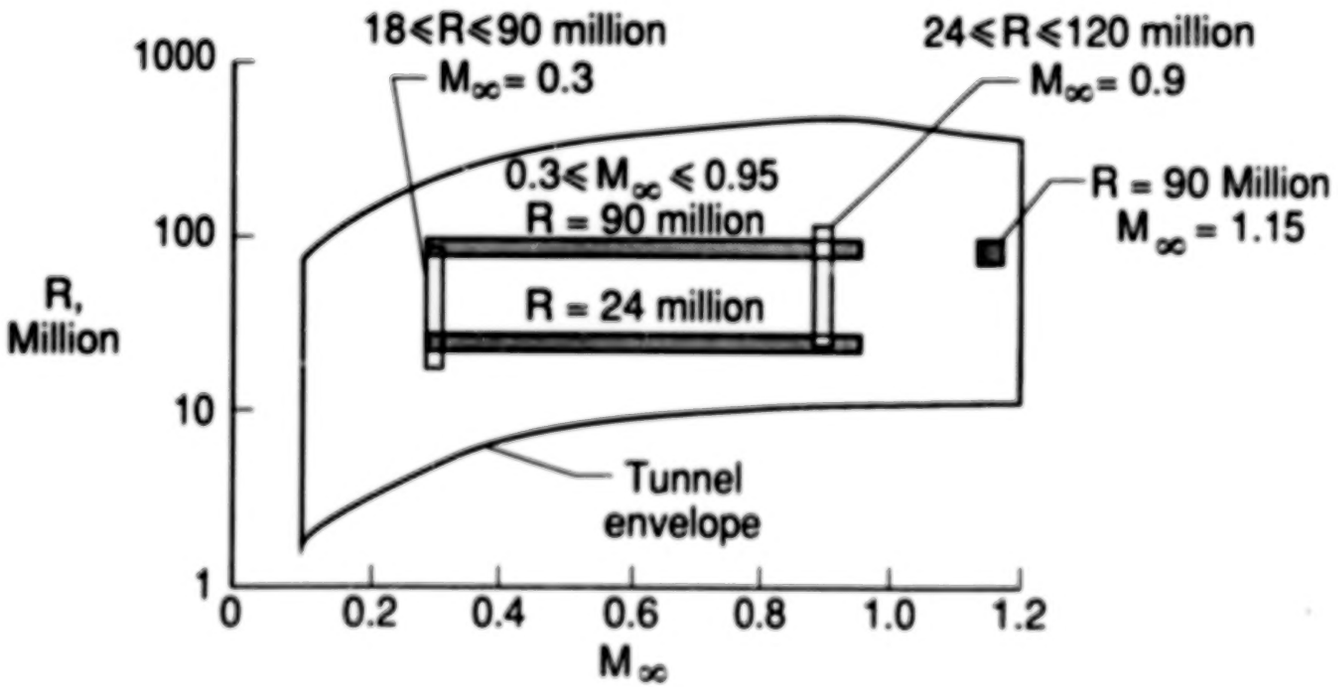

Figure 4.- Test program for NTF.

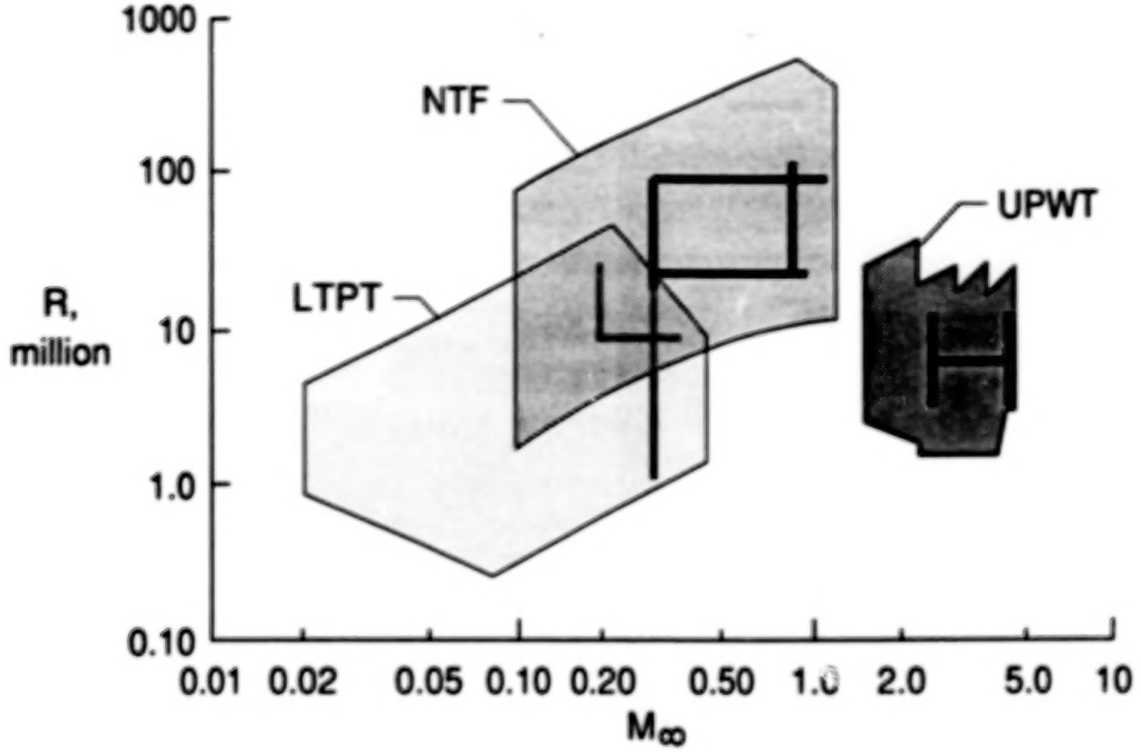

Figure 5.- Comprehensive test program.

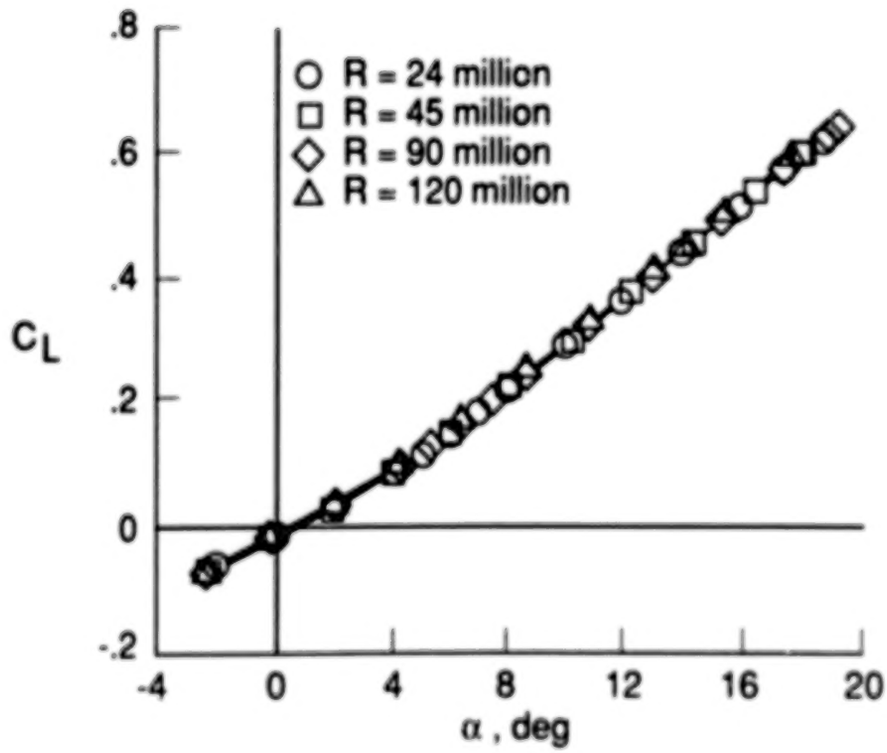

(a) Lift.

Figure 6.- Reynolds number effect on longitudinal aerodynamic properties. $M_\infty = 0.9$.

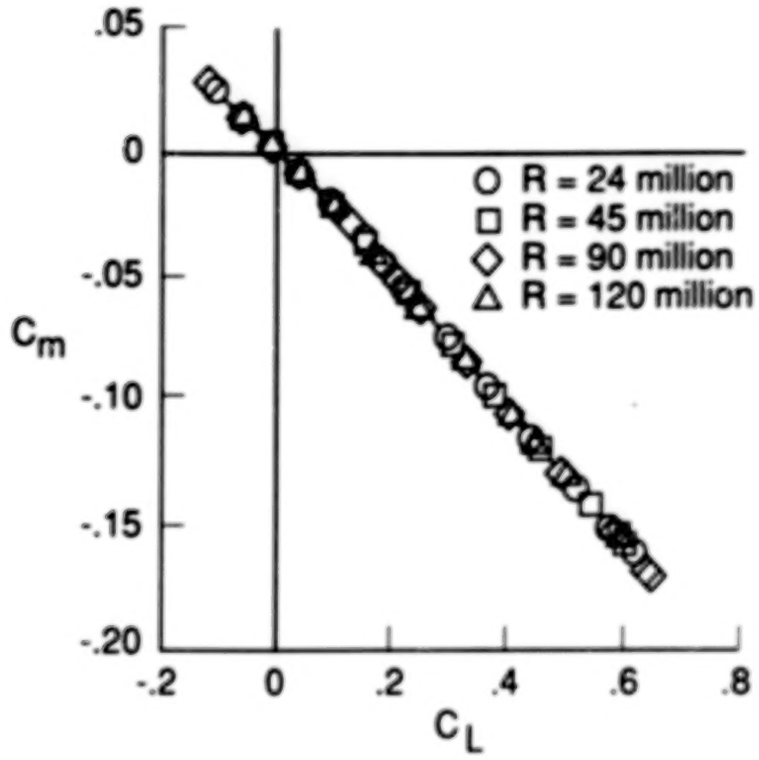

(b) Pitching moment.

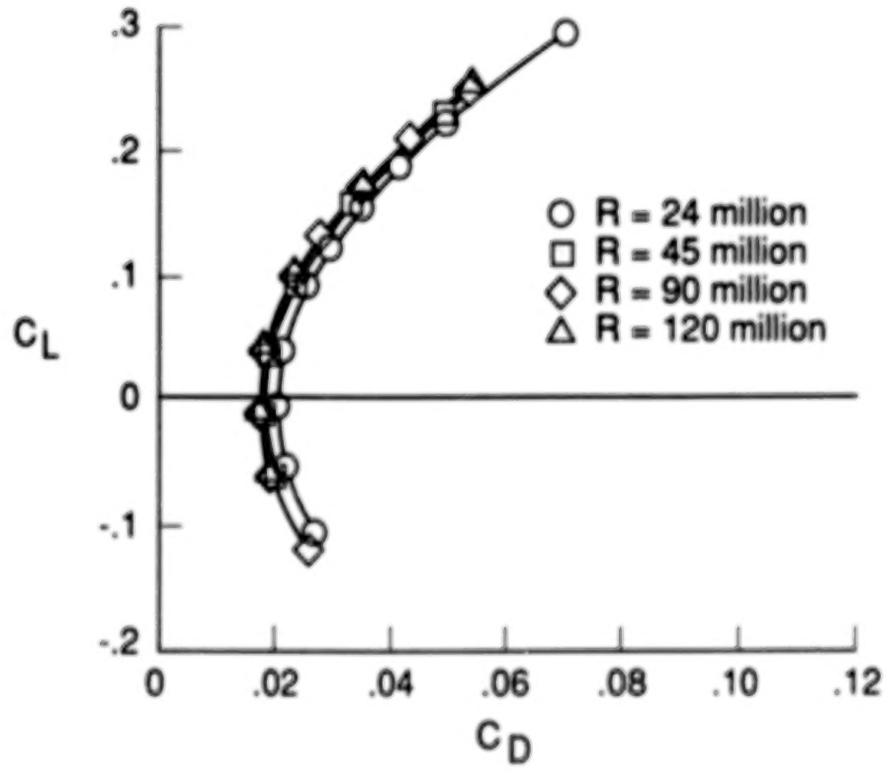

(c) Drag.

Figure 6.- Concluded.

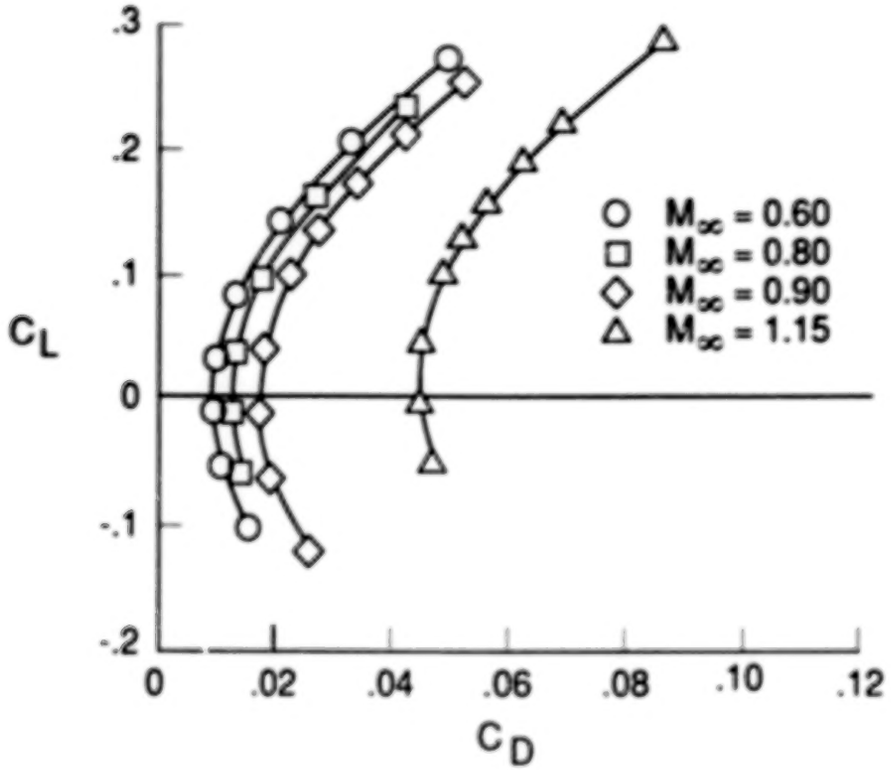

Figure 7.- Effect of Mach number on drag. R = 90 million.

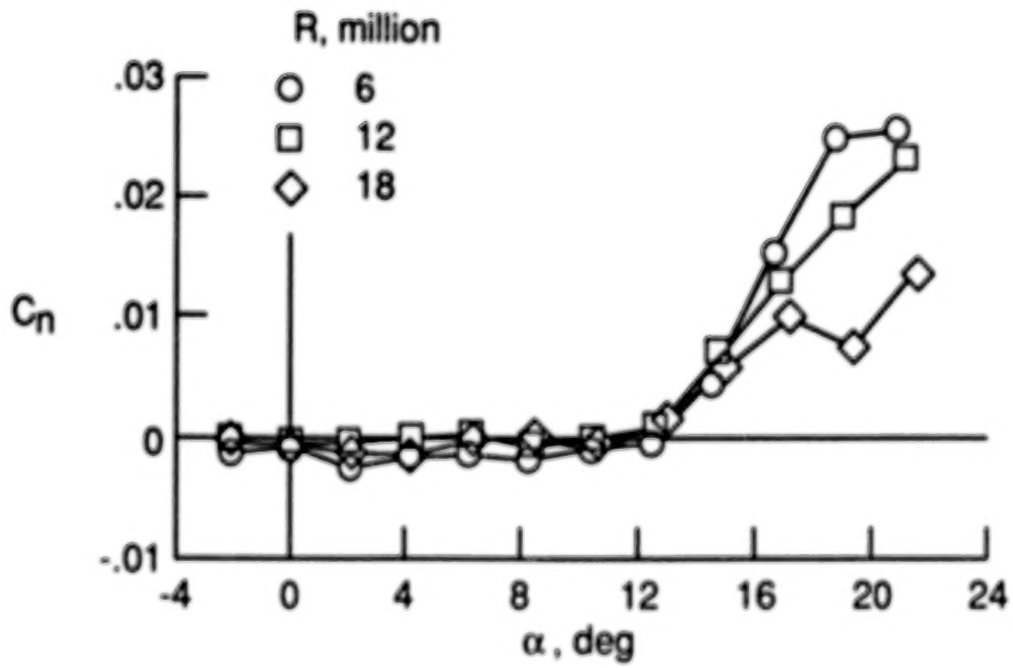

Figure 8.- Reynolds number effects on yawing moment. M_∞ = 0.3. After Luckring et al. (1988).

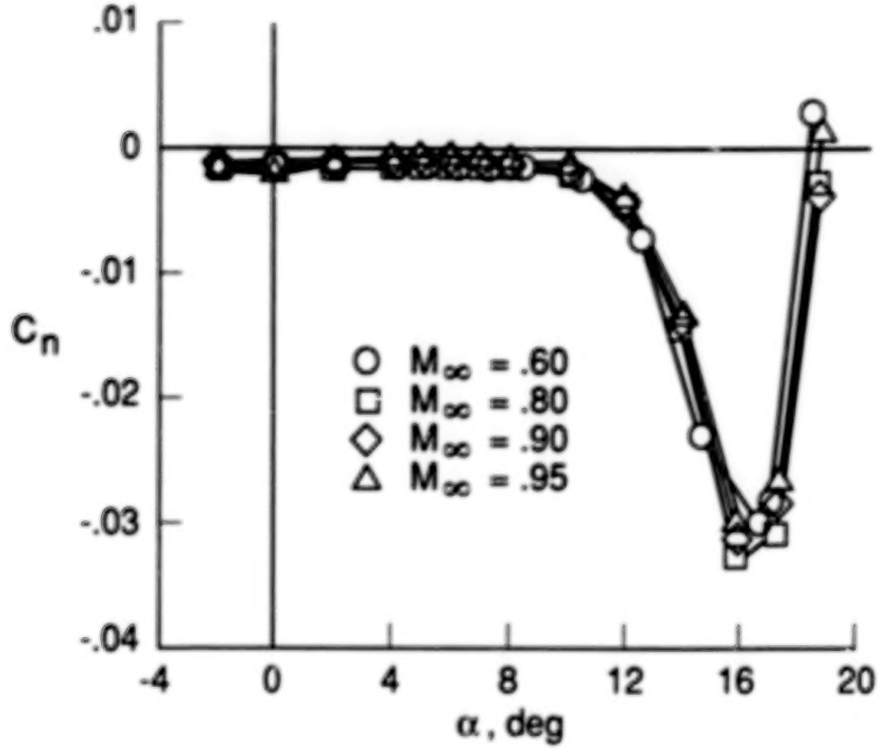

(a) R = 24 million.

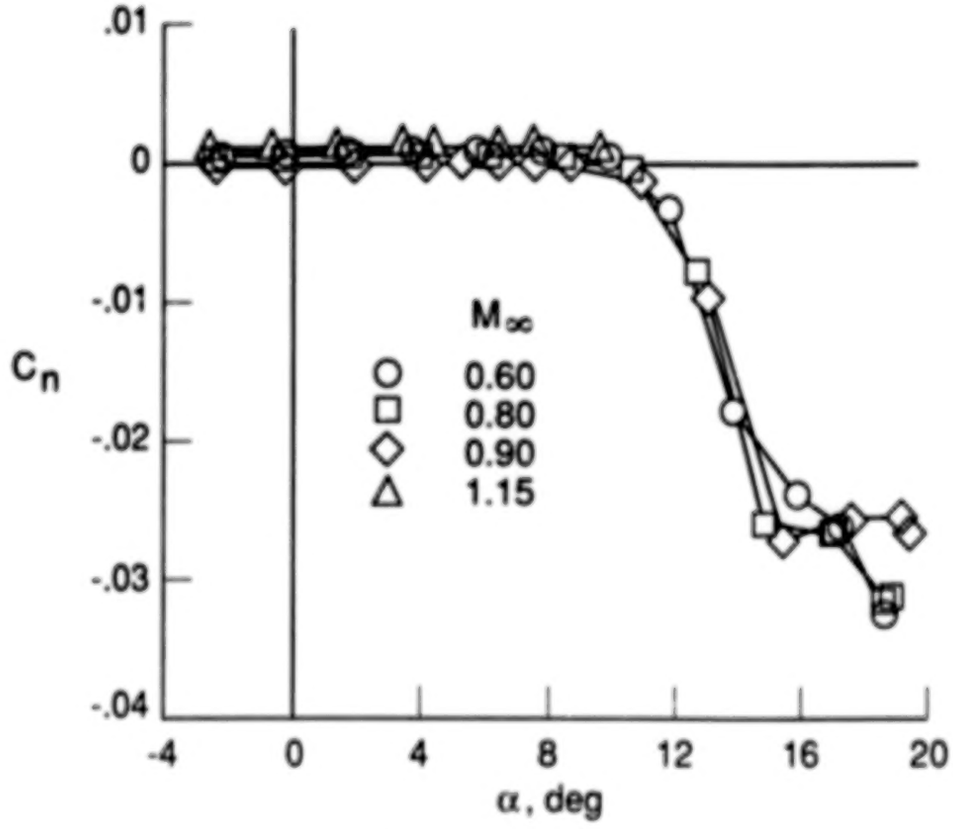

(b) R = 90 million.

Figure 9.- Effect of Mach number on yawing moment.

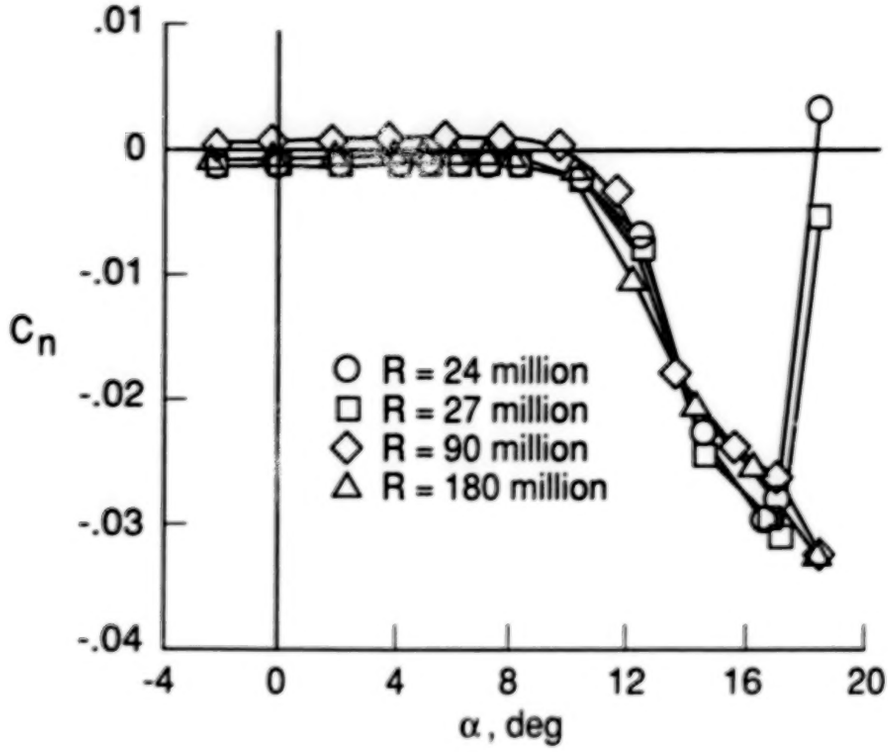

(a) $M_\infty = 0.6$

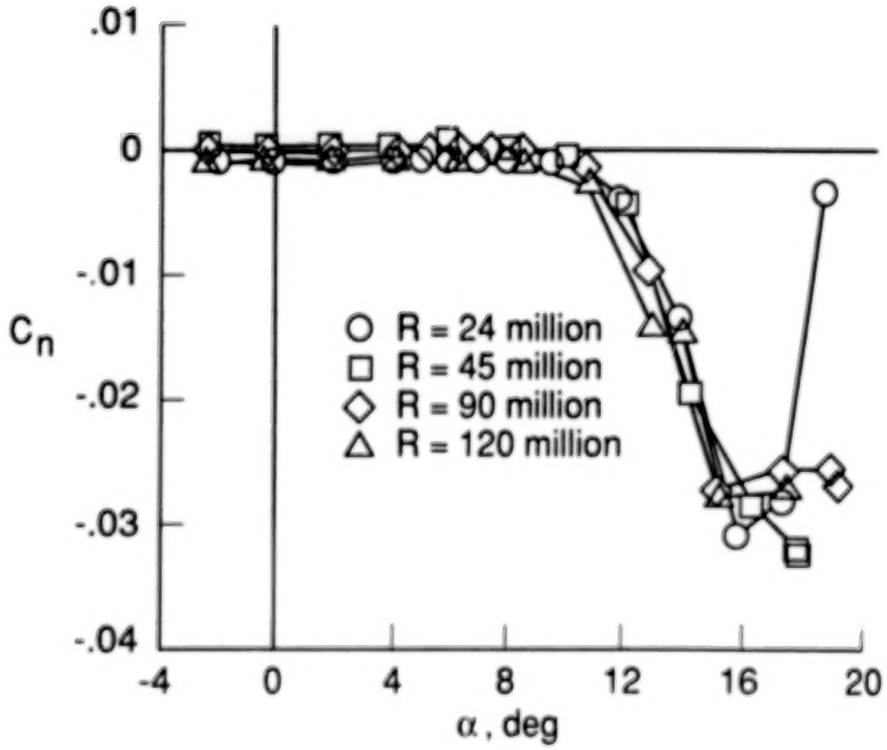

(b) $M_\infty = 0.9$

Figure 10.- Effect of Reynolds number on yawing moment.

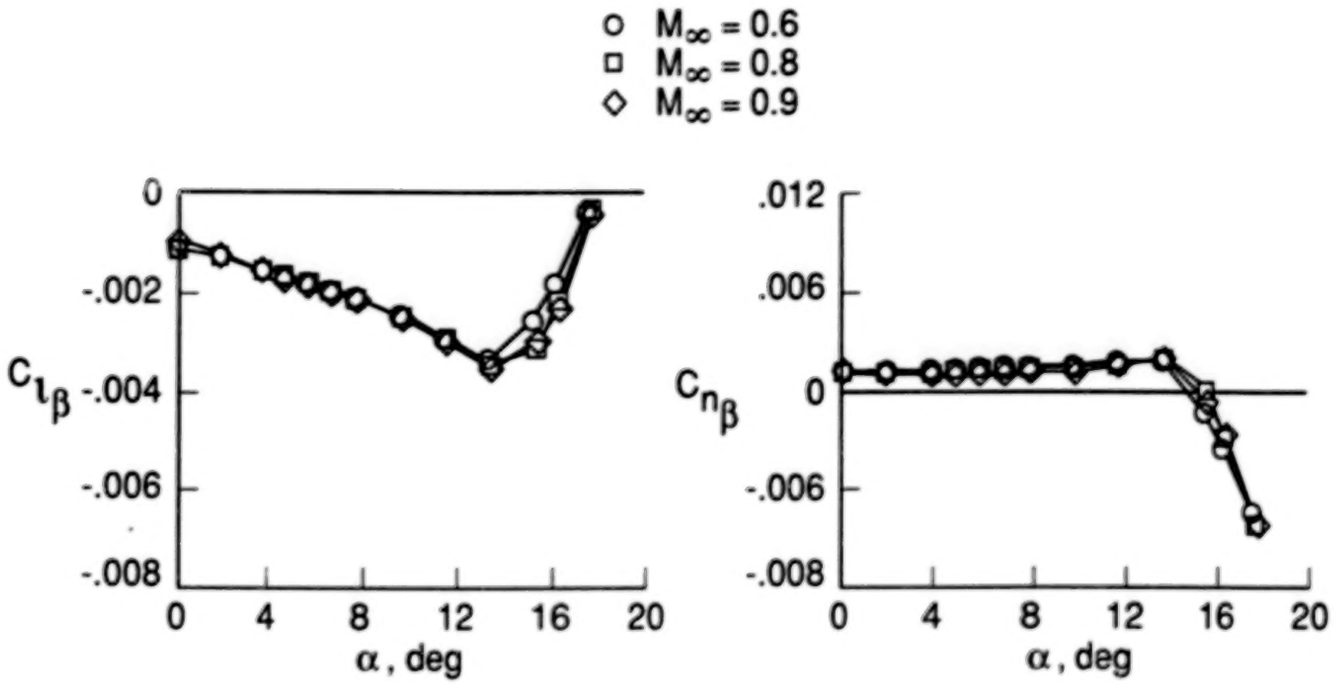

(a) R = 24 million.

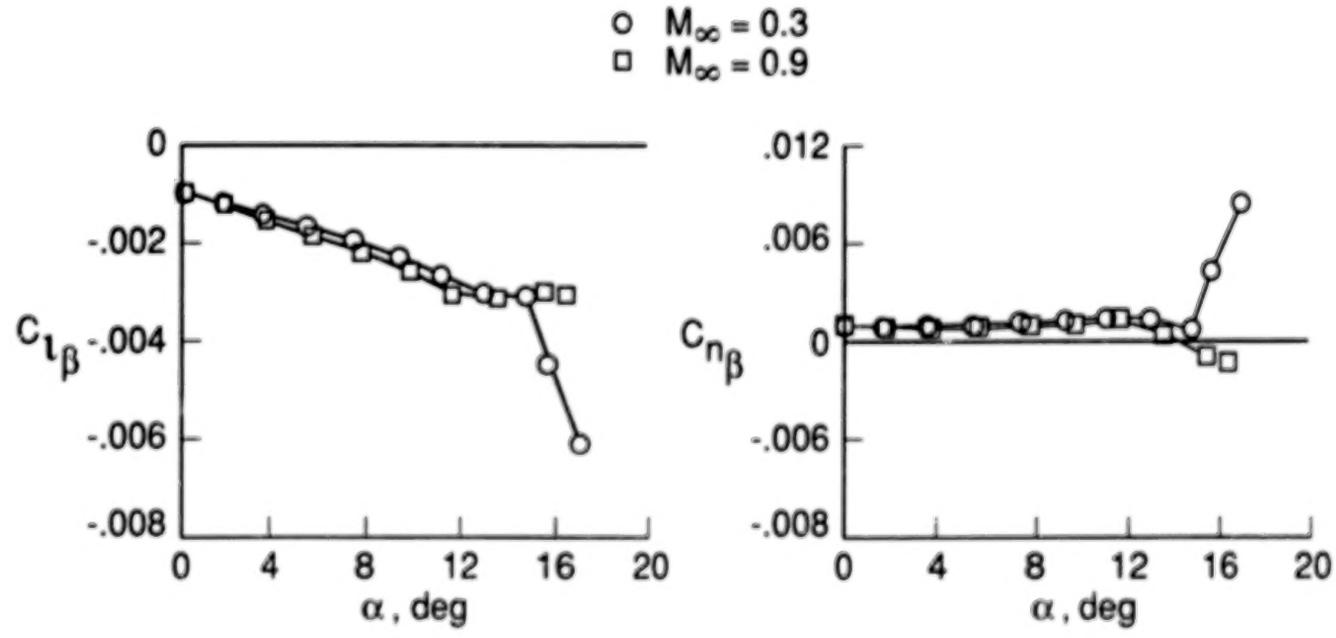

(b) R = 90 million.

Figure 11.- Effect of Mach number on lateral-directional stability.

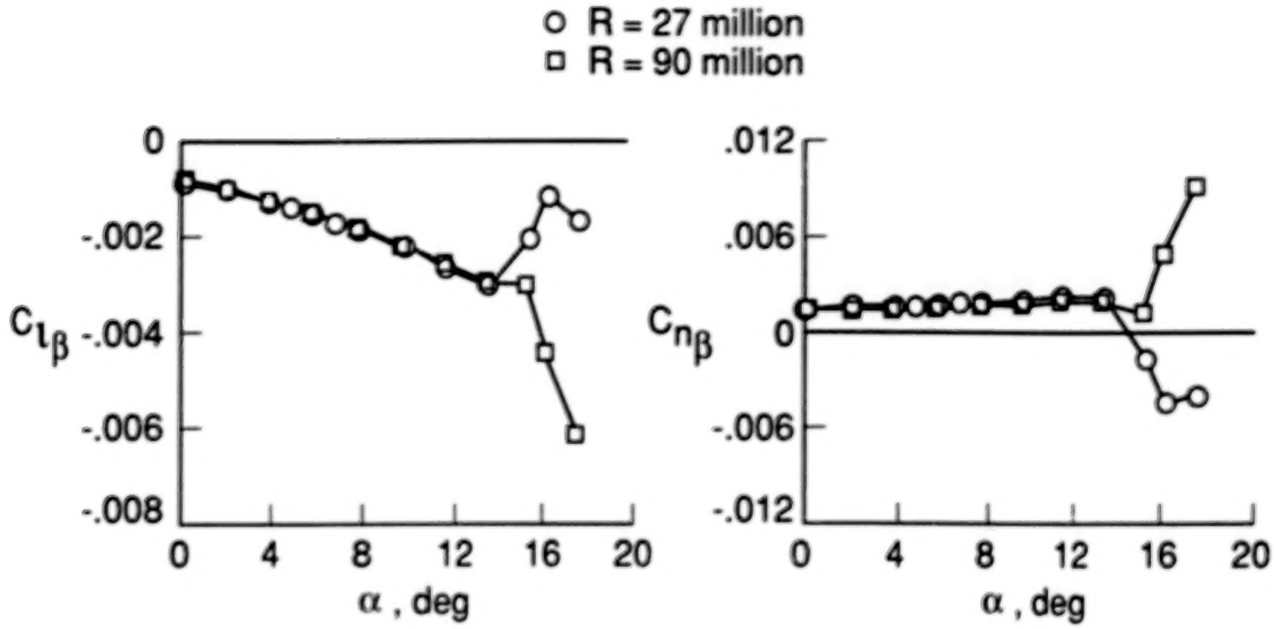

(a) $M_\infty = 0.3$

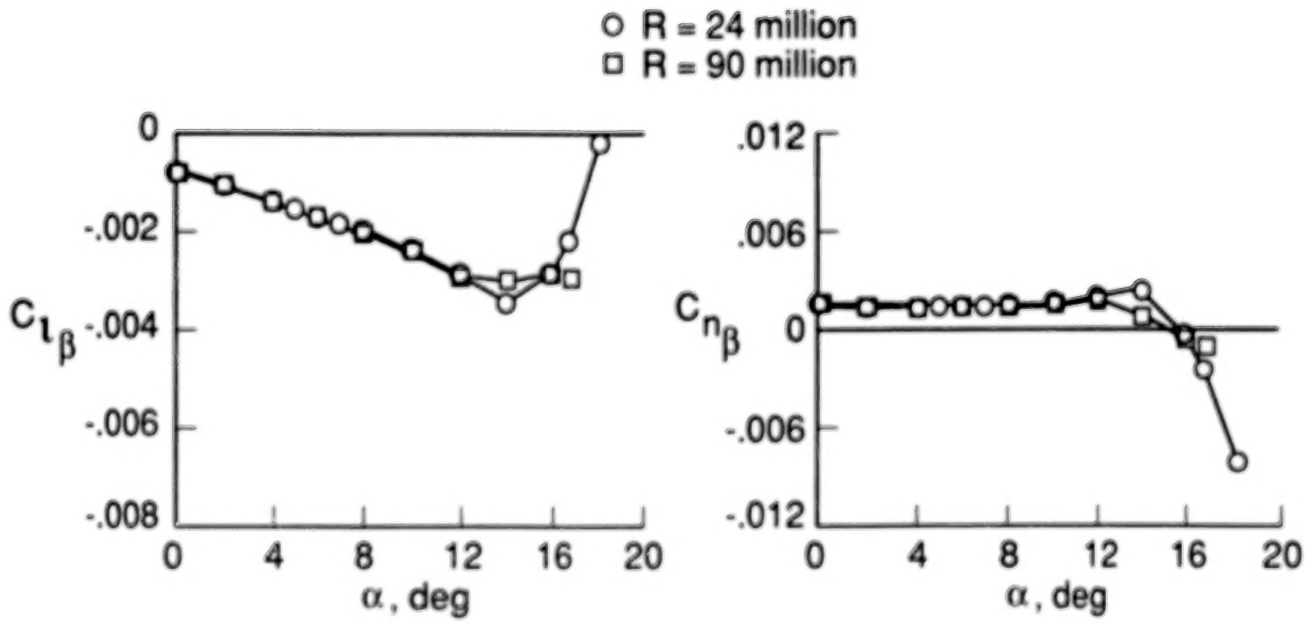

(b) $M_\infty = 0.9$

Figure 12.- Effect of Reynolds number on lateral-directional stability.

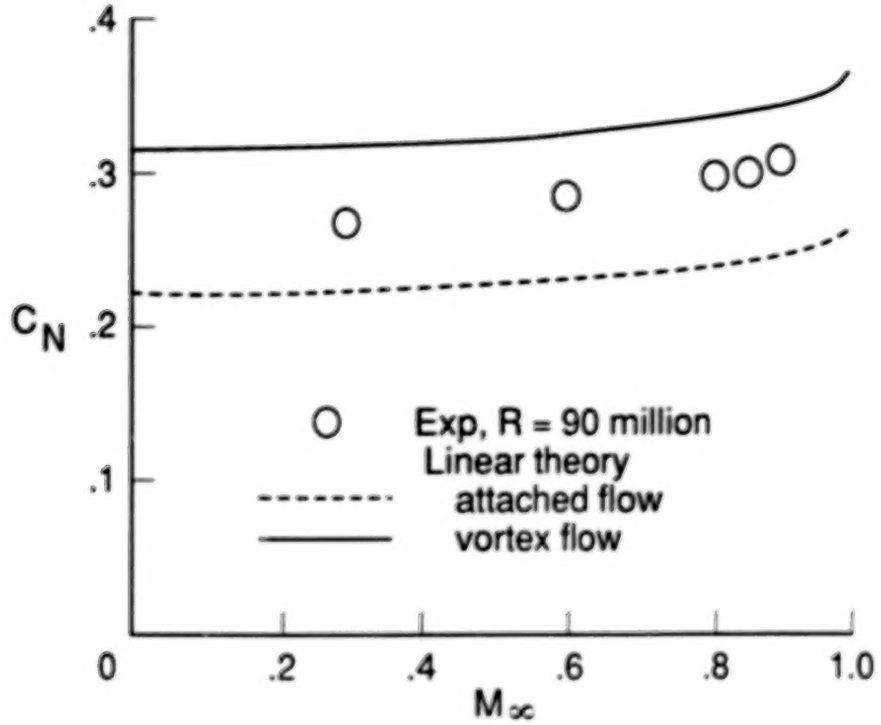

(a) Normal force, $\alpha = 10°$.

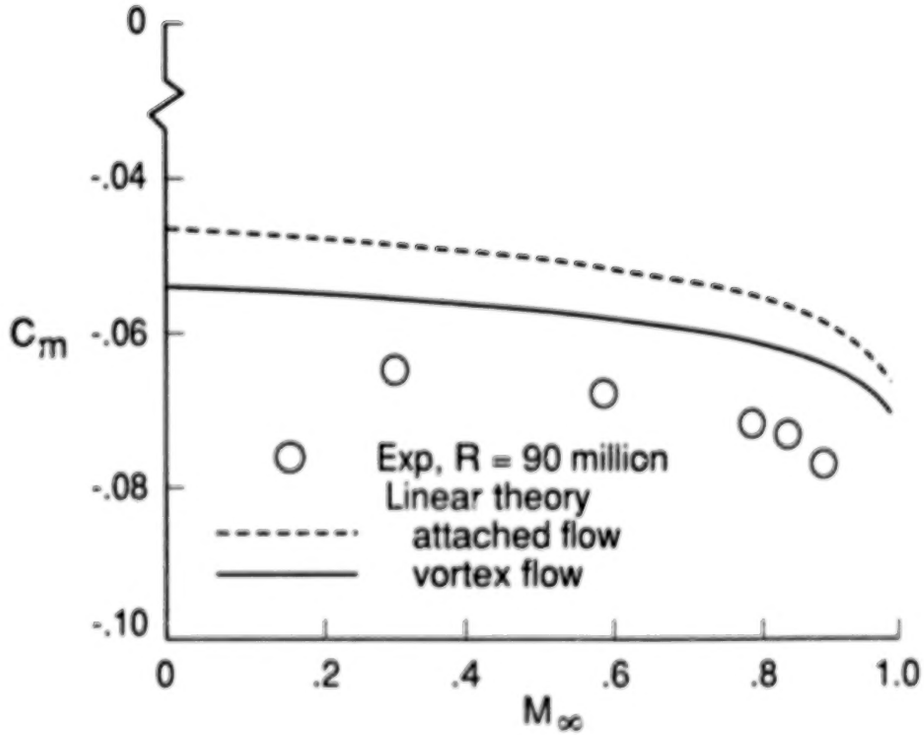

(b) Pitching moment, $C_L = 0.3$.

Figure 13.- Theoretical estimates for compressibility effects.

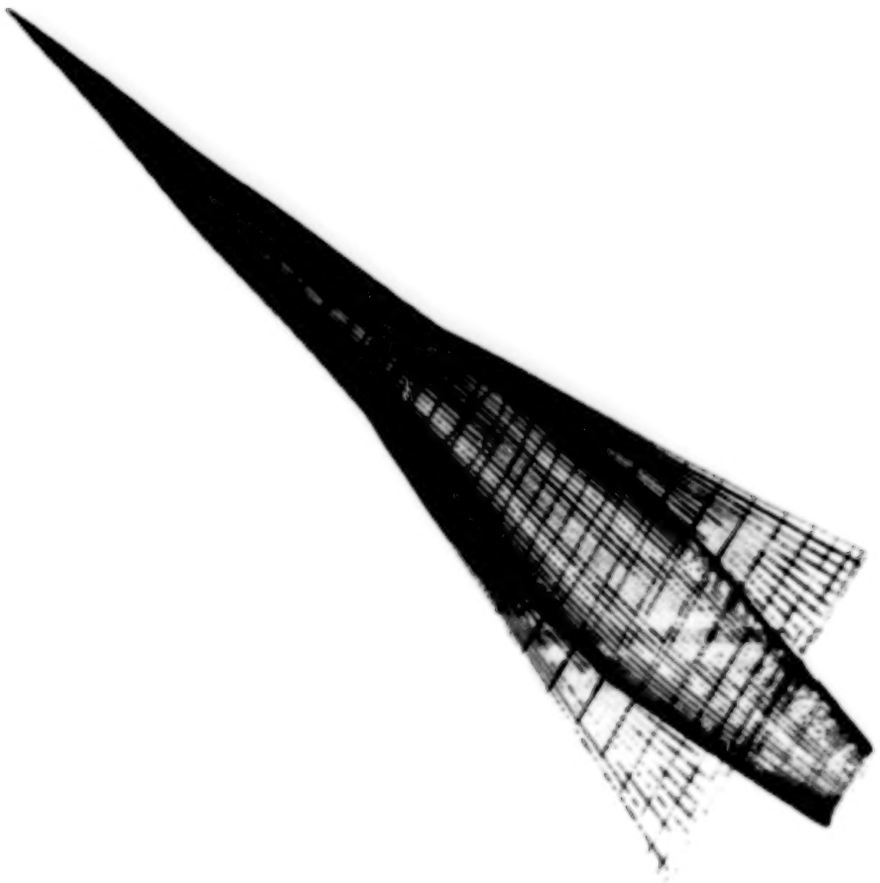

Figure 14.- Surface grid representation.

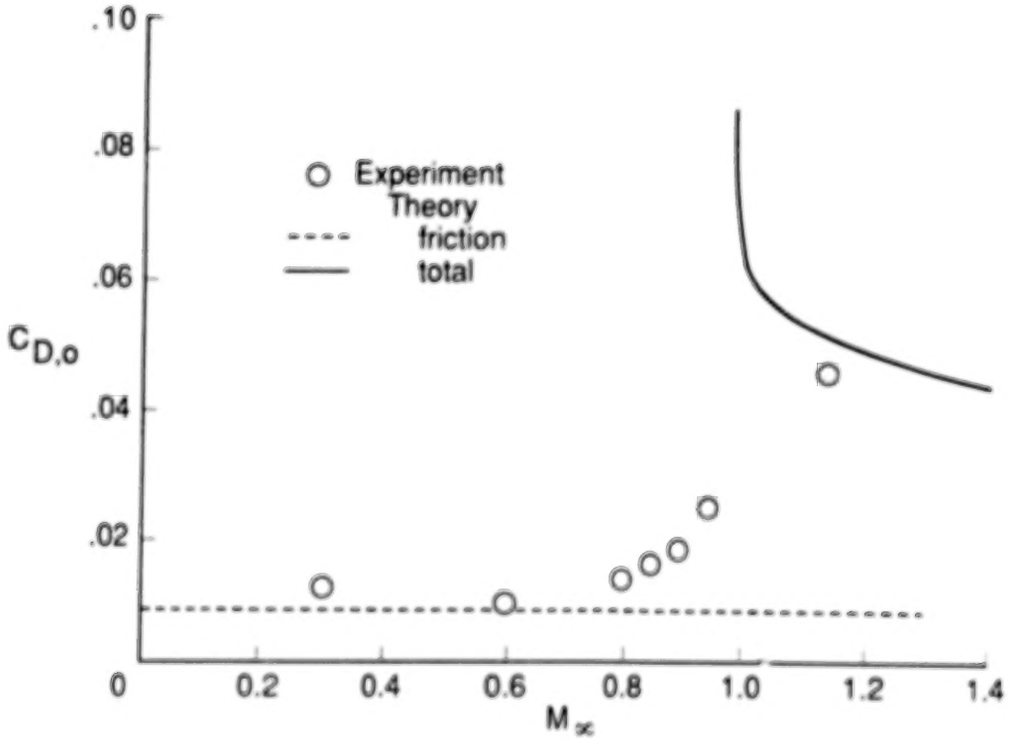

Figure 15.- Zero lift drag rise. R = 90 million.

N91-24135

LAMINAR-FLOW FLIGHT EXPERIMENTS

53-02
19850

*R. D. Wagner, *D. V. Maddalon, *D. W. Bartlett,
**F. S. Collier, Jr., and ***A. L. Braslow
*NASA Langley Research Center
Hampton, Virginia

**High Technology Corporation
Hampton, Virginia

***Analytical Services and Materials, Inc.
Hampton, Virginia

INTRODUCTION

On December 17, 1937, B. Melvill Jones presented the first Wright Brothers' lecture at Columbia University in New York (ref. 1). His lecture, which was entitled "Flight Experiments on the Boundary Layer," dealt specifically with the first British flight observations of transition of the boundary layer from laminar to turbulent flow. These data, Jones concluded, showed that it is possible to retain a laminar layer over at least one-third of the whole wing surface even when the chord Reynolds number is as high as 8 millions. In the 50 years since this presentation, much flight research has been performed to explore the potential of laminar-flow control for drag reduction. Both passive control and active control by suction (designated as natural laminar flow and laminar-flow control, respectively) have been researched and impressive results achieved. The successes of the early natural laminar-flow (NLF) flight testing were remarkable, with the achievement of an extent of laminar flow and transition Reynolds numbers which were not to be exceeded in flight for over 40 years. Nevertheless, mid-century manufacturing capabilities were such that insufficiently smooth or wave-free wing surfaces led to failure of attempts to transfer this technology to practice. The experience with laminar-flow control (LFC) nearly paralleled that of NLF. LFC was recognized as a potentially more powerful means for achieving extensive laminar boundary layer flow, although admittedly more complex from the systems standpoint. LFC flight research began in the 1940's and peaked in the 1960's with the USAF/Northrop X-21 program, the most ambitious LFC flight test to date, which attempted to achieve full chord and full span laminar flow on a swept wing (ref. 2). Two WB-66 aircraft were fitted with new, full chord suction controlled laminar-flow wings and flight tested over 3 years. The main result of the program was that laminar-flow control was observed to be aerodynamically achievable, but surface quality and structural complexity still appeared formidable barriers to LFC applications.

For a period of almost 10 years, research in NLF and LFC was dormant. The energy crisis of the early 1970's revived interest in the technology and flight testing resumed. Today, the prospects for a practical technology are brighter than ever. We have a greater understanding of the phenomena involved and new, less-complex systems concepts are evolving. Critically important to this new outlook is the fact that our marufacturing capabilities have dramatically advanced since the 1960's and the needed wing surface quality appears within our reach.

In this paper, the flight testing conducted over the past 10 years in the NASA LFC program (ref. 3) will be reviewed. The LFC program has been directed towards the most challenging technology application, the high subsonic speed transport. To place these recent experiences in perspective, earlier important flight tests will first be reviewed to recall the lessons learned at that time.

ACRONYMS

AFWAL	Air Force Wright Aeronautical Laboratory
TACT	Transonic aircraft technology
NACA	National Advisory Committee on Aeronautics
NPL	National Physics Laboratory
LFC	Laminar-flow control
mac	Mean aerodynamic chord
LTPT	Low-Turbulence Pressure Tunnel
Max	Maximum
PW	Pratt and Whitney
NLF	Natural laminar flow
LE	Leading edge
OASPL	Overall sound pressure level
rpm	Revolutions per minute
dB	Decibel
N-OASPL	Normalized overall sound pressure level
Hz	Hertz
HLFC	Hybrid laminar-flow control

SYMBOLS

a	Speed of sound
C_p	Pressure coefficient
$\bar{c}$	Mean chord
c	Chord
R_c	Reynolds number based on chord
R_T	Transition Reynolds number
R_x	Reynolds number based on x
U	Free-stream velocity
M	Mach number

x	Distance along chord in streamwise direction
ℓ	Liter
C_L	Lift coefficient
L	Lift
A	Area
M_{FAN}	Fan Mach number
N	Engine rpm
N_{TS}	N-factor for Tollmien-Schlichting (TS) calculation
N_{CF}	N-factor for crossflow (CF) calculation
P	Pressure
S	Surface distance along normal chord
t	Time

GREEK

ρ	Density
μ	Laminar coefficient of viscosity, or microns
Λ	Sweep angle
η	Span station
β	Sideslip

EARLY LAMINAR-FLOW FLIGHT RESEARCH

A brief review of some of the most significant past efforts on laminar flow is beneficial in understanding the needs for further research. Examples of some of the most pertinent flight tests will be presented to highlight the knowledge gained. In such a review, wind tunnel tests cannot be ignored because of the often elucidative impact they had.

The earliest known attempts to attain extensive regions of laminar flow in flight were made in the late 1930's and early 1940's. Both NLF with favorable chordwise pressure gradients and active LFC with boundary layer suction were investigated.

The B-18 flight test by the NACA in 1939 (ref. 4) was a major milestone in the development of NLF. Therein, an attempt was made to prolong the run of laminar flow to higher Reynolds number than had previously been achieved by flight testing a 17-foot chord, 10-foot span wooden NLF glove on the wing of the test aircraft (Figure 1). An exceptional effort was made to evaluate surface quality effects by working the wing to previously unattained smoothness and fairness. The flight test clearly displayed the importance of surface discontinuities and finish. In fact, the adverse effect of surface disturbances (surface waves, two-dimensional type steps, and three-dimensional type roughness) was the most pervasive factor observed in the early tests and continued to be the principal cause of limited laminar flow in most future flight and wind-tunnel tests. Although the severity of the surface disturbances was always shown to be aggravated by increased unit Reynolds number, it was not until considerable research (made possible by the development of the Langley Low-Turbulence Pressure Tunnel , LTPT) had been completed in the late 1940's and 1950's that an understanding of this phenomenon was developed, resulting in a quantitative ability to predict the magnitude of permissible three-dimensional disturbances (ref. 5). It was not until the 1960's that a quantitative ability to predict permissible waviness and two-dimensional type disturbances was developed.

The maximum transition Reynolds number, based on free-stream conditions and distance to the position of transition, attained in the B-18 flight tests was about 11.3 million with laminar flow to 42.5-percent chord on an NACA 35-215 section with only a 3-percent chord loss of laminar flow due to engine and propeller noise. This NLF transition Reynolds number was not to be exceeded in flight for over 40 years, until the NASA F-111/TACT NLF glove flight tests to be discussed later in this paper. The B-18 flight test was very encouraging in its time, because it indicated that the flight environment was possibly more benign for laminar flow than wind tunnels which until then had achieved laminar flow only at lower Reynolds number. The wind-tunnel tests were highly compromised because the higher unit Reynolds numbers of the tunnels exacerbated the roughness problem. Later wind-tunnel tests, in the quiet LTPT (ref. 6), suggested that the B-18 maximum length of NLF was constrained by the glove dimensions or achievable aircraft unit Reynolds number, and even higher transition Reynolds numbers might be obtained in flight. Indeed, the wind-tunnel experiments performed by Braslow (refs. 6 and 7) showed natural transition Reynolds numbers of 14 to 16 million for 6-series airfoils.

During World War II, several military aircraft were built with NACA 6-series airfoils, which were designed to achieve extensive natural laminar flow. Perhaps the most notable of these airplanes was the P-51 Mustang. But it is doubtful that much laminar flow was achieved on these aircraft because attention was not given to the surface quality that was required to maintain laminar flow. These aircraft flew in a harsh environment for obtaining laminar flow (i.e., at high speeds and low altitudes such that the unit Reynolds number was high) which placed stringent demands on surface smoothness and fairness. But after the war, attempts were made to see if NLF technology could be reduced to practice. The flight tests of King Cobra and Hurricane aircraft reported in references 8 through 10 are examples of such efforts (see figures 2 and 3). The King Cobra used production wing surfaces that were highly polished and filled to reduce waviness. The Hurricane employed an NLF section in a special, "low-drag construction" wing thought to be suitable for the maintenance of laminar flow. With highly polished surfaces good NLF performance was achieved on these aircraft, but underlying concerns with the practicality of the wing surface tolerances and maintenance defeated these efforts. Now, some 40 years later, the general aviation industry is just beginning to explore the use of NLF on aircraft for which the Reynolds number capability was more than demonstrated by the early NLF flight testing. Many general aviation aircraft now fly at higher altitudes, where unit Reynolds numbers are lower, and recent advancements in wing fabrication techniques now offer the possibility of routinely producing small aircraft with sufficient surface smoothness and fairness.

Active laminar-flow control with boundary-layer suction has been used in attempts to extend the laminar flow into the region of adverse chordwise pressure gradient, which is not possible to any appreciable degree with NLF. Suction through porous materials, multiple slots, and perforations were tried with various degrees of success (e.g. refs. 11-15). Three Vampire aircraft (figure 4 and refs. 12 through 14) with a number of suction surface configurations (continuous porous, perforated, and porous strips) and an F-94 aircraft (figure 5 and ref. 15) with suction through multiple slots were flight tested in the mid-1950's. The F-94 tests were very encouraging. With 69 slots between 41-to 95-percent chord, full-chord laminar flow to length Reynolds numbers of 36.4 million was obtained on the F-94. The addition of slots and suction in the favorable gradient (x/c less than 41 percent) was found to significantly broaden the lift-coefficient range for low drag with laminar-flow achievement. Laminar flow was lost behind shock waves on the F-94 when the aircraft speed was increased to the point where the local Mach number on the airfoil surface exceeded about 1.09. An important observation of the F-94 flight program was that the remains from insect impacts at low altitudes became subcritical at high speeds and altitudes above 20,000 feet for the boundary-layer flow of the unswept, F-94 wing. Unfortunately, this experience did not prevail in later flight test of swept wings, for which smaller critical roughness height has been observed in the regions of boundary-layer crossflow (ref. 16). The Vampire aircraft tests experienced unusual surface roughness difficulties. Continuous suction (from 6 to 98-percent chord) through a porous panel cloth (covered with nylon) or through 0.007 inch diameter perforations proved nearly as successful as the slotted F-94 surface, but each of these surfaces was thought to be impractical to manufacture and maintain. Two, "more practical" surfaces were tested, but with poor results. One incorporated porous strips of suction with sintered metal inserts; the other had

perforations, 0.020 inch in diameter (the smallest holes then thought to be practical for manufacturing). The metal inserts caused surface discontinuities under flight loads, and the larger perforations caused transition by introducing unstable secondary flow in the boundary layer.

In the early 1960's, the most ambitious LFC flight program to date was undertaken by the Northrop Company. Under U.S. Air Force sponsorship, two WB-66 aircraft were modified with slotted suction wings and designated X-21 experimental aircraft (figure 6 and ref. 2). At the end of the program, full-chord laminar flow with suction was routinely obtained at Reynolds number of about 20 to 25 million. This was only after a long and difficult effort to improve performance through the systematic isolation and solution of problems, many due to wing sweep.

The most troublesome phenomenon encountered with the X-21 involved leading-edge turbulence contamination, a problem unique to swept wings. On the X-21, and at about the same time on a swept slotted-suction wing mounted vertically on the fuselage of a Lancaster bomber (figure 7 and ref. 14 and 17), the significance of this problem became apparent. Although previous small-scale wind tunnel and flight experimentation by the British (refs. 18 and 19) had indicated the existence of the spanwise turbulence contamination problem; its significance had gone unrecognized until the large scale flight tests. Subsequent flight and wind-tunnel tests indicated that leading-edge scale was a predominant factor and that proper treatment of the inboard wing leading edge could prevent turbulence contamination of the swept wing from disturbances that propagate down the wing leading edge along the attachment line (e.g. ref. 16). Although this phenomenon is now understood, it requires careful attention in the design of large LFC aircraft.

Another adverse effect of wing sweep on the ability to attain laminar flow had been found earlier during flights by the British with an AW52 airplane in 1951 (ref. 18) with a natural laminar-flow airfoil. A series of tests were performed where transition was shown to occur very close to the leading edge as a result of the formation of streamwise vortices in the laminar boundary layer. Later, an inability to obtain laminar flow in the last 20-percent chord of a Vampire trainer aircraft (ref. 14) was attributed to the forward sweep of the trailing edge. This sweep-induced boundary-layer instability was caused by the large crossflows resulting from strong, favorable or adverse chordwise pressure gradients on swept wings. Research prior to the X-21 program (ref. 20) showed that the proper application of suction is effective in controlling this crossflow instability; a result borne out in the X-21 flight tests.

Although structural flaws in the X-21 wing design produced surface waves and discontinuities that required liberal use of filler for smoothness, extensive laminar flow was routinely obtained at cruise altitudes of 40,000 ft. at Mach 0.75. A composite of the best wing surface laminar-flow performance is shown in figure 8 with remarkably good results obtained on the upper and, to a lesser degree, the lower wing surfaces. Flexing of the wing in flight continually deteriorated the surface quality due to the filler loss, but a series of 12 flights showed good repeatability even with major surface discrepancies on the last flight, figure 9. Nonetheless, the X-21 wing structure was just not good enough to provide the surface quality needed for a convincing demonstration that LFC was ready for application. The poor laminar-

flow performance at lower altitudes and higher chord Reynolds number was undoubtedly due to the aggravated effects of poor surface quality at higher unit Reynolds numbers (figure 10). Still, maximum-length laminar-flow Reynolds numbers up to 45.7 million were observed in some areas.

Another phenomenon adverse to achieving laminar flow was also realized and investigated during the X-21 program. It was noted that flight through visible cirrus clouds, and sometimes very light haze, caused loss of laminar flow. At cruise altitudes, cirrus clouds are composed mainly of ice crystals; entrainment of the crystals in the boundary layer produced local turbulence leading to the loss of laminar flow (figure 11). Turbulent vortices shed by ice particles in the boundary layer were thought to trigger transition for certain combinations of particle size, concentration, and residence time in the boundary layer. At the termination of the X-21 program, concerns about this phenomenon and other unanswered issues on the operation of LFC aircraft were high.

In summary, when interest in laminar-flow technology was rekindled by the energy crisis in the early 1970's, the fundamental aerodynamic concepts of both passive and active laminar-flow control had been well established, verified in wind-tunnel tests and demonstrated in various flight tests. The aerodynamics of the technology appeared to be well in hand. Laminar flow to Reynolds numbers up to 16 million had been observed on two-dimensional NLF sections, and it was not clear that an upper bound on the transition Reynolds number had been reached. Suction control had been demonstrated for boundary layers in adverse pressure gradients and on swept wings at Reynolds numbers well above 16 million; specifically, full chord laminar flow to about 36 million chord Reynolds for the former and 46 million for the latter. Yet, no practical application had been made with any suction method. The ability to manufacture and maintain aircraft surfaces with admissible tolerances, considerably smaller than required for turbulent aircraft, and at acceptable cost was still viewed as a formidable challenge. Neither suction slots nor perforations could be manufactured economically within required tolerances, and the latter were believed to generate disturbances that adversely affected the ability to attain large length Reynolds numbers. Criteria for the proper design of slots were greatly improved during the X-21 flight program. With respect to perforated surfaces, early research indicated the need for hole diameters smaller than could be practically fabricated at that time. Porous surfaces with the required structural characteristics and aerodynamic smoothness were not available.

Over the past decade, NASA and the aircraft industry have launched programs to continue the development of this technology and to provide the information needed for objective decisions on its application to new aircraft. The flight tests reviewed in this paper have been an integral part of those efforts.

F-111/TACT NLF GLOVE FLIGHT EXPERIMENT

The NACA 6-series airfoils were originally developed for low-drag, NLF applications. In actuality, these airfoils were used on many of the early jet aircraft because they had very good performance as turbulent airfoils. However, modern supercritical airfoil technology has since led to improved airfoils with greatly enhanced turbulent performance (i.e., drag divergence Mach number, thickness ratio and lift coefficient capability). For this reason, in the late 1970's, the Boeing Company designed a new supercritical, NLF airfoil in a NASA contract study to evaluate NLF for transport aircraft applications (ref. 21). With the Boeing airfoil as a starting point, a new supercritical NLF airfoil was designed at the Langley Research Center and flight tested at the Ames-Dryden Flight Research Facility on the F-111/TACT aircraft (refs. 22-24). The objective of the flight test program was to investigate natural laminar flow at transonic speeds.

A supercritical, natural laminar-flow airfoil glove was installed on the right wing panel of the F-111/TACT aircraft (figure 12). The glove was made of fiberglass skins with an inner core of polyurethane foam and bonded to the metal wing skin. For symmetry, an uninstrumented glove was also installed on the left wing panel. The glove had a 6-foot span, a 10-foot chord, and was finished to "sail-plane" quality. The glove airfoil design pressure distribution (figure 13) had a favorable gradient that extended to about 70-percent chord on the upper surface ($dCp/dx/c = -0.4$) and to about 50-percent chord on the lower surface ($dCp/dx/c = -0.8$). The airfoil design lift coefficient was 0.5 at a Mach number of 0.77 and a Reynolds number of 25 million. On the upper surface at this condition, supersonic flow extended from about 20-percent chord to 70-percent chord where the favorable gradient terminated in a weak shock. The glove was installed on the airplane to achieve the design pressure distribution at 10 degrees of leading-edge sweep (figure 12); however, wind-tunnel tests had indicated that the pressure distributions at the higher sweep angles (up to 26 degrees) were acceptable for obtaining transition data at these conditions (i.e., no leading-edge peaks or premature adverse gradients). In hindsight, the low design sweep angle of the glove was very conservative, but at that time, some studies had been very pessimistic regarding the amount of laminar flow that could be obtained at even moderate sweep angles and Reynolds numbers approaching 30 million (ref. 21).

Results from the flight-test program (ref. 24) indicate that the maximum extent of laminar flow was about 55-percent chord on the upper surface at 10 degrees of sweep for a chord Reynolds number of 28 million. However, as the wing sweep was increased to 26 degrees, the transition location moved forward to the 10 to 20-percent chord range (figure 12). On the lower surface at 28 million chord Reynolds number, the maximum extent of laminar flow was about 50-percent chord (the start of the adverse gradient) and this was achieved to sweep angles as high as 15 degrees.

The wind-tunnel pressure distributions on the glove upper surface were much smoother than those obtained in flight (figure 13), particularly at the higher sweep angles. Although the majority of the wind-tunnel results have not been published, stability analyses are presented for five cases in reference 25. Based upon the wind-tunnel pressure distributions, these analyses

predicted transition locations significantly further aft than those measured in flight on the upper surface. The irregularities in the flight upper-surface pressure distributions, which led to premature transition, were apparently caused by shocks propagating onto the glove from the inboard wing and not by surface waves in the glove skin. In retrospect, the 6-ft. span of the glove was too small to isolate the glove from the flow on the remainder of the basic F-111/TACT wing over a broad range of conditions. Even for the design point at 10 degrees of sweep, there was a weak shock wave on the glove near 55-percent chord that limited the extent of laminar flow to this point instead of further aft near the pressure minimum (figure 13). Since the lower-surface flow was subcritical, the lower-surface flight pressures were much smoother than those obtained on the upper surface, and in several cases laminar flow was obtained to the pressure minimum (approximately 50-percent chord). However, the steeper favorable gradient on the lower surface (figure 13) was not suitable for achieving large runs of laminar flow at the higher sweep angles because of increased crossflow instability.

The F-111/TACT NLF experiment was brief, and consequently the transition data were very limited. However, the results were very encouraging. The maximum transition Reynolds numbers of about 15 million on the upper surface for 10 degrees of sweep, and 14 million on the lower surface at 15 degrees of sweep were significantly higher than values obtained in previous NLF flight tests. The closest comparable flight test had been conducted over 40 years earlier on the B-18 bomber previously discussed. During that test, a maximum transition Reynolds number of about 11.3 million was obtained.

F-14 VARIABLE SWEEP TRANSITION FLIGHT EXPERIMENT

Since the F-111/TACT NLF glove pressure distributions had not been designed to minimize crossflow at the higher sweep angles, and since the maximum extent of laminar flow on both the upper and lower surface was determined by adverse pressure gradients, even larger transition Reynolds numbers at moderate sweep angles seemed possible. In addition, the techniques for fabricating and bonding large and very smooth foam and fiberglass test surfaces or gloves to metal wings had been developed and proven acceptable for flight testing. Consequently, the F-111/TACT NLF experiment paved the way for a follow-on program that could provide a much broader transition data base.

The F-14 Variable Sweep Transition Flight Experiment was initiated in 1984 (refs. 26 and 27)) with flight tests being completed in 1987. These tests were conducted with an F-14 (figure 14) on loan to NASA from the Navy. Obtaining transition data was the primary objective of the program - not airfoil design verification. Therefore, only the upper surface of the wing was gloved in order to provide a laminar-flow test surface. The gloves extended from about 10-percent chord on the lower surface to about 60-percent chord on the upper surface (spoiler hinge line) and covered the majority of the variable-sweep outer panel (figure 15). Four rows of flush static pressure orifices and three arrays of hot-films were distributed along the span for determination of the local wing pressure distributions and transition locations. These data and the other associated flight parameters were monitored in real time on the ground during all the testing.

Two gloves were flight-tested during the program: one was a "clean-up" or smoothing of the basic F-14 wing (modified NACA 6-series airfoils), while the second involved significant contour modifications to the basic F-14 wing. The second glove, designed at NASA Langley (ref. 27), provided more moderate favorable pressure gradients than the "clean-up" glove, and achieved more of a two-dimensional type flow (straighter isobars) over a larger part of the span. Both gloves were constructed of fiberglass skins with an inner core of polyurethane foam (ref. 28). Measurements taken on the gloves with a mechanical deflection gauge having support feet two inches apart indicated wave amplitudes no larger than 0.002 in. Representative pressure distributions at several Mach numbers are presented in figures 16 and 17 for both gloves. The Langley glove design provided a wide variety of pressure distributions with different favorable gradients to about 50-percent chord over a broad Mach number range (0.6 to 0.8).

The transition location at 0.7 Mach number on the Langley-designed glove is presented in figure 18 as a function of wing sweep for altitudes of 20,000 ft. and 30,000 ft. Transition locations for the "clean-up" glove are presented in reference 27 and for the F-111/TACT NLF glove in figure 12 of the present paper. However, to compare various transition or laminar-flow experiments, transition Reynolds number is a more appropriate parameter for comparison than just transition location. Therefore, the maximum transition Reynolds number observed in several of the more significant flight and wind-tunnel experiments are presented in figure 19. For this figure, transition Reynolds number is based on free-stream conditions, rather than local conditions. In addition to the F-111 and F-14 experiments, included in figure 19 are results from several natural laminar flow tests: the B-18 flight test (ref. 4); the King Cobra flight test (refs. 8 and 9); a T-33 flight test (unpublished data from the Boeing Company); the 757 NLF glove flight test conducted by the Boeing Company (refs. 29 through 31); and low-speed wind-tunnel tests conducted in the 12-Foot Tunnel at NASA-Ames Research Center (ref. 32) and the LTPT at the Langley Research Center (refs. 6 and 7). Prior to the F-111 and F-14 flight tests, the highest NLF transition Reynolds numbers for airfoils or wings had been obtained in the LTPT at Langley and the 12-Foot Tunnel at Ames. These are very quiet tunnels and only until recently have airplanes (i.e., jet-powered aircraft) been able to match the Reynolds number capability of these facilities. More importantly, very few large aircraft have had the capability of providing large runs of laminar flow.

As previously discussed, results from the F-111/TACT NLF Glove Experiment had exceeded the prior maximum values for natural laminar-flow transition Reynolds numbers that had been obtained in flight on the B-18 and King Cobra. Results obtained during the F-14 VSTFE indicate maximum transition Reynolds number values exceeding F-111/TACT and wind-tunnel values up to 30 degrees of sweep. For the F-14 VSTFE, a maximum transition Reynolds number of about 17.6 million was obtained at 15 degrees of sweep, 13.5 million at 20 degrees, and 12 million at 25 degrees. Beyond 25 degrees of sweep, maximum transition Reynolds number decreased rapidly to about 5 million at 35 degrees of sweep. It should be pointed out that for all the maximum transition Reynolds number cases on both the F-111 and F-14, the amount of laminar flow was limited by either adverse pressure gradient or shock wave location. This suggests that even higher transition Reynolds numbers are possible in flight.

In comparison to the NLF tests, as would be expected, maximum transition Reynolds numbers for most suction or laminar-flow control experiments are much higher. As previously discussed, transition Reynolds numbers of about 30 to 36 million were obtained in flight on the Vampire and F-94, and a value of about 46 million was obtained in a small area of the X-21 wing. However, with suction only in the leading-edge region of swept wings, the transition Reynolds number for natural laminar-flow designs can be significantly increased — possibly doubled. This concept, called hybrid laminar-flow control (HLFC), is discussed later in the paper.

757 WING NOISE SURVEY AND NLF GLOVE FLIGHT TEST

In 1985, under a NASA contract, the Boeing Company performed a flight test to measure the acoustic environment in cruise on the wing of a 757 aircraft with a view towards the determination of the potential effects of the acoustic environment on boundary-layer transition (refs. 29, 30, and 31). Prior to this flight test, there were no extensive measurements of the noise environment on the wing of a commercial transport with wing-mounted, high-bypass-ratio turbofan engines. Engine noise concerns had led to conservatism in LFC aircraft design studies, with designs restricted to aft engine placement with a potentially severe adverse impact on performance and a degradation of LFC fuel savings potential. A major part of the 757 flight test was an attempt to achieve a limited amount of laminar flow over the wing and measure the impact of the engine noise intensity on the extent of laminar flow. Although the primary goals differed, an interesting parallel exists between the 757 and the B-18 tested some 45 years earlier. As with the B-18, the 757 experiments yielded encouraging results with regard to engine noise effects on laminar flow.

Boeing removed a leading-edge slat on the 757 wing just outboard of the starboard engine and installed a 10-foot span, NLF glove constructed of dense foam with a fiberglass epoxy overlay to produce a smooth, nearly wave-free surface (figure 20). The glove was designed to achieve laminar flow on both the upper and lower surface, with 20-to 30-percent chord laminar flow expected without adverse engine noise effects. This anticipated result was made possible in part by unsweeping the wing to 21 degrees at the glove location and by the favorable pressure distribution over the wing. A single microphone was installed on the glove leading edge and eight others were installed on each of the wing surfaces (upper and lower) — three on the glove and five distributed over the remaining wing surface (figure 20). Hot films were used to detect the transition front on the upper and lower surfaces. Measurements were made over cruise altitudes of 25 to 41 thousand feet at Mach numbers of 0.63 to 0.83. The starboard engine was throttled from maximum continuous thrust to idle at cruise speeds and altitudes.

Typical measurements of the overall sound pressure level (OASPL) at the design cruise condition are shown in figure 21. Generally, the OASPL is lower on the upper surface of the wing with measurements ranging from 111-to 131-decibels. On the lower surface, the measured levels ranged from 121-to 136-dB. Collectively, the acoustic data presents a rather confusing picture, undoubtedly due to the broad range of flight conditions and changing phenomena that influence the OASPL's on the wing. Additional uncertainty is due to the

acoustic instrumentation because the magnitude of probe interference and self noise generation are difficult to assess. However, some important observations that have strong implications in laminar-flow wing designs were made.

Some order in the acoustic data is achieved by normalization of the OASPL's with the ambient pressure over the altitude range of the test conditions. These data are shown for two microphone locations in figure 22. Normalized OASPL's are presented for a microphone on the glove and one aft of the glove for various flight Mach numbers and engine power settings; the latter reflected by fan exhaust Mach number variations. Flight Mach number and engine power setting effects are measureably different on the upper and lower wing surface. The lower surface normalized OASPL's show a strong dependence on engine power setting with about a 20 dB. increase occurring from engine idle (fan Mach number equal to 0.7) up to maximum continuous thrust (fan Mach number equal to 1.28) when the lower surface acoustic characteristics seem dominated by engine noise. Engine power setting has little influence on the OASPL's on the upper surface, but significant variations occur with flight Mach number. The wing appears to effectively shield the upper surface from radiated engine noise and the dominant noise sources are presumed to be of aerodynamic origin. The data present strong evidence that the wing upper-surface flow field has a major influence on the radiated acoustic field, particularly at higher cruise speeds when shock waves occur on the wing. The supercritical flow over the upper surface inhibits forward radiation of sound from downstream sources, aerodynamic or engine related.

Attempts have been made to analyze the 757 acoustic data and make comparisons with theoretical predictions (ref. 31). A procedure developed by the Lockheed Georgia Company under NASA contract has been used (ref. 33). To the authors' knowledge this is the only code available to make near field noise predictions that include all the potentially relevant noise sources at flight cruise conditions. However, the theory lacks inclusion of the important effects of scattering, refraction, and reflection of sound fields due to the airframe or flow fields about it. For this reason, predictions for only the lower surface OASPL's and spectra have been made. We will not discuss these results in any depth herein. Generally, the results indicate that our ability to predict the acoustic environment at high cruise speeds and altitudes is poor. Theory suggests that the lower wing surface noise should be dominated by the fan exhaust broad band shock noise at cruise thrust conditions, which is consistent with the observed correlation with the fan Mach number; but the predicted levels of OASPL are 10 to 40 dB. too high. Trailing-edge noise is predicted to be an important aerodynamic noise source, particularly at aft wing locations; the data doesn't confirm this. Convective and dynamic amplification effects have large impacts upon the predictions. These effects or the methodology for their implementation are made suspect by the data. Clearly, more analyses of these acoustic data are needed to unravel the confused picture presented by the data and theory. With further analyses, the broad range of conditions for the 757 data could possibly permit useful calibration of the Lockheed code.

The amount of laminar flow obtained on the NLF glove was very encouraging. This result indicates that the acoustic environment may be benign enough to achieve extensive laminar flow on wings with wing-mounted engines. The results are summarized in figure 23 wherein the design condition and conditions of

maximum extent of laminar flow are shown. A maximum of nearly 30-percent chord laminar flow was obtained on both surfaces. At the design condition, best results were obtained on the upper surface, athough laminar flow was not uniform across the gloved span and was most extensive inboard. The upper surface pressures on the glove showed peaks in the outboard region which presumably led to earlier boundary-layer transition. Transition was more uniform across the lower surface with 26-percent chord laminar flow achieved when the aircraft was sideslipped to reduce the leading-edge sweep by 6.8 degrees.

On the upper wing surface, the extent of laminar flow was essentially unaffected by engine power setting. Since the power setting had no effect on the upper-surface noise levels, the unchanging extent of laminar flow is not surprising. On the lower surface, however, the noise levels varied over 20 dB., but almost imperceptibly small (2 to 3-percent chord decreases at most) changes in the extent of laminar flow were observed. Over the range of flight conditions, boundary-layer stability analysis (ref. 31) identified stationary crossflow vortices in the boundary layer to be highly unstable and possibly the dominant disturbances leading to transition. The results for the design flight condition are typical (figure 24). The crossflow disturbance amplification is two to three orders of magnitude greater than the amplification of Tollmien-Schlichting disturbances in both the upper and lower surface boundary layers. The small observed effect of variations in engine noise level on the transition location on the lower surface may indicate that engine noise does not have a significant effect on crossflow disturbances. If crossflow disturbance growth in the leading edge is controlled by suction, laminar flow much more extensive than achieved in this flight test could be possible even in the presence of engine noise. However, in an HLFC application, the Tollmien-Schlichting wave growth may be comparable or greater than the crossflow disturbance growth; engine noise might then be expected to limit the extent of laminar flow.

FLIGHT DATA/BOUNDARY-LAYER STABILITY THEORY CORRELATIONS

Under NASA contract, the Boeing Company has attempted to correlate the F-111/TACT and 757 data using linear boundary-layer stability theory (refs. 24 and 31). Their approach attempts to account for an interaction of crossflow disturbances and the Tollmien-Schlichting disturbances as predicted by linear stability theory by cross plotting the amplification N factors for these disturbances at transition. Stationary crossflow vortices and oblique Tollmien-Schlichting waves (inclined to the streamline at the angle of greatest amplification) are considered. A total of 21 flight-test cases were analyzed for the 757 NLF glove and are shown in figure 25. Included are points for the F-111/TACT NLF glove flight test that were reported in reference 24. One point from a 20 degree swept NLF glove on a T-33 aircraft (unpublished data by the Boeing Company) is also included. The F-111/TACT and 757 data complement one another, since the former is mostly for conditions where Tollmien-Schlichting waves were dominant, and in the latter, crossflow disturbances were dominant. The band enclosing the data is the Boeing recommended transition criteria.

This approach has been critized because only stationary crossflow vortices and Tollmien-Schlichting waves are examined and their interaction is presumed. Stationary crossflow vortices have been shown to not always be the most highly amplified crossflow like disturbances in the boundary layer (ref. 34). But whether or not a particular type of disturbance is present in the boundary layer would seem to be the major question. The existence of stationary crossflow vortices is well established with observations in many experiments. Some authors have reported observations of non-stationary disturbances in the crossflow field (refs. 34 and 35); Kohama (ref. 36) suggests that these observances are, in fact, evidence of secondary instabilities produced by growth of the primary instabilities, stationary crossflow vortices. The existence of an interaction of Tollmien-Schlichting and crossflow disturbances is likewise a controversial issue, and the authors of references 37 and 38 have proposed that in transition predictions one need only consider the most amplified disturbance, with transition occurring when an N factor of around 7 to 11 first occurs. More analyses of data are required to determine the best approach.

In stability analyses underway at Langley, the F-14, JetStar, and 757 transition data are being examined with the maximum amplification option of reference 39, but these analyses are also including surface and in-plane streamline curvature effects (refs. 34 and 40). The initial efforts have concentrated on transition data for conditions where Tollmien-Schlichting wave growth is small and crossflow-like disturbances dominate the transition process. Stability analyses are performed for both stationary and nonstationary crossflow disturbances.

Illustrated in figures 26 through 29 are results for two typical flight conditions on the "clean-up" glove of the F-14 aircraft. These flight conditions produce strong, favorable pressure gradients (figures 26 and 28) that lead to little or no Tollmien-Schlichting wave growth and dominance of crossflow-like disturbances. The crossflow Reynolds number development (figures 26 and 28) is indicative of strong crossflow vortices, and transition occurs for both conditions when this parameter exceeds 400, a value somewhat higher than the 175 to 300 range observed at low speeds. Previous analyses (ref. 41) indicate that the effects of compressibility on crossflow-like disturbances are small; comparison of the N factors for stationary and nonstationary crossflow vortices, with and without compressiblilty effects, confirms this, as shown in figures 27 and 29. Also, stationary crossflow vortices are not the most highly amplified disturbances for these conditions, but indeed, nonstationary vortices with frequencies of about 2000-to 3000-Hertz are more highly amplified. In the absence of significant compressibility effects, the incompressible code developed by Malik and Poll (ref. 34) has been used to examine surface and inplane curvature effects on the disturbance development. These effects, shown in figures 27 and 29, are quite significant; the N factors of the most highly amplified waves are reduced from about 15 to around 10 at the measured transition location. Similar calculations are shown for two conditions on the 757 NLF glove (figures 30 and 31). Curvature effects are again large, and with these effects included, the N factors at transition are around 10. Crossflow Reynolds numbers at transition fall in the range of 300 to 500.

The magnitude of the curvature effects in all the flight data analyzed to date gives rise to concerns over any previous attempts to correlate transition data with stability codes ignoring curvature effects and questions the generality of those correlations. Immediate plans are to begin examination of data for flight conditions with stronger Tollmien-Schlichting wave growth to explore the possibility of interactions of Tollmien-Schlichting waves and crossflow vortices.

THE NASA LEADING-EDGE FLIGHT TEST

Earlier in this paper, some of the key laminar-flow flight programs that laid the foundation for today's knowledge were briefly reviewed. These flight tests removed any doubt that extensive laminar flow could be achieved in flight. They did not, however, resolve concerns relative to the practicality of producing surfaces sufficiently smooth and wavefree, and of maintaining the required surface quality during normal service operations. In the late 1970's, with the recent significant progress made in the development of new materials, fabrication techniques, analysis methods, and design concepts, a reexamination of these issues appeared warranted.

Previous experience had shown that the leading-edge region of the swept wing presented the most difficult aerodynamic problems associated with attainment of laminar flow. In addition, the leading edge is subject to foreign object damage, insect impingement, rain erosion, icing, and other contaminants. Also, an anti-icing system, an anti-contaminant system, and a suction and perhaps purge system must all be packaged into a relatively small leading-edge box volume. Most of these problems are common to all the concepts under consideration for the achievement of extensive laminar flow, and solutions are needed to establish the practicality of laminar flow for various types of aircraft.

In 1980, the NASA Leading-Edge Flight Test (LEFT) program was initiated as a flight validation of two leading-edge systems then under development in NASA contract efforts with industry. The flight program objectives were to (1) demonstrate that required leading-edge systems can be packaged into a wing leading-edge section of a size representative of a commercial transport aircraft, and (2) demonstrate systems performance under operational conditions representative of subsonic commercial transport aircraft. Complete LFC leading-edge systems were installed in the leading-edge box of a JetStar airplane (figure 32). Descriptions of the systems illustrated in figures 33 and 34 are provided in references 42 and 43. Two leading-edge test articles were built and flown using a perforated and a slotted suction concept. Each spanned about 6-foot of the wing and had the same external contour, dimensionally about equivalent to the leading-edge box of a DC-9-30 at the mean aerodynamic chord. The wing leading-edge sweep was 30 degrees. Different systems were used in each test article. One used suction through approximately 1 million, 0.0025-inch diameter, 0.035-inch spaced, electron-beam perforated holes in a 0.025-inch thick titanium skin to maintain laminar flow on the test article upper surface. A Krueger-type flap served as a protective shield against insect impact on this leading edge. In future applications, the Krueger shield could also serve as a high-lift leading-edge device. A

freezing-point depressant liquid, Propylene Glycol Methyl Ether (PGME) was sprayed on the perforated, wing upper surface from nozzles mounted underneath the shield to augment the insect shield protection and to provide an anti-icing capability. To prevent clogging of the perforations by the wetting fluid, a purging system was included to clear the LFC passages by pressurizing the subsurface and thus remove PGME fluid from the LFC ducts and surface. The second test article used suction through 27 narrow spanwise slots (about 0.004-inch wide) on both upper and lower titanium surfaces. This test article contained anti-contaminant and anti-icing systems consisting of PGME fluid dispensed through dual purpose slots in the leading edge. Purge was also provided for this leading edge.

After an initial flight test program to optimize the system's performance, the LEFT systems were flight tested in a simulated airline service in different geographical areas, seasons, and weather conditions in the United States (figure 35). During the simulated service, one-to four-flights per day were made from three "home base" airports (Atlanta, Pittsburgh, and Cleveland). A total of 62 flights to 33 airports were made. Flights were made from Atlanta in July 1985, Pittsburgh in September 1985, and Cleveland in February 1986. The weather experienced thus varied from severe summer to severe winter conditions. To realistically simulate typical transport operations, an on-off operation of all systems was imposed; no adjustments were made prior to or during flights. Transport cruise flight conditions were emphasized, but investigations were also made of the ability to attain laminar flow at other than cruise conditions. References 44 through 47 provide a summary description of the program results.

The emergence of electron-beam perforated titanium as a practical manufacturing surface which meets laminar-flow waviness specifications with practical aircraft fabrication methods is considered a major development of the LEFT program. The perforated titanium leading-edge presented no difficult fabrication problems. This test article yielded clearly superior performance (relative to the slotted configuration) and was in virtually the same condition when flights ended in October 1987, as when flights began in November 1983. Four years of flying resulted in no degradation of laminar-flow performance as a result of service, and no evidence of any deterioration in surface quality was observed. Essentially, complete laminar flow on the test article was consistently obtained from 10,000 to 38,000 feet altitude with no need for any special maintenance.

The results obtained with the slotted-surface test article, however, were not as favorable. Fabrication of this configuration involved some extremely difficult problems that led to a suction surface that was only marginally acceptable with respect to surface smoothness and waviness. This was reflected in consistently poorer laminar-flow flight performance than for the test article with the perforated surface. Still, as much as 80 percent of the slotted upper surface suction area was observed to be laminar in routine flight service.

Since no attempt was made to obtain laminar flow beyond the front spar, the LEFT tests should not be interpreted as showing that perforations are aerodynamically better than slots. Indeed, the perforated approach should be pursued with caution because additional flight testing is required to larger

values of length Reynolds number. At higher Reynolds number, the experience of the early flight tests with larger holes (i.e., progressive performance deterioration with increased Reynolds number) could be repeated. Slots may, therefore, be preferred at higher Reynolds number. Accordingly, it is clear that more development of fabrication techniques for slotted suction surface configurations is required; some initial work in this direction has been undertaken (ref. 48).

The LEFT program relaxed concerns about the operational loss of laminar flow when entering clouds or haze. It provided some confirmation of an extensive analysis of world-wide cloud-cover (based on 6250 flight hours of specially instrumented commercial aircraft) which resulted in an estimate of 6 percent for the amount of flight time spent in clouds and haze (ref. 49). During the simulated service flights, measurements were also taken of the time spent in clouds and haze. These LEFT results, based on 6 hours and 52 minutes of data taken during 13 flights within the United States, showed that clouds and haze were encountered about 7 percent of the time (ref. 47). No effort was made to avoid cloud encounters, and a sample of one flight including a cloud penetration is shown in figure 36. As expected, laminar flow was lost during cloud penetrations, but was regained afterwards. The small percentage of time that clouds are encountered indicates that laminar flow loss during cloud penetrations in cruise will not appreciably decrease the large economic and fuel gains predicted for laminar-flow transport aircraft. However, potential cloud encounters en route and flight management to avoid clouds could be operational considerations for future aircraft.

To summarize the LFC systems performance during the simulated service, all operational experience was positive. No dispatch delays were encountered due to the LFC systems. There was no need to adjust suction system controls throughout the test range of cruise altitude, Mach number, and lift coefficient. Laminar flow was obtained after exposure to heat, cold, humidity, insects, rain, freezing rain, snow, ice, and moderate turbulence. The insect alleviation systems were required during descent as well as ascent and were effective when used. Perforated test article results indicated that the supplemental spray system is not necessary for LFC transport airplanes equipped with a properly designed insect shield/high-lift device, although the spray system may be necessary for anti-icing purposes. Ground deicing of the LFC test articles was no more difficult than normal deicing of commercial transports, and snow and ice accumulation was easily eliminated using hand-held deicing equipment. The NASA LEFT simulated airline service flights demonstrated that effective practical solutions for the problems of suction laminar-flow aircraft leading edges are available for commercial transport aircraft.

The LEFT program has been the only laminar-flow flight test with suction since the X-21 ended in 1965. The original intent of the LEFT program was to examine systems suitable for future laminar-flow control aircraft, but these systems would be equally applicable to hybrid laminar-flow control aircraft that use suction only in the leading-edge box.

HLFC FLIGHT EXPERIMENT

One of the most significant developments of the NASA research on laminar flow in the last few years has been the recognition of a hybrid laminar-flow control concept that integrates LFC and NLF and avoids the objectionable characteristics of each. The leading-edge sweep limitation of NLF is overcome by applying suction in the leading-edge box to control crossflow instabilities. Wing shaping for favorable pressure gradients to allow NLF over the wing box removes the need for inspar LFC suction and greatly reduces the system complexity. The possibility of achieving extensive laminar flow on commercial or military transport aircraft is offered with a system no more complex than that already proven in the Leading-Edge Flight Test Program on the NASA JetStar. To explore this possibility, the NASA Langley Research Center, the Air Force Wright Aeronautical Laboratory, and the Boeing Commercial Airplane Company have initiated a cooperative flight program. A high Reynolds number HLFC Flight Experiment will be performed on a 757 aircraft equipped with a partial-span HLFC system for the upper surface of the left wing.

The test aircraft and test region are illustrated in figure 37. A 20-foot span of the wing just outboard of the left engine pylon will be modified. A new leading-edge box will be installed with suction achieved through a perforated titanium surface. The structural concept will be similar to that used on the JetStar for the Leading-Edge Flight Test and will include a leading-edge Krueger integrated into the full wing high-lift system and designed to also be an insect shield for the wing (figure 38). The leading-edge box will be contoured to achieve the desired pressure distribution over the test surface (figure 39). Analyses indicate that this can be accomplished without changing the inspar contour of the 757. Indeed, measurements of the 757 production wing surface have shown that only minor shaving or filling of some rivets will be necessary to meet laminar-flow smoothness and fairness criteria. The inspar production wing surface will thus serve as the test surface downstream of the new leading-edge box.

The HLFC concept, untried to date in flight or in the wind tunnel, will be evaluated to chord Reynolds numbers over 30 million at the cruise conditions of modern transport aircraft. An extended flight test program is planned for calendar year 1990 to achieve operational experience with HLFC and to fully evaluate the potential for future applications. Success could lead to the long-awaited transfer of this technology to the drawing board and ultimately to practice.

CONCLUDING REMARKS

The potential benefits of laminar-flow technology have been so enticing that possibly no other technology has received such persistent attention in flight research over so long a time. The misgivings of the critics are fading with the accomplishments of this research. The aerodynamic issues seem nearly resolved, and the manufacturing capabilities of the airframe industry appear to have advanced to the point that the aerodynamic criteria for smooth, wave-free wing surfaces is a practical production goal. The current NASA, AFWAL, and

Boeing HLFC Flight Experiment could provide the verification needed to place this technology in practice. Initial applications may provide only modest improvements, but with the confidence of success, bolder steps could revolutionize aircraft design.

REFERENCES

1. Jones, B. M.: Flight Experiments on the Boundary Layer. JAS, Vol. 5, No. 3, pp. 81-94. January 1938.

2. Whites, R. C.; Sudderth, R. W.; and Wheldor, W. G.: Laminar Flow Control on the X-21. Astronautics and Aeronautics, Vol. 4, No. 7, July 1966.

3. Wagner, R. D.; and Fischer, M. C.: Developments in the NASA Transport Aircraft Laminar Flow Program. AIAA-83-0090, January 1983.

4. Wetmore, J. W.; Zalovcik, J. A.; and Platt, R. C.: A Flight Investigation of the Boundary-Layer Characteristics and Profile Drag of the NACA 35-215 Laminar-Flow Airfoil at High Reynolds Numbers. NACA L-532, 1941.

5. von Doenhoff, A. E.; and Braslow, A. L.: Effect of Distributed Surface Roughness on Laminar Flow. Chapter of Boundary Layer and Flow Control-Its Principles and Applications, Volume 2, edited by G. V. Lachmann, Pergamon Press, New York, 1961.

6. Braslow, A. L.: Investigation of Effects of Various Camouflage Paints and Painting Procedures on the Drag Characteristics of an NACA 65(421)-420, a = 1.0 Airfoil Section. NACA CB No. L4G17, July 1944.

7. Braslow, A. L.; and Visconti, F.: Investigation of Boundary-Layer Reynolds Number for Transition on an NACA 65(215)-114 Airfoil in the Langley Two-Dimensional Low-Turbulence Pressure Tunnel. NACA TN 1704, October 1948.

8. Gray, W. E.; and Fullam, P. W. J.: Comparison of Flight and Tunnel Measurements of Transition on a Highly Finished Wing (King Cobra). RAE Report Aero 2383, 1945.

9. Smith, F.; and Higton, D.: Flight Tests on King Cobra FZ.440 to Investigate the Practical Requirements for the Achievement of Low Profile Drag Coefficients on a "Low Drag" Aerofoil. ARC Report, R&M 2375, 1950.

10. Plascoff, R. H.: Profile Drag Measurements on Hurricane II z. 3687 Fitted with Low-Drag Section Wings. RAE Report No. Aero 2153, 1946.

11. Zalovcik, J. A.; Wetmore, J. W.; and von Doenhoff, A. E.: Flight Investigation of Boundary-Layer Control by Suction Slots on an NACA 35-215 Low-Drag Airfoil at High Reynolds Numbers. NACA WR L-521, 1944.

12. Head, M. R.: The Boundary Layer With Distributed Suction. R&M No. 2783, British A. R. C., 1955.

13. Head, M. R.; Johnson, D.; and Coxon, M.: Flight Experiments on Boundary Layer Control for Low Drag. R&M No. 3025, British A. R. C., March 1955.

14. Edwards, B.: Laminar Flow Control - Concepts, Experiences, Speculations. AGARD Report No. 654. Special Course on Concepts for Drag Reduction, 1977.

15. Pfenninger, W.; Groth, E. E.; Whites, R. C.; Carmichael, B. H.; and Atkinson, J. M.: Note About Low Drag Boundary Layer Suction Experiments in Flight on a Wing Glove of a F94-A Airplane. Reference No. NAI-54-849 (BLC-69), Northrop Aircraft, Inc., December 1954.

16. Pfenninger, W.: Laminar Flow Control Laminarization. AGARD-R-654, June 1977.

17. Landeryou, R. R.; and Porter, P. G.: Further Tests of a Laminar Flow Swept Wing with Boundary Layer Control by Suction. Report Aero. No. 192, College of Aeronautics, Cranfield (England), May 1966.

18. Gray, W. E.: The Effect of Wing Sweep on Laminar Flow, RAE TM Aero. 255, 1952.

19. Anscombe, A.; and Illingworth, L. N.: Wind Tunnel Observations of Boundary Layer Transition on a Wing at Various Angles of Sweepback. R and M No. 2968, British A. R. C., 1956.

20. Pfenninger, W.; Gross, L.; and Bacon, J. W., Jr.: Experiments on a 30 Degree Swept, 12 Percent Thick, Symmetrical, Laminar Suction Wing in the 5-Foot by 7-Foot Michigan Tunnel. Northrop Corp., Noair Division Report. NAI-57-317 (BLC-93), February 1957.

21. Boeing Commercial Airplane Company: Natural Laminar Flow Airfoil Analysis and Trade Studies, NASA CR-159029. May 1979.

22. Anom.: Advanced Aerodynamics and Active Controls - Selected NASA Research, NASA CP-2172, October 1980.

23. Anom: Advanced Aerodynamics - Selected NASA Research, NASA CP-2208, September 1981.

24. Boeing Commercial Airplane Company: F-111 Natural Laminar Flow Glove Flight Test Data Analysis and Boundary-Layer Stability Analysis. NASA CR-166051. January 1984.

25. Runyan, L. J.; and Steers, L. L.: Boundary-Layer Stability Analysis of a Natural Laminar Flow Glove on the F-111 TACT Airplane, Viscous Flow Drag Reduction, Vol. 72, Progress in Astronautics and Aeronautics, pp. 17-32, 1980.

26. Rozendaal, R. A.: Variable Sweep Transition Flight Experiment (VSTFE) - Parametric Pressure Distribution, Boundary-Layer Stability Study and Wing Glove Design Task. NASA CR-3992, 1986.

27. Anom: Research in Natural Laminar Flow and Laminar Flow Control. NASA CP-2487, Part 3, March 1987.

28. Bohn-Meyer, M.: Constructing Gloved Wings for Aerodynamic Studies, AIAA 88-2109, May 1988.

29. Boeing Commercial Airplane Company: Flight Survey of the 757 Wing Noise Field and Its Effect on Laminar Boundary Layer Transition. NASA CR-178216, Vol. I - Program Description and Data Analysis. March 1987.

30. Boeing Commercial Airplane Company: Flight Survey of the 757 Wing Noise Field and Its Effect on Laminar Boundary Layer Transition. NASA CR-178217, Vol. 2 - Data Compilation. March 1987.

31. Boeing Commercial Airplane Company: Flight Survey of the 757 Wing Noise Field and Its Effect on Laminar Boundary Layer Transition. NASA CR-178419, Vol. 3 - Extended Data Analysis. May 1988.

32. Boltz, F. W.; Kenyon, G. C.; and Allen, C. Q.: Effects of Sweep Angle on the Boundary-Layer Stability Characteristics of an Untapered Wing at Low Speeds. NASA TN D-338, 1960.

33. Swift, G; and Mangur P.: A Study of the Prediction of Cruise Noise and Laminar Flow Control Noise Criteria for Subsonic Air Transports. NASA CR-159104, August 1979.

34. Malik, M. R.; and Poll, D. I. A.: Effect of Curvature on Three-Dimensional Boundary Layer Stability. AIAA Journal, Vol. 23, No. 9, pp. 1362-1369. September 1985.

35. Poll, D. I. A.: Some Observations of the Transition Process on the Windward Face of a Long Yawed Cylinder. J. Fluid Mech., Vol. 150, pp. 329-356. January 1985.

36. Kohama, Y.: Some Expectation on the Mechanism of Cross-Flow Instability in a Swept Wing Flow, Acta Mechanica 66, pp. 21-38, 1987.

37. Hefner, J. N.; and Bushnell, D. M.: Status of Linear Boundary Layer Stability Theory and the e^N Method, With Emphasis on Swept Wing Applications. NASA TP-1645, 1980.

38. Anom: Research in Natural Laminar Flow and Laminar-Flow Control. NASA CP-2487, Part I, pp. 219-244, March 16-19, 1987.

39. Malik, M. R.: Cosal-4 A Black Box Compressible Stability Analysis Code for Transition Prediction in Three-Dimensional Boundary Layers. NASA CR-165925, 1982.

40. Collier, F. S., Jr.; and Malik, M. R.: Stationary Disturbances in Three-Dimensional Boundary Layers. AIAA Paper 87-1412, June 1987.

41. Mack, L. M.: Boundary Layer Stability Theory. AGARD Report No. 709, Special Course on Stability and Transition of Laminar Flows, VKI, Brussels, 1984.

C-2

42. Etchberger, F. R.: Laminar Flow Control Leading Edge Glove Flight Aircraft Modification Design, Test Article Development, and Systems Integration. NASA CR-172136, 1983.

43. Douglas Aircraft Company Staff: Laminar Flow Control Leading Edge Glove Flight Test Article Development. NASA CR-172137, 1984.

44. Fisher, D. F.; and Fischer, M. C.: The Development Flight Tests of the JetStar LFC Leading-Edge Flight Experiment. NASA CP-2487, pp. 117-140, 1987.

45. Maddalon, D. V.; Fisher, D. F.; Jennett, L. A.; and Fischer, M. C.: Simulated Airline Service Experience with Laminar Flow Control Leading-Edge Systems. NASA CP-2487, pp. 195-218, 1987.

46. Powell, A. G.; and Varner, L. D.: The Right Wing of the LEFT Airplane. NASA CP-2487, pp. 141-161, 1987.

47. Davis, R. E.; Maddalon, D. V.; and Wagner, R. D.: Performance of Laminar Flow Leading Edge Test Articles in Cloud Encounters. NASA CP-2487, pp. 163-193, 1987.

48. Goodyear, M. D.: Application of Superplastically Formed and Diffusion Bonded Aluminum to a Laminar Flow Control Leading Edge. NASA CR-178316, 1987.

49. Jasperson, W. H.; Nastrom. G. D.; Davis, R. E.; and Holdeman, J. D: GASP Cloud - and Particle Encounter Statistics, and Their Application to LFC Aircraft Studies (2 Vols.). NASA TM 85835, October 1984.

ORIGINAL PAGE IS
OF POOR QUALITY

(CIRCA 1940)

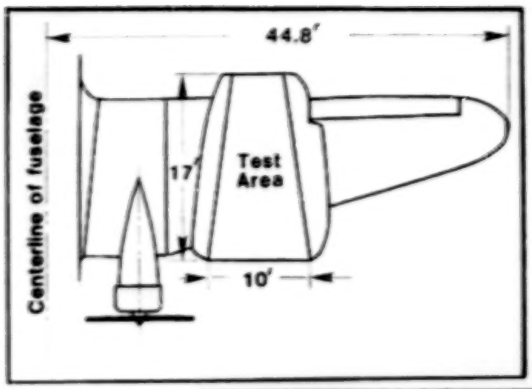

- NACA 35-215 Airfoil
- Wooden Glove (±1/1000 inch Waves)
- Transition Reynolds No. ~ 11.3 x 10^6 at 42.5% Chord
- Engine/Propeller Noise Reduced Laminar Run by 3% Chord

Figure 1. - The B-18 NLF Glove Flight Test.

(CIRCA - 1945)

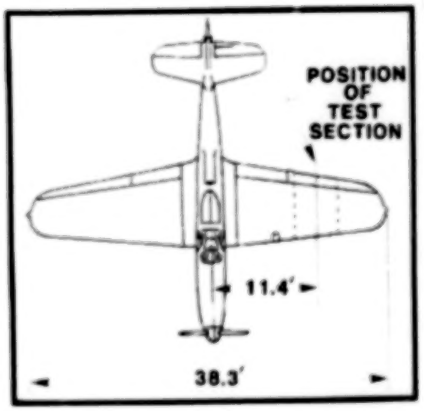

- NACA 662X-116 section
- Polished and filled production wing surface (±1/1000 inch waves)
- Transition Reynolds No. ~11x10^6
- Transition beyond $C_{p_{min}}$
- Operational evaluations
  - Insects
  - Dust & rain
  - Maintenance
  - Surface quality deterioration

Figure 2. - The King Cobra NLF Flight Test.

ORIGINAL PAGE IS
OF POOR QUALITY

(CIRCA - 1945)

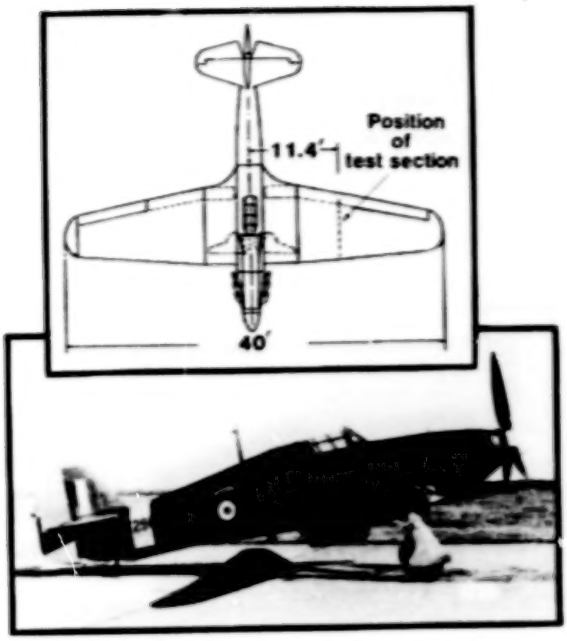

- N.P.L. Section $C_{p_{min}}$ @ 50% c
- Polished, filled special low drag construction wing (± 1/1000 inch waves)
- No spars, stringer stiffened thick wing skins
- Expected low drag performance achieved
- Laminar flow to 50 – 60% c

Figure 3. - The Hurricane NLF Flight Test.

(CIRCA 1955)

- Multiple Suction Surfaces:
  - Porous Monel Cloth (Nylon Covered)
  - Perforated Sheet (0.007 & 0.020 inch dia.)
  - Porous Strips (Sintered metal)
- Full Chord LFC at $M_\infty = 0.7$ and $R_c \sim 30 \times 10^6$ with:
  - Monel Nylon Cloth
  - 0.007 inch Perforations

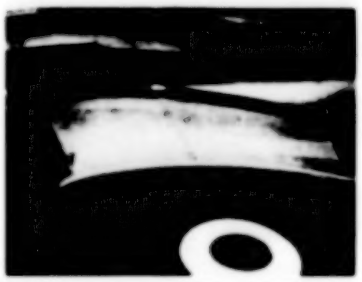

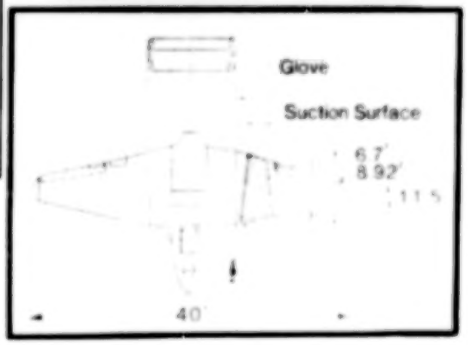

Figure 4. - The Vampire LFC Flight Experiments.

ORIGINAL PAGE IS
OF POOR QUALITY

(1954-1957)

- Modified NACA 65 213 airfoil
- Slotted suction surfaces
  - 12 slots (41 to 95% chord)
  - 69 slots (41 to 95% chord)
  - 81 slots (8 to 95% chord)
- Full chord laminar flow
  - $.06 \leq M_{\infty} \leq 0.7$
  - $12.2 \times 10^6 \leq R_C \leq 36.4 \times 10^6$
- For $M_{LOCAL} > 1.09$, shocks caused loss of laminar flow

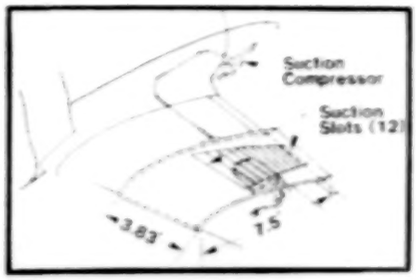

Figure 5. - The F-94 LFC Flight Experiments.

(1963 - 1965)

Step-by-step growth in laminar area throughout program

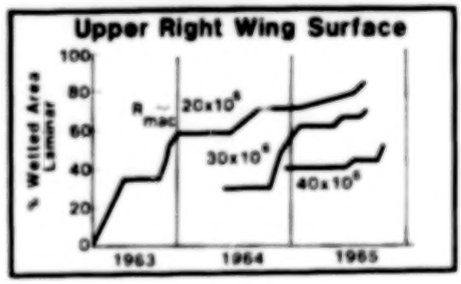

Figure 6. - The X-21 LFC Flight Program.

ORIGINAL PAGE IS
OF POOR QUALITY

(CIRCA 1965)

Figure 7. - The Lancaster Swept LFC Wing Flight Experiment.

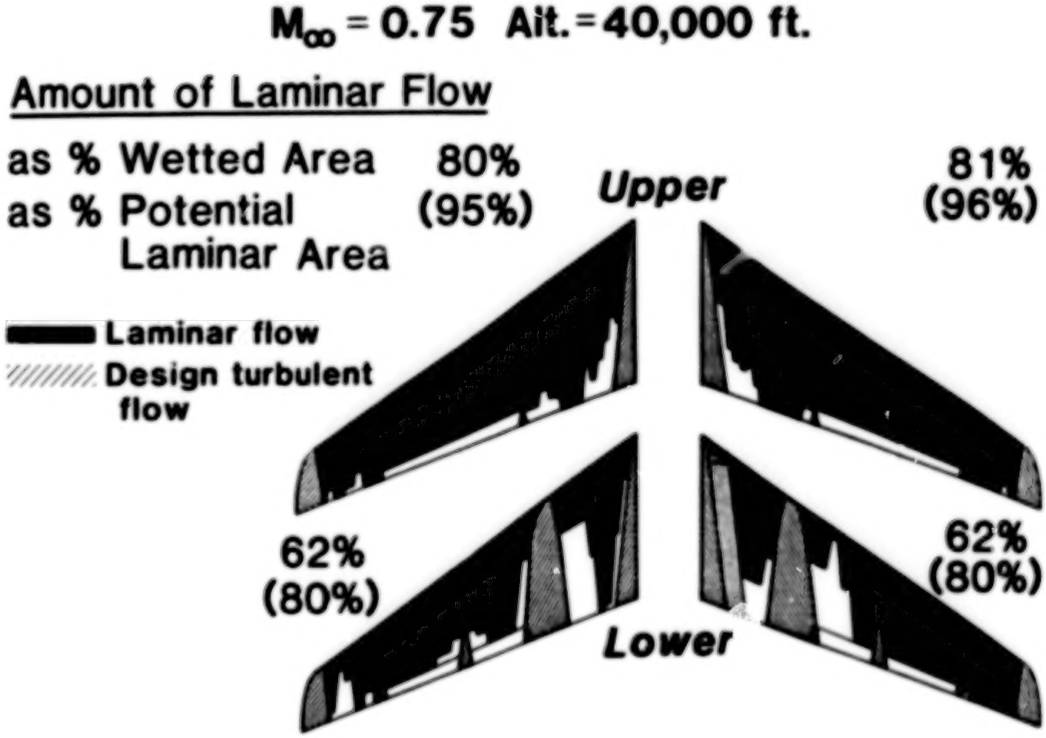

Figure 8. - The X-21 maximum laminar flow areas.

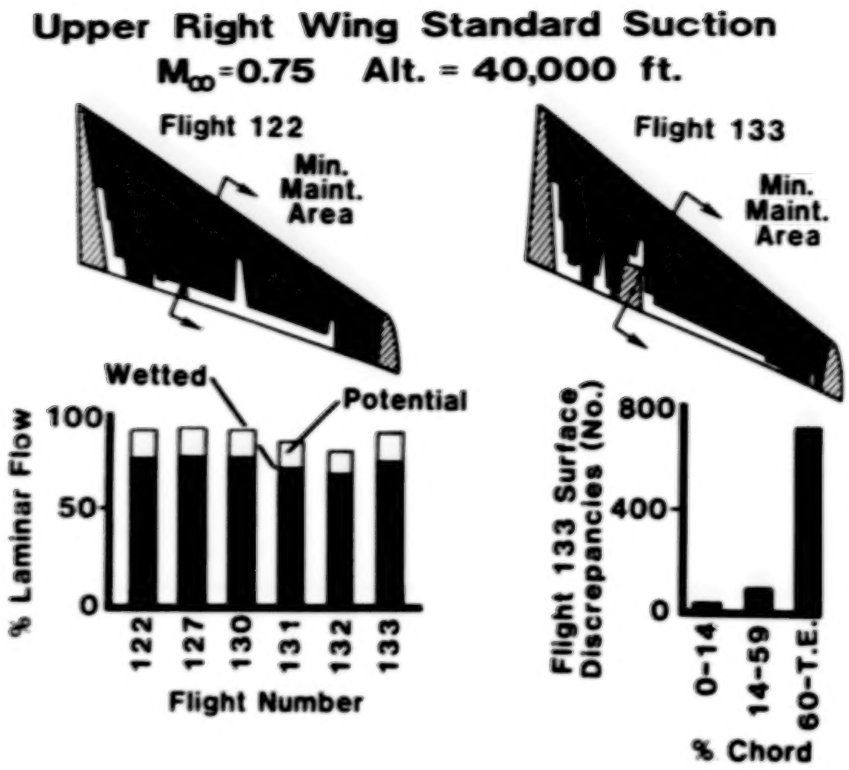

Figure 9. - Maintenance effects on the repeatability of laminar flow on the X-21.

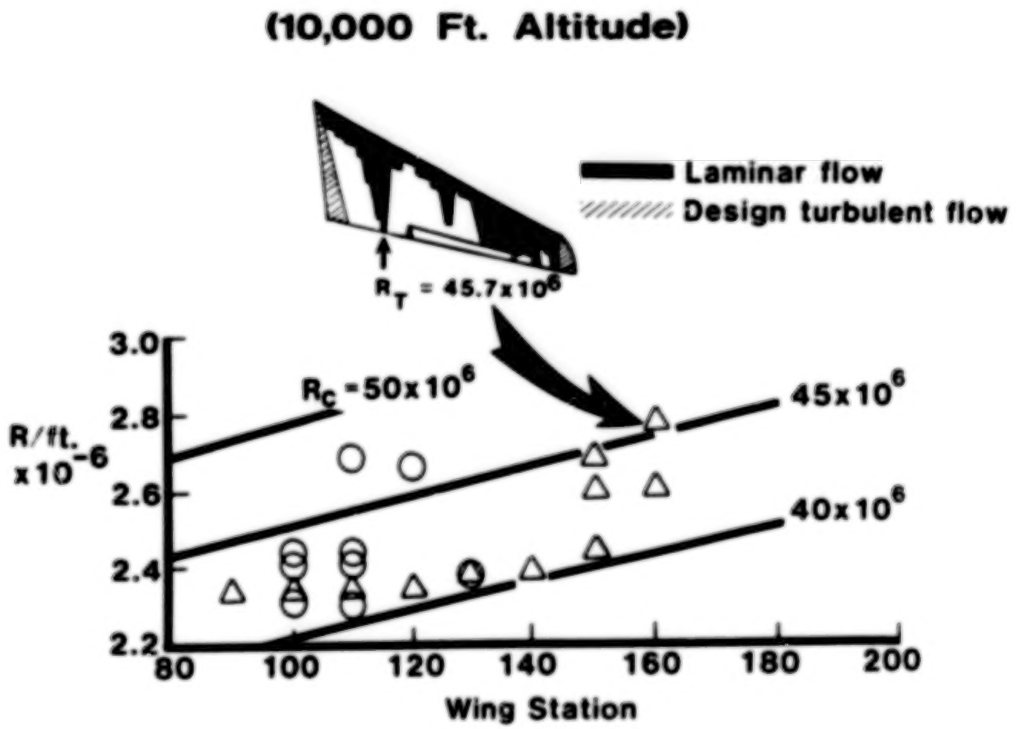

Figure 10. - X-21 high chord Reynolds number results.

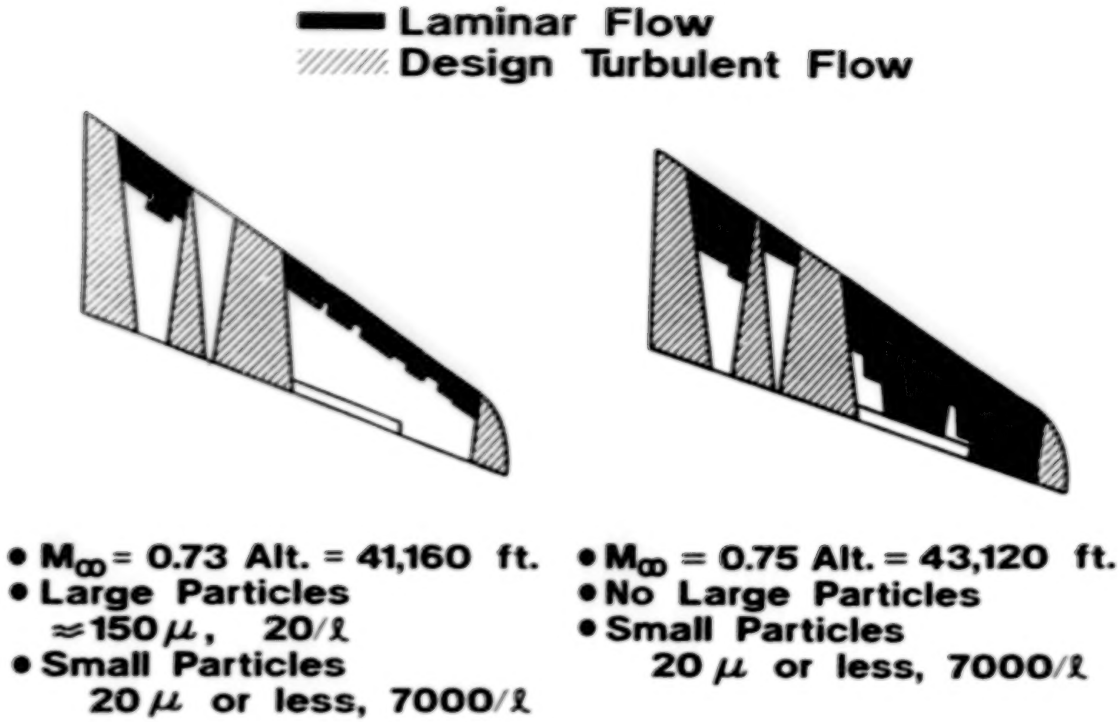
Laminar Flow
Design Turbulent Flow
• M_∞ = 0.73 Alt. = 41,160 ft.
• Large Particles
≈150 μ, 20/ℓ
• Small Particles
20 μ or less, 7000/ℓ
• M_∞ = 0.75 Alt. = 43,120 ft.
• No Large Particles
• Small Particles
20 μ or less, 7000/ℓ

Figure 11. - Effect of ice particle encounters on X-21 results.

ORIGINAL PAGE
BLACK AND WHITE PHOTOGRAPH

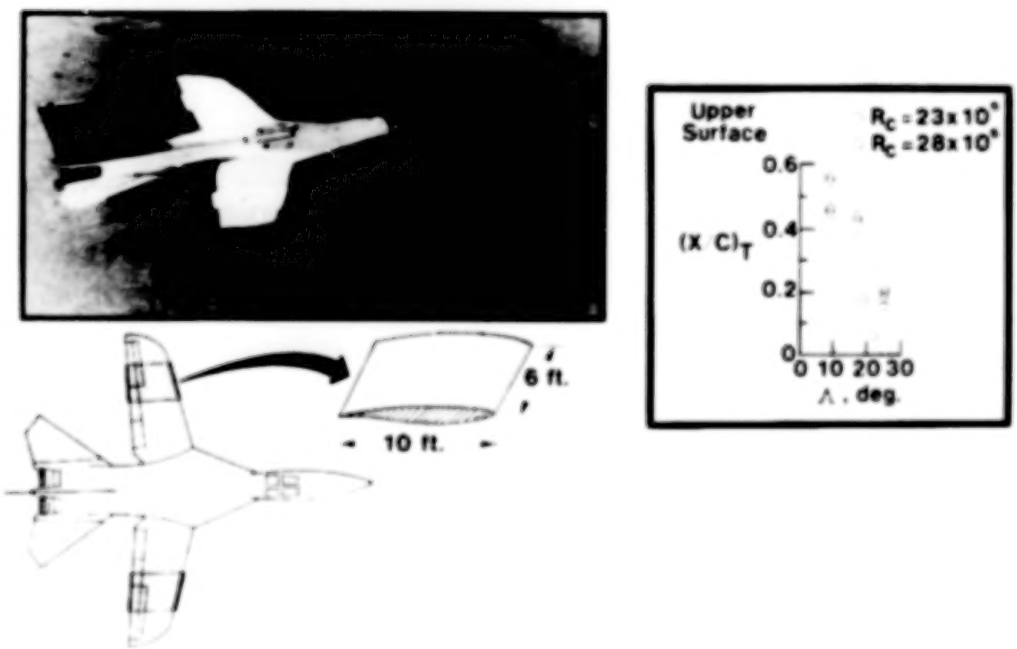

Figure 12. - The F-111/TACT NLF Glove Flight Experiment.

ORIGINAL PAGE IS
OF POOR QUALITY

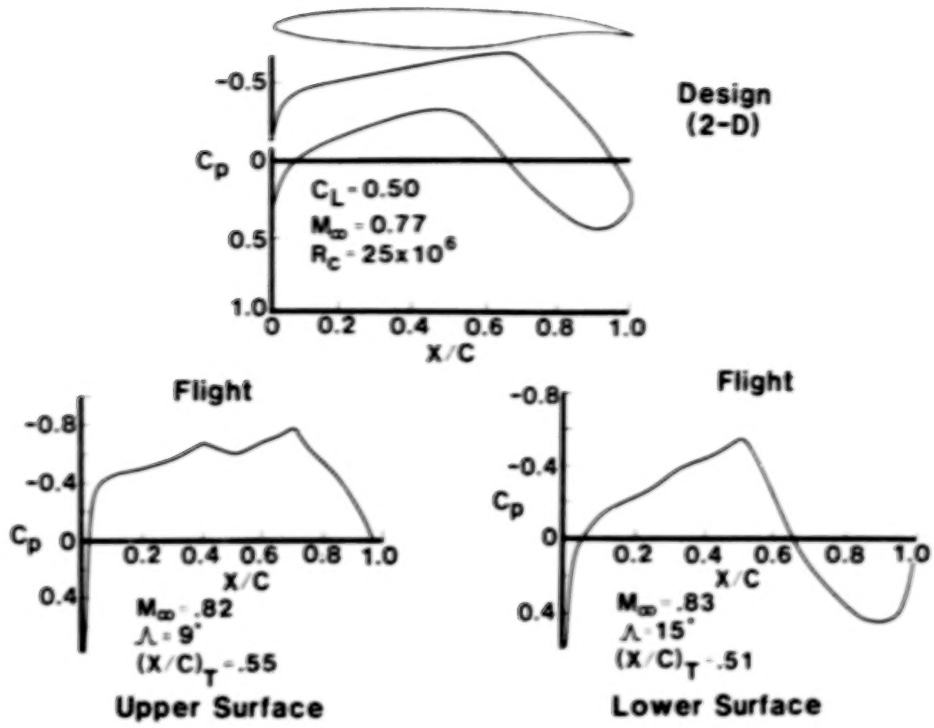

Figure 13. - Design and flight pressure distributions for the F-111/TACT NLF glove.

ORIGINAL PAGE
BLACK AND WHITE PHOTOGRAPH

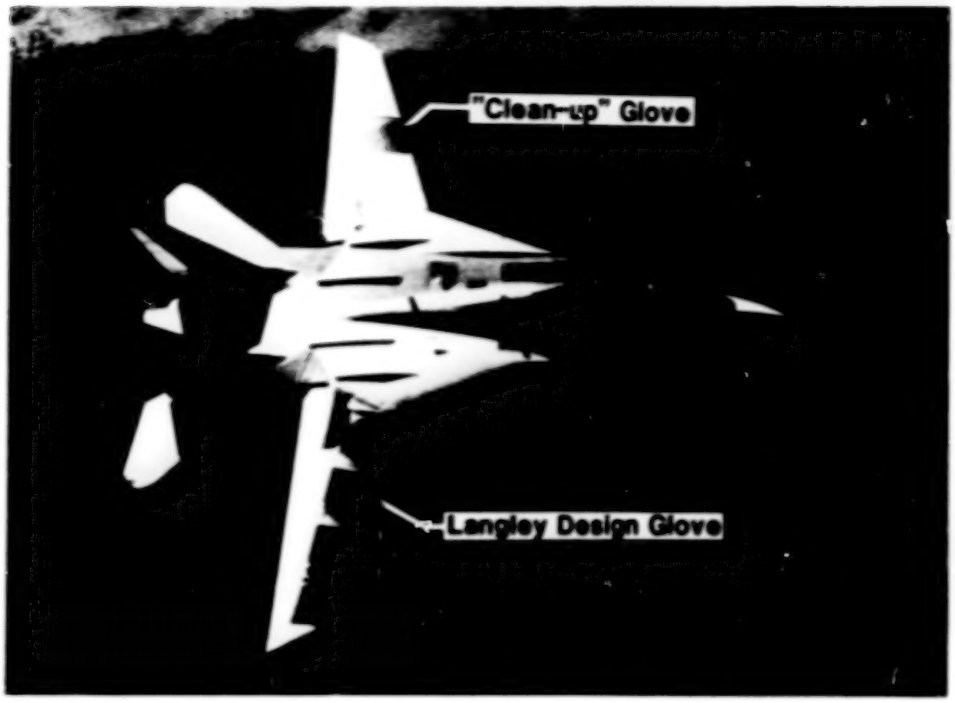

Figure 14. - F-14 test-bed aircraft for the Variable Sweep Transition Flight Experiment (VSTFE).

ORIGINAL PAGE IS
OF POOR QUALITY

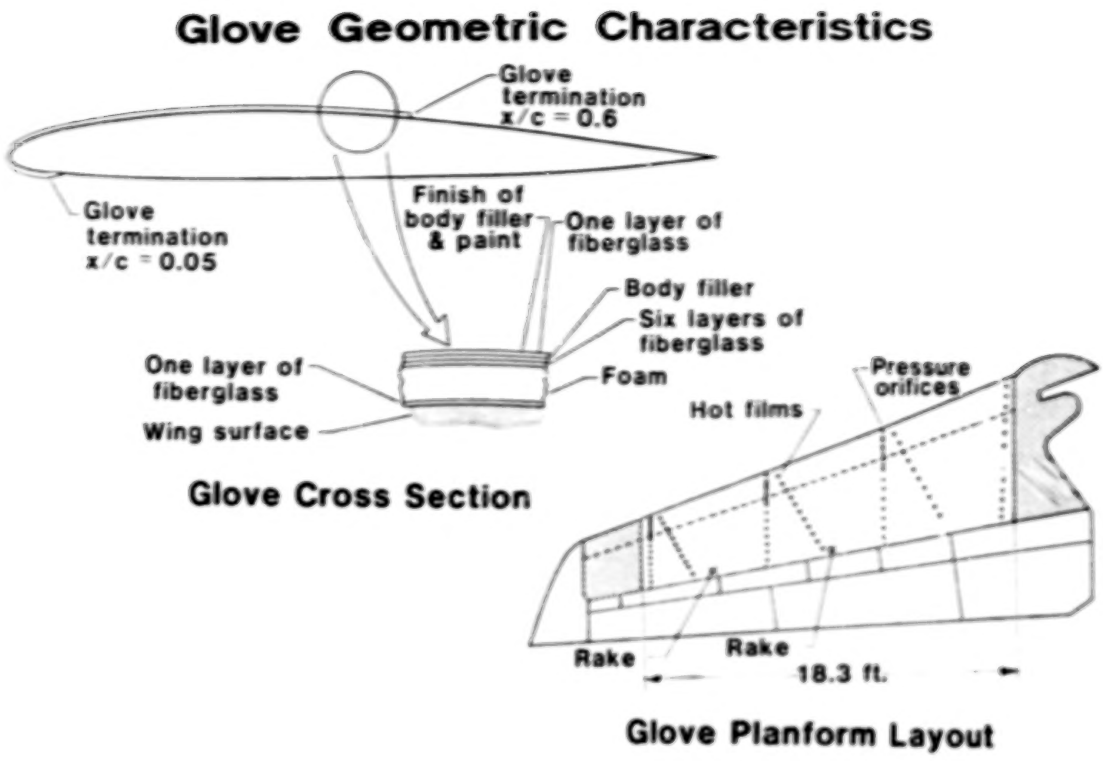

Figure 15. - F-14 VSTFE glove details.

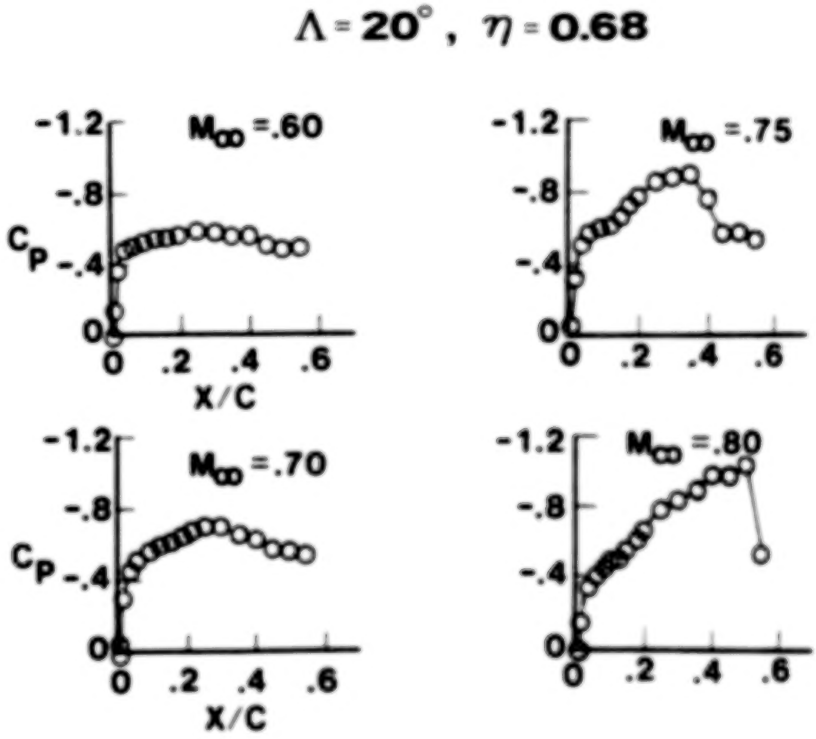

Figure 16. - F-14 VSTFE "clean-up" glove pressure distributions.

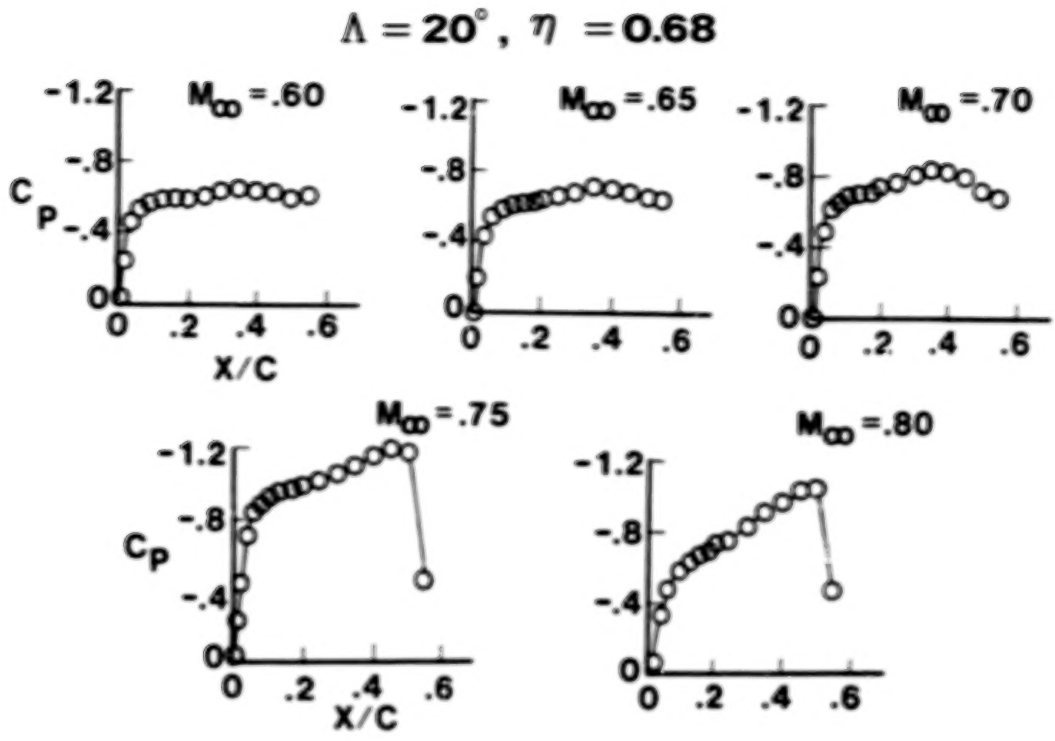

Figure 17. - F-14 VSTFE "Langley-design" glove pressure distributions.

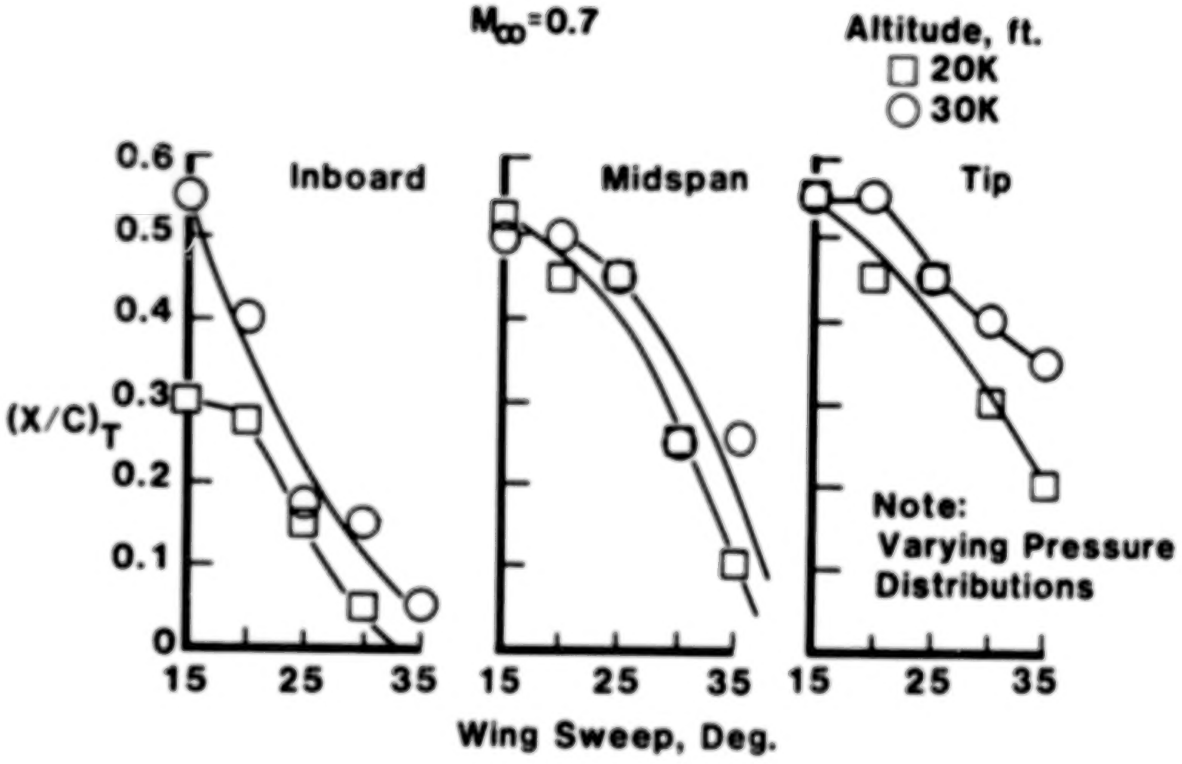

Figure 18. - Maximum transition location for the VSTFE "Langley-design" glove.

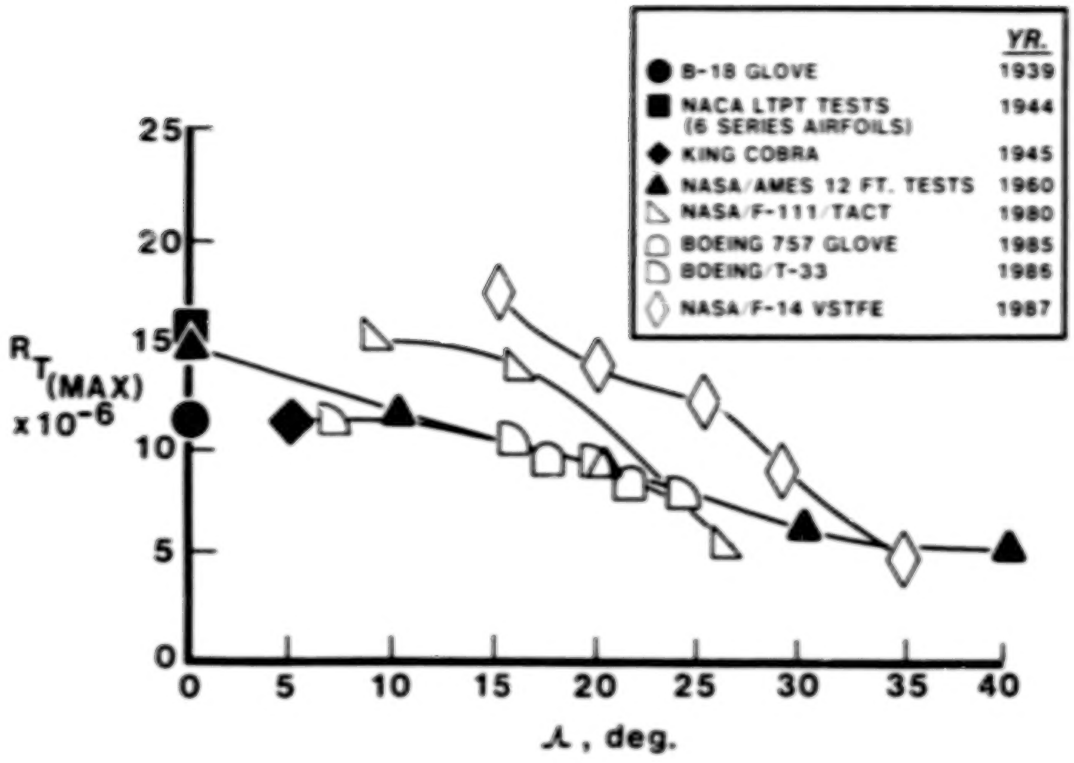

Figure 19. - Maximum transition Reynolds number for several natural laminar flow experiments.

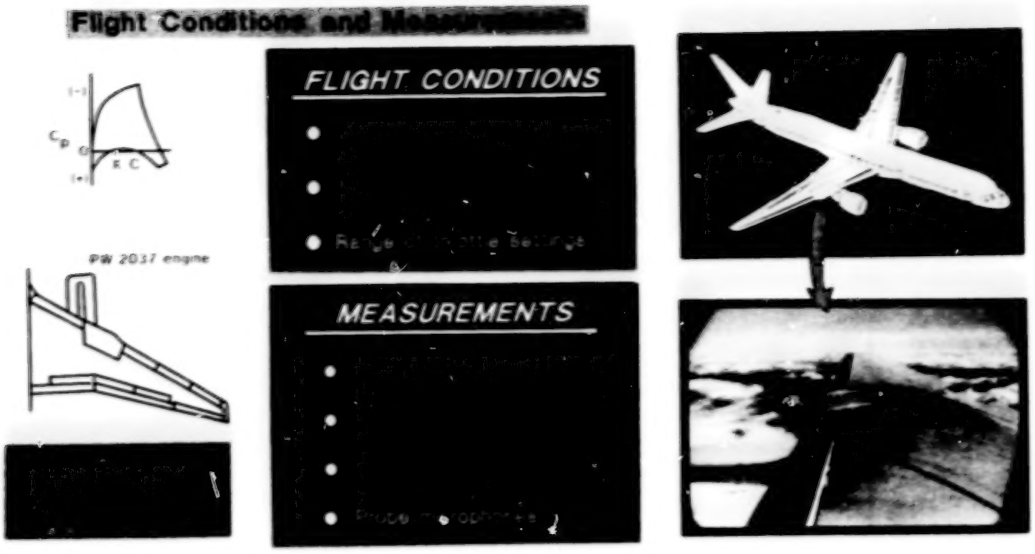

Figure 20. - The 757 Wing Noise Survey and NLF Glove Flight-Test Program.

ORIGINAL PAGE IS
OF POOR QUALITY

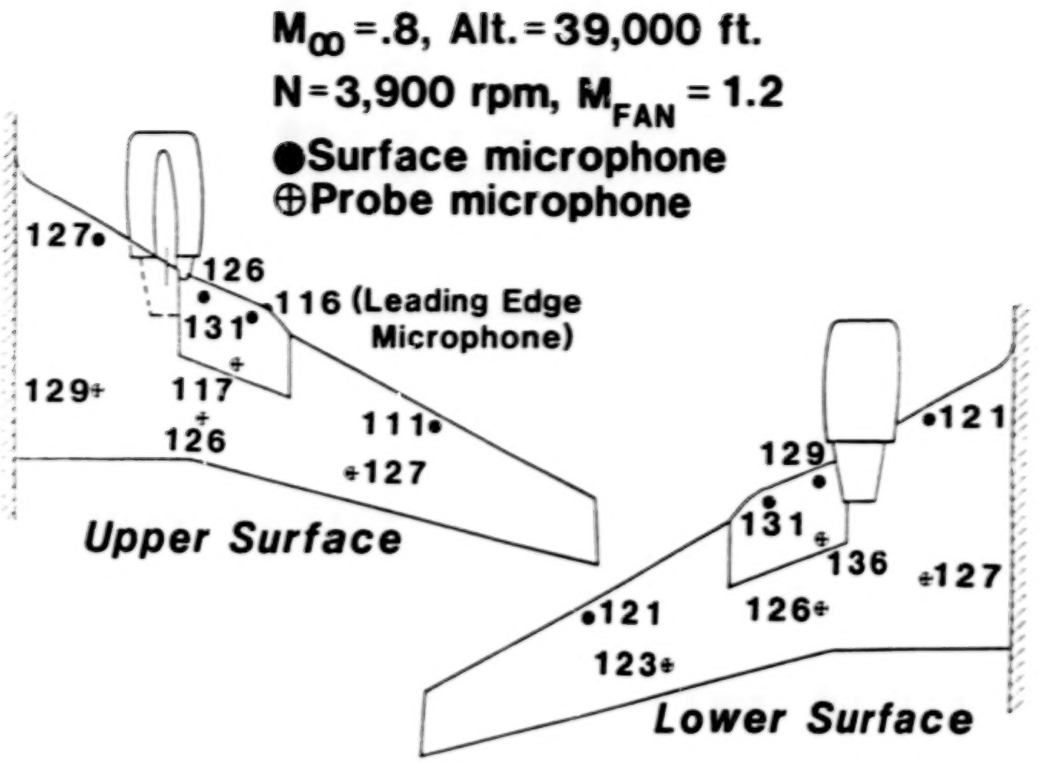

Figure 21. - Overall sound pressure level distribution on the 757 wing at cruise conditions.

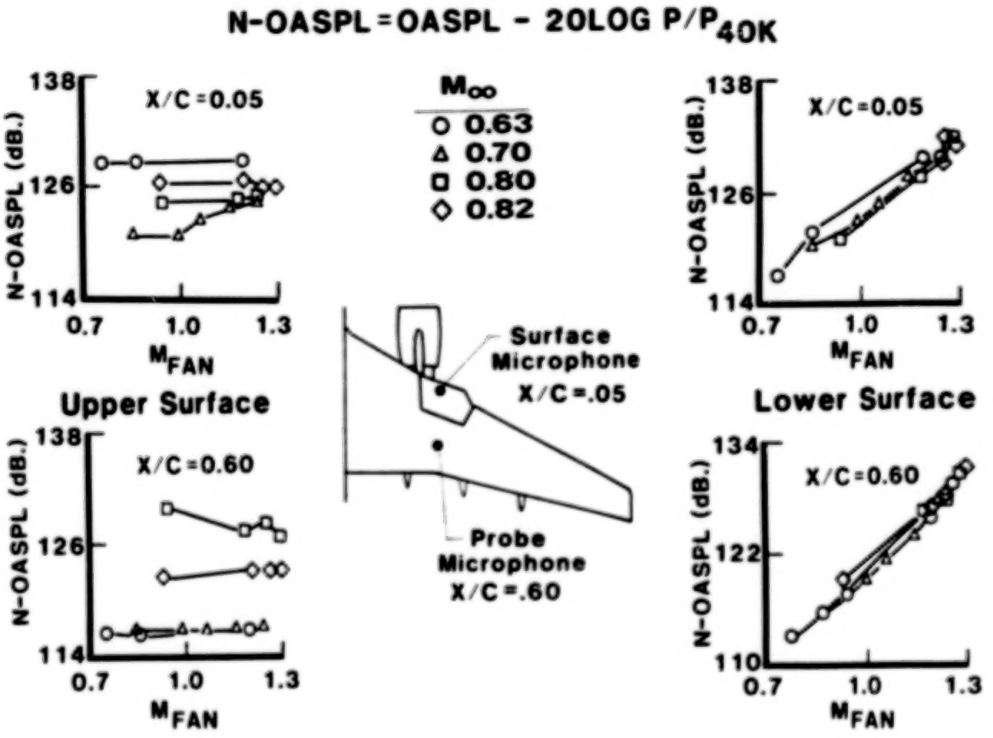

Figure 22. - Normalized overall sound pressure level versus fan Mach number for the 757 wing.

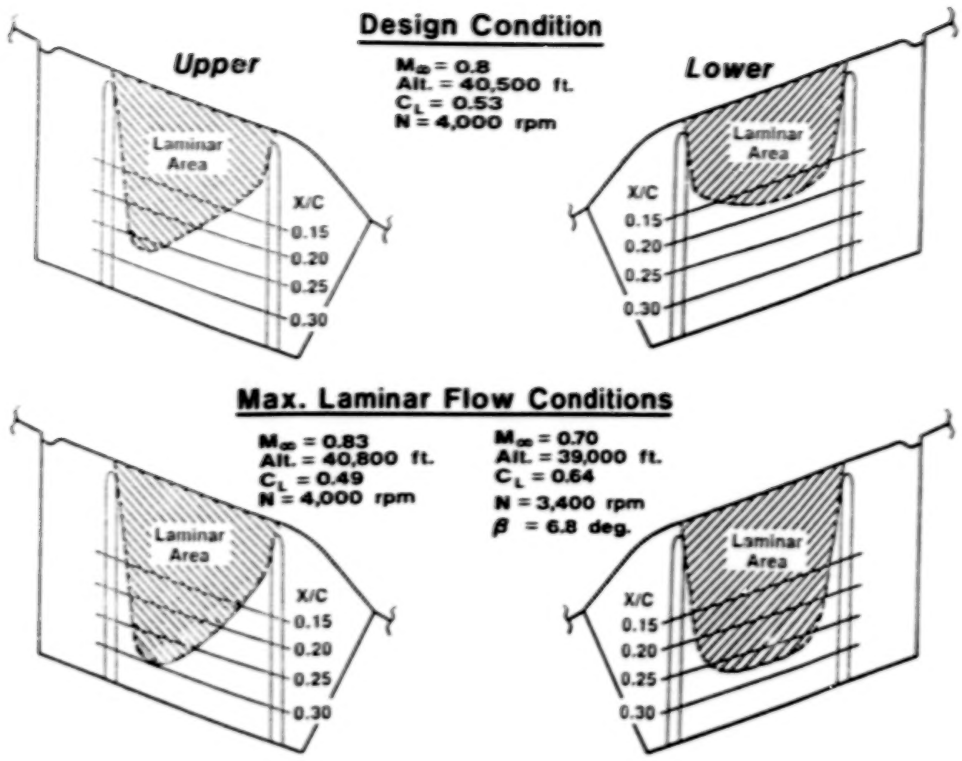

Figure 23. - Measured extent of laminar flow on the 757 NLF glove.

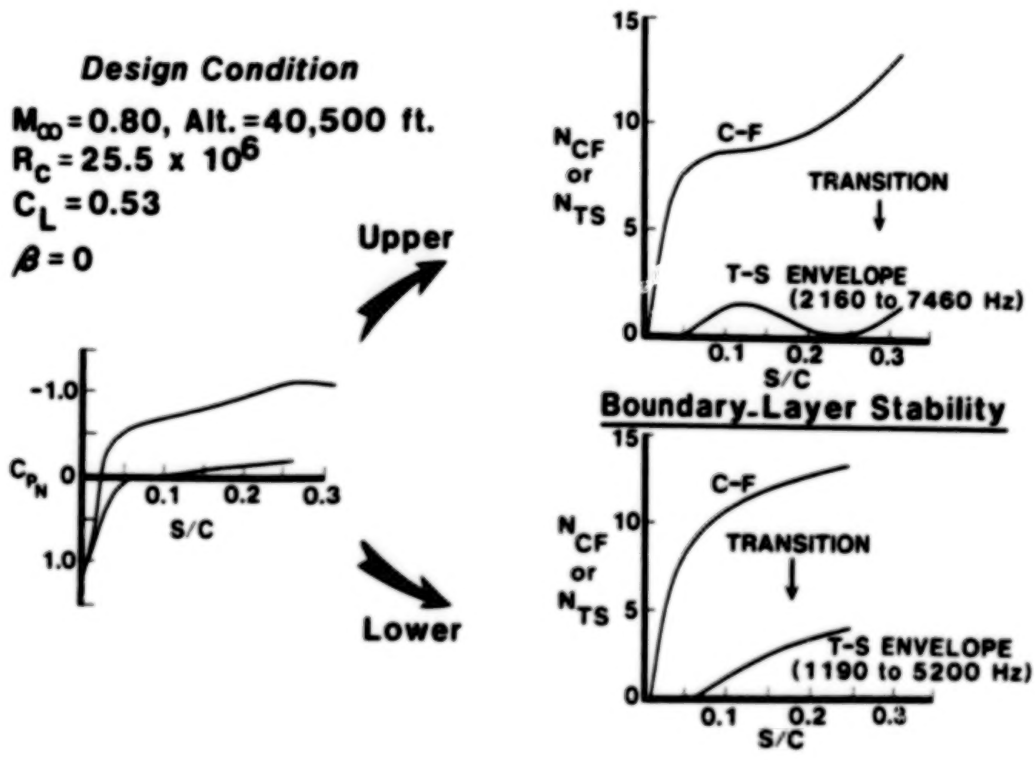

Figure 24. - Boundary-layer stability calculation at the design condition for the 757 NLF glove.

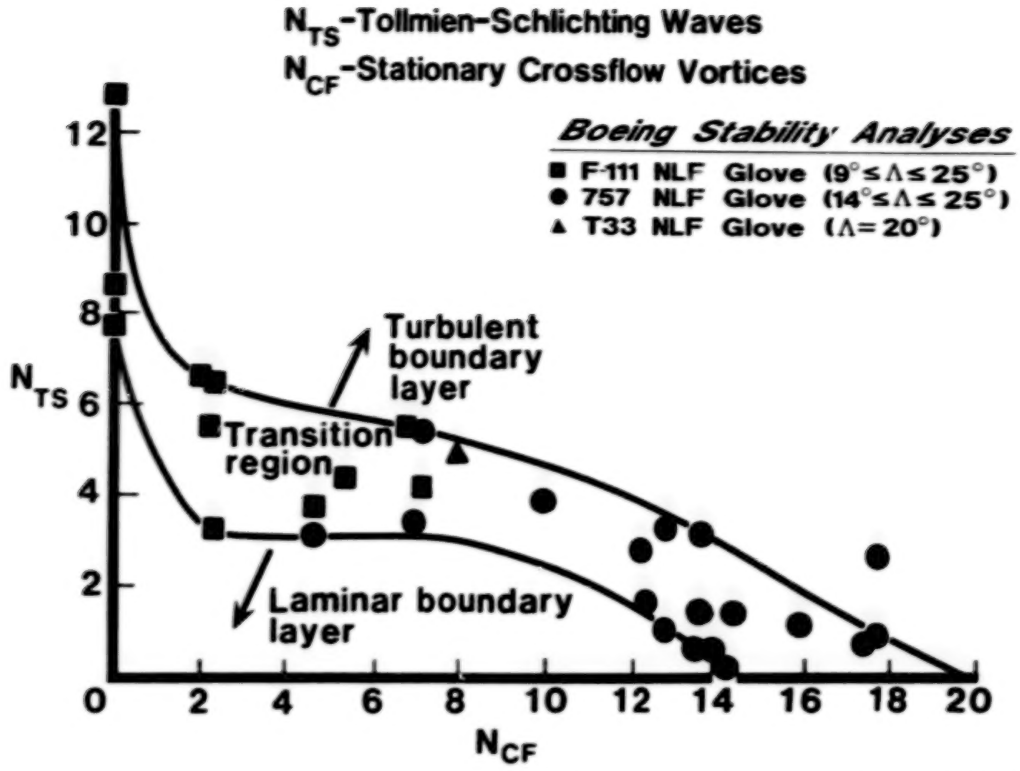

Figure 25. - Boeing stability analyses correlation of the Tollmien-Schlichting vs. crossflow N-factors with flight transition data.

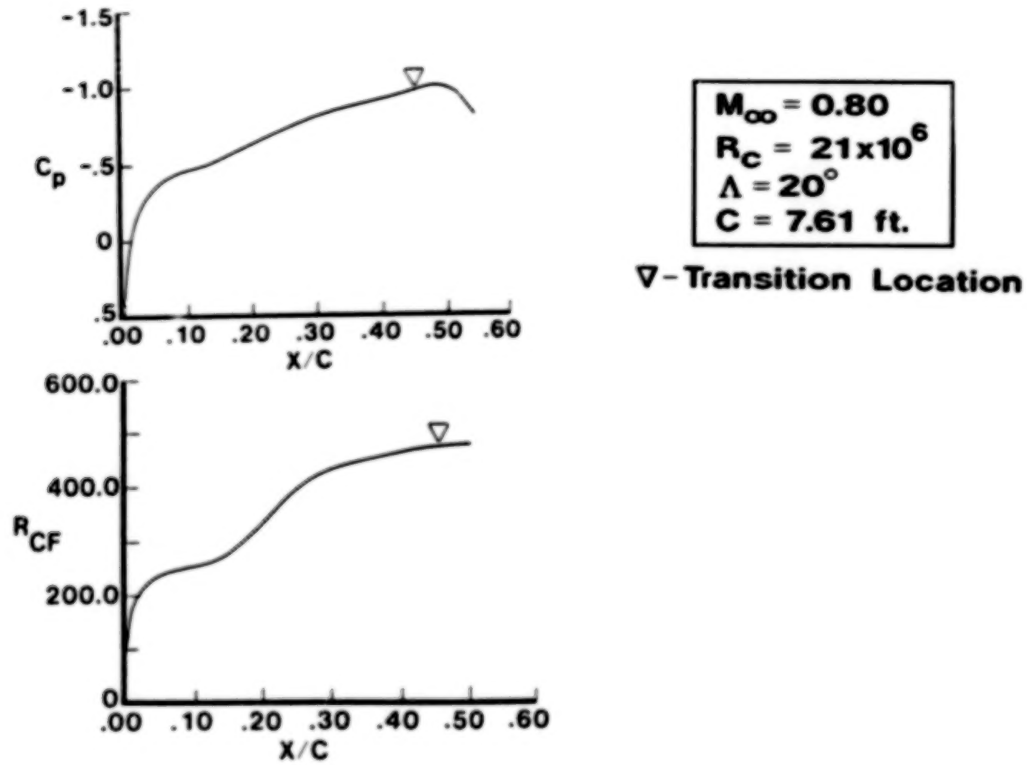

Figure 26. - F-14 "clean-up" glove pressure and crossflow Reynolds number distributions at a Mach number of .80 and a chord Reynolds number at 21 X 10^6.

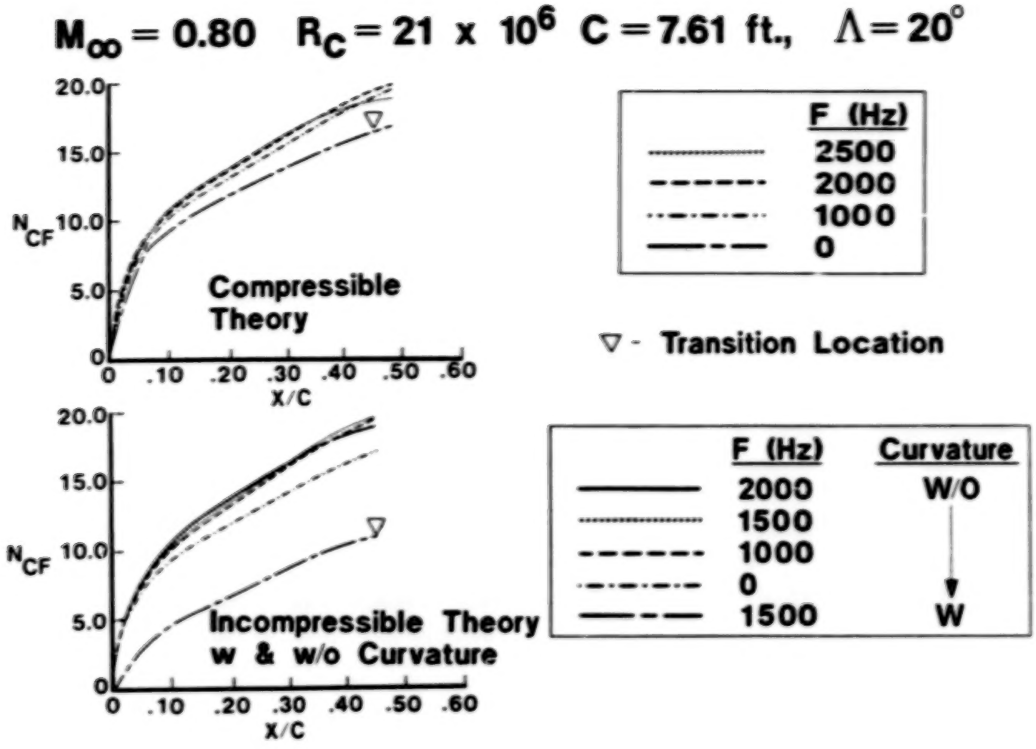

Figure 27. - Crossflow N-factors (with and without curvature effects) for the F-14 "clean-up" glove at a Mach number of .80 and a chord Reynolds number of 21 X 10^6.

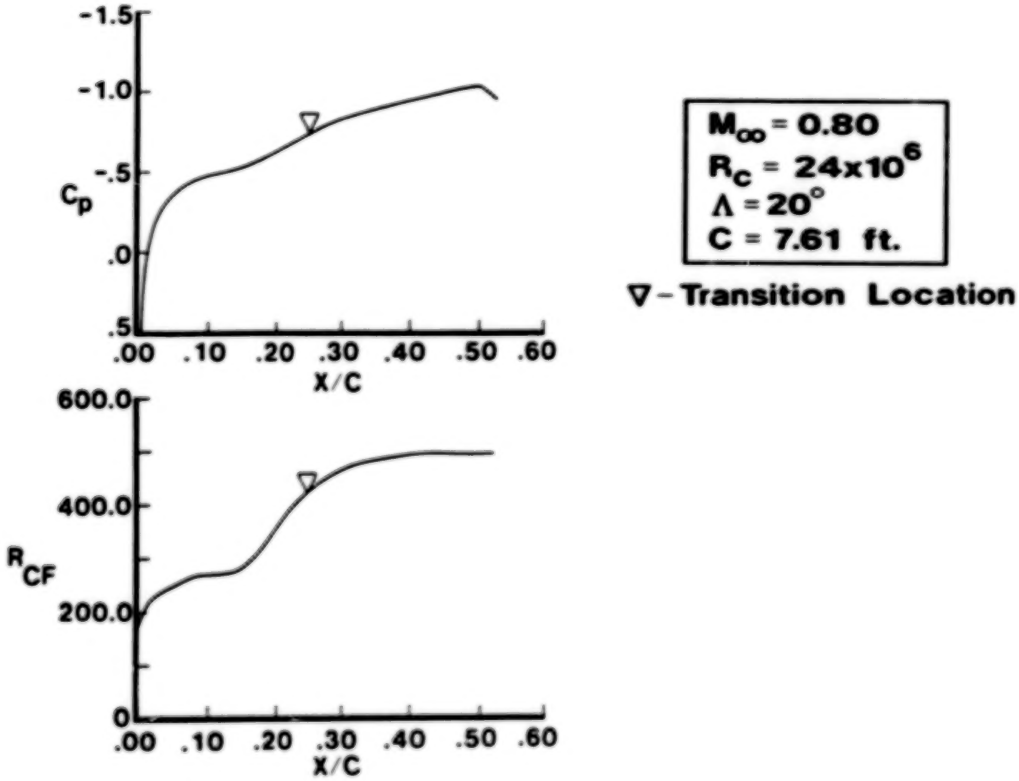

Figure 28. - F-14 "clean-up" glove pressure and crossflow Reynolds number distributions at a Mach number of .80 and a chord Reynolds number of 24 X 10^6.

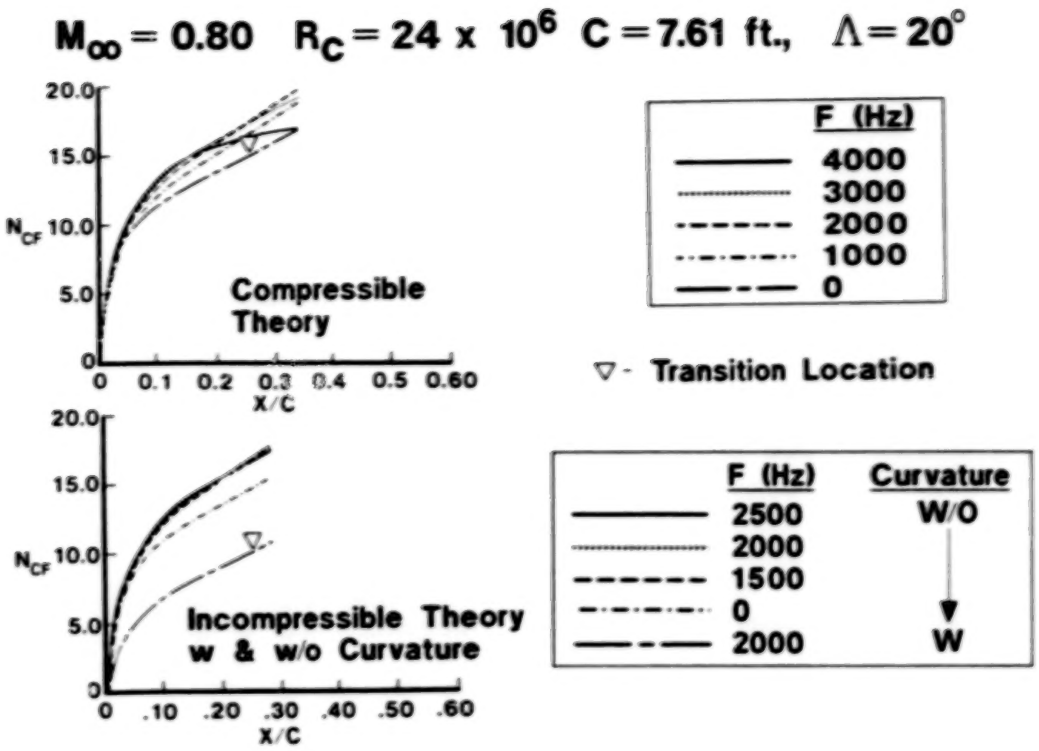

Figure 29. - Crossflow N-factors (with and without curvature effects) for the F-14 "clean-up" glove at a Mach number of .80 and a chord Reynolds number of 24 X 10^6

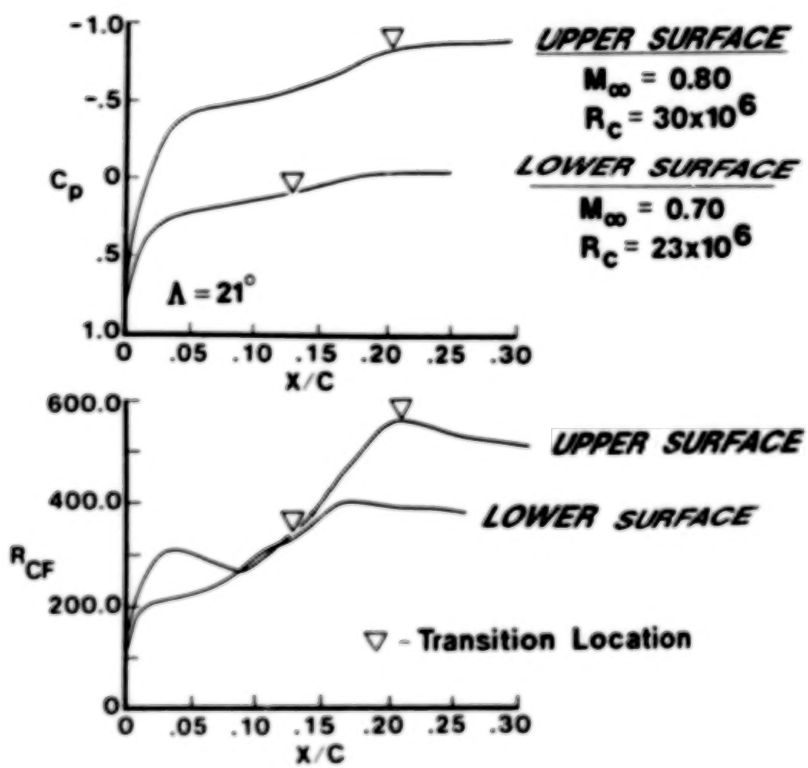

Figure 30. - 757 NLF glove pressure and crossflow Reynolds number distributions on the upper and lower surface at two flight conditions.

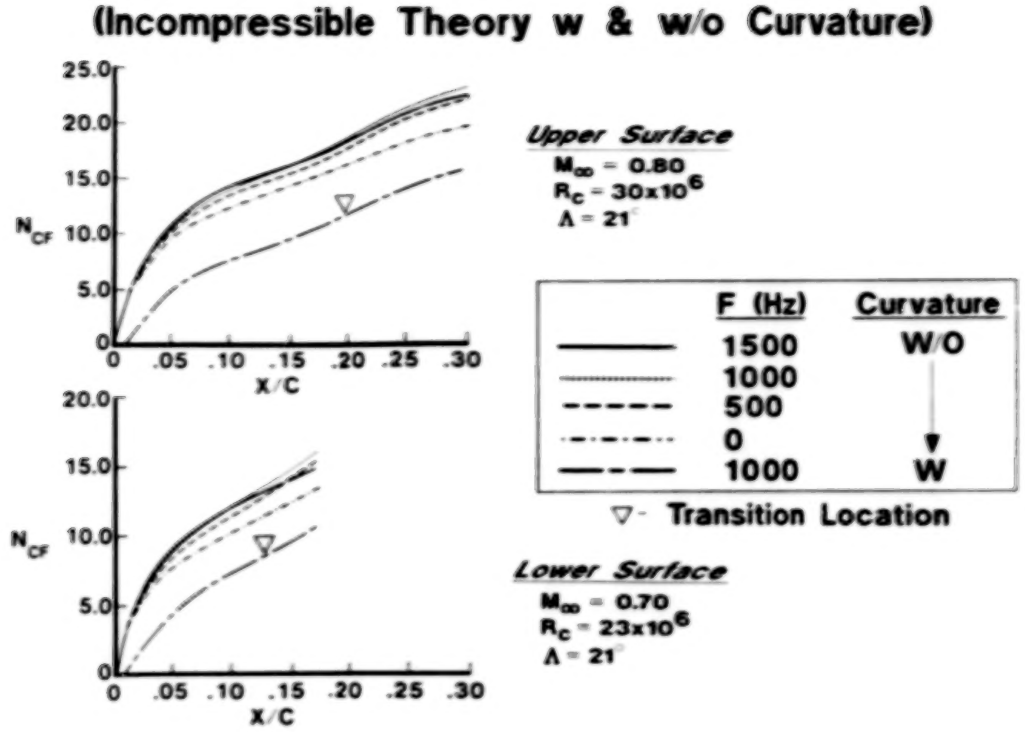

Figure 31. - 757 NLF glove crossflow N-factors (with and without curvature effects) on the upper surface and lower surface at two flight conditions.

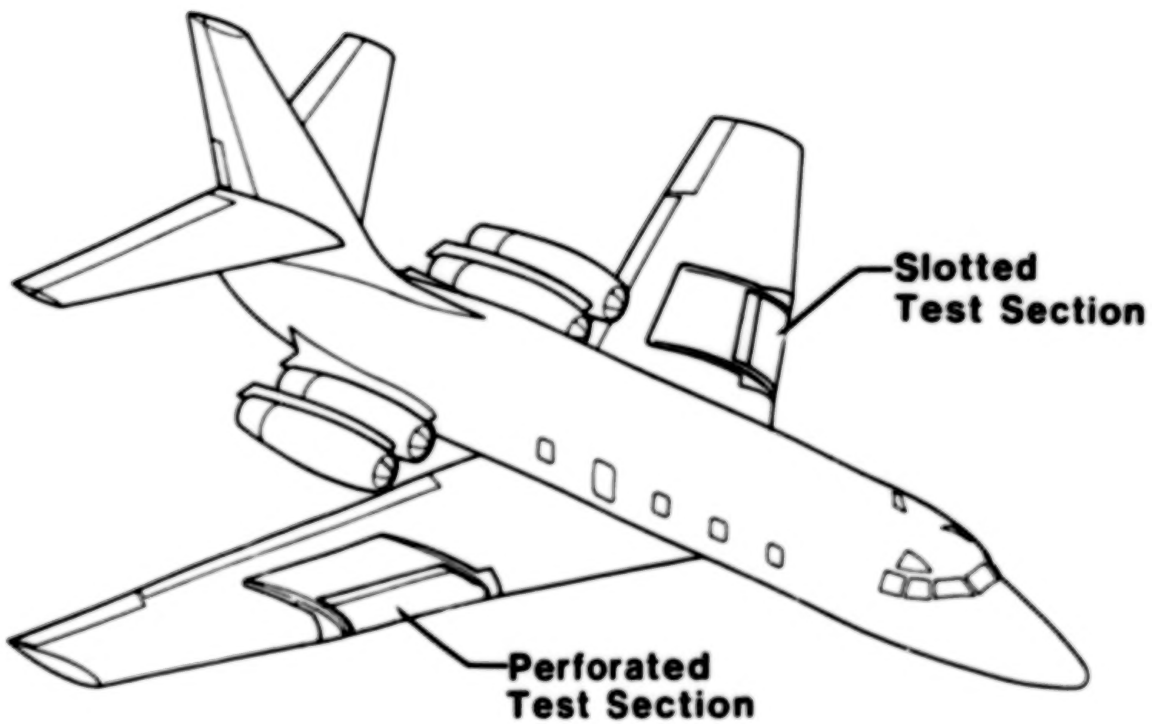

Figure 32. - JetStar test-bed aircraft for the NASA leading-Edge Flight Test Program.

- Suction on upper surface only
- Suction through electron-beam-perforated skin
- Leading-edge shield extended for insect protection
- De-icer insert on shield for ice protection
- Supplementary spray nozzles for protection from insects and ice

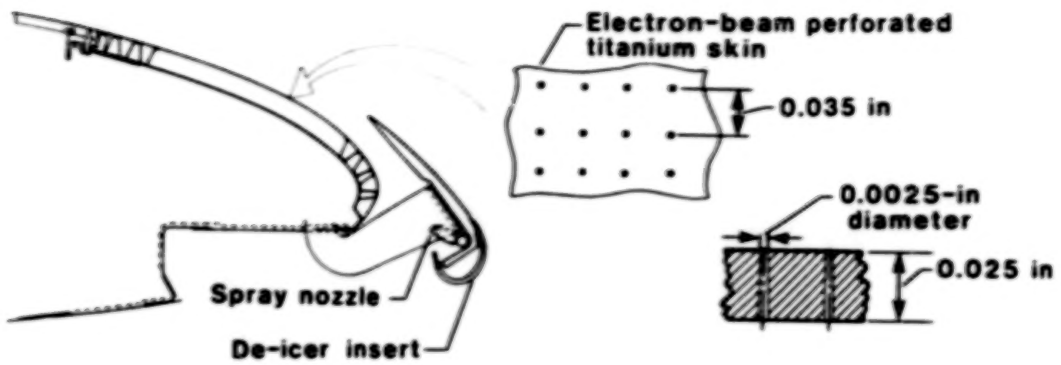

Figure 33. - The Leading-Edge Flight Test Program perforated test article.

- Suction on upper and lower surface
- Suction through spanwise slots
- Liquid expelled through slots for protection from insects and icing

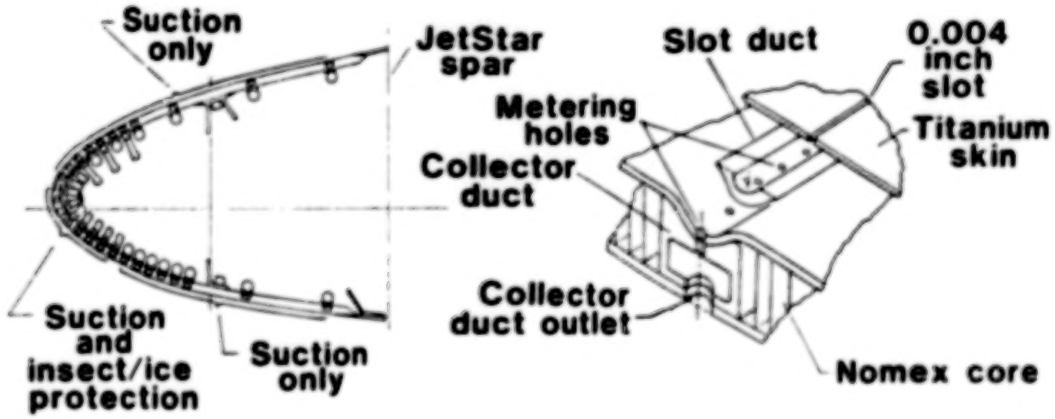

Figure 34. - The Leading-Edge Flight Test Program slotted test article.

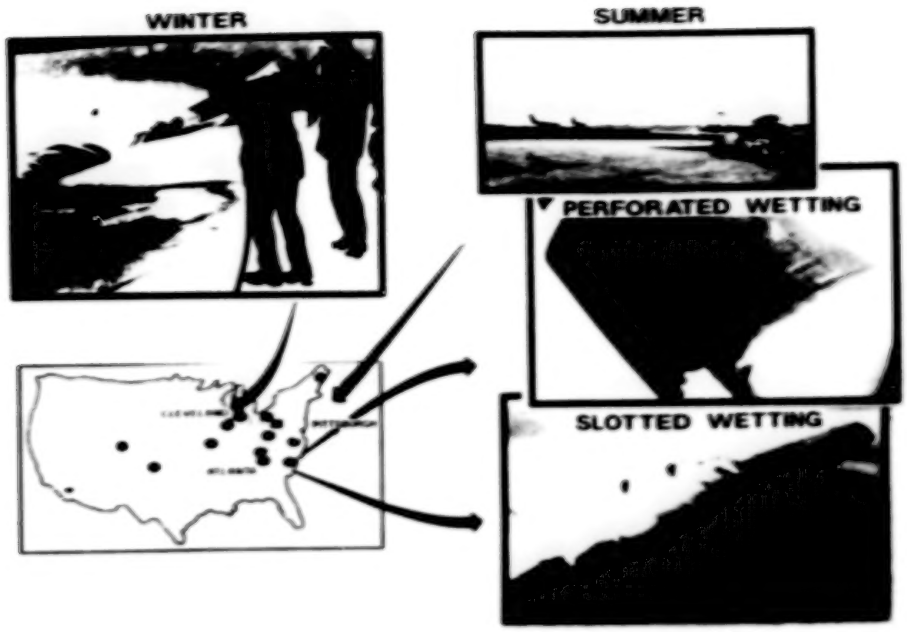

Figure 35. - The Leading-Edge Flight Test Program simulated airline service.

ORIGINAL PAGE IS
OF POOR QUALITY

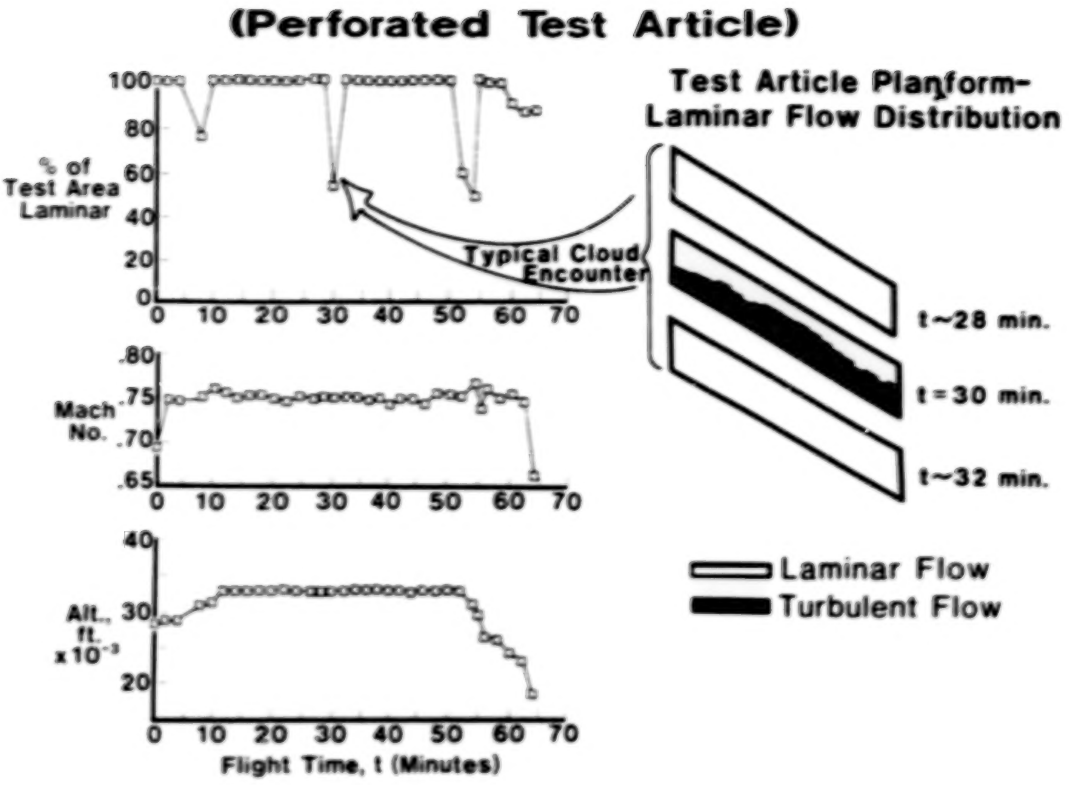

Figure 36. - Typical flight profile from the LEFT Program simulated airline service.

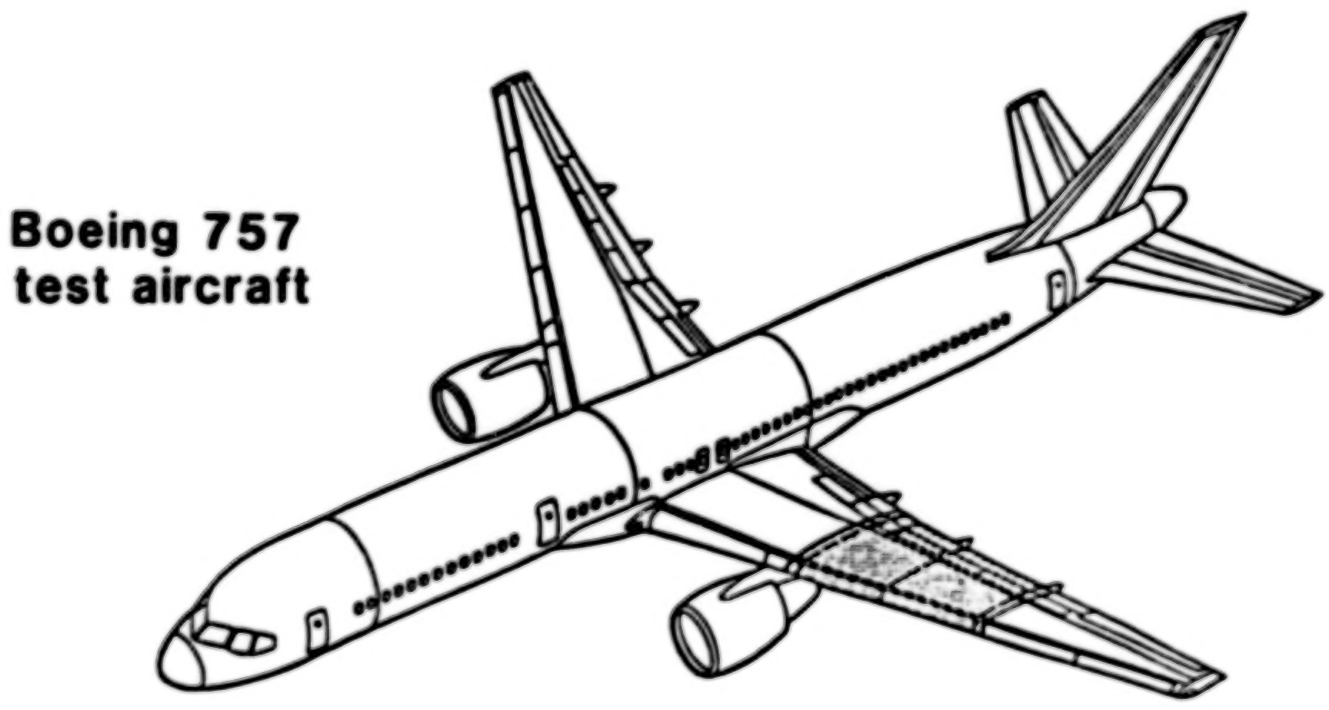

Figure 37. - The 757 test-bed aircraft for the Hybrid Laminar Flow Control (HLFC) Flight Experiment.

Technical Features:

- Cruise Conditions
  - M_∞= 0.8
  - $R_C \geq 30 \times 10^6$
  - Alt.=34K to 42K ft.
- Laminar Flow, 38 to 62% chord
- Suction to Front Spar
- Microperforated Titanium Suction Surface
- All Metal Construction
- Operational Systems
  - Leading Edge Krueger/Insect Shield
  - Anti-icing

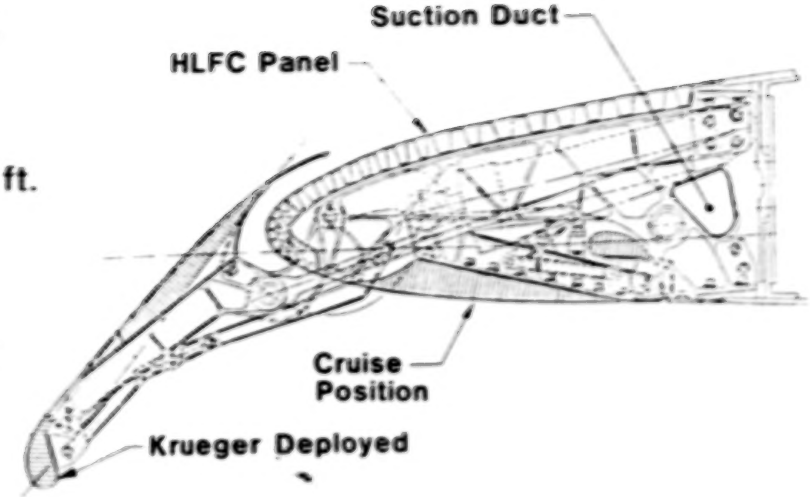

Milestones:

• Contract Award	Nov '87
• Critical Design Review	Dec '88
• First Flight	Feb '90
• Complete Program	Nov '90

Figure 38. - The HLFC Flight Experiment technical features and milestones.

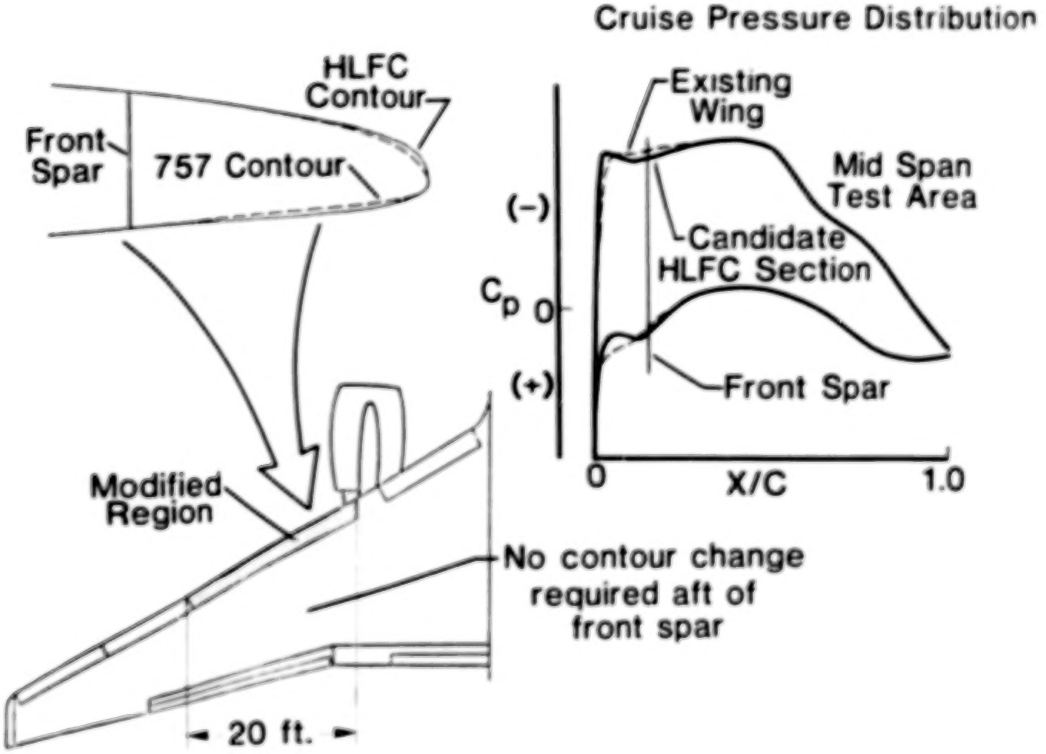

Figure 39. - The 757 wing leading-edge modification for the HLFC Flight Experiment.

N91-24136

LAMINAR-FLOW WIND TUNNEL EXPERIMENTS

54-02
19351

William D. Harvey, Charles D. Harris,
William G. Sewall, and John P. Stack
NASA Langley Research Center
Hampton, Virginia

SUMMARY

Although most of the laminar flow airfoils recently developed at the NASA Langley Research Center have been intended for general aviation applications, new low-drag airfoils have been designed for transonic speeds and wind tunnel performance tested. The objective was to extend the technology of laminar flow to higher Mach and Reynolds numbers and to swept leading edge wings representative of transport aircraft to achieve lower drag and significantly improved operation costs. This research involves stabilizing the laminar boundary layer through geometric shaping (Natural Laminar Flow, NLF) and active control involving the removal of a portion of the laminar boundary layer (Laminar-Flow Control, LFC), either through discrete slots or perforated surface. Results show that extensive regions of laminar flow with large reductions in skin friction drag can be maintained through the application of passive NLF boundary-layer control technologies to unswept transonic wings. An even greater extent of laminar flow and reduction in the total drag level can be obtained on a swept supercritical airfoil with active boundary-layer control.

INTRODUCTION

Long-range market forecasts, operating costs, and strong competition among the airlines have provided incentives for the development of new commercial transport aircraft with substantially improved fuel consumption and operating costs (ref 1). One method of improving fuel consumption is through new laminar-flow technologies and advanced theories in aerodynamics (refs. 2-4), whereby drag reductions are made possible by extending and maintaining laminar boundary layers on wing surfaces, thus reducing skin friction drag. The most direct technique for maintaining a laminar boundary layer is through the passive, or natural laminar-flow (NFL) approach which utilizes favorable pressure gradients to avoid Tollmien-Schlicting instability that leads to transition. These favorable pressure gradients are provided by judicious shaping of the airfoil geometry (refs. 5-9). Maintaining laminar flow by favorable pressure gradient alone becomes increasingly more difficult with increasing Reynolds number and wing sweep at transonic speeds; however, and some form of active or laminar-flow control (LFC) may be required (refs. 2-4, 10, 11).

Natural laminar-flow airfoils have been developed and extensively applied in the past on gliders with very low-drag coefficients realized in flight at low-speeds and Reynolds numbers. More recently, carefully designed NASA laminar-flow airfoils for general aviation aircraft have been developed and wind tunnel tested (refs. 6-9, 12-15) with significantly improved performance characteristics at higher Reynolds numbers than those in the past. Several of these new low-drag airfoils have been applied on different general aviation (GA) aircraft. For example, the NLF(1)-0416 is in production on the Swearingin SX-300 and Freedom Master FM-2 aircraft and the NLF(1)-0215F on the NEKO Lancair 210 and Prescott Pusher 200 aircraft (refs. 6, 7). A Cessna 210 aircraft (refs. 16, 17) has been equipped with a full-span glove of the NLF(1)-0414F (refs. 8, 12) over the original wing for flight tests which verified performance predictions. Also, the NLF(1)-0414 has been slightly modified and applied on the prototype CIRRUS VK 30 aircraft for flight certification.

The above airfoils for general aviation application have achieved drag coefficients that are lower than conventional turbulent airfoils used for either GA or transport aircraft, as illustrated in figure 1. The faired curves are measured drag polars for several different airfoils (with flap deflection) at subsonic and transonic speeds for a chord Reynolds number of 6 million. The low-speed turbulent LS(1)-0417 airfoil is discussed in reference 18 and the 11-percent thick supercritical airfoil in reference 19. The drag polars for the NLF(1)-0215F and NLF(1)-0414F airfoils show a low drag coefficient "bucket" over a rather wide range of lift coefficients which is primarily due to the reduction of skin friction through long runs of laminar flow on both the upper and lower surfaces. These long runs of laminar flow were promoted by shaping the pressure distributions to minimize the amplification of local disturbances that influence transition on the forward portion of the airfoil.

Conventional airfoils for transonic aircraft operate at substantially higher Mach numbers, Reynolds numbers, and sweep than general aviation aircraft and are usually designed for fully turbulent boundary layers which result in higher drag values. From figure 1 it can be seen, for example, that the drag obtained on the NLF(1)-0414F airfoil is about 40- to 50-percent lower than either the turbulent low-speed LS(1)-0417 or supercritical airfoil drag over a range of lift coefficients. The challenge then, is to extend the technology of NLF and LFC to higher Mach numbers, Reynolds numbers, and sweep with low drag. The performance verification of such laminar-flow concepts on airfoils at transonic speeds requires wind tunnels with excellent flow quality environments.

This paper presents experimental wind tunnel results and analysis for two advanced NASA laminar-flow airfoils designed for high subsonic and transonic flow conditions.

SYMBOLS

c Wing or airfoil chord

C_d Drag coefficient, $\frac{\text{section drag force}}{q_\infty c}$

C_L Lift coefficient, $\frac{\text{section lift force}}{q_\infty c}$

C_p Pressure coefficient, $\frac{p - p_\infty}{q_\infty}$

C_Q Suction coefficient, $\frac{(\rho w)_w}{(\rho u)_\infty}$

f frequency

M Mach number

N Natural logarithm of ratio of distance amplitude to its value at the neutral stability point

R Reynolds number per unit length, $\frac{\rho U_\infty}{\mu}$

R_c Reynolds number based on chord, $\frac{\rho U_\infty c}{\mu}$

t Thickness

x Chordwise distance measured from leading edge

α Angle of attack

ρ	Density
δ_f	Flap angle
Λ	Sweep angle
μ	Viscosity

Subscripts:

c	Chord
CF	Cross flow
max	Maximum value
min	Minimum value
N	Normal to leading edge
s	Suction
t	Total
tr	Transition
TS	Tollmien-Schlichting
w	Wall or wake
∞	Free stream

LOW-DRAG AIRFOIL TESTING

This section presents a review of the mechanisms which cause transition; comments on the ability to properly simulate flight conditions in a transonic wind tunnel; and discusses recent advances made in diagnostic instrumentation as applied to low-drag airfoil testing.

One of the most important parameters to be determined during performance verification of low-drag airfoils is the location of boundary-layer transition. Equally important, however, is understanding the mechanisms which cause transition. Transition depends on many factors, including Tollmien Schlichting instability (TS), cross-flow instability (CF), attachment line contamination (AL), and Görtler vortices (GV).

The boundary-layer profile in the direction of the external flow is very similar to that of a two-dimensional boundary layer and by a process of receptivity, small disturbance waves (TS) are developed. These small disturbances grow initially through a linear process, followed by a nonlinear growth and breakdown to transition. For unswept wings, TS disturbance waves are the dominant cause of transition and adverse pressure distributions and increasing Reynolds number have a major influence in their growth.

Wind tunnel experiments on swept wings (ref. 10) have shown that transition may occur near the leading edge due to the instability of cross-flow velocity profiles in the boundary layer. Cross-flow (CF) velocity profiles exhibit inflection points near the surface, and boundary-layer stability theory shows that this instability will lead to transition (refs. 20-24). The major parameters that influence cross-flow instability are wing sweep, pressure distribution, and Reynolds numbers.

Spanwise turbulent contamination, induced by instability of the wing-fuselage juncture boundary-layer or leading-edge roughness, can propagate along the leading-edge of swept wings (ref. 25). The occurrence of such a disturbance along the leading-edge attachment line (AL) could result in the entire wing surface boundary layer becoming fully turbulent for attachment line momentum thickness Reynolds numbers exceeding about 150. Attachment line transition is dependent on wing sweep angle, leading-edge radius, Reynolds number, and flow acceleration in and along the attachment line region.

On the lower surfaces of cambered airfoils, Görtler vortices (GV) may develop as a result of a centrifugal instability of the flow over regions of concave surface geometry (refs. 26-29). Such disturbance vortices are counter rotating pairs that lift off the surface and travel streamwise while remaining in the boundary layer. Görtler vortices are normally highly unstable and quickly lead to transition, however, their growth may be damped when traveling from concave to convex curvature regions.

All of these instabilities are very important (refs. 30-32), and particular attention must be given to avoiding these phenomena when designing and performance testing swept laminar-flow airfoils.

LAMINAR-FLOW TESTING IN TRANSONIC WIND TUNNELS

There are certain limitations in transonic test capabilities which must be considered. Since low-drag airfoil testing is fundamentally a boundary-layer

stability problem, the ability to properly simulate flight conditions in a wind tunnel can be strongly affected by Reynolds number scale (ref. 33), environmental disturbance levels (refs. 34-36), model surface conditions (refs. 37-41), and tunnel wall interference (refs. 42-44). Also important are the methods and instrumentation used to measure disturbance levels and boundary-layer transition characteristics.

DIAGNOSTIC INSTRUMENTATION

The test results obtained with any model is a direct function of the test section flow characteristics. Transonic tunnels are, in general, not well calibrated in terms of free-stream dynamic quantities, but pressure, density, and temperature fluctuations are very important flow disturbance sources and must be known to properly evaluate the turbulence levels (ref. 36). Hot-wire anemometers were used to measure mass flow fluctuations from which components of velocity fluctuations ($\tilde{u}$, $\tilde{v}$, $\tilde{w}$) have been derived. The acoustic environment was also measured using either pressure transducers or microphones.

Another type of anemometry consists of individual thin-film sensors, which may be attached directly to the model surface or flush mounted (ref. 45). It operates on principles similar to the hot-wire anemometer and is used to detect transition. The single-type film sensors (ref. 45) have recently been configured in a multiple sensor array (ref. 46) to simultaneously detect separation and reattachment locations or shock-boundary layer phenomena. More details about advancements in instrumentation for transonic testing are presented in reference 47.

Figure 2 shows the locations of individual thin-film sensors which were deposited on the ends of tiny quartz rods and mounted flush with the surface of a model. The sensors were maintained at 80 °C above local recovery temperature by a constant temperature anemometer. The installation technique for the hot-film sensors on this model is given in reference 45. Examples of output RMS voltage traces and their corresponding boundary-layer states are also shown in figure 2. The amplitude of the fluctuating sensor voltages indicates the relative state of the boundary layer based on assigned arbitrary values of intermittency from 1 to 10. The low amplitude dynamic signal indicates the lower shear stress that is representative of a laminar boundary layer (intermittency factor = 1). The higher amplitude dynamic signal indicates the higher shear stress that represents a turbulent boundary layer (intermittency factor = 10). The transitional boundary layer has both the laminar and turbulent type signals (intermittency factor = 3 to 8) , and it is the relative amount of each, or intermittency factor, which indicates the degree of transition.

Figure 3 shows an example of the Multielement Dynamic Shear Stress Sensor (MEDS') technique (ref. 47) that was used to detect shock-induced separation on the upper surface of an airfoil at transonic speeds. The MEDS' consists of a large number of closely spaced (0.1-inch) individual Nickel films that were vacuum deposited on a thin substrate of thickness 0.000010 inches in a straight line array. The substrate is bonded to the model surface with sensor array oriented streamwise and leads removed at the model spanwise ends. The figure illustrates that shock-induced separation can be clearly detected by the phase reversal phenomenon observed by P. Stack and S. Mangalam (ref. 46) in low-frequency dynamic shear stress signals. When the shear stress fluctuations from adjacent surface thin-film sensors are correlated, a zero phase is observed upstream of the shock (fig. 3(a)). A -180° phase shift is observed across the shock-induced separation

(fig. 3(b)); a +108° phase shift is observed across reattachment (fig. 3(c)); and the signals are again in phase downstream of the shock-induced separation and reattachment (fig. 3(d)).

TRANSONIC FACILITIES

A brief description of the transonic wind tunnels used to obtain the data presented in this paper follows.

8-Foot Transonic Pressure Tunnel

The NASA Langley 8-Foot Transonic Pressure Tunnel (8-Ft. TPT) is a closed-circuit single-return variable density continuous-flow wind tunnel with a contraction ratio of 20:1. The test section walls are slotted (5-percent porosity) top and bottom, with solid sidewalls fitted with windows for schlieren flow visualization. In 1981, the facility was modified for flow quality improvements and reconfigured for testing of a large-chord swept laminar-flow control (LFC) airfoil at transonic speeds (refs. 11, 48). A honeycomb and five screens were installed in the settling chamber to suppress the disturbance levels in the test section. A contoured liner was installed on all four walls of the test section to simulate free-air streamlines about an infinite yawed wing. This contoured liner produces a contraction ratio of 25:1 and covers the floor and ceiling slots. An adjustable sonic throat ($0.78 \leq M_\infty \leq 0.84$) is located at the end of the test section to block upstream propagation of diffuser noise. The honeycomb and screens were installed as permanent additions to the facility and the liner as a temporary addition, to be removed at the end of the LFC experiment (ref. 48).

The combination of honeycomb, screens, and choke provide very low disturbance levels of $\tilde{p}/p_\infty$ and $\tilde{u}/u_\infty \approx 0.055$ percent, in the test section at $M_\infty = 0.8$ and $R/ft = 3 \times 10^6$, based on conventional single hot-wire measurements and data reduction techniques. However, results also obtained using a new and more accurate three-wire, hot-wire probe technique at the same test conditions indicated a disturbance level of $\tilde{u}/u_\infty \approx 0.3$ percent (ref. 47).

OHIO STATE UNIVERSITY 6- BY 22-INCH TRANSONIC TUNNEL (6 x 22 TT)

The Ohio State University 6- by 22-Inch Transonic Tunnel is a closed-circuit blowdown type facility (ref. 49). The test section is 6-inches wide and 22-inches high, has plane parallel sidewalls, perforated walls on the top and bottom with separate, self-aspirated plenums, and an array of bars in the exhaust to choke the flow and fix the test section Mach number.

Air is supplied from a 1500 cubic foot storage tank at 2600 psi through two preset control valves, enters the settling chamber through a distribution device and a perforated bulkhead, passing through a honeycomb and six screens, and enters the test section through a three-stage contraction region. Models are mounted in a circular sidewall port, which may be rotated for angle-of-attack from 0° to ±180°. Model pressure distributions are acquired by scanivalves, and Kulite gages are used for diagnostic testing. Wake profiles for the determination of drag are acquired by means of a single traversing probe at transonic speeds or by multiple probes at low speeds.

The maximum stagnation pressure is 4.423 atmospheres with a Mach number range from 0.2 to 1.1. The operational unit Reynolds number range is dependent upon Mach number. For example,

M	R/ft
0.2	2 to 7 x 10^6
.4	4 to 14 x 10^6
.8	7 to 23 x 10^6

RESULTS AND DISCUSSION

Unswept High-Speed NLF Airfoils

High subsonic cruise speeds provide a more difficult design challenge than low subsonic cruise speeds when laminar-flow wings are used. At high speeds, low sweep is desirable to minimize cross-flow boundary-layer instabilities and leading-edge contamination; high sweep is desirable to minimize wave drag and delay transonic drag rise. Consequently, a compromise must be made to prevent boundary-layer instabilities from causing transition near the leading edge and, at the same time, not reduce the drag-rise Mach number to an intolerably low value. Since thinner airfoils rather than reduced sweep are an alternate way of delaying drag rise, airfoil/wing thickness will also be a variable. Another negative factor in high-speed design is the larger Reynolds numbers that are inherent and the adverse effect they have on all instability mechanisms. Careful tailoring of the airfoil contour and the associated pressure distributions is an important activity at low speed but at high speed it is a "make-or-break" one. Favorable gradients required for laminar flow drive the design C_L's down and the wing area up. The need for highly accurate inviscid and viscous flow codes as well as boundary-layer stability routines is clear.

Based on the encouraging results obtained by geometric shaping to achieve extensive laminar flow on both surfaces of the low-speed NLF(1)-0414F airfoil in the wind tunnel (ref. 12) and in-flight (ref. 16), effort has been recently directed towards extension of the concepts to higher speed NLF airfoils. Details of one of the resulting two-dimensional concepts, HSNLF(1)-0213F, are reported in references 13 and 15. Wing body integration of the airfoil is discussed in reference 13 and design of an integrated trailing-edge flap is presented in reference 14.

The HSNLF(1)-0213F, has been fabricated of metal and tested (ref. 15) in the NASA Langley LTPT and 6- by 28-Inch TT to investigate its low-speed high-lift characteristics and high-speed drag-rise characteristics. The airfoil was designed for a lift coefficient of 0.26, Mach number of 0.70, Reynolds number of R_c = 11 x 10^6, and t/c = 0.134. This particular airfoil was designed for application to an essentially unswept wing but could be used for a swept wing as well.

The HSNLF(1)-0213F airfoil profile and design pressure distribution are shown in figure 4. The design shockless pressure distribution was expected to provide laminar flow rearward to about x/c = 0.55 on the upper and x/c = 0.70 on the lower surfaces up to $R_c \leq 10 \times 10^6$. The upper surface forward of 50-percent chord employs the NLF(1)-0414F airfoil geometry; the upper surface aft of the 50-percent chord was modified from that of the NLF(1)-0414F to minimize the possibility of turbulent separation (refs. 2, 13, 15). The bottom side of the nose was slightly modified to minimize off-design pressure peaks on the lower surface. At the same time, the

pressure distribution at the design Mach number and lift coefficient remains essentially subcritical, thereby avoiding recompression shock waves.

Initially, the HSNLF(1)-0213F airfoil was tested both at low speeds ($M \leq 0.3$) and high speeds ($0.35 \leq M \leq 0.80$) and the results are presented in reference 15. Near the design lift coefficient, $0.23 \leq C_l \leq 0.25$, the low-speed tests revealed both low-drag coefficients (0.0038) and transition locations with individual surface thin-film sensors at $x/c = 0.50$ on the upper surface and $x/c = 0.60$ on the lower surface. However, at the design Mach and Reynolds numbers, the high-speed test showed much higher drag coefficients (0.0078 to 0.0083) at the design Mach and Reynolds numbers. This higher drag level was attributed to premature transition caused by poor tunnel flow quality in the NASA Langley 6 x 28 TT.

To investigate the laminar-flow potential of the HSNLF(1)-0213F airfoil, another wind tunnel test was conducted on the same metal model that was used in the NASA Langley 6 x 28 TT, with multielement thin-film sensors to detect transition, separation, reattachment, and shock location (ref. 46). The 6- by 22-inch transonic wind tunnel at the Ohio State University (ref. 49) was used for this experiment. Test requirements and facility capabilities limited the maximum chord Reynolds numbers to 5.0 million. Limited test results were also obtained on a composite model in this same facility.

Some of the results from this experiment are shown in figures 5 and 6, where comparisons have been made between the experimental and theoretical pressure distributions. Included with the pressure distributions are the locations for the beginning, peak, and end of transition as indicated by the thin-film sensors on the model's upper surface that extend from $0.3 \leq x/c \leq 1.0$. The theory (ref. 50) has no laminar boundary layer; the start of the turbulent boundary layer was arbitrarily set at 0.40c on the upper and 0.50c on the lower surfaces.

The shock-free experimental and theoretical pressure distributions presented in figure 5, at the design Mach number and lift coefficient agree very well up to the recompression zone for both the upper and lower surfaces. The theory then shows a stronger pressure recovery than the experiment. Good agreement exists between the measured and predicted drag of $C_d = 0.0057$. No wall interference corrections were made to the experimental data.

The hot-film sensors (refs. 46, 47) on the upper surface indicate the beginning of transition at $x/c = 0.50$, near minimum pressure, followed rapidly by peak transition at $x/c = 0.545$, then fully turbulent flow developing at $x/c = 0.593$. No boundary-layer separation was indicated by these upper surface sensors. It should be noted that, while the measured transition location agrees with the design objective, the results are limited to a Reynolds number of 4.2 million instead of the design 11 million.

Figure 6 shows another experimental and theoretical pressure distribution comparison at an off-design Mach number of 0.77 which results in a strong shock wave on the upper surface, as indicated by both experiment and theory (ref. 50). However, the experiment shows that the beginning of the shock is approximately 0.10c ahead of the theoretical location, along with significantly reduced suction levels, followed by an entirely different pressure distribution than shown by theory. It should be noted that the theory (ref. 50) has no provision for shock-boundary layer

interaction, and there were no wall interference corrections made to the data. Thin-film sensors in the region of the shock wave indicated an attached laminar separation bubble just downstream of the beginning of transition, which occurred at the shock wave itself (fig. 3). Therefore, the laminar boundary layer extends rearward to the shock wave which interacts with a laminar separation bubble and causes it to shift forward. The experimental pressure distribution following the separation bubble, i.e., after the reattachment point, develops a positive gradient.

Figure 6 not only shows large differences between measured and predicted pressure distributions, but also between drag coefficients that are caused by interaction of the laminar boundary layer and shock wave that are not accountable by the theory. For the design case (fig. 5), good agreement exists between theoretical predictions of pressure distribution and drag since there is no shock or boundary-layer separation.

Figure 7 shows a comparison of the transonic drag-rise with increasing Mach number obtained on the same metal model of the HSNLF(1)-0213F airfoil in two wind tunnels. Also shown for comparison is a single-drag value at M = .7 obtained on a composite model of the HSNLF(1)-0213F in the O.S.U. 6 x 22 TT. The angle of attack was set at zero and the resulting lift coefficients ranged from 0.26 to 0.28. From figure 7, it appears that measured and predicted low to moderate drag coefficients (fig. 5), ranging from about 0.0057 to 0.0065, can be attained on the metal model up to a Mach number of 0.73 at $R_c = 4.2 \times 10^6$. Apparently, much lower drag values of about 0.0045 are possible at the design M = 0.7 with the smooth composite model compared to that obtained for the metal model in the same tunnel. With transition fixed at 0.05 chord, the drag coefficient increases to 0.0083 while the drag-rise Mach number is reduced to about 0.715.

SWEPT SUPERCRITICAL LFC AIRFOILS

The concept of combining geometric shaping and boundary-layer control through suction on airfoils to achieve very low drag dates back to the late 1930's when the feasibility of achieving full-chord laminar flow on conventional swept wings, with suction applied through many closely spaced surface slots, was established by Pfenninger (refs. 10, 51). Results were obtained on large-chord wing sections (modified NACA-66012) of 30° sweep and t/c = 0.12 in three different wind tunnels (ref. 10) and flight (refs. 37, 39). Flight tests on the X-21 and F-94 aircraft (refs. 52, 53) achieved full-chord laminar flow to $R_c = 22 \times 10^6$ at $M_\infty = 0.80$ and $R_c = 36 \times 10^6$ at $M_\infty = 0.72$, respectively. The X-21 wing was swept 33° and the F-94 wing was unswept. Since this research demonstrated the potential for significant drag reduction through application of boundary-layer control, interest was generated in evaluating the feasibility of combining boundary-layer control with supercritical airfoil technology at conditions which are typical of high-performance transports. About 1975, Dr. Werner Pfenninger proposed such an experiment and a large chord swept supercritical airfoil, with suction capability on both the upper and lower surfaces, was designed, constructed, and tested in the NASA Langley 8-Ft. TPT (fig. 8). This NASA airfoil is designated SCLFC(1)-0513F. Details of the airfoil and suction system design along with the test setup have been reported (ref. 11). One of the major objectives of the experiment was to evaluate the feasibility of slotted and perforated suction surface concepts for laminarization in a large supercritical zone.

As mentioned above, requirements for this test included modification of the wind tunnel to achieve the desired flow quality and test section wall contouring to simulate free air flow about an infinitely yawed model at the design Mach number (refs. 44, 48).

Slotted and Perforated Models

The LFC airfoil model has an aspect of about 1.0. It consists of a wingbox structure to which three upper and three lower surface suction panels and a trailing-edge flap are attached (fig. 9). Figure 10 is a sketch showing the slotted suction surface with the internal airflow metering and ducting system. Laminar flow control by boundary-layer removal on the slotted configuration was achieved with suction through closely-spaced spanwise slots (fig. 10) on the airfoil surface. After passing through the slots and small underlying plenums, the air passed through appropriately spaced metering holes and was collected by spanwise ducts of constant cross section with suction nozzles located at the ends. Air from the nozzles passed through model evacuation lines, through airflow control boxes which controlled the amount of suction to the individual duct nozzles, through variable nozzles, through hoses to a collector manifold and, finally, to a 10,000 CFM compressor with a 4.5:1 compression ratio which supplied the suction.

In the upper surface midspan region where full-chord laminar flow was expected, the suction slots extended rearward onto the flap to x/c = .96. On the lower surface, suction extended rearward to x/c = .84. Outside of the laminar midspan region, the upper surface spanwise slots extend rearward only to the flap hinge line at x/c = .89. A photograph of the swept LFC airfoil installed in the test section of the 8-Ft. TPT is shown in figure 11. Figure 11(a) is a downstream view looking at the swept leading-edge upper surface, and figure 11(b) is an upstream view of the trailing edge. Suction ducts to control the boundary layer in the model/tunnel junctures may be seen in the liner at the floor and ceiling (fig. 11(a)).

Figure 12 is a sketch of the swept LFC airfoil model illustrating replacement of the slotted upper surface with three perforated suction surface panels. The perforated panels were designed and fabricated by McDonnell Douglas Aircraft Company under contract to the NASA Langley ACEE Project Office (ref. 54). The original bottom surface slotted panels were retained for this configuration. Figure 13 is a sketch showing the perforated suction surface and internal airflow metering and ducting system. This surface was fabricated with fiberglass flutes or hat sections with a continuous perforated skin bonded to the outer part of the hat sections resulting in alternating suction and nonsuction areas. These areas extend spanwise and are constant in width. The active suction and nonsuction area widths are nominally 0.60-in. and 0.3-in. wide, respectively. The perforations in the surface skin, produced by electron beam drilling, are approximately 0.0025 inches in diameter on 0.025-inch spacing, yielding an open area porosity ratio of 0.8 percent. Beneath each suction strip are spanwise flutes and ducts that are connected through a number of metering holes. Calibrated suction nozzles are provided in each duct and are connected via hoses to the suction compressor through the same control used for the slotted model. The perforated suction surface extends from $0.02 \leq x/c \leq 0.89$ along the entire span. The turbulent wedge regions at the ends of the model are very similar to those for the slotted model and the suction applied and controlled is also similar.

Experimental Results

Figures 14 and 15 show a comparison of the measured and theoretical chordwise pressure distributions at midspan and $M_{design} = 0.82$ for chord Reynolds numbers of 10 and 20 x 10^6. Figure 14 shows the measured pressure distribution for the slotted model to be essentially shock free at $R_c = 10 \times 10^6$ with full-chord laminar flow (as evidenced by the surface thin-film gages used for detecting transition) on both upper and lower surfaces (see figs. 16, 17). The higher and less uniform than design velocities on the upper surface were attributed to classical problems associated with wind tunnel testing--model deformation and wall interference. Local Mach numbers measured on the test section wall opposite the upper surface indicate that the supersonic bubble on the airfoil was larger than design and extended practically to the wall. The larger bubble was believed to be due to the inability to account for three-dimensional boundary-layer displacement thickness effects with the accuracy desired in the design analysis of the contoured liner wall (ref. 44).

The pressure distribution for the perforated model at $R_c = 10 \times 10^6$ (fig. 14) is very similar to that of the slotted model except for slightly higher velocities on the upper surface and with a very weak shock appearing at about $x/c = 0.70$. Even with the higher velocities and weak shock on the perforated upper surface, full-chord laminar flow was achieved (fig. 18) for $R_c = 10 \times 10^6$. These higher upper surface velocities are related to the more positive 0.71° angle of attack required for the perforated model as compared to the 0.51° angle of attack for the slotted model. The higher angle of attack was required to minimize the strength of the shock at the end of the supersonic zone as discussed below.

Measurements under simulated loading conditions indicated that the perforated model deformed more in the chordwise direction than the slotted model. Because of the larger deformation, the rear panel of the perforated model was closer to the test section wall opposite the upper surface than was the slotted model when both were positioned at $\alpha = 0.51°$. This resulted in a saddle back shaped upper surface pressure distribution with a strong shock near $x/c = 0.70$ and a sonic bubble which impinged on the wall. Since the angle of attack was adjusted by rotating the model about $x/c = 0.24$, increasing the angle moved the trailing edge of the model away from the wall, weakening the upper surface shock and reducing the extent of the sonic bubble.

In order to reduce the velocities nearer to design, it was necessary to modify the perforated model mounting blocks and translate the model 0.25-inch further from the wall above the upper surface. With this translation, the angle of attack could be reduced to 0.71° without strengthening the upper surface shock. At these conditions, the upper surface pressure was very near that for the slotted model and the extent of the sonic bubble was about the same for the two models.

With increases in Reynolds number, transition moved forward gradually on the upper surface and rapidly on the lower surface (figs. 16-18). Figure 15 compares the resulting pressure distributions at $R_c = 20 \times 10^6$ and indicates very similar distributions for the two models except for the previously mentioned higher velocities on the upper surface of the perforated model and the tendency for the perforated model to show a developing shock on the lower surface near midchord. The laminar boundary layer on the lower surface (both models used the same three slotted lower surface panels, fig. 9) was unable to withstand the adverse pressure gradient

leading into the trailing edge cusp region above approximately $R_c = 14 \times 10^6$ where transition moved rapidly forward and the flow separated in the rear cusp. With decreasing extents of laminar boundary layer and the appearance of separation on the lower surface, the local effective area distribution of the test section changes, resulting in higher free-stream Mach numbers being required to achieve the design plateau pressure distribution as Reynolds number increased. A loss in model lift and increase in drag also occur with decreasing extents of laminar flow.

It should be noted that, in general, as the free-stream Mach number increases, the corresponding static pressure decreases rapidly, causing the local differential pressure drop across a given suction surface to become large with corresponding increased suction requirements. This trend may become a challenge for designers of high transonic-supersonic LFC transports.

Analysis of spanwise pressure distributions and transition patterns at M_{design} showed that the flow was nearly two dimensional over the slotted and perforated models but that the leading edge peak pressure coefficient tended to vary along the span. In addition, transition tended to move forward with increases in Reynolds number in a somewhat non two-dimensional fashion. In general, transition tended to be more rearward toward the ceiling where leading-edge pressure peaks were lowest, and more forward toward the floor where they were higher.

The measured and theoretical suction coefficient ($C_Q = \frac{(\rho w)_w}{(\rho u)_\infty}$) distributions required to maintain full-chord laminar flow over both the slotted and perforated upper surfaces at $M_{design} = 0.82$ and $R_c = 10 \times 10^6$ are shown in figure 19. The design suction requirements were based on shock-free flow and minimum level required to maintain laminar flow. The measured suction required for full-chord laminar flow on the slotted model was higher than that predicted, in some cases by as much as 50 percent, and generally represents the maximum suction capability of the system. The measured suction requirements on the perforated model were much higher than on the slotted, particularly over the seven suction ducts on the forward panel ($x/c < 0.26$). The relative magnitude of the measured suction requirements over the next five suction ducts on the center panel ($0.26 < x/c < 0.59$) varies somewhat, but over the remaining nine suction ducts on the aft panel ($x/c > 0.59$), the available suction capability of the perforated panel was much lower than that theoretically required or that available on the slotted model. The measured suction distribution over the aft panel of the perforated model represents the maximum suction capability of the panel as designed and installed. The measured suction distribution over the forward and center panels represents the maximum suction available after extensive hardware modification has been made to increase their suction capability. These modifications include enlarging all metering holes in the flutes (fig. 13) in the two panels, enlarging the laminar nozzle extensions in the two panels, and adding a second suction nozzle to each laminar duct in the forward panel.

There was, of course, an infinite combination of individual duct suction levels and overall suction distribution possibilities. The distributions shown (fig. 19) consist, in general, of the maximum suction capability of each suction duct combined with the maximum suction capacity of the compressor system used to provide suction to the model. Small local variations may be permissible within these overall distributions without an adverse effect on the extent of laminar flow within the resolution permitted by the chordwise spacing of thin films. (See fig. 2). Reductions in the overall suction level of the distributions, by varying compressor

controls in amounts large enough for the sum of the suction drag over the entire upper surface to be measurably different, generally resulted in either a detrimental effect on the laminar-flow pattern (transition behavior) or an increase in wake drag. The higher than theoretically predicted suction requirements on the upper surface of both models are attributed to uneven velocities/pressures on the upper surface discussed above and the wind tunnel environment.

The higher suction requirements on the forward region of the perforated model compared to the slotted model was attributed to several factors. These factors include the less rigid construction of the perforated panels and the resulting greater, and more uneven, deformation under load; the waviness of the perforated surface, some of which is associated with the corrugated substructure, is also greater than on the slotted panels.

Since the lower slotted suction surface was the same for either the slotted or perforated model upper surfaces, an example comparison between the measured and predicted suction is shown in figure 20 for $M = .82$ and $R_c = 10 \times 10^6$. The measured higher than predicted suction requirements are attributed to the suction control required for the minimization of centrifugal Görtler type boundary-layer instabilities and interactions with cross flow in the concave regions of the lower surface (fig. 8).

The contributions to the total section drag coefficient for the slotted LFC airfoil at $M_\infty = 0.82$ are shown in figure 21 over a chord Reynolds number range of 10 to 20 million. The division of suction drag contributions between the upper or lower surfaces may be made since the suction drag is computed duct-by-duct and integrated over each surface independently. The wake drag is separated into upper and lower surface components on the basis of the assumption that the wake can be divided between the upper- and lower-surface at the point on the wake rake where the stagnation pressure loss is the greatest. The data (fig. 21) indicate that the larger contribution to the total drag is from the lower surface. With full-chord laminar flow over the upper and lower surfaces for $R_c \leq 12 \times 10^6$, the contribution to the total drag was about 1/3 due to wake and 2/3 due to suction drag. The sharp rise in wake drag on the lower surface between 14 and 15 million Reynolds number is associated with rapid forward movement of transition (fig. 17) and separation of the boundary layer in the lower aft cusp. The contribution of the suction drag is about 40 percent for the upper and 60 percent for the unconventional lower surface (fig. 21).

Wind tunnel tests have been conducted earlier on several swept LFC airfoils at low speeds (refs. 10, 51) with extensive laminar flow and low drag. These airfoils had suction applied only on the upper surface. Figure 22 shows the upper-surface pressure distributions and minimum total drag measured at the design lift condition ($C_L = .3$) on two earlier low-speed LFC airfoils of different sweep as compared to the present supercritical LFC airfoil with $C_L = .55$. The low-speed LFC designs, based on standard NACA airfoil profiles, have favorable pressure gradients over the first 50 percent or more of the chord, and much less severe adverse pressure gradients aft, than the supercritical design. The higher design C_L of the SCLFC(1)-0513F airfoil does not permit a long run of favorable pressure gradient. Figure 22 shows only the upper-surface measured minimum profile drag coefficients corresponding to the upper-surface pressure distributions at $R_c = 10 \times 10^6$. As might be expected, the supercritical design has a somewhat larger suction drag penalty than the NORAIR model, which has the greatest extent of favorable pressure gradient (fig. 22), and only a slightly larger suction drag penalty than the

University of Michigan 5- by 7-Foot Tunnel model, while the wake drag contribution is about the same in all cases. An increase in wake drag for $M_\infty \approx 0.70$ is observed on the slotted LFC airfoil (fig. 22) and attributed to the formation of a weak shock wave near the leading-edge as the supersonic bubble begins to develop. As the bubble develops near the leading edge ($0.78 < M_\infty < 0.80$), full-chord laminar flow still exists, but periodic turbulent bursts occur over the upper surface causing an increase in wake drag. It may be concluded that the basic phenomenon of applying suction laminarization over an extensive supercritical zone with full-chord laminar flow at $R_c = 10 \times 10^6$ is feasible as demonstrated on a swept LFC airfoil at high lift conditions. It is clear, however, that the "nonideal" transonic wind tunnel test environment (refs. 42, 44) and surface waviness (refs. 40, 41) do cause a loss in the amount of laminar flow achieved. Consequently, the data obtained are conservative; i.e., one should do better in flight.

Figure 23 shows the in-flight upper surface wing and glove pressure distributions for the X-21 and F-94 aircraft compared with that measured on the SCLFC(1)-0513F airfoil. Full-chord laminar flow was achieved for each experiment and conditions shown. The present wind tunnel model has not only a larger local Mach number but extent of sonic zone than the flight (refs. 52, 53) results, and also has a much higher lift coefficient. The X-21 wing and F-94 glove have favorable pressure gradients in the nose region and much less severe adverse gradients in the aft region than the supercritical airfoil.

Figure 24 shows a comparison of the drag measured on the upper surface of these three configurations. With full-chord laminar flow on the present model for $R_c \leq 12 \times 10^6$, the total drag level was about the same as that measured in flight on the X-21 or F-94. Detailed suction drag measurements were not determined in flight on the X-21, but an estimate of the total drag was made from reference 55. The higher total drag measured for the present LFC airfoil for $R_c \geq 12 \times 10^6$ was discussed earlier and is attributed mainly to the surface deformation, waviness, and the wind tunnel environment. However, the indicated drag level for the upper surface of the SCLFC(1)-0513F airfoil, obtained with full-chord laminar flow, is about one-third that of the upper surface of a conventional turbulent airfoil.

High-Speed HLFC Airfoils

Another and more practical concept for obtaining long runs of laminar flow at high Mach number is a hybrid configuration which would combine suction over forward regions of the upper surface with natural laminar-flow (NLF) concepts over rearward regions (refs. 2, 3). An attempt was made to simulate such hybrid laminar-flow control (HLFC) conditions during the 8-Ft TPT LFC experiment by turning off suction over regions of the upper surface. On the lower surface, suction was maintained for $0 \leq x/c \leq 0.25$ to control the flow between the lower surface and tunnel wall. This simulation of HLFC involved first establishing laminar flow to the most rearward location, then progressively turning off upper surface suction starting with the most rearward suction duct and measuring the extent of laminar flow that was maintained downstream of the turn-off points. The variation of transition location on the upper surface with chordwise extent of suction is shown in figure 25 for $M_\infty = 0.82$ and two chord Reynolds numbers. The results indicate that laminar flow could be maintained well beyond termination of suction. With no suction, laminar flow was present back to about 15- and 25-percent chord, depending on R_c. At $R_c = 10 \times 10^6$, the measured total drag was $C_d \approx 0.0012$ with $0 \leq (x/c)_{suction} \leq 0.96$ and increased to $C_d \approx 0.0025$ with no suction. The C_{dw} contribution increases and

becomes a larger fraction of $C_{d_{total}}$ as suction is reduced to zero. Clearly, this simulated HLFC approach must be considered somewhat "nonidealistic" and the results conservative since no effort was made to seal or smooth the unsucked regions of the airfoil. Furthermore, the pressure distributions (figs. 14 and 15) are not like that which would be designed for an HLFC configuration.

Almost any form of LFC could be considered a hybrid configuration, since, from a practical standpoint, one would probably not apply suction control over the full chord on both surfaces. Furthermore, considerable research is required to establish the effectiveness of suction control through shock boundary-layer interaction regions that occur at off-design conditions. Thus, the attractiveness of a form of HLFC that requires limited suction control in the leading-edge region for cross-flow instability followed by a favorable pressure gradient to maintain attached laminar flow (as far rearward as possible) is substantial. This concept would provide the maximum drag reduction with minimum suction requirements and complexity at design and off-design transonic speeds.

NASA Langley has designed, fabricated, and is currently installing an HLFC airfoil in the 8-Ft TPT for testing. The HLFC concept was originated by P. J. Bobbitt and the design was carried out by S. H. Goradia and J. C. Ferris and is reported in reference 56. It should be noted that constraints were placed on the HLFC design that required utilization of the present LFC airfoil and liner configurations in order to minimize costs and schedules for fabrication and testing. Only the upper mid and aft model surface regions ($0.25 \leq x/c \leq 1.0$) were altered in order to achieve a somewhat favorable pressure gradient downstream of suction turn off. The upper forward perforated and lower three-slotted surface panels were retained (figs. 9, 12). A new flap was designed and required to match the new upper aft surface camber change.

Figure 26 shows the HLFC airfoil design upper surface pressure and suction distribution for $M_\infty = 0.81$, $C_L = 0.47$, $R_c = 15 \times 10^6$ and sweep angle of 23°. Suction control is applied from $0.025 \leq x/c \leq 0.20$ through the original perforated panel for the HLFC concept. The HLFC type pressure distribution yields somewhat less lift than that for LFC in an effort to avoid shocks and aft separation. Predicted drag coefficients (fig. 27) for the upper surface of the HLFC airfoil are expected to be on the order of two times the drag levels for the full-chord laminar-flow shockless LFC airfoil for $R_c < 12 \times 10^6$.

DRAG REDUCTION SUMMARY

Figure 28 is an attempt to summarize the drag reduction achieved for the HSNLF(1)-0213F and SCLFC(1)-0513F airfoils designed for transonic operation, compared with several other recent NASA laminar-flow airfoils developed for low speeds shown as a hatched region in the figure. The results shown are for the minimum total drag measured which includes both wake and suction drag. The symbols are for drag values measured on these airfoils with extensive laminar flow over the upper and lower surfaces compared to fully turbulent flow conditions on airfoils as also indicated by hatched band. The values shown correspond to the minimum drag levels measured with α and $\delta_f = 0°$ but for different R_c's. The data (fig. 28) indicate that an average drag value of about 0.0085 exists when the flow is turbulent and $M_\infty \cos \Lambda \leq 0.75$ and about 0.0035 with laminar flow achieved by NLF or LFC. This represents a total drag reduction of about 60 percent that has been achieved and extended to transonic speeds with the new NASA airfoils. Apparently,

the presence of a shock on the unswept HSNLF(1)-0213F airfoil with laminar flow causes wave drag that influences drag rise for $M_\infty \geq 0.7$.

STABILITY METHODS ANALYSIS

Empirical relations, derived from earlier low-speed and Reynolds number experiments, are available and may be used for predicting transition (refs. 57, 58). More sophisticated approaches have been developed to determine the transition location on swept and unswept wings for incompressible (refs. 20, 59) and compressible (refs. 60, 61) flow.

The more sophisticated methods used for design and analysis of the airfoils herein have been described and presented earlier (refs. 20, 59-61). These methods are based on the temporal stability theory for laminar boundary layers where the local amplification rates are obtained as solutions of the governing Orr-Sommerfeld equation as functions of the frequency, wavelength, and orientation angle of the disturbance. If it is assumed that a disturbance has an initial amplitude A_o at some location X_o in the boundary layer, then the amplification ratio A/A_o at any downstream point X can be calculated. This amplification ratio can be expressed as an exponential function e^N where N is referred to as the amplification exponent or N-factor. N-factors may be related to the growth of disturbance amplitudes and used, based on experience, to predict transition conditions. These analysis methods only apply in linear attached flow regions and calculations must be carried out to the extent that the amplification exponent N becomes a maximum for all frequencies. When using the N-factor method for design, one is left with the arbitrary or empirical choice of a limiting N-value for transition. When used for analysis, limiting N-values are determined by the experimental transition locations.

Calibration of Stability Codes

A number of computer codes are available to calculate N-factors for Tollmien-Schlichting (TS) waves and cross-flow (CF) vortices. Some examples are the incompressible SALLY (ref. 59) and MARIA (ref. 20) codes and the compressible MACK (ref. 61) and COSAL (ref. 60) codes. The MARIA code is the most straightforward and economical to apply but is restricted to CF calculations only. The SALLY code may be used for CF or TS analysis.

Experimental transition data have been recently obtained and analyzed on NLF and LFC airfoils (refs. 3, 62), on bodies of revolution (ref. 63), in wind tunnels and on wings or gloves in flight (refs. 3, 62, 64-70). The measured pressure profiles and suction distributions from a number of these experiments were used as input to the above mentioned codes to calculate local disturbance growth rates and integrated amplification ratios (N-factors). N-factors calculated at the experimently measured transition locations for both TS and CF disturbances were compared to determine which instability was the most amplified.

Figures 29 and 30 are an attempt to summarize the calculated lowest N-factors at measured transition for TS and CF, respectively. It should be noted that there exists higher referencable N-factor values than shown in the figures; only the lower values were chosen to establish a low N-factor boundary and Mach number trend. In figure 29, calculated N-factors for situations where the TS instabilities dominate (CF negligible) is given; figure 30 is for situations where CF dominates (TS

negligible). The N-factors shown for the NASA NLF(1)-0414 wind tunnel and Cessna 210 flight tests and the NASA SCLFC(1)-0513 wind tunnel tests with slotted suction surface were calculated using the envelope method of solution in the SALLY and COSAL codes, with identical input data for each point (ref. 62). All other results on figures 29 and 30 (refs. 64-70) were calculated using either the SALLY, COSAL, or MACK codes. The incompressible TS N-factors (open symbols) approach a constant lower limit of about N = 9--while those N-factor values obtained with the compressible codes (solid symbols) decrease over the indicated speed range (solid curve) and are about 50 percent lower at $M_\infty \cos \Lambda \approx 0.8$. These trends (fig. 29) are intended to establish a theory calibration of the allowable lower limit for disturbance amplification. The limited number of incompressible CF N-factors (fig. 30) have a minimum value of 9 while those from the compressible code decrease to values of 4 or 5. The results strongly indicate that, on the average, a constant (N = 9) but conservative N-factor value can be used in applying the incompressible codes. However, knowledge of both the conservative trend and level of the N-factor (figs. 29, 30) is required when applying the compressible codes. The consistency of this correlation validates and extends the use of both incompressible and compressible linear stability theory for conservative design to high speeds. The fact that the lower limit of the N-factor trend from the compressible codes decrease with $M_\infty \cos \Lambda$ implies that "compressibility effects" are not conservative in stability analysis; i.e., transition takes place with less amplification than for incompressible flow.

All of the N-factors calculated and presented in figure 29 for the LFC airfoil were based on the beginning of transition location (ref. 62). However, if the transition point is selected further downstream of this location, the incompressible or compressible boundary-layer codes generally predicted laminar separation leading to a very rapid increase in the growth of the N-factor over a very narrow frequency range. This also caused arbitrary selection of amplification factors that could be on the order of twice or more those values shown in figure 29 for the SCLFC(1)-0513F airfoil. Calculated values of N_{TS} along the slotted LFC airfoil chord were found to vary depending upon the chordwise extent of applied suction and accuracy with which transition location could be determined. For example, with laminar flow over less than 30-percent chord on the upper suface, the calculated N_{TS} values were from 8.5 to 17.5 (ref. 62). However, with laminar flow beyond 30-percent chord, the N_{TS} values were found to decrease dramatically below these values to about 1 or 2. Thus, it becomes very important to account for this chordwise variation in N-factor for a given design case. The indicated trends (figs. 29-30) could be attributed to the wind tunnel disturbance environment; however, flight N-factors are shown that agree with the wind tunnel data.

Figure 31 is an attempt to evaluate the influence of transonic wind tunnel turbulence level on the calculated N-factors at transition on models. Shown for comparison are calculated values of N_{TS} on the slotted SCLFC(1)-0513F airfoil in the Langley 8-Ft TPT (ref. 62) and two bodies of revolution in the NASA Ames 12-Ft PWT (ref. 63). Also shown is the empirical relation for the variation of N_{TS} with turbulence level generated by MACK (ref. 71) for $\tilde{u}/u \geq 0.1$ percent. With the exception of a single data point ($N_{TS} = 10.5$), all of the calculated values tend to fall within a horizontal band between N_{TS} values of about 5 to 8 indicating little or no influence of tunnel turbulence level as suggested by references 63 and 71. In fact, the LFC airfoil results shown for $\tilde{u}/u \approx 0.2$ percent ($M_\infty = 0.7$) are for essentially full-chord laminar flow on both surfaces up to $R_c \leq 22 \times 10^6$. For $\tilde{u}/u \approx 0.05$ percent ($M_\infty = 0.82$) full-chord laminar flow existed for $R_c = 10^7$ and

N_{TS} = 4.5 and with $0.2 < (x/c)_{tr} < 0.3$ the N_{TS} = 7.5 for $R_c = 2 \times 10^7$. Therefore, the present limited results (figs. 29, 30) suggest the need for further calculations and analysis in order to complete the calibration of compressible boundary-layer stability theories. Note that the $\tilde{u}/u$ values just quoted are for single hot-wire measurements.

CONCLUDING REMARKS

Significant amounts of laminar flow have been achieved through passive (NLF) or active (LFC) methods at high speeds. This has been demonstrated on recently developed low-drag airfoils which use boundary-layer suction control or favorable pressure gradient. Wind tunnel tests of these concepts, from subsonic to transonic speeds, have shown significant improvements in lift-to-drag ratio over previous airfoils.

Natural laminar flow was maintained over 50-percent chord and shock-free conditions on an unswept airfoil designed for high speed and moderate lift. A reduction in the drag of about 40 to 50 percent over turbulent designs was realized. Suction laminarization, through either a slotted or perforated surface, over a large supercritical zone has been shown to be feasible to high-chord Reynolds numbers even under "nonideal" surface and test environment conditions on a swept LFC airfoil at high-lift coefficients. With essentially shock-free flow at $M_\infty = 0.82$, full-chord laminar flow on the upper and lower surface was achieved for $R_c \leq 12 \times 10^6$. As Reynolds number increased above $R_c \geq 12 \times 10^6$, transition moves gradually forward on the upper surface but laminar flow was maintained over most of the supersonic zone on the slotted and perforated surfaces for $M_\infty = 0.82$. The extent of suction laminarization was found to be slightly less for the perforated surface than for the slotted surface and attributed to a less rigid model and a more wavy surface. A reduction in the drag level of about 80 percent for the upper surface only and about 60 percent for both upper and lower surfaces was achieved with full-chord LFC.

Calculations using measured wind tunnel and flight data show differences in the trends and the lower bounds of the amplification ratios as calculated by incompressible and compressible linear boundary-layer stability theory. Lower N-factor levels have been obtained from the compressible stability theory than the incompressible; consequently, compressible calculations are not conservative, as previously thought.

REFERENCES

1. Maglieri, Domenic J.; and Dollyhigh, Samuel M.: We have Just Begun to Create Efficient Transport Aircraft. Astronautics and Aeronautics, Feb. 1982, pp. 26-38.

2. Bobbitt, P. J.; Waggoner, E. G.; Harvey, W. D.; and Dagenhart, J. R.: A Faster "Transition" to Laminar Flow. SAE-851855, Oct. 1987.

3. Harvey, W. D.: Boundary-Layer Control for Drag Reduction. SAE-872434, Nov. 1987.

4. Harvey, W. D.; McGhee, R. J.; and Harris, C. D.: Wind Tunnel Testing of Low-Drag Airfoils. NASA CP-2413, Apr. 1985.

5. Abbot, Ira H.; and von Doehhoff, Albert E.: Theory of Wing Sections. New York, Dover Publications, 1959.

6. Somers, Dan M.: Design and Experimental Results for a Natural-Laminar-Flow Airfoil for General Aviation Application. NASA TP-1861, 1981.

7. Somers, Dan M.: Design and Experimental Results for a Flapped Natural-Laminar Flow Airfoil for General Aviation Application. NASA TP-1865, 1981.

8. Viken, J. K.: Aerodynamic Design Considerations and Theoretical Results for a High Reynolds Number Natural Laminar Flow Airfoil. M. S. Thesis, George Washington University, Jan. 1983.

9. Viken, J. K.: Boundary-Layer Stability and Airfoil Design. NASA CP-2413, Apr. 1985.

10. Pfenninger, W.: Special Course on Concepts for Drag Reduction, Chapter 3 - Laminar Flow Control, Laminarization. AGARD Report 654, Jun. 1977.

11. Harris, Charles D.; Harvey, William D.; and Brooks, Cuyler, W.: The NASA Langley Laminar Flow Control Experiment on a Swept, Supercritical Airfoil. NASA TP-2809, 1988.

12. McGhee, R. J.; Viken, J. K.; Pfenninger, W.; Beasley, W. D.; and Harvey, W. D.: Experimental Results for a Flapped Natural-Laminar-Flow Airfoil with High Lift/Drag Ratio. NASA TM-85788, Apr. 1986.

13. Waggoner, Edgar G.: Computational Wing Design Studies Relating to Natural Laminar Flow. NASA CP-2413, Apr. 1986.

14. Morgan, Harry L., Jr.: High-Lift Flaps for Natural Laminar Flow Airfoils. NASA CP-2413, Apr. 1986.

15. Sewall, W. G.; McGhee, R. J.; Viken, J. K.; Waggoner, E. G.; Walker, B. S.; Millard, B. F.: Wind Tunnel Results for a High-Speed Natural Laminar Flow Airfoil Design for General Aviation Aircraft. NASA TM-87602, 1987.

16. Befus, J.; Nelson, R.; Latas, J., Sr.; and Ellis, D.: Flight Test Investigations of a Wing Designed for Natural Laminar Flow. SAE TP-871044, Apr. 1987.

17. Murri, Daniel G.; Jordan, Frank L.; Nelson, Randy; Davis, Patrick J.: Wind-Tunnel Investigation of a General Aviation Airplane Equipped with a High Aspect-Ratio, Natural Laminar-Flow Wing. SAE TP-871019, 1987.

18. McGhee, Robert J.; and Beasley, William D.: Wind Tunnel Results for a Modified 17-Percent-Thick Low-Speed Airfoil Section. NASA TP-1919, Nov. 1981.

19. Whitcomb, R. T.: Review of NASA Supercritical Airfoils ICAS Paper 74-10, Aug. 1974.

20. Dagenhart, J. R.: Amplified Crossflow Disturbances in the Laminar Boundary Layer on Swept Wings with Suction. NASA TP-1902, 1981.

21. Reed, H. L.: Wave Interactions in Swept Wing Flows. AIAA Paper 84-1678, 1984.

22. Reed, H. L.: Disturbance-Wave Interactions in Flows with Crossflow. AIAA Paper 85-0494, Jan. 1985.

23. Mack, L. M.: On the Stability of the Boundary Layer on a Transonic Swept Wing. AIAA 79-0264, Jan. 1979.

24. Nayfeh, A. H.: Effect of Streamwise Vortices on Tollmien-Schlichting Waves. Journal of Fluid Mechanics, vol. 107, 1981, pp. 441.

25. Poll, D. I. A.: Leading Edge Transition on Swept Wings. AGARD CP-224, 1977, pp. 21-1 to 21-11.

26. Nayfeh, A. H.: Influence of Görtler Vortices on Tollmien-Schlichting Waves. AIAA Paper 87-1206, Jun. 1987.

27. Hall, P.; Bennett, J.: Tayler-Görtler Instabilities of Tollmien-Schlichting Waves and Other Flows Governed by the Interactive Boundary-Layer Equations. Journal of Fluid Mechanics, vol. 171, 1986, pp. 441.

28. Mangalam, S. M.; Dagenhart, J. R.; and Kalburgi, V.: Influence of Suction and Curvature on the Growth of Görtler Vortices on an Airfoil. AIAA-87-0481, Jun. 1987.

29. Malik, M. R.: Wave Interaction in Three-Dimensional Boundary Layers. AIAA Paper 86-1129, 1986.

30. Herbert, T.; Morkovin, M. V.: Dialogue on Bridging Some Gaps in Stability and Transition Research. Laminar-Turbulent Transition, R. Eppler and H. Fasel, eds., Springer-Verlag, 1980.

31. Saric, William S.; and Reed, Helen L.: Three-Dimensional Stability of Boundary Layers. Proceeding Perspectives in Turbulence Symposium, Göttingen, West Germany, May 11-15, 1987.

32. Morkovin, M. V.: On the Many Faces of Transition Viscous Drag Reduction. C. S. Wells, ed., Plenum Publ., 1969.

33. Harvey, W. D.; and Pride, J. D.: The NASA Langley Laminar Flow Control Experiment. AIAA Paper 82-0567, Mar. 1982.

34. Pate, S. R.: Effects of Wind Tunnel Disturbances on Boundary-Layer Transition with Emphasis on Radiated Noise: A Review. AIAA Paper 80-0431, Mar. 1980.

35. Harvey, W. D.; and Bobbitt, P. J.: Some Anomalies Between Wind Tunnel and Flight Transition Results. AIAA Paper 81-1225, Jun. 1981.

36. Stainback, P. Calvin; Johnson, Charles B.; and Basnett, Constance B.: Preliminary Measurements of Velocity, Density, and Total Temperature Fluctuations in Compressible Subsonic Flow. AIAA 83-0384, Jan. 1985.

37. Gray, W. E.: Transition in Flight on a Laminar-Flow Wing of Low Waviness (King Cobra). R.A.E. Report 2364, Mar. 1950.

38. Gray, W. E.; and Fullam, P. W. J.: Comparison of Flignt and Wind Tunnel Measurements of Transition on a Highly Finished Wing (King Cobra). R.A.E. Report 2383, Jun. 1950.

39. Spee, B. M.: Investigations on the Transonic Flow Around Airfoils. NLR TR-6912225, Mar. 1971.

40. Carmichael, B. H.: Surface Waviness Criteria for Swept and Unswept Laminar Suction Wings. Northrop Rpt. NOR-59-438, 1959.

41. Carmichael, B. H.: Surface Imperfection Experiments on a Swept Laminar Suction Wing. Northrop Rpt. BLC-124, NOR-59-454, 1959.

42. Newman, P. A.; Kemp, W. B.; and Garriz, J. A.: Wall Interference Assessment and Correlations. Transonic Symposium: Theory, Application, and Experiment. NASA CP-3020, 1989, pp. 817-852.

43. Pfenninger, W.; Gross, Lloyd; and Bacon, John W., Jr.: Experiments on a 30° Swept 12-Percent Thick Symmetrical Laminar Suction Wing in the 5- by 7-Foot Michigan Tunnel. Rep. NAI-57-317 (BLC-93), Northrop Aircraft Inc., Feb. 1957.

44. Newman, Perry A.; Anderson, E. Clay; and Peterson, John B, Jr.: Aerodynamic Design of the Contoured Wind Tunnel Liner for the NASA Supercritical Laminar Flow Control, Swept Wing Experiment. NASA TP-2335, Sept. 1984.

45. Dagenhart, J. Ray; and Stack, John P.: Boundary-Layer Transition Detection Using Flush-Mounted Hot-Film Gages and Semiconductor Dynamic Pressure Transducers. AIAA Paper 82-0593, Mar. 1982.

46. Stack, John P.; Mangalam, Siva M.; and Kalburgi, Vijay: The Phase Reversal Phenomena at Flow Separation and Reattachment. AIAA 88-0408, Jan. 1988.

47. Bobbitt, P. J.: Instrumentation Advances for Transonic Testing. Transonic Symposium, NASA Langley Research Center, Hampton, VA, April 19-21, 1988.

48. Harris, Charles D.; and Brooks, Cuyler, W.: Modifications to the Langley 8-Foot Transonic Pressure Tunnel for the Laminar Flow Control Experiment. NASA TM-4032, 1988.

49. Lee, J. D.; Gregorek, G. M.; and Korkan, K. D.: Testing Techniques and Interference Evaluation in the OSU Transonic Airfoil Facility. AIAA 78-1118, Jul. 1978.

50. Bauer, F.; Garabedian, P.; Korn, D.; and Jameson, A.: Supercritical Wing Sections II. Volume 108 of Lecture Notes in Economics and Mathematical Systems, Springer-Verlag, 1975.

51. Lachman, G. V. (editor): Boundary Layer and Flow Control. Vol. II, Pergamon Press, 1961.

52. Pfenninger, W.; and Growth, E.: Low Drag Boundary Layer Suction Experiments in Flight on a Wing Glove of an F-94A Airplane with Suction Through a Large Number of Fine Slots. Boundary Layer and Flow Control, vol. 2, G. V. Lachmann, ed., 1961, pp. 981-999.

53. Fowell, L. R.; and Antonatos, P. P.: Laminar Flow Control Flight Test Results, Some Results from the X-21A Program. Recent Developments in Boundary Layer Research, Part IV, May 1965. AGARDograph 97, pp. 1-76.

54. Maddalon, Dal V.: Design and Fabrication of Large Suction Panels with Perforated Surfaces for Laminar Flow Control Testing in a Transonic Wind Tunnel. NASA TM-89011, Aug. 1986.

55. Whites, R. C.; Sudderth, R. W.; and Wheldon, W. G.: Laminar Flow Control on the X-21. Astronautics and Aeronautics, Jul. 1966, pp. 38-43.

56. Goradia, S. H.; Bobbitt, P. J.; Ferris, J. C.; and Harvey, W. D.: Theoretical Investigations and Correlative Studies for NLF, HLFC, and LFC Swept Wings at Subsonic, Transonic, and Supersonic Speeds. SAE Paper 871861, Oct. 1987.

57. Van Ingen, J. L.; Blom, J. J. H.; and Goei, J. H.: Design Studies of Thick Laminar Flow Airfoils for Low-Speed Flight Employing Turbulent Boundary-Layer Suction Over the Rear Part. AGARD CP-365, May 1984.

58. Klebanoff, P. S.; and Tidstron, K. D.: Evolution of Amplified Waves Leading to Transition in a Boundary Layer with Zero Pressure Gradient. NASA TN D-195, 1958.

59. Srokowski, A. J.; and Orszag, S. A.: Mass Flow Requirements for LFC Wing Design. AIAA Paper 77-1222, Aug. 1977.

60. Malik, M. R.; and Orszag, S. A.: Efficient Computation of the Stability of Three-Dimensional Compressible Boundary Layers. AIAA Paper 81-1277, Jun. 1981.

61. Mack, L. M.: Transition Prediction and Linear Stability Theory. AGARD CP-224, Jan. 1970.

62. Berry, Scott A.; Dagenhart, J. Ray; Viken, Jeffery K.; and Yeaton, Robert B.: Boundary-Layer Stability Analysis of NLF and LFC Experimental Data at Subsonic and Transonic Speeds. SAE TPS-871859, Oct. 1987.

63. Vijgen, P. M. H. W.; Dodbele, S. S.; Pfenninger, W.; and Holmes, B. T.: Analysis of Wind Tunnel Boundary-Layer Transition Experiments on Axisymmetric Bodies at Transonic Speeds Using Compressible Boundary-Layer Stability Theory. AIAA 88-0008, Jan. 1988.

64. Hefner, J. N.; and Bushnell, D. M.: Application of Stability Theory to Laminar Flow Control. AIAA Paper 79-1493, Jul. 1979.

65. Runyan, L. J.; Navran, B. H.; and Rozendaal, R. A.: F-111 Natural Laminar Flow Glove Flight Test Data Analysis and Boundary Layer Stability Analysis. NASA CR-166051, 1984.

66. Runyan, L. James: Boundary Layer Stability Analysis of a Natural Laminar Flow Glove on the F-111 Tact Airplane. Symposium on Viscous Drag Reduction, Dallas, Texas, Nov. 7-8, 1979.

67. Croom, Cynthia C.; Manuel, Gregory S.; and Stack, John P.: In-Flight Detection of Tollmien-Schlichting Instabilities in Laminar Flow. SAE Paper 871016, Apr. 1987.

68. Boeing Commercial Airplane Company: Flight Survey of the 757 Wing Noise Field and Its Effects on Laminar Boundary Layer Transition. Vols. I and II. NASA CR-178216, 1987.

69. Rozendaal, R. A.: Natural Laminar Flow Flight Experiments on a Swept Wing Business Jet - Boundary Layer Stability Analysis. NASA CR-3975, May 1986.

70. Rozendaal, R. A.: Variable-Sweep Transition Flight Experiment (VSTFE) Stability Code Development and Clean-Up Glove Data Analysis. NASA CP-2487, March 1987.

71. Mack, L. M.: Transition and Laminar Instability. JPL Publication 77-15, 1977.

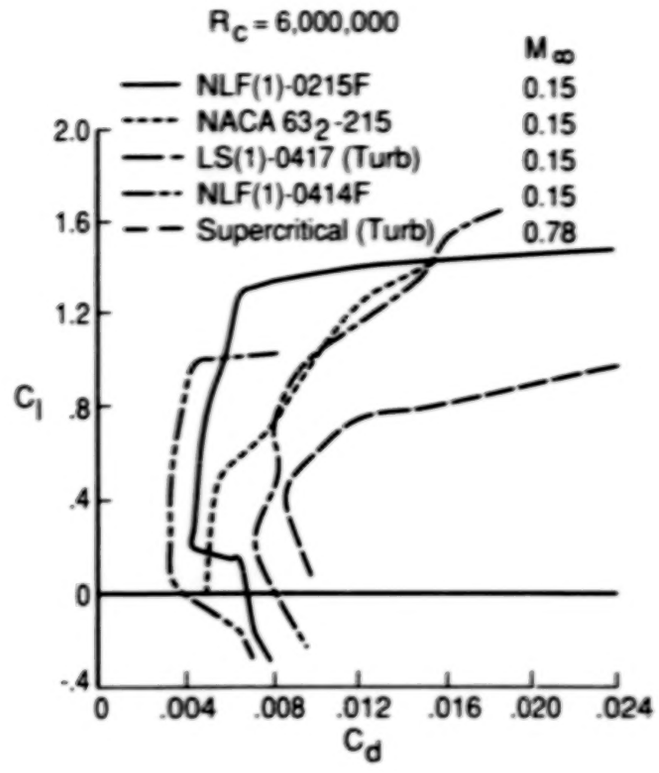

Figure 1. Comparison of drag polars on airfoils at low and high speeds with and without flap deflection.

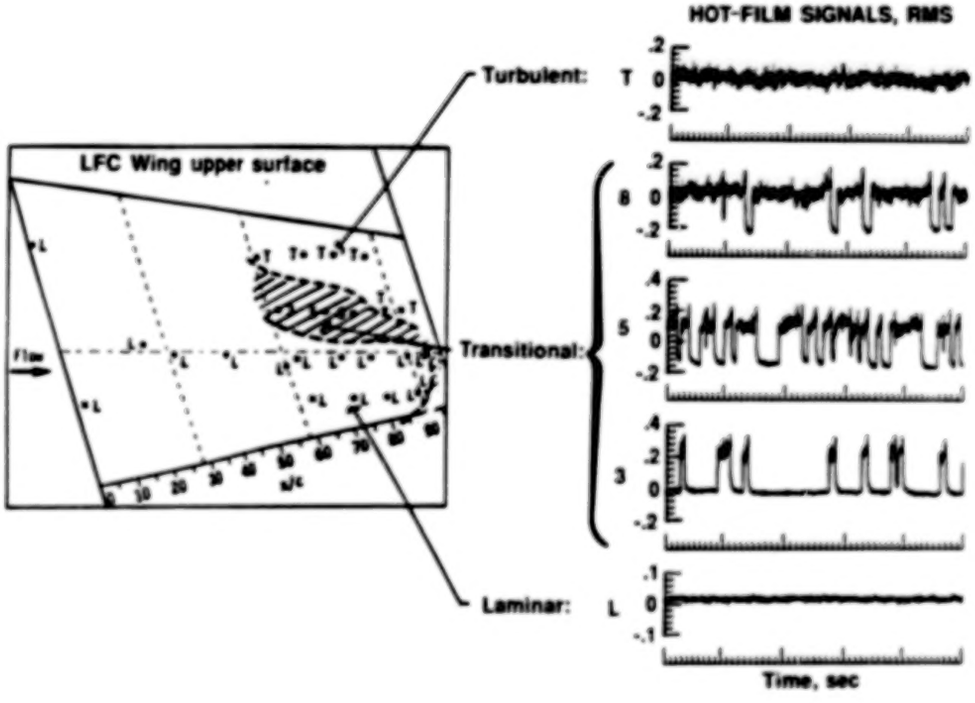

Figure 2. An example of flush-mounted surface hot-film gage locations, RMS output signals, and laminar pattern.

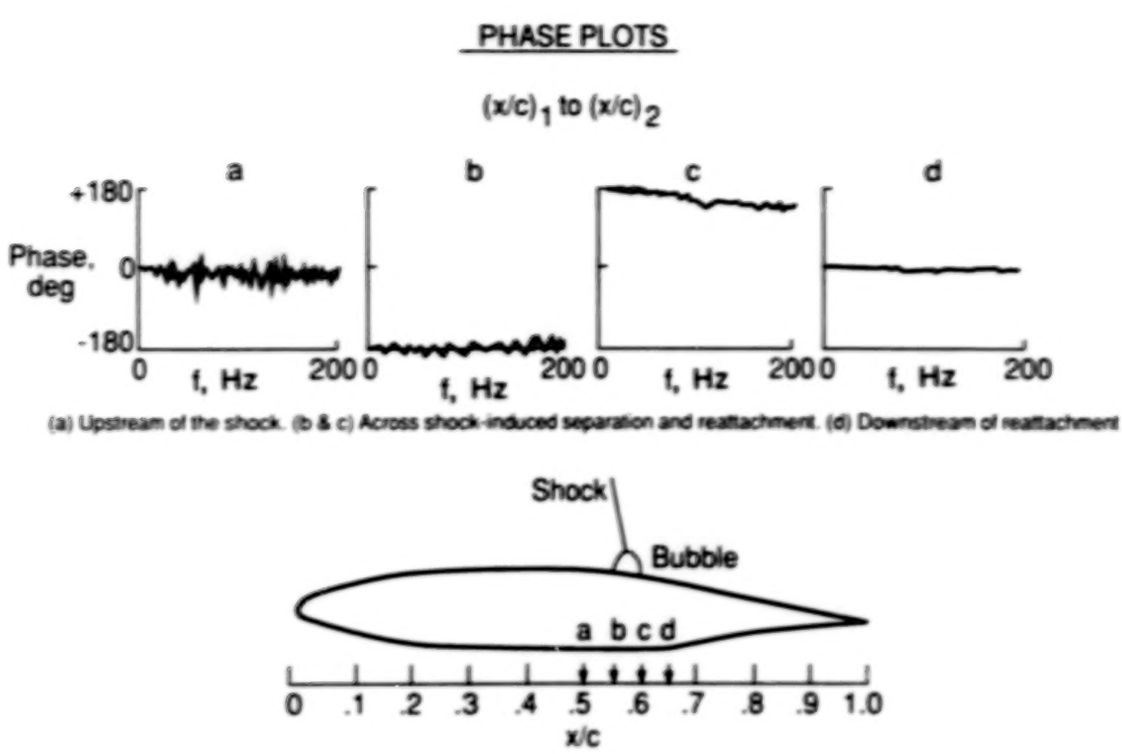

Figure 3. Example of multielement dynamic shear stress sensor detection of shock-induced separation by phase reversal.

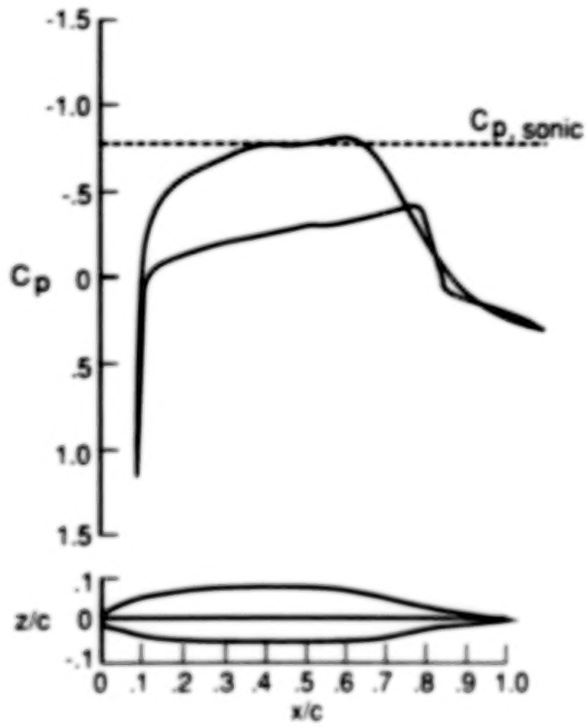

Figure 4. Design theoretical pressure distribution and geometry for HSNLF(1)-0213 airfoil. $M_\infty = .7$, $C_L = .26$, $R_c = 11 \times 10^6$, $\Lambda = 0°$.

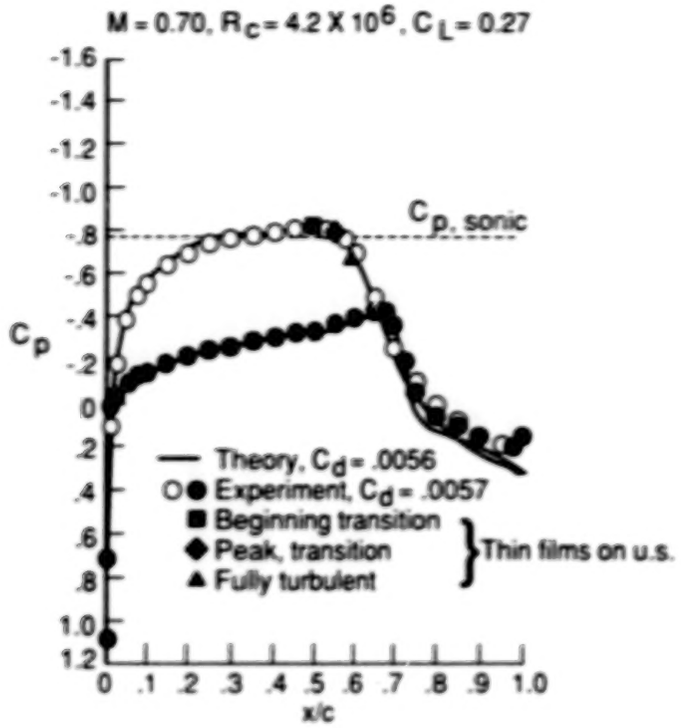

Figure 5. Comparison of experimental and theoretical pressure distributions for HSNLF(1)-0213 airfoil.

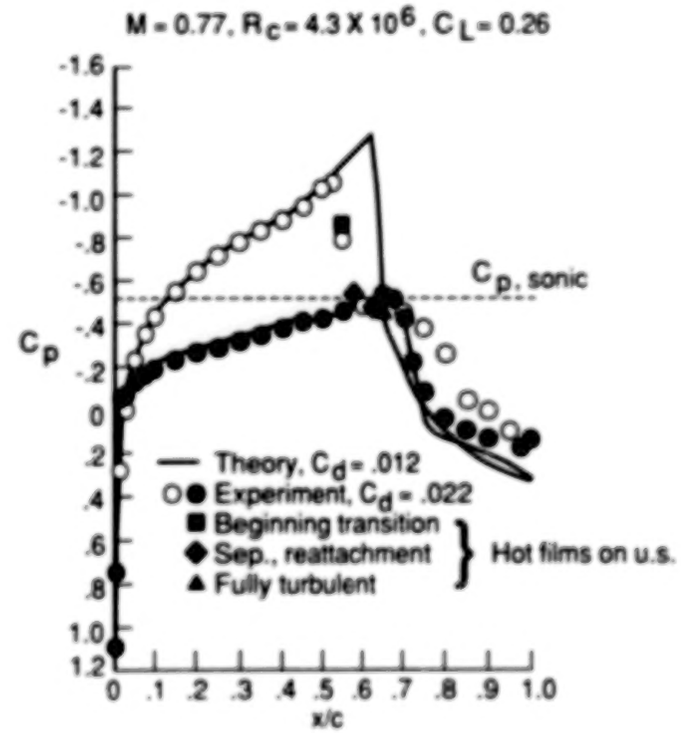

Figure 6. Comparison of experimental and theoretical pressure distributions for HSNLF(1)-0213 airfoil at off-design conditions.

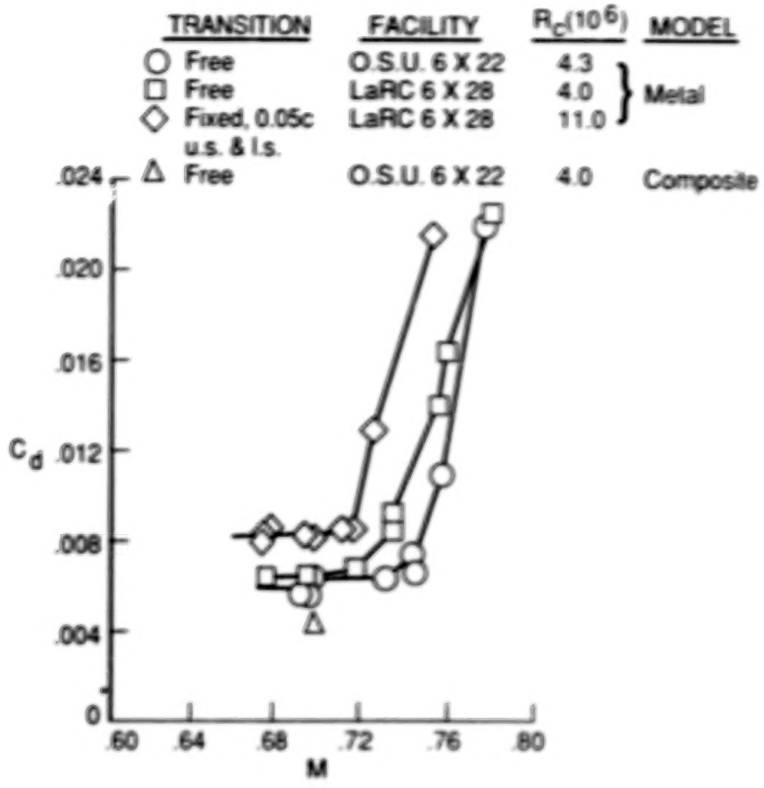

Figure 7. Effect of Mach number on drag coefficient for the HSNLF(1)-0213 airfoil in two different wind tunnels at zero angle of attack.

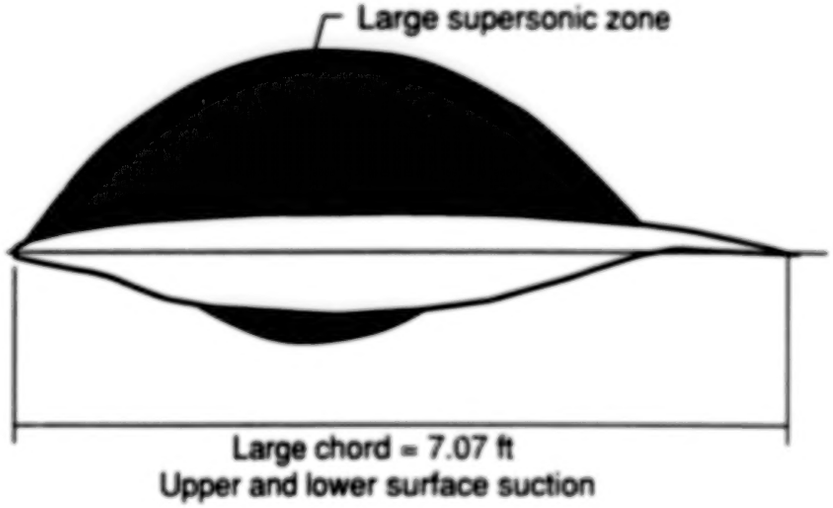

FREE-STREAM DESIGN CONDITIONS	DESIGN CONDITIONS NORMAL TO LEADING EDGE
$M_\infty = 0.82$	$M_\infty = 0.755$
$\Lambda = 23^0$	$c_N = 6.508$ ft
$c = 7.07$ ft	$R_{c,N} = 16.9 \times 10^6$
$R_c = 20 \times 10^6$	$(t/c)_N = 13.0$ percent
$C_l = 0.47$	$C_{l,N} = 0.55$

Figure 8. Schematic of swept SCLFC(1)-0513F airfoil, sonic zones, and design conditions.

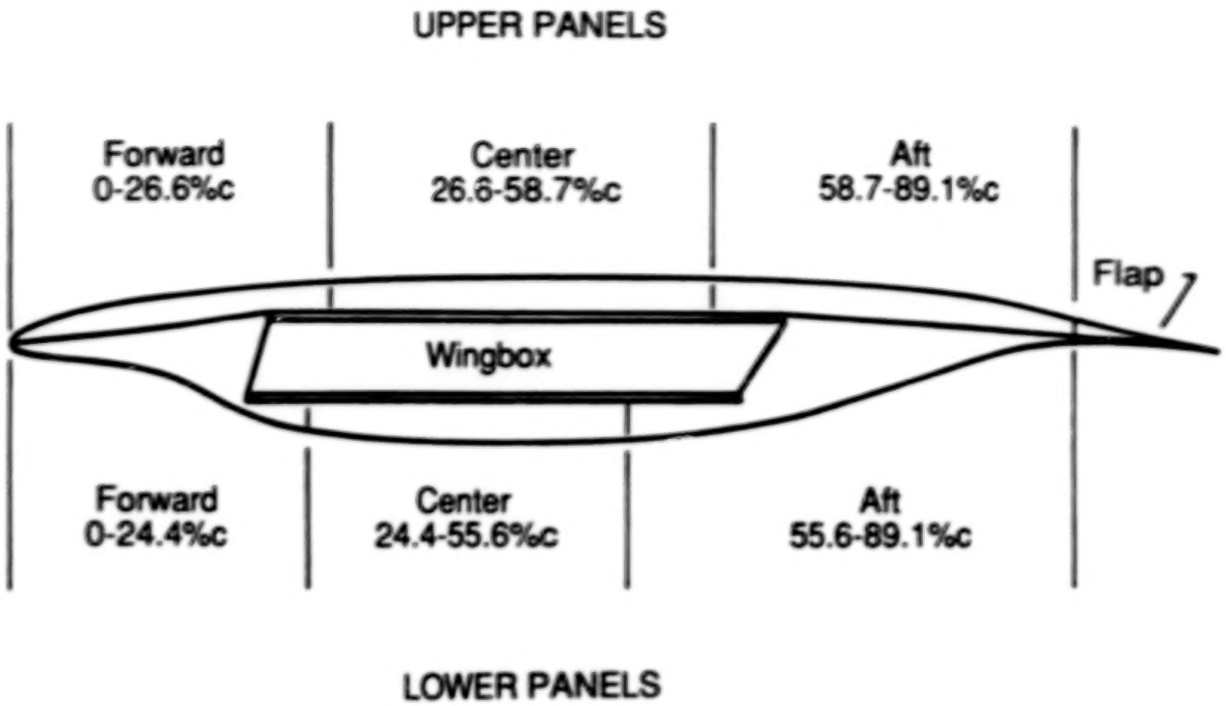

Figure 9. Schematic of SCLFC(1)-0513F airfoil wingbox and suction panel assembly.

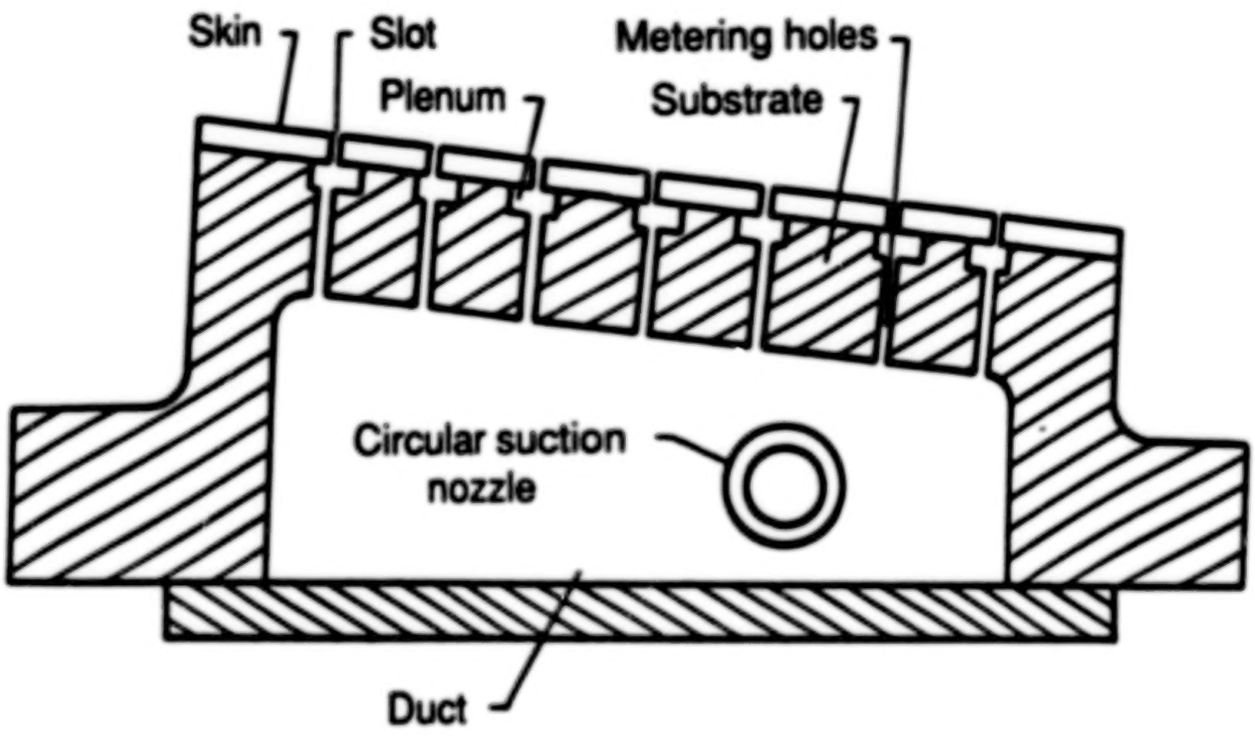

Figure 10. Schematic section of slotted suction surface panel concept.

(a) View looking downstream at model leading edge and upper surface.

Figure 11. Photograph of swept supercritical LFC airfoil model and contoured wall liner in the Langley 8-Foot Transonic Pressure Tunnel.

ORIGINAL PAGE
BLACK AND WHITE PHOTOGRAPH

ORIGINAL PAGE IS
OF POOR QUALITY

ORIGINAL PAGE IS
OF POOR QUALITY

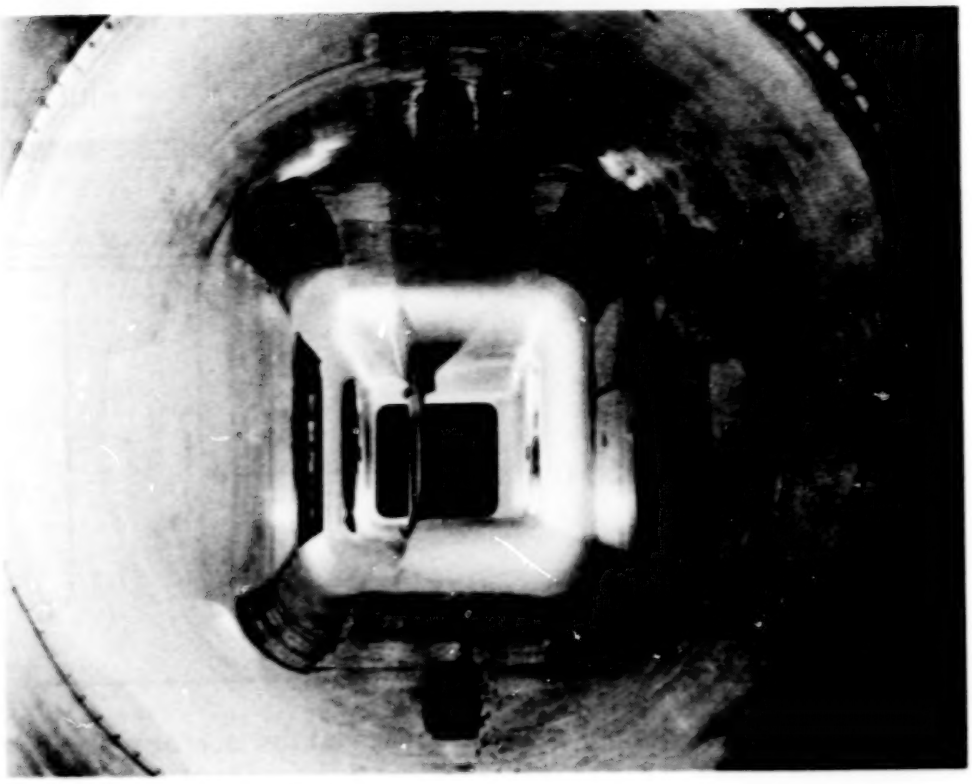

(b) View looking upstream at model trailing edge and liner step.

Figure 11. Concluded.

ORIGINAL PAGE
BLACK AND WHITE PHOTOGRAPH

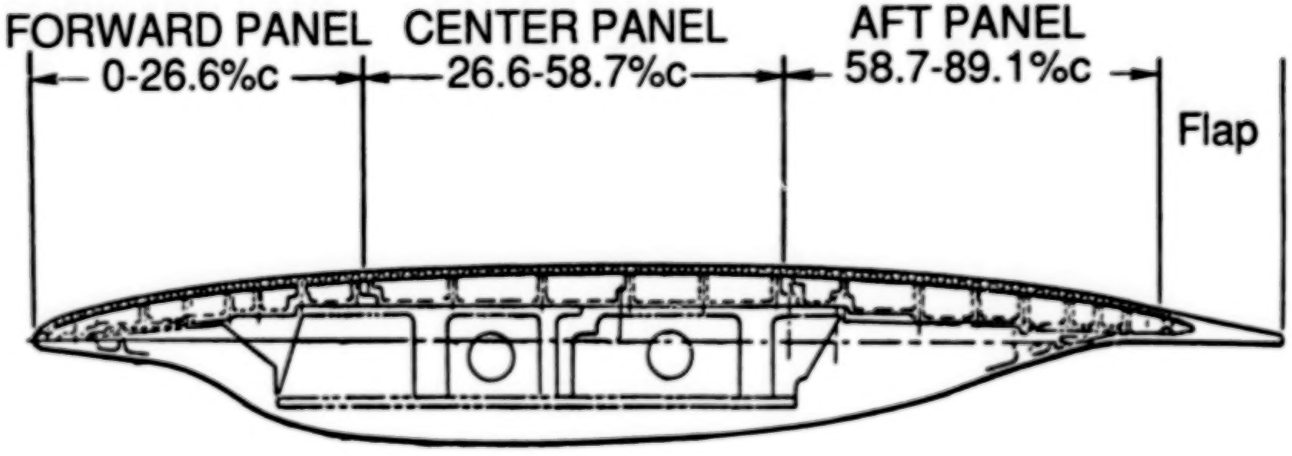

Figure 12. Schematic of LFC airfoil model with porous upper surface panels.

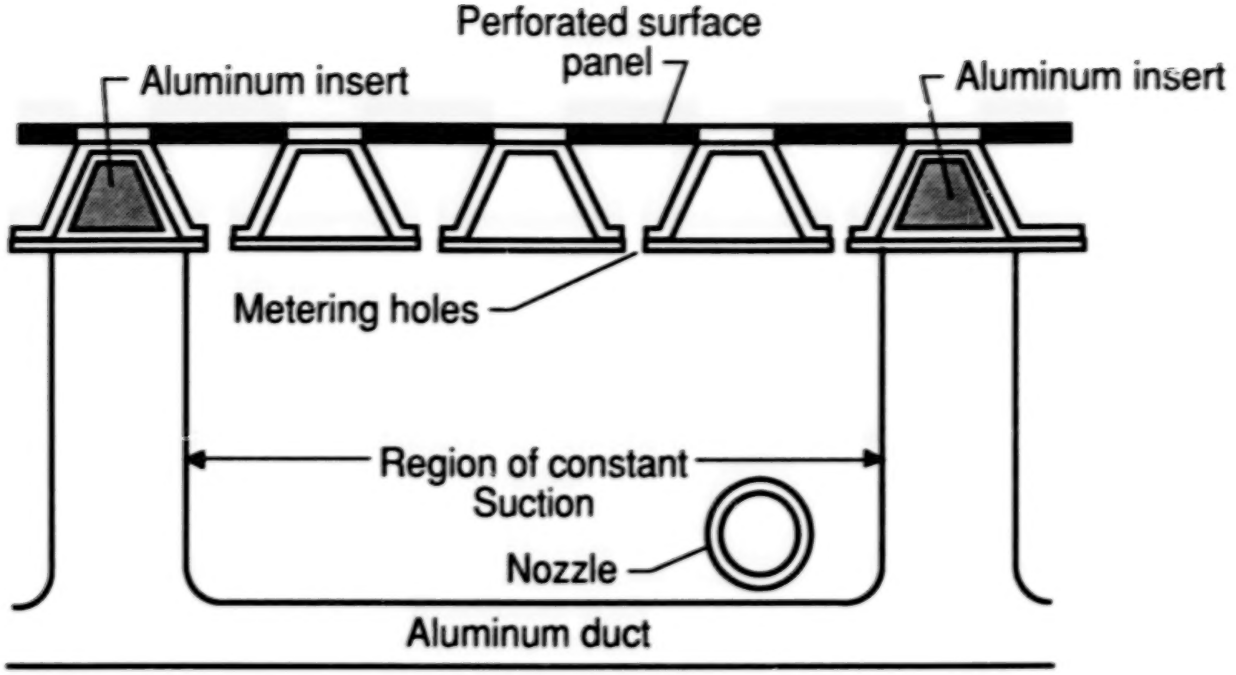

Figure 13. Schematic section of perforated suction surface panel concept.

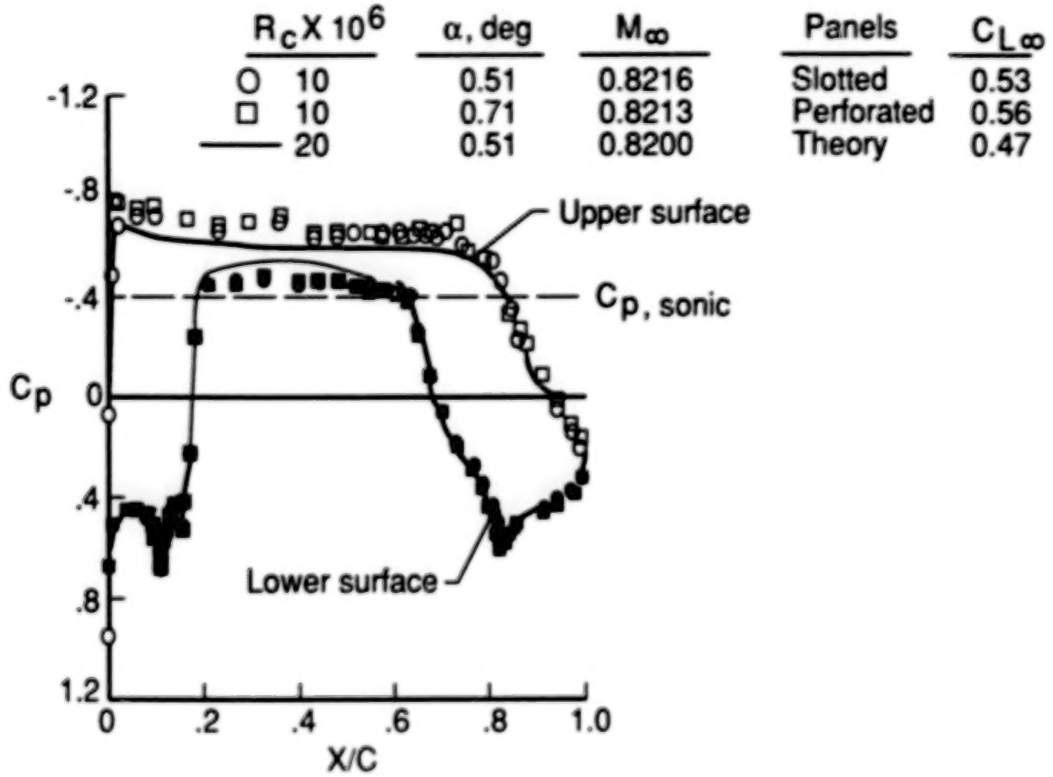

Figure 14. Comparison of experimental and theoretical pressure distributions for SCLFC(1)-0513F airfoil with slotted and perforated surface.

$R_c = 10 \times 10^6$.

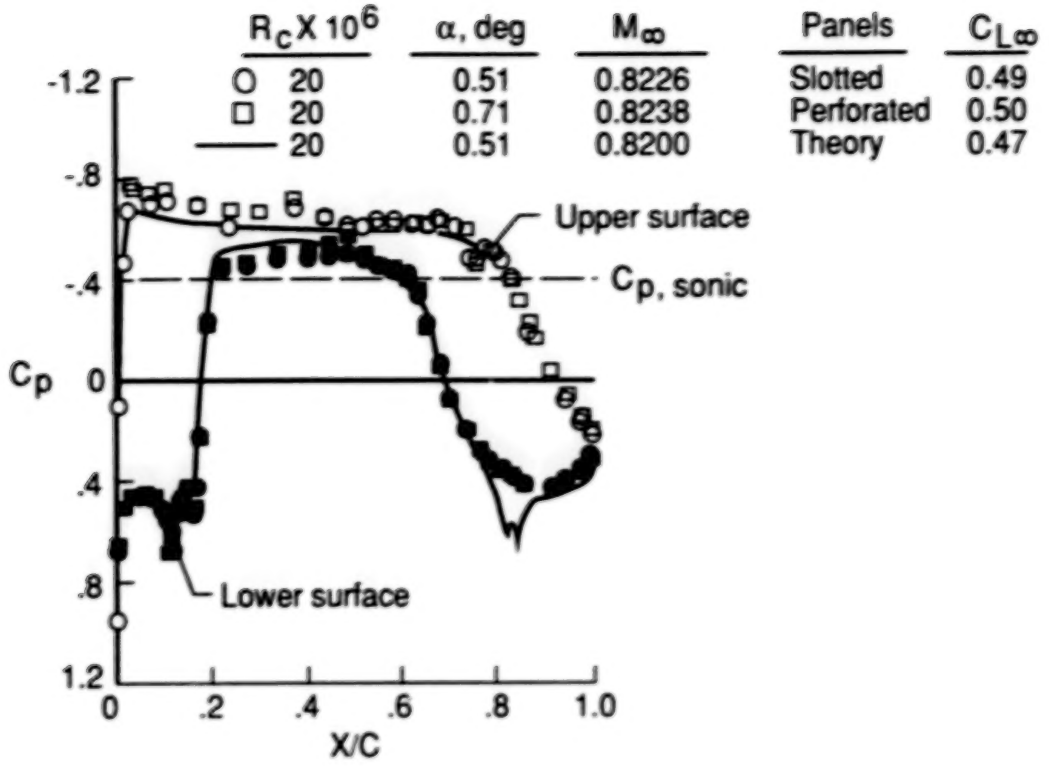

Figure 15. Comparison of experimental and theoretical pressure distributions for SCLFC(1)-0513F airfoil with slotted and perforated surfaces.
$R_c = 20 \times 10^6$.

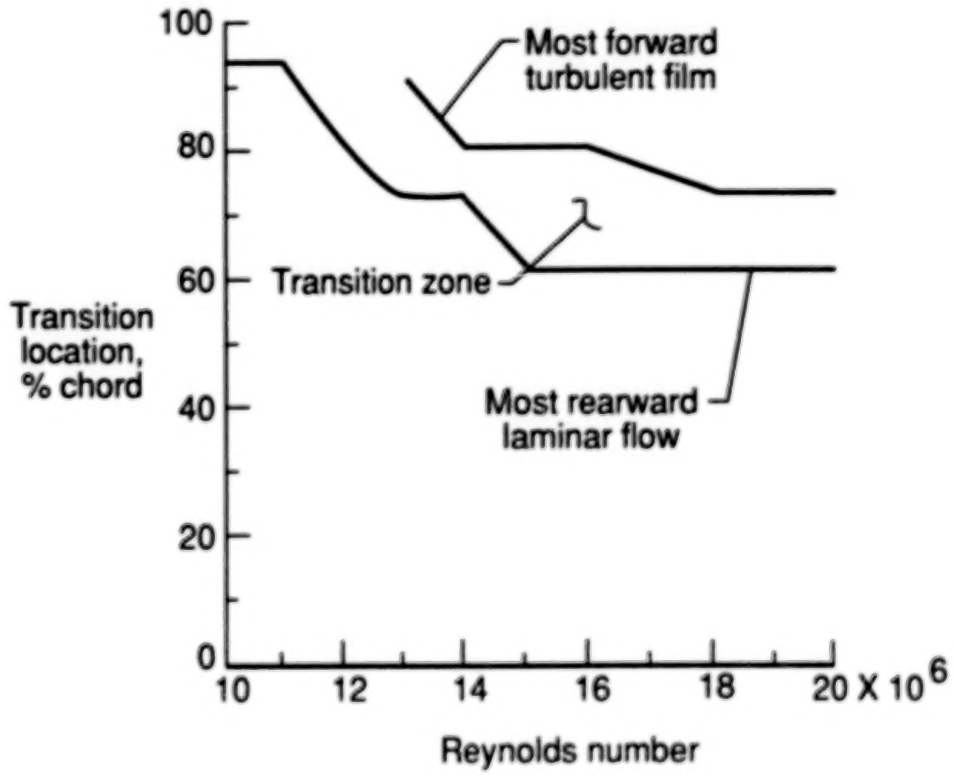

Figure 16. Measured transition location on upper surface of slotted SCLFC(1)-0513F airfoil. $M_\infty = 0.82$.

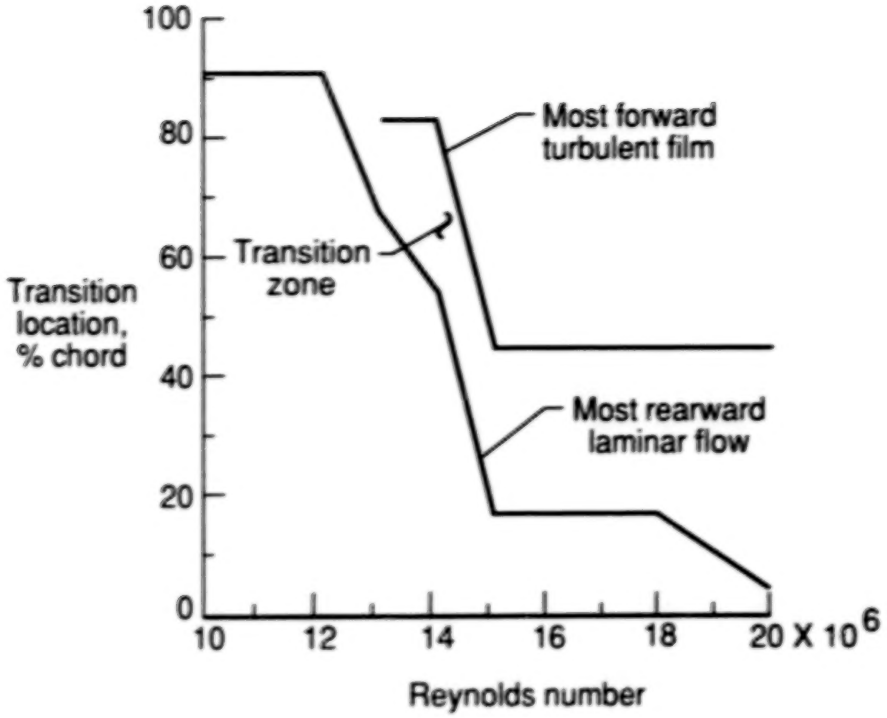

Figure 17. Measured transition location on lower surface of slotted SCLFC(1)-0513F airfoil. M = 0.82.

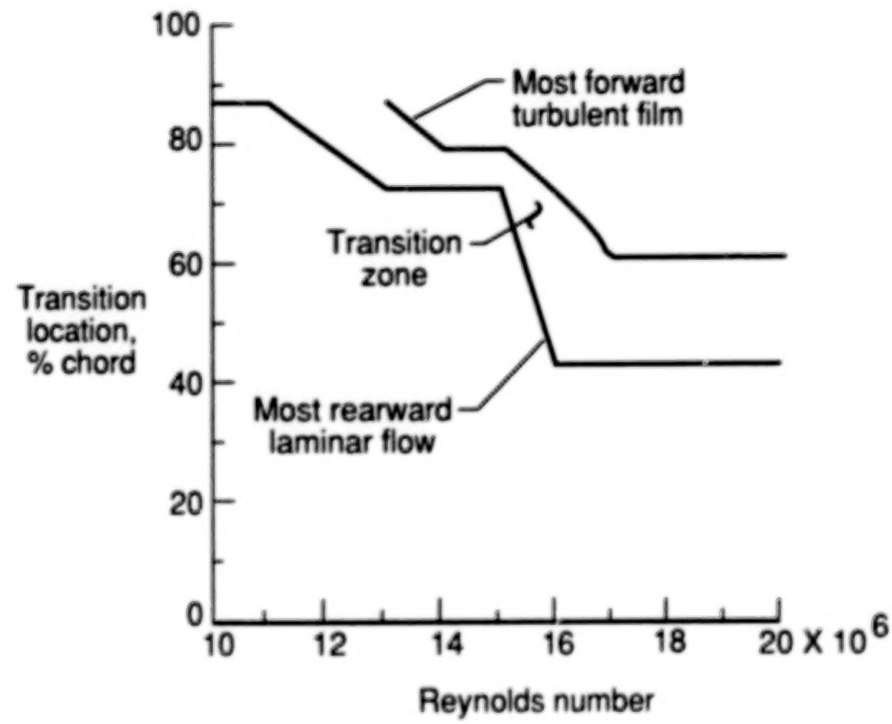

Figure 18. Measured transition location on upper surface of perforated SCLFC(1)-0513F airfoil. M_∞ = 0.82.

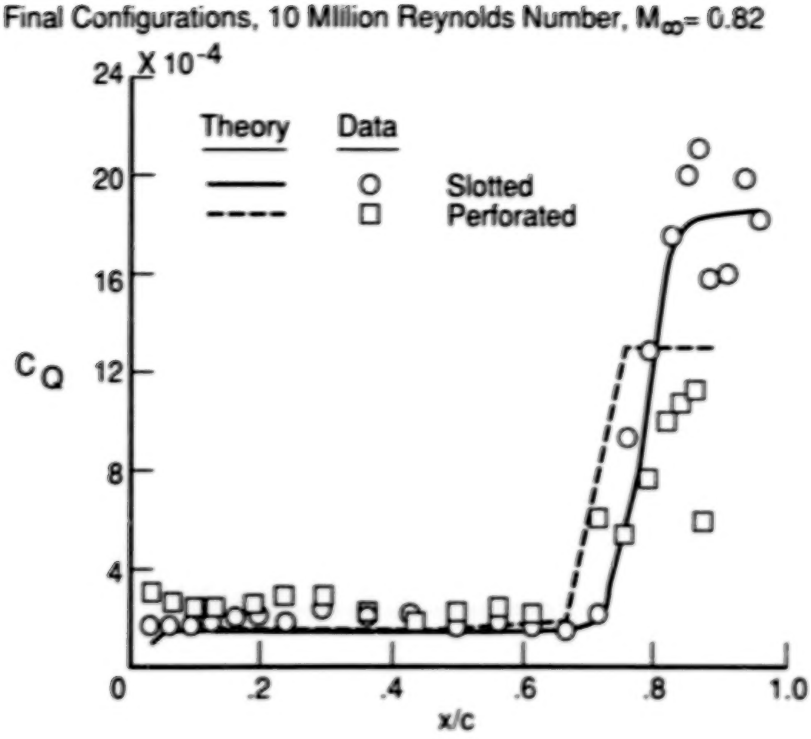

Figure 19. Comparison of experimental and theoretical suction distributions on upper surface of slotted and perforated SCLFC(1)-0513F airfoil models. M_∞ = 0.82, R_c = 10 x 10^6.

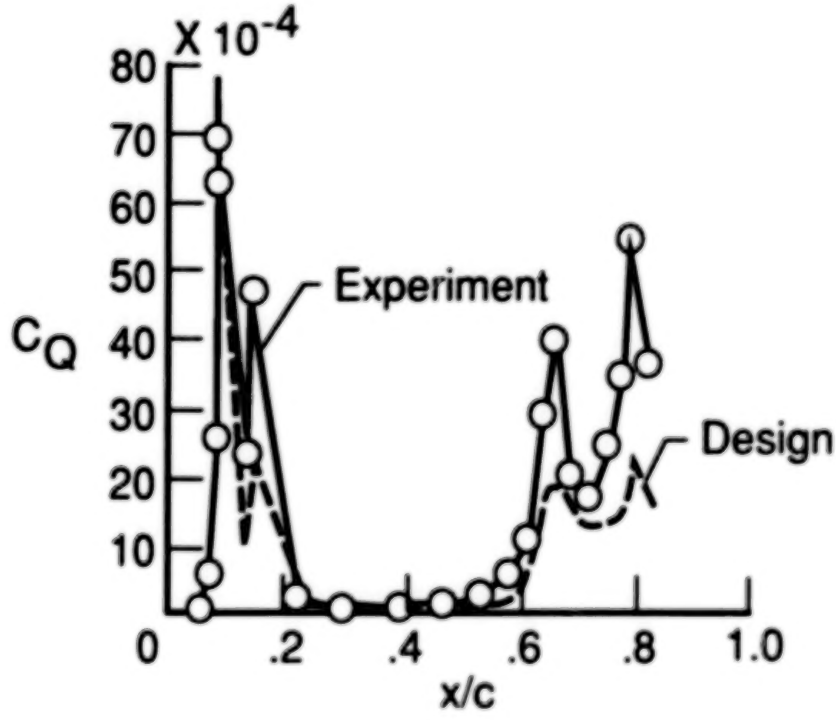

Figure 20. Comparison of experimental and theoretical suction distributions on the lower surface of slotted SCLFC(1)-0513 airfoil model. M_∞ = 0.82, R_c = 10 x 10^6.

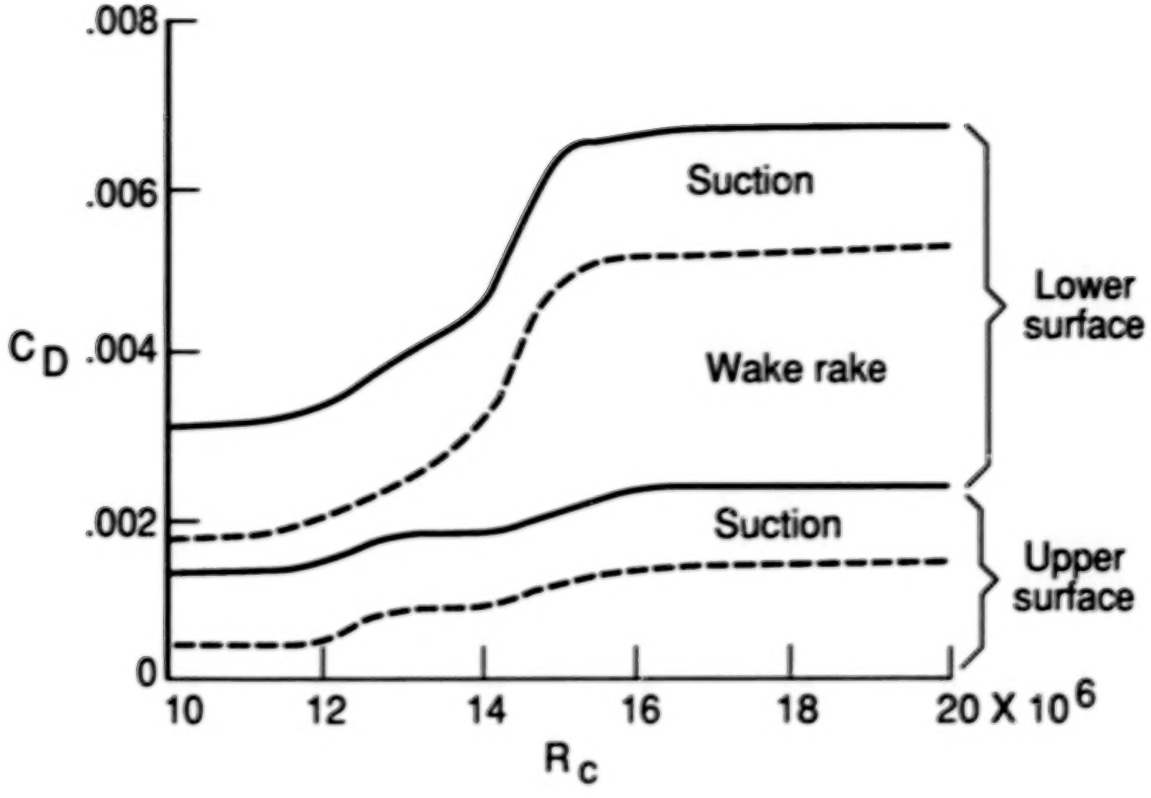

Figure 21. Measured variation of drag with chord Reynolds number on SCLFC(1)-0513F airfoil with slotted suction surface. M_∞ = 0.82.

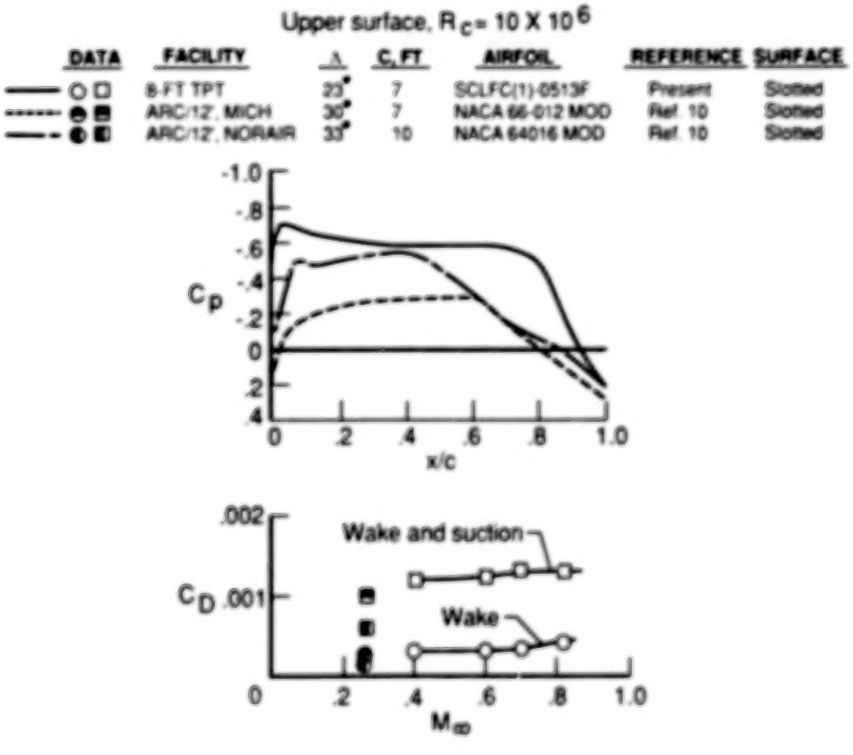

Figure 22. Comparison of measured pressure distributions and total drag for upper surface only on LFC wind tunnel models over speed range.

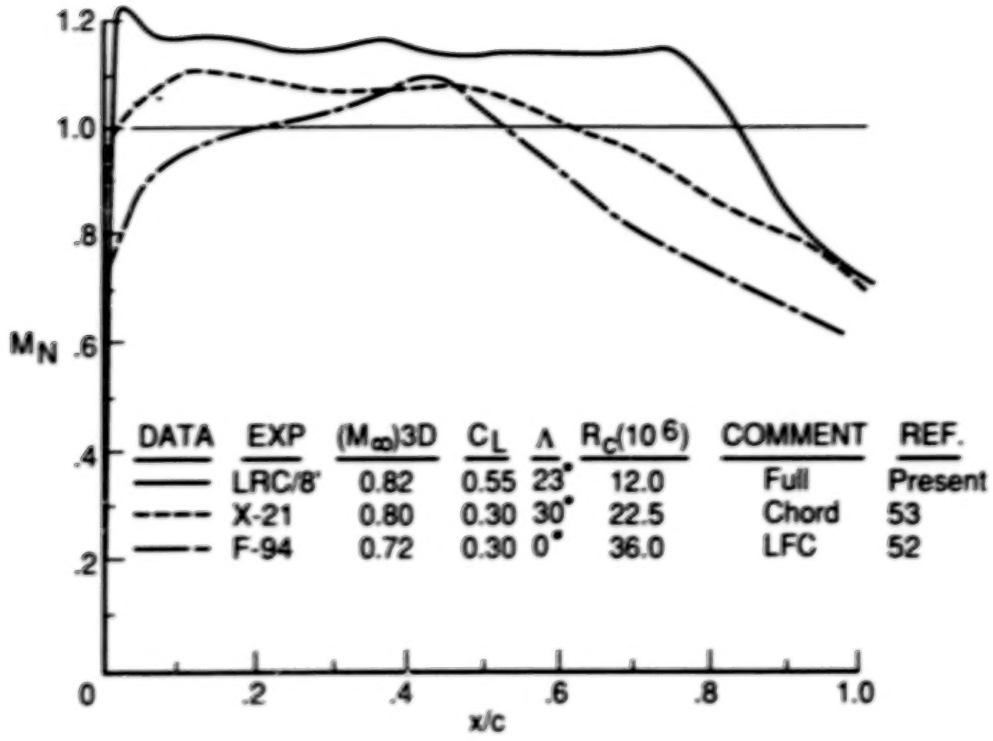

Figure 23. Comparison of measured local Mach number distributions on upper surface of wind tunnel and flight LFC wings at transonic speeds.

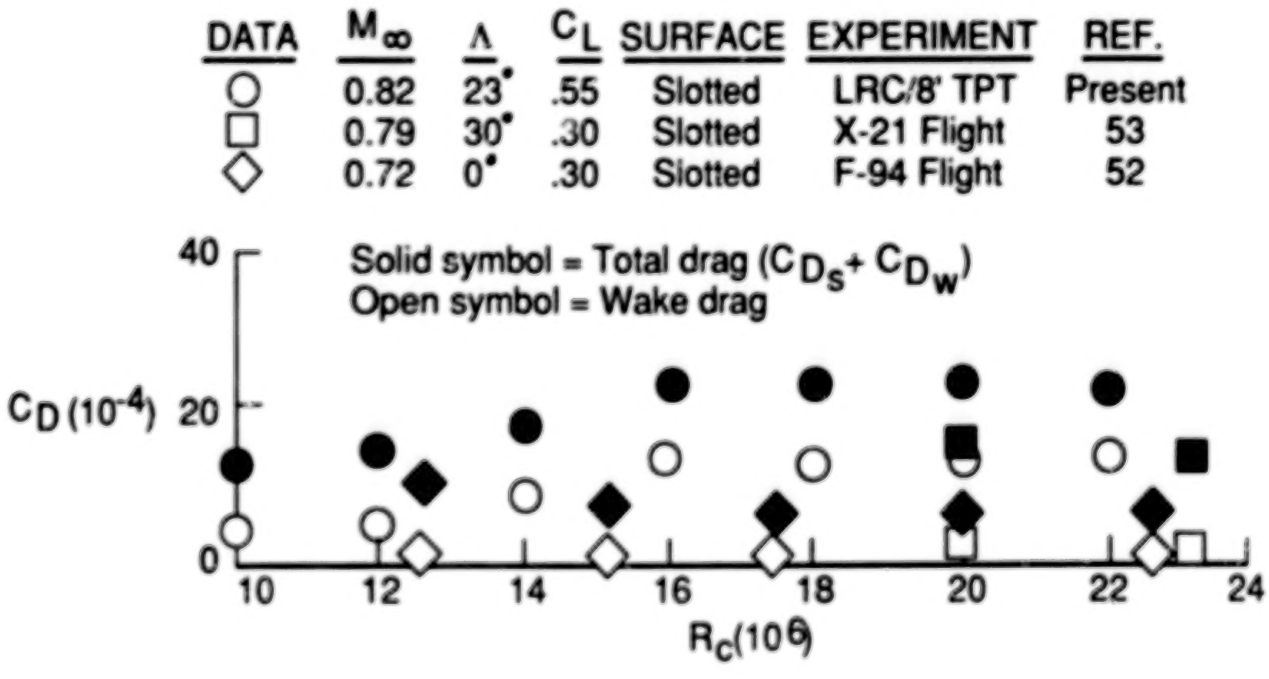

Figure 24. Comparison of drag coefficients for upper surface of swept and unswept transonic suction wings.

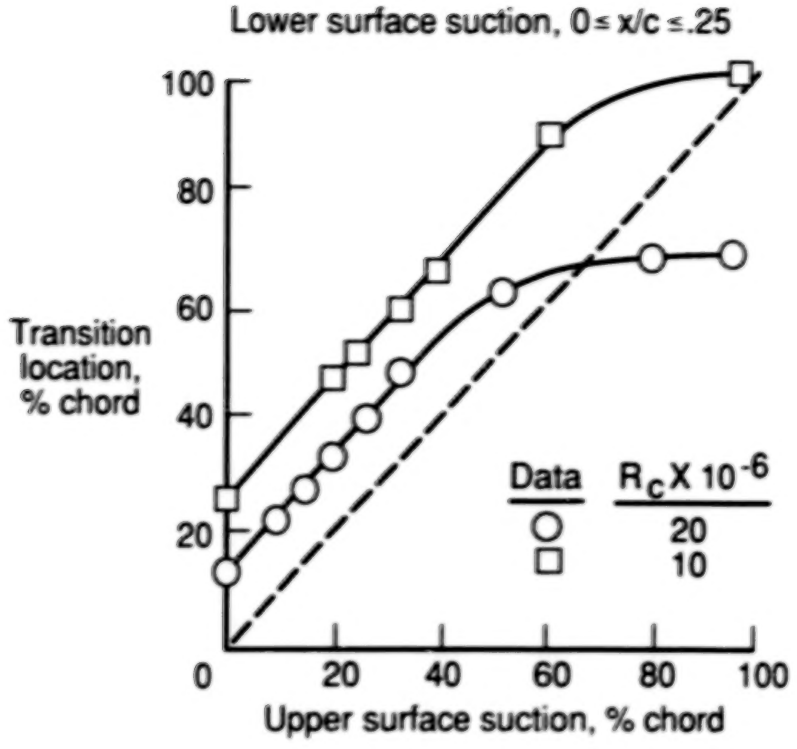

Figure 25. Variation of measured transition for simulated hybrid LFC on swept SCLFC(1)-0513F airfoil with slotted upper surface.

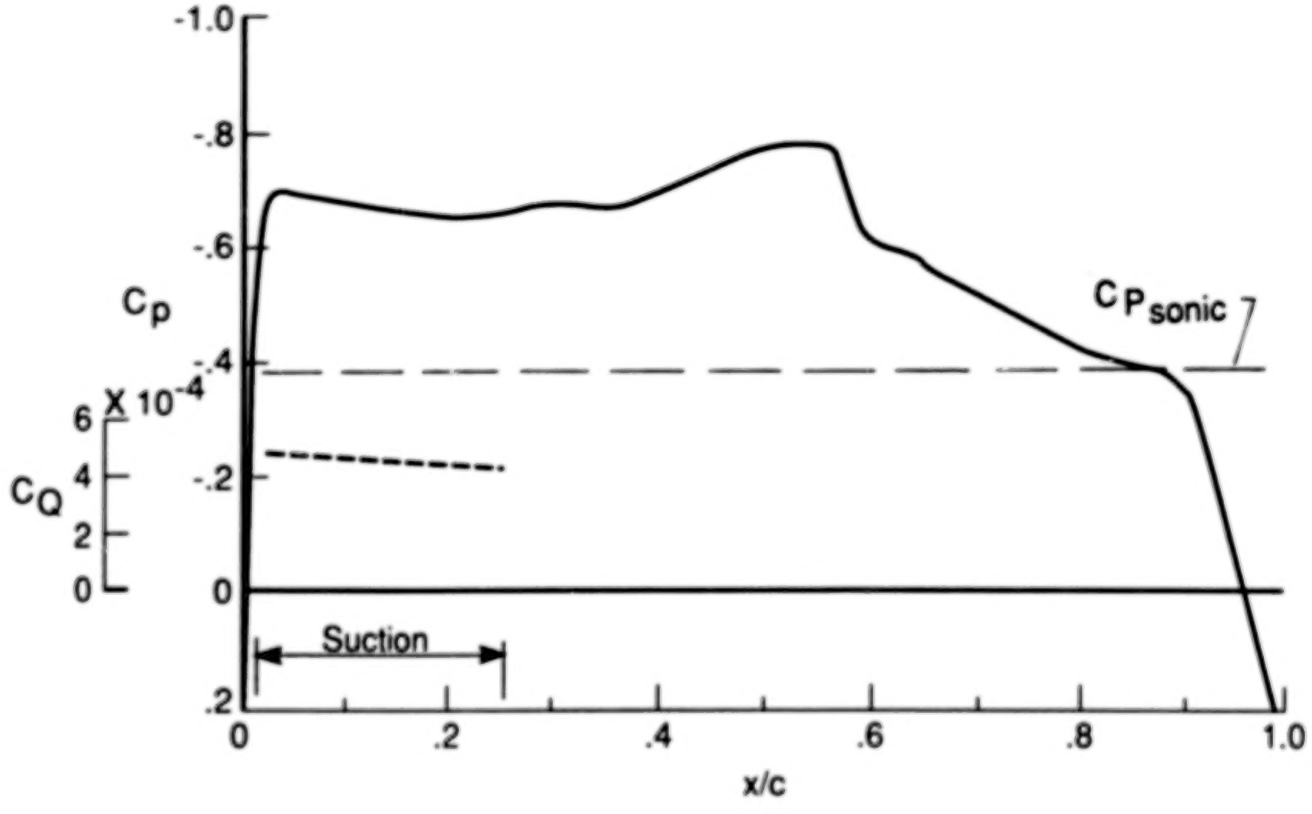

Figure 26. Design theoretical pressure and suction distributions on upper surface of hybrid LFC airfoil. $M_\infty = 0.811$, $C_L = 0.47$, $R_c = 15 \times 10^6$, $\Lambda = 23°$.

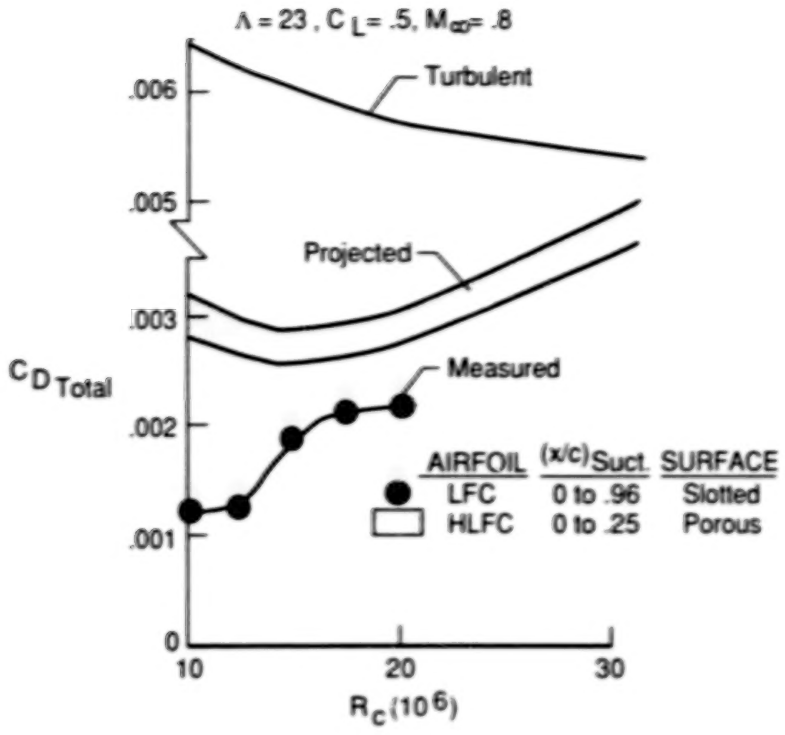

Figure 27. Measured and projected effect of suction extent on drag for LFC and HLFC airfoil upper surface.

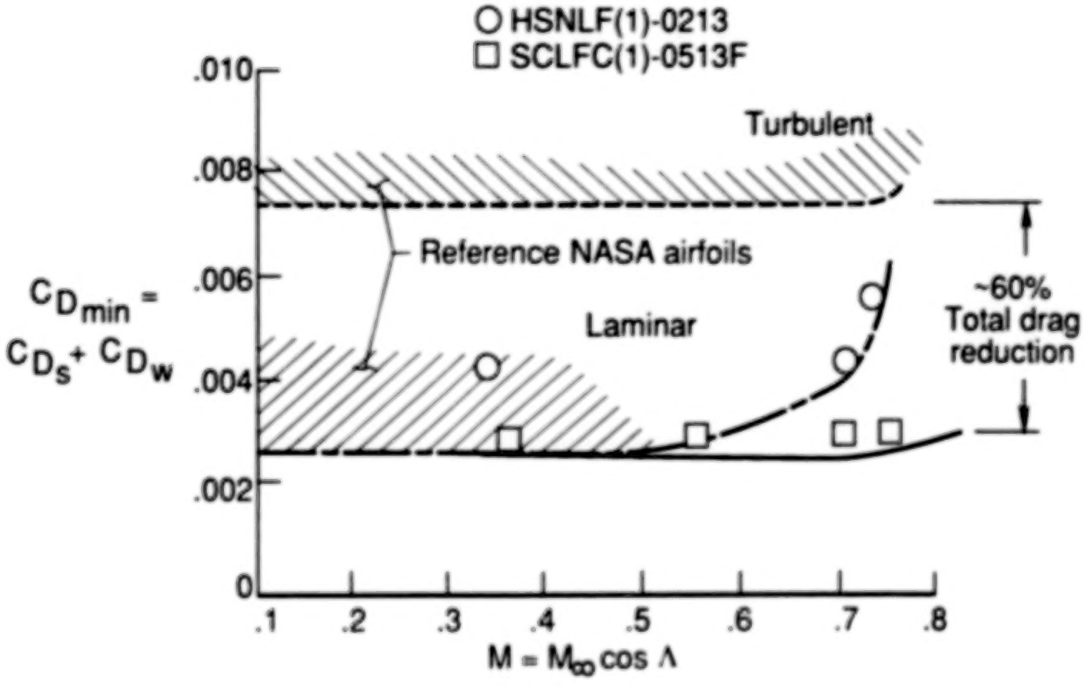

Figure 28. Comparison of measured minimum drag on NASA advanced low-drag airfoils, with and without suction, at transonic speeds with previous results (hatched areas).

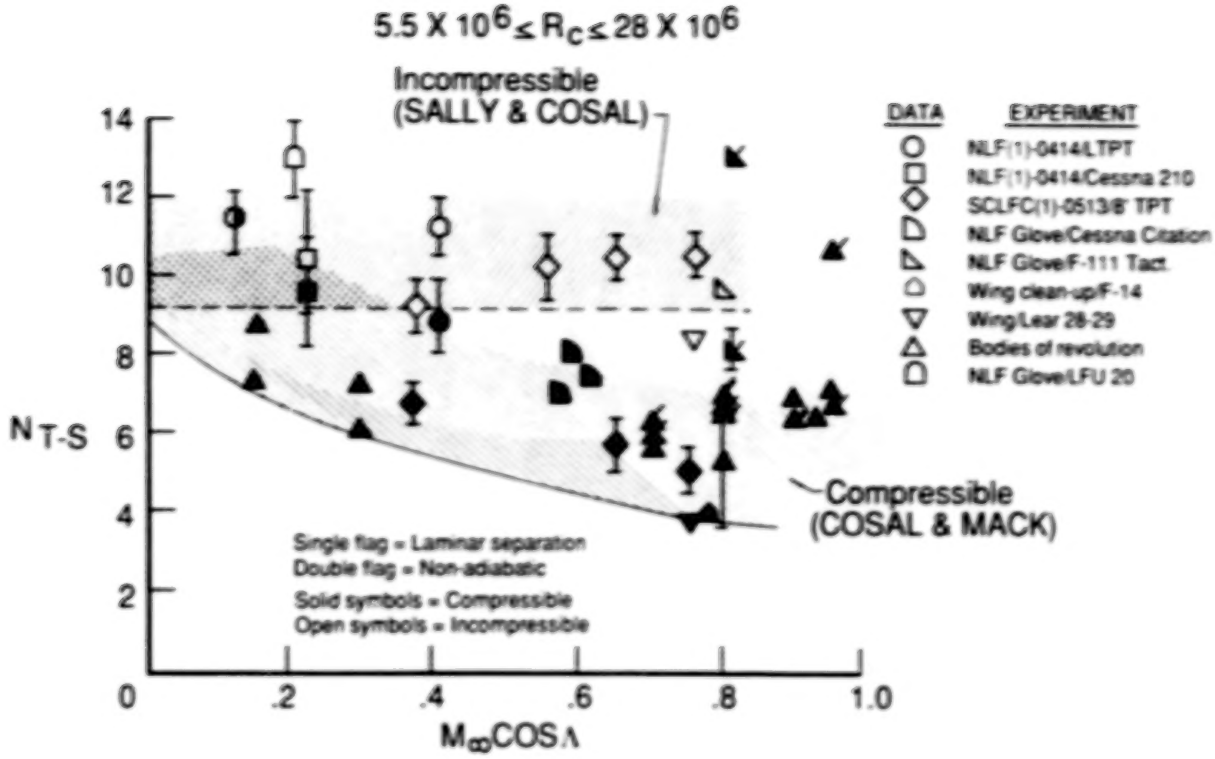

Figure 29. Minimum allowable Tollmien-Schlichting disturbance amplification N-factors at measured transition.

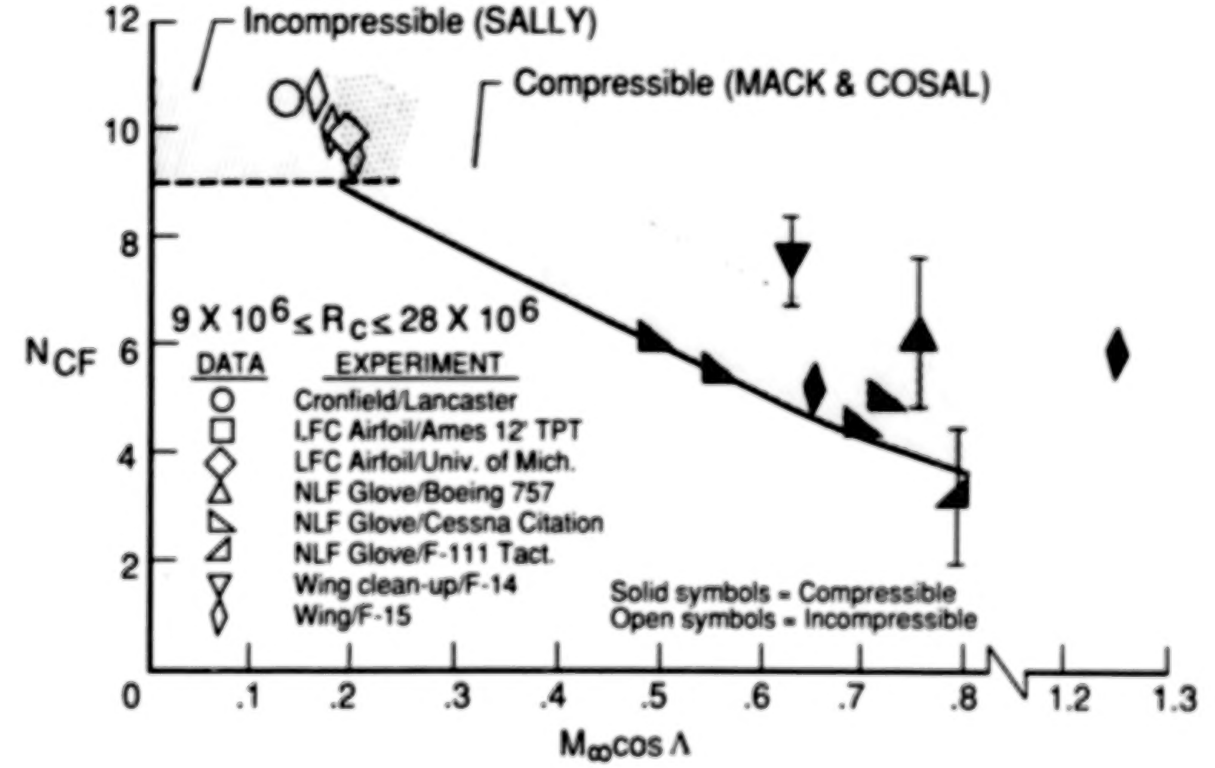

Figure 30. Minimum allowable crossflow disturbance amplification N-factors at measured transition.

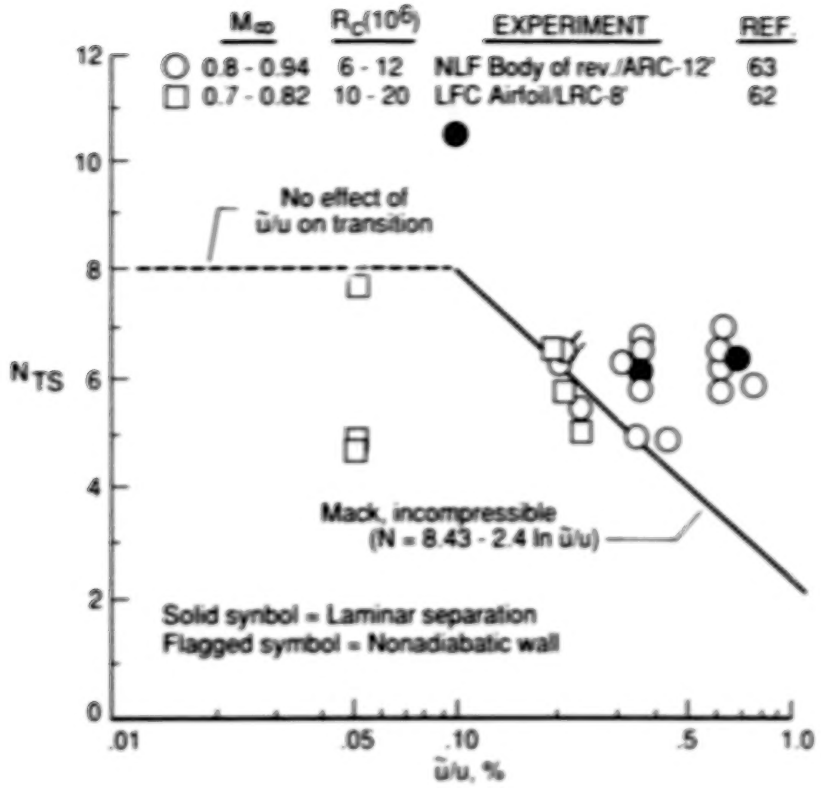

Figure 31. Variation of compressible N-factors at transition with turbulence level.

N91-24137

COMPUTATIONAL SUPPORT OF THE X-29A ADVANCED TECHNOLOGY DEMONSTRATOR FLIGHT EXPERIMENT

55-05
19352

E. G. Waggoner
NASA Langley Research Center
Hampton, Virginia

B. L. Bates
Vigyan Research Associates, Inc.
Hampton, Virginia

INTRODUCTION

The X-29A Advanced Technology Demonstrator, figure 1, has been designed and developed to demonstrate the advantages of forward wing sweep along with other advanced technologies. Grumman Aerospace Corporation designed and fabricated the flight vehicle under a contract sponsored by the Defense Advanced Research Projects Agency and managed by the Air Force. A number of advanced technologies have been incorporated into the design. These include, in addition to the obvious forward-swept wing, a closely coupled canard, thin supercritical wing sections, discrete variable camber, aeroelastic tailoring, three-surface control, relaxed static stability, and a triple-channel digital flight control system.

An extensive flight-test program has been defined and is under way at NASA Ames/Dryden Flight Research Facility to acquire high-quality data which will be used to evaluate and correlate the original design analyses and ground-test results with flight results. One of the objectives of the flight program is to isolate the benefits of specific technologies. However, when one considers the complex interactions occurring in the flight environment and the difficulty of extracting specific parametric variations from the available data, the task takes on herculean proportions.

A cooperative program has been defined between the Fluid and Flight Mechanics Branch at NASA Ames/Dryden and the High-Reynolds-Number Aerodynamics Branch at NASA Langley to support and complement specific flight test objectives. In addition to the flight test elements, the program consists of wind tunnel experiments and computational fluid dynamics to enhance the understanding of interacting technologies and to isolate individual benefits. The following sections will present brief overviews of the flight and ground experimental elements and a more complete discussion of the computational support.

This paper will mainly address issues and questions associated with the forward swept wing and closely coupled canard. The primary focus will be on research questions which must be addressed to obtain high quality ground and flight test data. These data will be used in conjunction with computational predictions to complement the analyses required to comprehensively understand the interacting technologies.

BENEFITS OF THE X-29A WING AND CANARD

Before the three phases of the program are discussed, it is appropriate to include a brief discussion of the benefits associated with the forward-swept wing and the canard. For transonic flight, wing sweep is used to delay the onset of drag rise. Uhad, et al. (ref. 1) demonstrated experimentally that a forward-swept wing offers potentially lower wing profile drag than an equivalent aft-swept wing for a transonic maneuvering design point. This yields higher sustained lift coefficients at transonic maneuvering conditions. If one compares aft- and forward-swept tapered wings, the local sweep angles for the forward-swept wing increase as one progresses from the wing leading edge to the trailing edge, while the opposite is true for an aft-swept wing. This results in lower wave drag losses for similar flow conditions and shock locations. Moore and Frei (ref. 2) similarly showed that the trade-off between forward- and aft-swept wings could favor the forward-swept wing. Their comparison configurations

PRECEDING PAGE BLANK NOT FILMED

held the wing area, aspect ratio, taper ratio, and shock sweep constant between the forward- and aft-swept wings. The forward swept wing had significant reductions in the wing bending moment at the pivot resulting from an inboard shift in the wing center of pressure. If one maintains the same shock sweep for the comparisons, the forward swept wing has a lower leading-edge sweep. This allows specific supercritical airfoils to be used which have demonstrated reductions in profile drag with decreasing leading-edge sweep. If one imposes a constraint of constant bending moment at the pivot and removes the constraint of constant aspect ratio, the forward-swept wing yields a higher aspect ratio in comparison to the aft-swept wing. This, of course, is beneficial in reducing induced drag.

Improved handling characteristics for forward swept wings at higher angles of attack were demonstrated in an experimental wind tunnel program (ref. 3). In general, flow separation on a forward-swept wing begins inboard and progresses toward the wing tip. In contrast, the tendency for an aft-swept wing is for the wing tip to separate first with the separation progressing inboard. The X-29A wing shows a mild break in the lift curve slope at low speeds and moderate angles of attack (10-12 degrees) resulting from inboard separation. However, the lift and pitching moment data are well behaved to high angles of attack with no pitch-up tendencies. Data also showed the X-29 full-span ailerons can maintain adequate roll control to very high angles of attack.

In addition to the benefits derived form the forward-swept wing, the close-coupled canard yields distinct advantages for the configuration. The canard and wing were designed in conjunction to yield an approximately elliptical span loading distribution on the wing at the maneuver design point. The canard is in the strong upwash field of the wing which results in an effective moment arm at subsonic speeds which is twice that of the geometric moment arm. Another advantage of the close-coupled canard results from the effect of the canard downwash on wing-root separation. At higher angles of attack, the lift generated by the canard to trim the configuration results in a downwash over the inboard part of the wing. This allows the inboard flow to stay attached to higher angles of attack than would be possible without the canard influence. The effect of the canard on the wing loading is presented in figure 2. These data are from the 1/8-scale model test at NASA Ames (ref. 4). The strong influence of the canard on wing span loading is evident as the canard deflection angle is changed at a given angle of attack. The loading is markedly shifted outboard as the canard deflection is increased.

FLIGHT TEST PROGRAM

As a subset of the flight-test objectives for the complete X-29A flight program, specific objectives have been identified which are associated with the forward-swept wing and close-coupled canard. To meet these objectives, extensive data must be gathered and analysed over a wide range of flight conditions. The aircraft has been extensively instrumented to gather these data, and software has been developed to assist in data manipulation and analysis. Figure 3 indicates some of the instrumentation which will be used. Static pressure orifices are arrange in five rows on the wing (η = 0.2, 0.31, 0.49, 0.70, and 0.91) and two rows on the canard (η = 0.28 and 0.65). These pressure data are extremely informative relative to inferences concerning wing-canard interactions and stall onset and progression. In addition, in-flight flow visualization will also be used to qualitatively identify flow characteristics through the use of flow cones. These are similar to tufts having a small plastic cone attached to the free end to enhance visibility and increase durability.

One of the potential problems associated with a forward-swept wing is aeroelastic divergence. In order to build a wing using conventional materials and manufacturing techniques strong enough to counteract this divergence, a significant weight penalty is incurred. Krone (ref. 5) presented the concept of advanced aeroelastically tailored composites, which are used in the X-29A vehicle, to overcome this problem. The concept uses a buildup of specifically oriented plies of composite laminate to form the wing skins. The orientation and characteristics of the plies can be designed to have the strength necessary to overcome divergence. An additional advantage is that the technique can be used to tailor the aeroelastic twist distribution at maneuvering conditions.

A wing-deflection measurement system is installed on the right wing of the flight-test aircraft. Two fuselage-mounted receivers with different focal lengths are used to monitor 12 targets mounted on the

wing surface, figure 3. These data can be reduced to determine discrete deflections at each of the targets or integrated to determine the average twist angle and section translation for the various span locations. These data will have several uses including validation of structural design methodology. The data are critical in order to provide valid, reliable, transonic computational predictions of the configuration flow field for the flight vehicle. The supercritical wing is an efficient but sensitive performer at transonic speeds. Small changes in flow conditions or geometry (such as aeroelastic deflections) can have significant effects on the flow over the wing surface including shock location, shock strength, flow separation, and buffet onset.

A number of challenges have been encountered as the flight-test program has progressed. Some of these difficulties have centered around data analysis. The aircraft's negative static margin and the use of canard, wing flaps, and strake flap simultaneously, figure 1, for pitch control make it exceedingly difficult to separate the effect of specific variables. In normal flight the deflections of these control surfaces are controlled by the Automatic Camber Control (ACC) system. Hence, the ability to isolate specific stability derivatives is quite limited. However, the Manual Camber Control (MCC) system was implemented to limit the number of parameters allowed to vary for control purposes. This allows the flap to be fixed at a discrete setting during a given portion of the flight, thereby reducing the number of control surfaces whose deflections are varying. An example of different inferences derived from data for similar flight maneuvers using the two different modes (ACC and MCC) is presented by Waggoner, Jennett, and Bates in reference 6.

NTF MODEL AND WIND TUNNEL TEST

A 1/16-scale model of the X-29A, figure 4, is being designed and fabricated for testing in the National Transonic Facility (NTF) at NASA Langley. The NTF was conceived to provide high-Reynolds-number test capability for aerodynamic research and development testing of commercial and military aircraft configurations. The NTF is a closed-circuit, single-return, fan-driven, wind tunnel capable of continuous operation over a Mach number range of 0.2 to 1.2. It is capable of operating at very low temperatures (−320°F) by injecting nitrogen at cryogenic temperatures into the stream. By operating at elevated pressures and cryogenic temperatures, a maximum chord Reynolds number of 120 million at Mach number of 1.0 for a chord of 0.82 feet is achievable (ref. 7).

The X-29A test program is intended to provide significant data which will complement the flight-test program. In addition to providing basic data for flight-to-tunnel and code-to-tunnel correlation studies, Reynolds number effects on a number of sensitive flow areas will be investigated. Over the complete NTF testing schedule for the X-29A, it is anticipated that Reynolds number effects will be determined on wing surface pressures and wing-canard interactions; supercritical design; shock/boundary layer interactions; performance, stability and control; and high-angle-of-attack characteristics.

1/16 SCALE MODEL

The NTF model has been fabricated by Grumman Aerospace Corporation under contract with NASA Langley. The model can be used to simulate aerodynamic control surface deflections through the use of variable incidence canards and interchangeable sets of wing flaperon, rudder and strake flap parts. The design of the model allows for the simulation of four wing flap settings, seven strake flap settings and four rudder settings. In addition, six positions are available for the variable incidence canard. The external lines of the X-29A are modeled in significant detail. Flow through nacelles will afford the first simulated inlets for cryogenic operation in the NTF. The flow through ducts will simulate the mass flow rate for a condition near the cruise design point. Although the provisions to simulate various mass flow rates are not anticipated, the calibration of the inlets for various Reynolds numbers presents a significant challenge.

Data acquisition planned for the test program includes aerodynamic force and moment data, wing pressure distributions and wing deformation characteristics. An extensive array of instrumentation will

support this task. Static pressure orifices are located at span locations corresponding to wing stations 50 and 114. The orifice locations were chosen to correspond closely to the orifice locations on the number-one flight-test aircraft. A 48-port electronic sensing pressure (ESP) module will be mounted in the model nose, as well as an accelerometer-type angle of attack indicator.

Two, six-component, 1.75-inch diameter, internal strain-gage balances have been constructed. Each is intended to be used over a different load range. The normal force design loads of the two balances are 1500 and 2500 pounds. It was desirable to have static pressure measurements on the canards. However, because of the size of the canard (1/8-inch thick at mid-span) and small diameter of the shank attachment to the fuselage, it was not feasible. In lieu of this, a three-component strain-gage balance is built into the left canard to measure shear, bending and torsion. A wing-root bending-moment gage allows for real-time evaluation of model dynamics.

Deflection of the wings during the wind tunnel test will be measured by use of a video model deformation system. These measurements will be used to determine the magnitude of differences in wing shape between the model and flight vehicle under similar flow conditions.

The fabrication of the model was somewhat unique. The left wing and fuselage half and right wing and fuselage half were each machined as one piece out of a high-nickel-content steel suitable for cryogenic models (Vascomax 200). The two halves were then welded together yielding a one-piece wing fuselage model. The interchangeable flaps also presented a serious design problem. The flap elements are quite thin and were designed to attach to the wing through a tongue-in-groove arrangement. This design was necessary to ensure compatibility with the severe thermal test environment. The thin tongues on the flaps and the precision machine work for the grooves presented a challenge for the model craftsmen.

NTF MODEL TEST PROGRAM

The model design point simulates flight Reynolds number at M = 0.9 and 30,000 ft. with the NTF operating at minimum tunnel dynamic pressure. Simulated 8-g flight at these conditions yields a $C_N \cdot q$ limit of 2,700 psf for the 1/16-scale model. A comparison of the tunnel-test-to-flight envelope is presented in figure 5. Superimposed on the envelope are the sting divergence limit boundary for the low-angle of attack support system and the envelope of Reynolds numbers attainable with this model in the NASA-Ames 11-Foot Tunnel. Because of the versatility of the NTF, note that even with the sting divergence limit imposed, much of the airplane flight envelope below M = 1.2 can be simulated with the 1/16-scale model in the NTF. At Mach numbers less than 0.7, the entire angle-of-attack range can be tested at flight Reynolds numbers for the entire flight envelope.

The model will be tested over a Mach number range from 0.3 to 1.2 at Reynolds numbers from 2 to 35 million. Initially, the angle of attack will be limited to 20° ; however, with the high-alpha sting, angles of attack up to 60° can be achieved.

COMPUTATIONAL SUPPORT OF THE X-29A EXPERIMENT

A comprehensive computational program has been identified to support both flight and ground testing of the X-29A. The effort up to the present time has concentrated on the applicability of potential flow methods. The following sections will briefly describe the codes which have been used, describe the code calibration effort and present selected results.

COMPUTATIONAL TECHNIQUES

Three primary computational techniques have been identified to support the initial computational phase of the program. A three-dimensional, small-disturbance, transonic analysis code for wing-fuselage-canard combinations (CANTATA), a three-dimensional full-potential, transonic analysis code for wing-fuselage combinations (TAWFIVE), and an aerodynamic/structural analysis system (TAPS) will be

employed to exploit the advantages of each technique. Salient features of the computational techniques are discussed below.

CANTATA Analysis Code - The Canard/Tail Transonic Analysis code (CANTATA, ref. 8) is characterised by a unique grid-embedding technique which provides excellent resolution for either a wing-fuselage-canard or wing-fuselage-tail configuration. The code solves for the flow field about the configuration of interest in the direct mode employing an ADI scheme. Design via numerical optimisation is available in the code but is not anticipated to be used in the current application. Using finite difference approximations, a modified small-disturbance potential-flow equation is iteratively solved in a system of multiple embedded grids. The modifications to the classical small-disturbance equation are in the form of extra terms, which, when added to the equation, provide more accurate resolution of shock waves with large sweep angles and a better approximation of the critical velocity where the full-potential equation changes from elliptic to hyperbolic type.

Viscous effects are approximated by coupling a modified Bradshaw boundary-layer computation to the finite-difference potential-flow solution. The modified method provides a technique to extend a two-dimensional boundary-layer calculation to account for first order viscous effects (ref. 9). The viscous effects are incorporated in the solution by adding the boundary-layer displacement slopes to the wing surface slopes. This modifies the wing surface to an equivalent "fluid" wing shape which is then analyzed by the potential flow code.

The basic concepts inherent to the code have been extensively validated by several researchers (refs. 10-12). These studies have, in general, been for aft-swept wings and for single lifting surface configurations.

TAWFIVE Analysis Code - A computer code for the Transonic Analysis of a Wing and Fuselage with Interacted Viscous Effects, references 13 and 14, is also used in this study. The code utilizes the interaction of three-dimensional inviscid and viscous flow solvers to obtain transonic flow-field solutions about wing-fuselage combinations. The outer inviscid flow field is solved using a conservative, finite volume, full potential method based on FLO-30 by Caughey and Jameson (ref. 15). No modifications were made to the internal grid-generation algorithm in FLO-30, which is a body-fitted, sheared, parabolic coordinate system.

A three-dimensional boundary layer for the wing is computed using a compressible integral method. The code has the capability of computing laminar or turbulent boundary layer with the methods of Stock (ref. 16) or Smith (ref. 17), respectively. An important feature of the code is Street's treatment of the wake (ref. 13). The wake model used in FLO-30 was replaced with a model which satisfies flow tangency on the wake displacement body and the pressure jump condition resulting from wake curvature. These changes in the code can make significant differences in results obtained on various configurations.

Transonic Aeroelastic Programs System - The Transonic Aeroelastic Program System (TAPS) developed by Campbell (ref. 18) is a method which allows the effects of static aeroelastic wing deflections to be included in steady transonic aerodynamic calculations. The method interacts a three-dimensional transonic computer code with viscous effects and a linear finite element structural analysis code to calculate wing pressures and deflections. The nonlinear nature of the transonic flow makes it necessary to couple the aerodynamic and structures codes in an iterative manner. TAPS has been arranged in a modular fashion so that different aerodynamic or structural programs may be used with a minimum of coding changes required.

For the current study the TAPS program has been utilized to help understand the correlations of computations and wind tunnel data with data obtained from the flight test. The flight vehicle has been analyzed in the TAPS program to predict the wing deflections under flight loads. These calculations will be described in detail in a subsequent section.

CODE CALIBRATION EFFORT

The first phase of the computational effort will involve calibration of the transonic aerodynamic codes for application to the X-29A configuration. Although these codes have been applied to numerous configurations, the X-29A is such a unique configuration that a calibration phase is required. This utilizes

both code-to-code and code-to-experiment comparisons. In general, for transonic analysis codes in widespread use for analysis and design, there exists an inverse relationship between the physics included in the governing flow equations and the complexity of geometry for which one is realistically capable of obtaining a solution. The two transonic potential flow codes discussed previously illustrate this point. The TAWFIVE code solves the full-potential flow equation coupled with a three-dimensional boundary-layer analysis for a wing-body configuration. The CANTATA code, on the other hand, solves a simplified flow equation (extended small disturbance) on a more complex (wing-fuselage-canard) geometry.

The X-29A has a very complex geometry from a computational standpoint. The body, figure 6, was extremely difficult to model, particularly in the wing-fuselage juncture region. The discontinuous trailing edge resulting from the body strake geometry offered another challenge. The effects of the inlet on the flow over the canard and the dihedral effects for the wings were unknown. In addition, there is little experience to draw from in solving flow fields including viscous effects about swept-forward wing configurations. Hence, there were a number of compelling reasons to undertake the code calibration phase of this effort.

The first task addressed was to generate a detailed computational model of the fuselage, figure 6. The objective was to make as few compromises as possible to the geometry while generating a model for which computational mappings could be generated by the codes. The wing and canard geometry has also been modeled; however, this has been a much more straightforward task. The compromises to the wing geometry consisted of a modified trailing edge in the vicinity of the body stake for each of the codes and modeling a wing without any dihedral in the CANTATA code because of its Cartesian grid structure.

The actual comparisons on the configuration have been performed in a systematic manner. The approach will be described here and selected comparisons from the various steps will be presented in the following section. The initial computations were performed on the wing-fuselage combination using the TAWFIVE and CANTATA codes. These computations were also compared to available wind tunnel data on the wing-fuselage configuration. The differences between the computations and experimental data were evaluated in light of previous experience. Code-to-code differences were analyzed in light of known differences (full-potential vs. small-disturbance, conservative vs. non-conservative, etc.) between the codes on computational results. Comparisons have also been made between computations on the fuselage-canard geometry. Each of these sets of calculations and comparisons will help to understand the wing-canard interactions. These analyses will also allow the wing-fuselage-canard configuration to be analyzed with significantly greater confidence than if the full configuration were analyzed initially.

Computations on the wing-fuselage-canard configuration in the CANTATA code have been compared between available wind tunnel data on the 1/8-scale model and flight data. The available experimental data was surveyed to determine if comparable test points existed between the wind tunnel and flight tests. Comparisons of these data were accomplished at appropriate conditions. Differences between these data were attributed to either aeroelasticity or Reynolds number. Calculations with the TAPS program were accomplished to investigate aeroelastic effects. These data were compared with deflection measurements from the flight system.

The use of any computational technique benefits from the accuracy inherent in the method. However, it is also realized that a code can be used effectively if one understands the computational limitations and the effects of any inaccuracies which may be present. This becomes increasingly important as one approaches the boundaries of practical applicability for a given code. The approach undertaken in this study has identified some practical limitations of the computations for this complex configuration.

SELECTED COMPARISONS

Initially, computations were performed on the X-29A wing-fuselage combination and compared with available wind-tunnel data from the 1/8-scale model tested at NASA-Ames (ref. 4). Results are presented for a subsonic Mach number (M = 0.6) and a high-transonic Mach number (M = 0.9). The computational results are inviscid with no aeroelastic effects included. The transonic analyses were performed at the experimental angles of attack and Mach numbers. These results demonstrate the code-

to-code differences and cover the range of applicability for the codes up to flow conditions where the flow shows sign of significant separation on the wing.

Results are compared at M = 0.6, α = 7.7°, in figure 7. The comparisons are quite good at this condition. Notice that generally the full-potential code (TAWFIVE) predicts more expansion at the leading edge on the upper surface. Because of the grid density at the trailing edge, the CANTATA results seem to be more sensitive to the flaperon geometry. Also note the differences in the computational predictions at the wingtip. The TAWFIVE code predicts the upper-surface leading-edge peak quite well. However, the small-disturbance results compare better with the experiment aft of the leading edge.

The comparison presented in figure 8 are at M = 0.9 and α = 6.9°. The comparisons on the outboard part of the wing are fairly good, although the experimental results show trailing-edge (η = 0.7) and shock-induced (η = 0.49) separations. On the inboard portion of the wing, the lower surface pressures are predicted fairly well; however, the upper surface pressures show some discrepancies. At η = 0.31 and 0.19 the experimental and computational results on the upper surface forward of the shock do not match well. While the experimental data are sparse in this region, it does not appear that the characteristics of the flow are predicted with either computational technique. In general, the two codes predict similar flow patterns over the wing span for the flow conditions observed. Comparisons for the fuselage-canard configuration also showed consistent predictions between the two codes.

The next step in the calibration effort involved computations on the wing-fuselage-canard configuration. The first significant incongruence between the actual configuration and the geometric capabilities of the CANTATA code was uncovered. The grid structure for both the canard and wing grids is Cartesian. This results in the boundary conditions for both surfaces being applied in parallel planes. Because of the dihedral in the wing, the locus of wing leading-edge points intersects the canard wake. This in conjunction with the closely coupled lifting surfaces results in a significant interaction between the wing and canard. The comparison presented in figure 9 shows the effect of relative wing-canard vertical position on the wing pressure distribution near mid span. The calculations were made with the wing 3 inches (full scale) above and below the plane of the canard. When the wing is positioned above the canard plane, the loading over the inboard wing sections is collapsed. By comparisons with wind tunnel experimental data, it became obvious that positioning the wing slightly below the canard yielded the most reasonable flow simulation.

Comparisons between wind tunnel data from reference 4 and computational predictions for the complete configuration are included in figures 10 and 11. The comparisons are strikingly similar for these M = 0.9, low lift (figure 10) and M = 0.95, moderate lift (figure 11) conditions. The inboard region on the uppers surface is predicted adequately. As one observes the comparisons outboard of the leading-edge break, the characteristic of the experimental pressures on the upper surface is not captured in the computations. This difference was observed in all the comparisons at M = 0.9 and above. The pressure distribution on the canard is predicted reasonably well except at the leading edge on the upper surface. An expansion observed in the experimental data is not evident at all in the computations. This difference could be the result of geometric compromises related to the inlet or to a vortex originating from the forebody or inlet lip. The accentuated expansions and compressions near the wing trailing edge are the result of computationally modeling the discrete hinge-lines for the segmented trailing-edge flap system. Based on these comparisons at the higher Mach numbers, plus comparisons at subsonic conditions, it was felt that an adequate computational model had been generated.

At this point the focus on the experimental data shifted from the data obtained in the controlled wind tunnel environment to data obtained in the dynamic flight environment where the uncertainties are increased. Before proceeding with comparisons between the computations and the flight test data, it was of interest to determine how well the flight and wind tunnel data compared. Because of the large number of parameters which had to be matched (Mach, angle of attack, canard, wing flap, and strake flap deflections, etc.), only a few conditions were identified for comparison between the wind tunnel test and flight test. Comparisons at M = 0.8 and M = 0.9 are presented in figure 12. At M = 0.8 and α = 2.2°, the comparisons between flight and wind tunnel data are excellent at both of the span stations shown. At higher Mach numbers and angles of attack the comparisons were not quite as good. It was interesting to note, as shown in figure 12b, that a very good comparison was obtained when the tunnel data were compared at an elevated angle of attack relative to the flight data. Several hypotheses

were purposed to explain this anomaly including wind tunnel wall interference, Reynolds number effects, and aeroelastic deformation. Wing deflection data were available at some flight conditions. A flight test point of interest was identified and the configuration was analyzed in TAPS. The resulting predicted deflections are compared with the measured deflections in figure 13. The measured deflections from the flight test also show an error range with the data. TAPS overpredicted the deflections along the entire span. However, the inclusion of the computational (overpredicted) deflections in the solution did not yield differences between the rigid and aeroelastic solutions as large as those observed between the flight and tunnel experiments at comparable angles of attack. These anomalies accentuate the need for the experiment in the NTF.

The final set of comparisons is between computational predictions and flight test data at M = 0.6, 0.8, and 0.91 and moderate lift levels (figures 14, 15, and 16). The comparisons at M = 0.6 and 0.8 are quite good on both the wing and canard. At the outboard span location on the wing the upper-surface leading-expansion is slightly underpredicted at M = 0.6. At the inboard location on the wing at M = 0.8 the leading edge expansion is overpredicted in the computations. The upper-surface leading-edge flow is predicted adequately at M = 0.91 for the inboard station yet the level of expansion from 20% to 30% chord is not predicted accurately. At M = 0.91 the characteristic of the upper-surface flow is not predicted at the outboard span location. The characteristics of the experimental and computational pressure distributions are similar to those observed in the comparisons of wind tunnel and computational predictions in figures 10 and 11. The influence of the rather bulbous flap-track fairings is evident in comparisons on the lower surface at the outboard span location for M = 0.8 and 0.91. There was no attempt to model these fairings computationally.

There is evidence of flow expansion at the inboard canard location leading edge for all three Mach numbers which is not predicted computationally. At M = 0.91 the expansion appears to terminate in a shock at approximately 10% chord. While not shown in these figures, this expansion migrates outboard along the canard with increasing angle of attack. Except for this anomaly the canard flow is predicted well.

Overall the comparisons between the experimental data and computational predictions are encouraging. However, there were differences observed for which the causes were difficult to isolate. In particular, at higher Mach numbers the flow on the outboard part of the wing, as well as the canard leading edge was not predicted well computationally. These observations identify the need for obtaining high-Reynolds-number data under controlled conditions.

SUMMARY AND CONCLUSIONS

This paper has presented an overview of a major cooperative effort between NASA Ames/Dryden Flight Research Facility and NASA Langley in support of the X-29A flight-test program. The effort involves flight testing, wind tunnel testing in the NTF, and computational support. Each phase in the effort has distinct advantages and disadvantages relative to the data which are obtained. For example, the flight data could be considered "gospel" without scaling or wall interference effects. However, as was previously discussed, it is difficult to isolate the influences of individual parameters. Wind tunnel testing allows the component build-up and parametric variation of independent variables. Hence, individual influences and interference effects can be isolated. However, the data can suffer from scaling effects and/or wall interference. In addition, although the range of variables tested can cover the airplane capability, testing all combinations of each variable quickly expands to a prohibitively large matrix. While physical geometry and fluid physics modeling comparisons are often made, CFD allows the gaps between tunnel and flight data to be filled. It also allows evaluation of flight conditions outside the cleared flight envelope and estimation of the effects of configuration modifications. Hence, it is easy to see from this simplified discussion that each phase of the effort complements the other phases.

An adequate computational representation of the X-29A configuration has been developed. Comparisons between computational predictions and both flight and wind tunnel experimental data have been made a a range of transonic conditions. At freestream Mach numbers less than 0.9, the comparison of pressure distribution between the computations and experiment is quite good on both the wing

and the canard. Anomalies have been observed for moderate lift coefficients at M = 0.9 and above. The computations show no evidence of the flow expansion observed on the canard leading-edge. In addition, the experimental pressure distribution over the mid-span of the wing has a different character than that predicted computationally. Further computational and experimental investigations of these discrepancies are required to understand these anomalies.

The flight testing of the X-29A aircraft is well under way and a significant amount of data is becoming available. The NTF wind tunnel test model is virtually complete and the NTF test will commence during the Fall 1988. Computational support is continuing with the focus on understanding the anomalies which have been identified. The data available from the three-phase effort will greatly enhance the understanding of the complex flow phenomena and aerodynamics of the X-29A aircraft.

REFERENCES

1. Uhad, G. C.; Weeks, T. M.; and Large, R.: Wind Tunnel Investigations of the Transonic Aerodynamic Characteristics of Forward-Swept Wings. Journal of Aircraft, 20(3), pp. 195-202, March 1983.
2. Moore, M.; and Frei, D.: X-29 Forward Swept Wing Aerodynamic Overview. AIAA Paper 83-1834, 1983.
3. Grafton, S. B.; Gilbert, W. P.; Croom, M. A.; and Murri, D. G.: High-Angle-of-Attack Characteristics of a Forward-Swept Wing Fighter Configuration. AIAA Paper 82-1322, August 1982.
4. Charletta, R.: Series I Transonic/Supersonic Testing in a 12.5% Scale Grumman Design 712, X-29A Forward-Swept Wing Demonstrator Aircraft Model in the NASA ARC 11-Foot and 9x7-Foot Wind Tunnels, at Moffett Field California. AER/T-AMES-5?8-1-11,97, August 1982.
5. Krone, N. J., Jr.: Divergence Elimination with Advanced Composites. AIAA Paper 75-1009, August 1975.
6. Waggoner, E. G.; Jennett, L. A.; and Bates, B. L.: X-29 Flight Test Program Including Wind Tunnel and Computational Support. SAE Paper 861642, October 1986.
7. Gloss, B. B.: Initial Research Program for the National Transonic Facility. AIAA Paper 84-0585, March 1984.
8. Aidala, P.: Canard/Tail Transonic Analysis. Air Force Wright Aeronautical Laboratories Report AFWAL-TR-85-3087, October 1985.
9. Mason, W. H.; et al.: An Automated Procedure for Computing the Three-Dimensional Transonic Flow Over Wing-Body Combinations, Including Viscous Effects. Air Force Flight Dynamics Laboratory Report AFFDL-TR-122, Vol. I, October 1977.
10. Waggoner, E. G.: Validation of a Transonic Analysis Code for Use in Preliminary Design of Advanced Transport Configurations. ICAS Paper 84-1.4.2, September 1984.
11. Boppe, C. W.: Computational Aerodynamic Design: X-29, the Gulfstream Series and a Tactical Fighter. SAE Paper 851789, October 1985.
12. Rosen, B. S.: Transonic Analysis of Canted Winglets. AIAA Paper 84-0302, January 1984.
13. Street, C. L.: Viscous-Inviscid Interaction for Transonic Wing-Body Configurations Including Wake Effects. AIAA Paper 81-1266, July 1981.
14. Melson, N. D.; and Street, C. L.: TAWFIVE: A User's Guide. NASA TM-84619, September 1983.
15. Caughey, C. A.; and Jameson, A.: Recent Progress in Finite Volume Calculations for Wing-Fuselage Combinations. AIAA Paper 79-1513, July 1979.
16. Stock, H. W.: Integral Method for the Calculation of Three-Dimensional Laminar and Turbulent Boundary Layers. NASA TM-75320, 1978.
17. Smith, P. D.: An Integral Prediction Method for Three-Dimensional Compressible Turbulent Boundary Layers. RAE R&M 3739, 1974.

18. Campbell, R. L.: Calculated Effects of Varying Reynolds Number and Dynamic Pressure on Flexible Wings at Transonic Speeds. NASA CP 2327, Part 1, April 1984, pp. 309-327.

ORIGINAL PAGE IS
OF POOR QUALITY

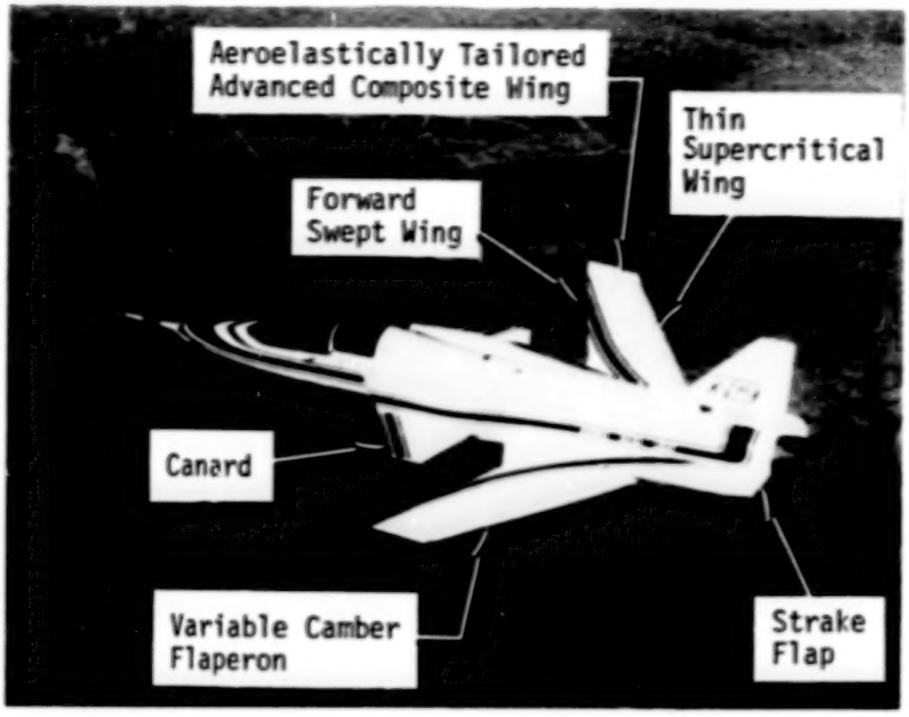

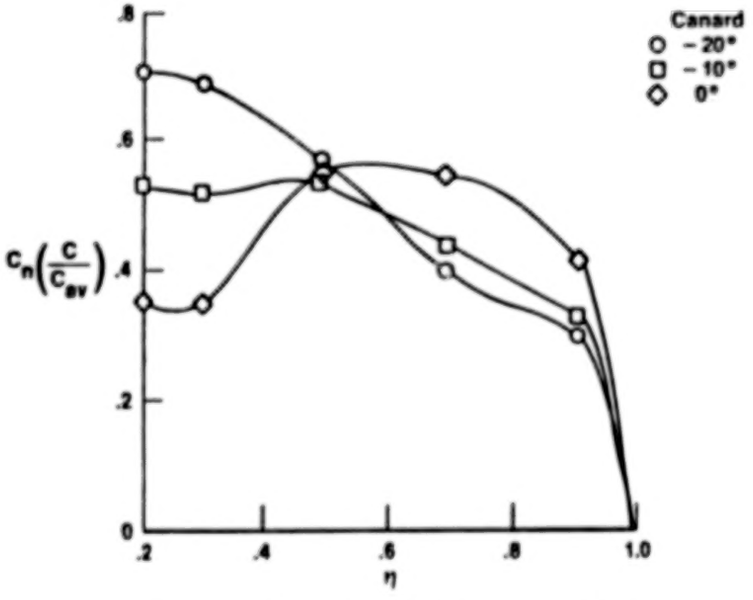

Figure 2 - Comparison of wind tunnel model wing span load for several canard settings

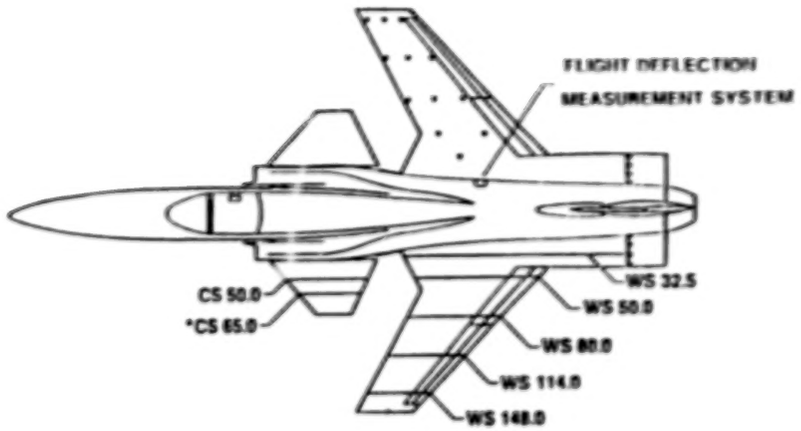

*This row was not on wind tunnel model

Figure 3 - Static pressure orifice locations and deflection measurement system

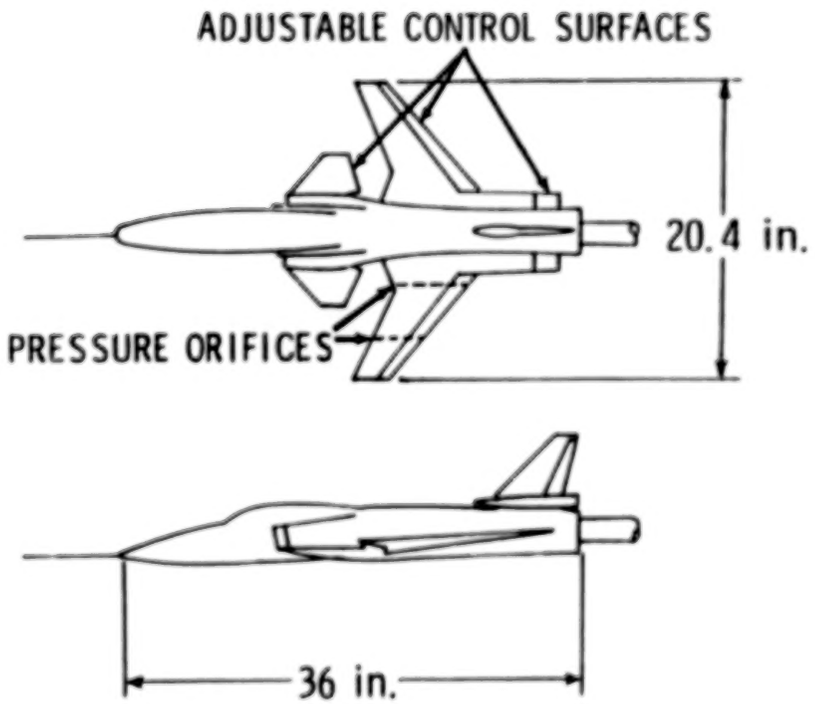

Figure 4 - 1/16-scale X-29 model

ORIGINAL PAGE IS
OF POOR QUALITY

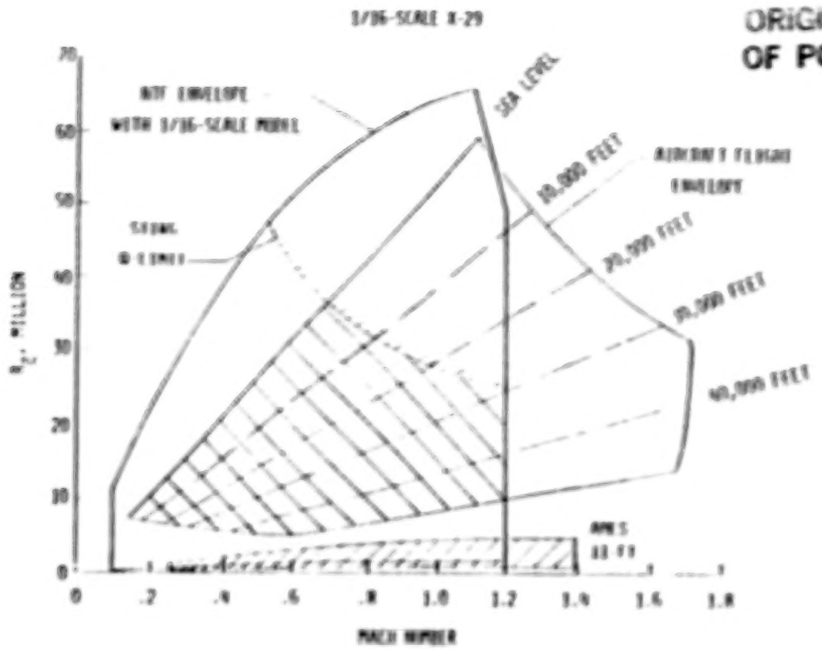

Figure 5 - Comparison of NTF and X-29A flight envelopes

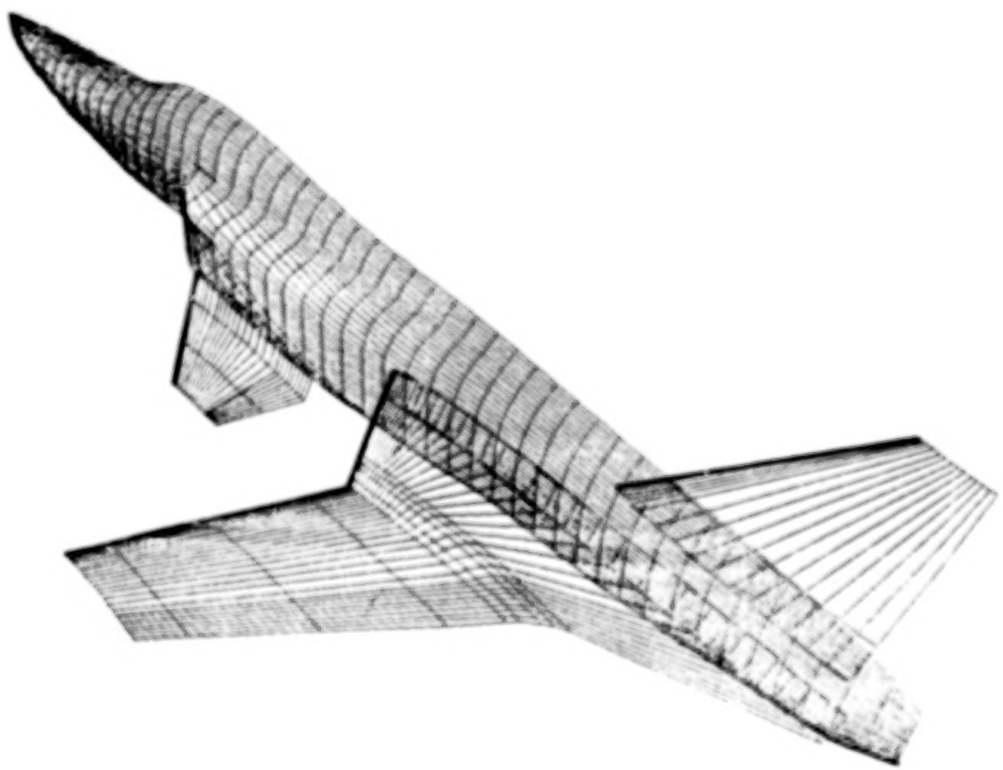

Figure 6 - Wire frame representation of the computational model

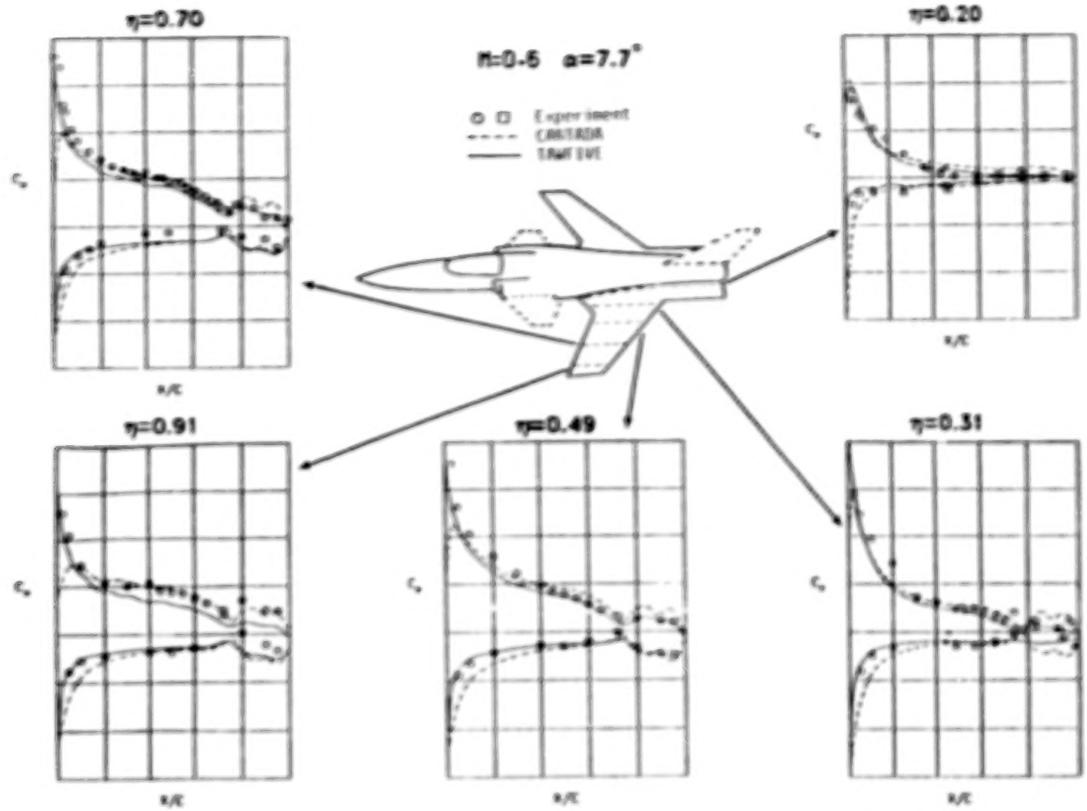

Figure 7 - Comparison of computations and wind tunnel results M=0.6, α = 7.7°

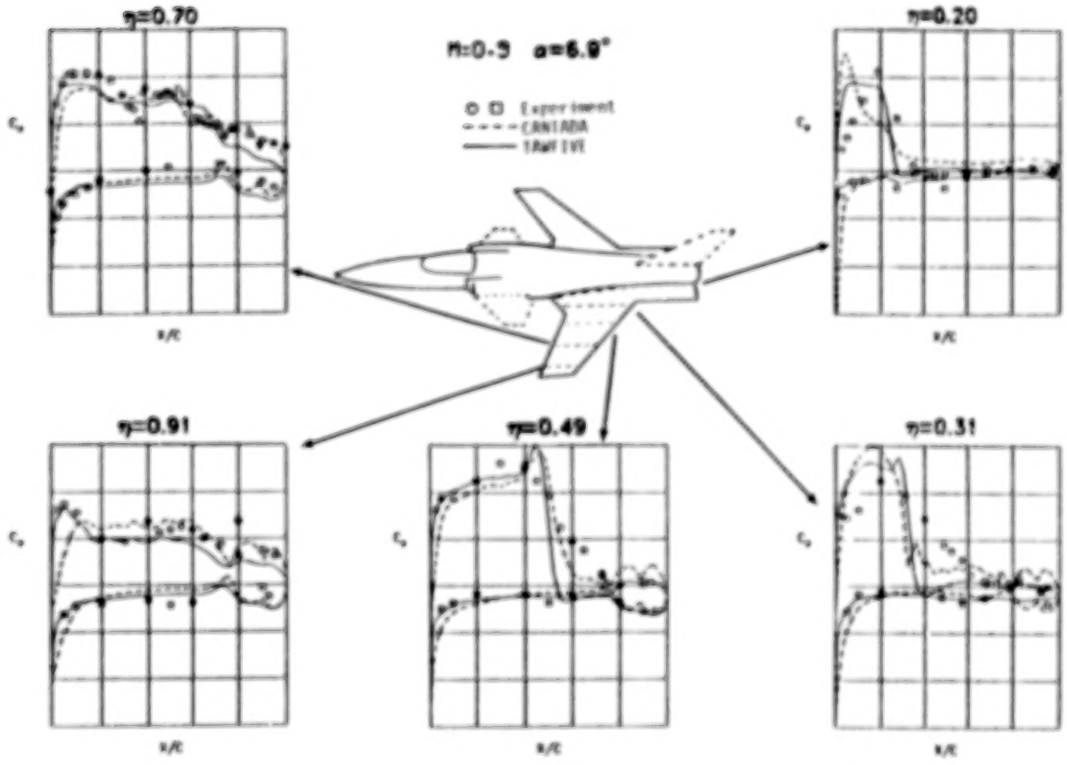

Figure 8 - Comparison of computations and wind tunnel results M=0.9, α = 6.9°

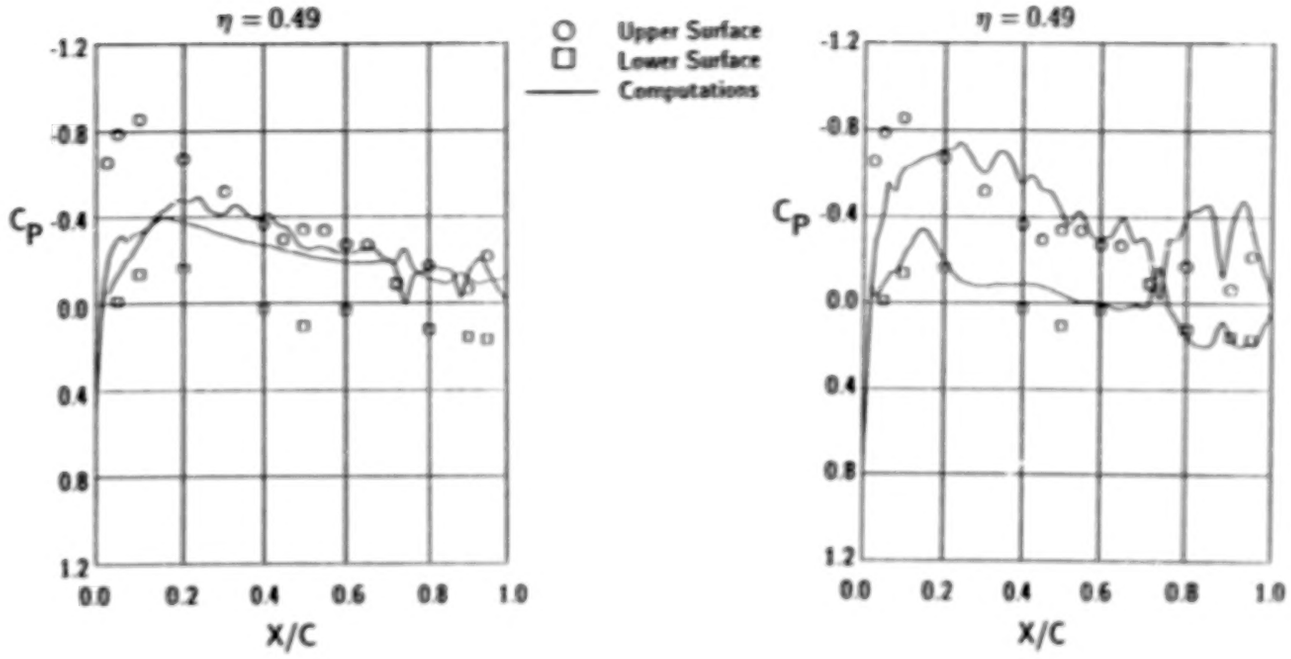

a) Wing above canard

b) Wing below canard

Figure 9 - Effect of wing/canard position on wing pressure distribution - M=0.9, α = 4.7°

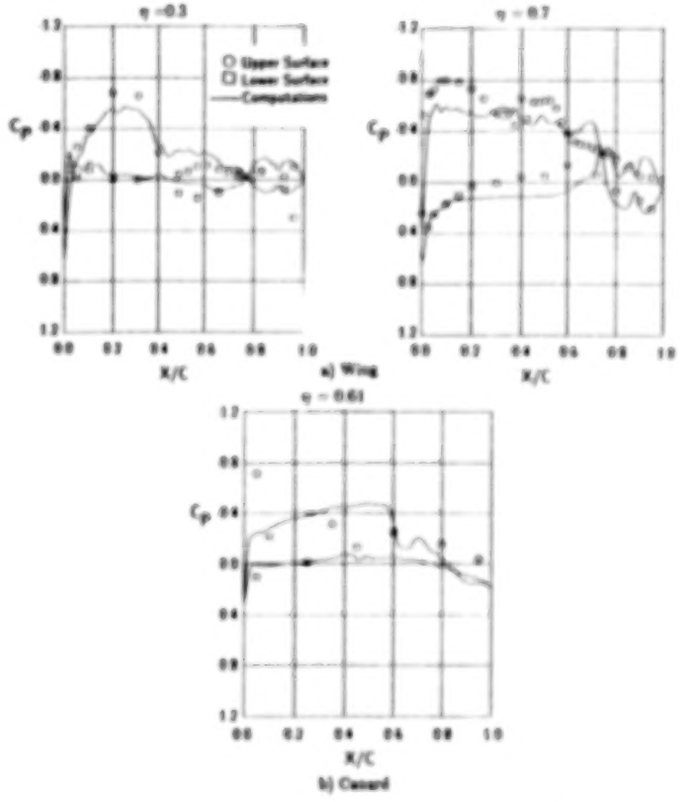

Figure 10 - Comparison of computational results and wind tunnel data - M=0.9, α = 2.1°

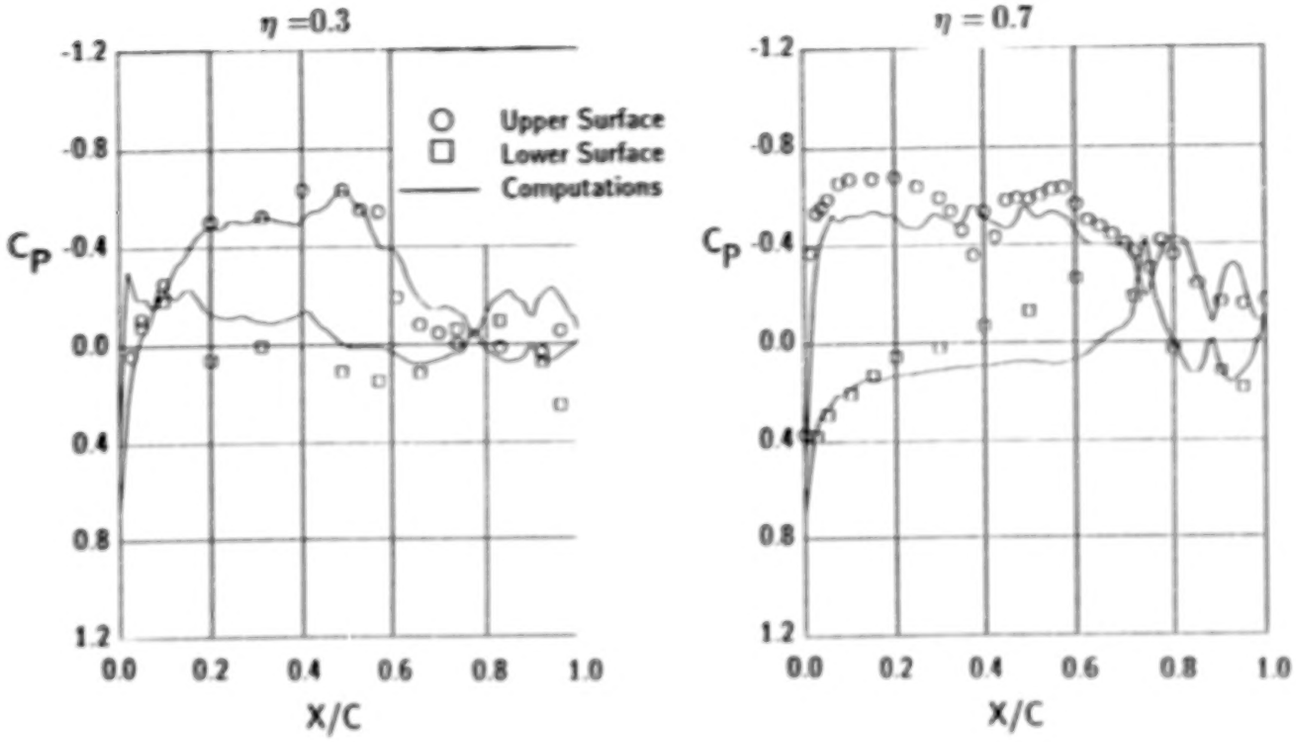

a) Wing

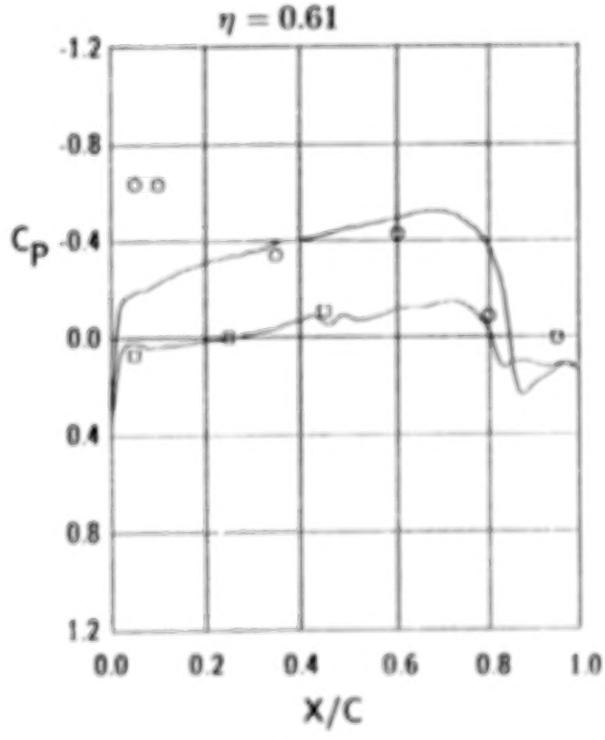

b) Canard

Figure 11 - Comparison of computational results and wind tunnel data - M=0.95, α = 5.9°

ORIGINAL PAGE IS
OF POOR QUALITY

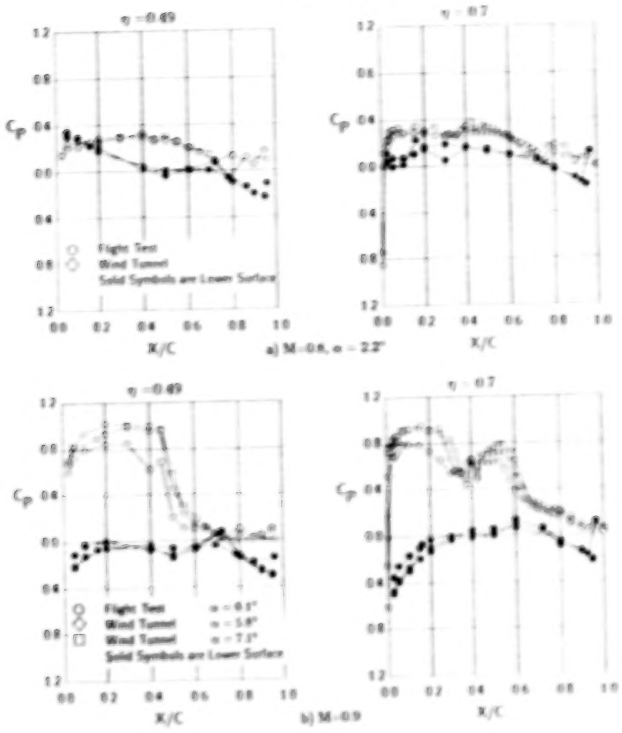

Figure 12 - Comparison of wind tunnel and flight test data

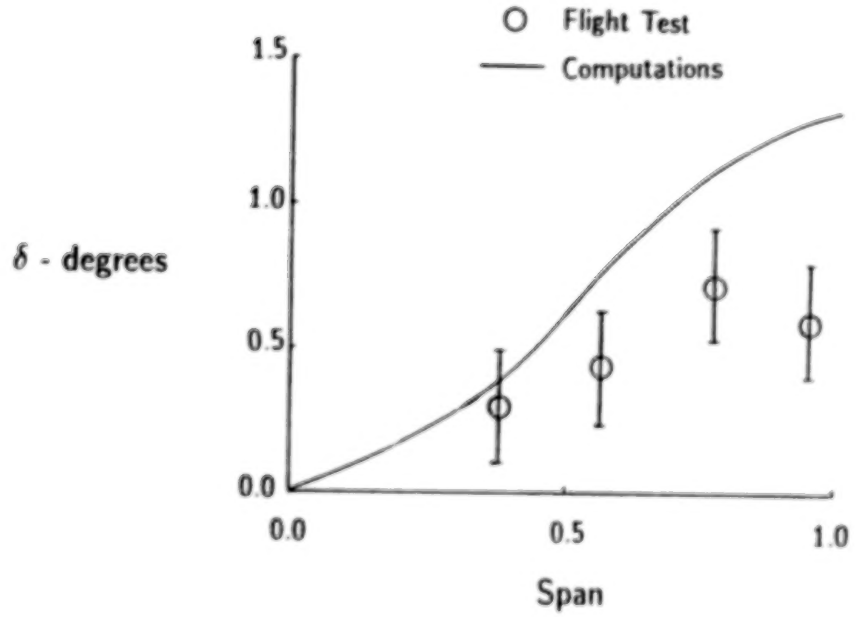

Figure 13 - Comparison of measured and predicted wing deflections - M=0.92, α = 7.5°

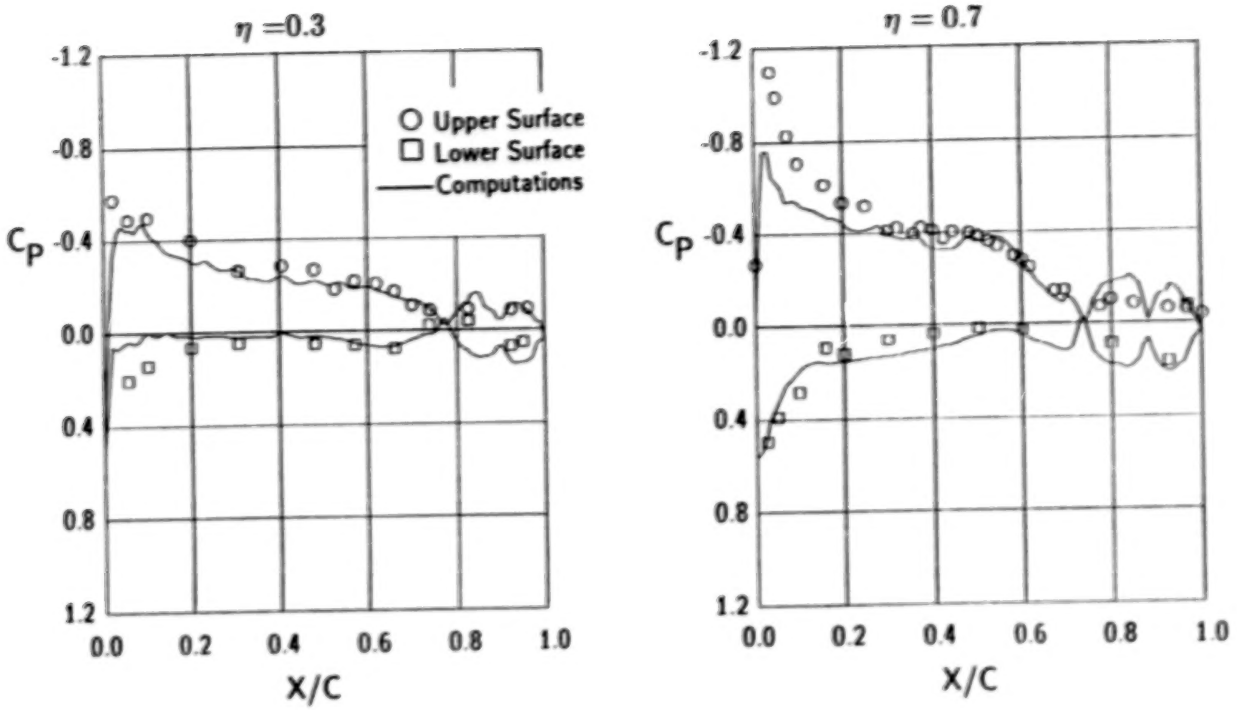

a) Wing

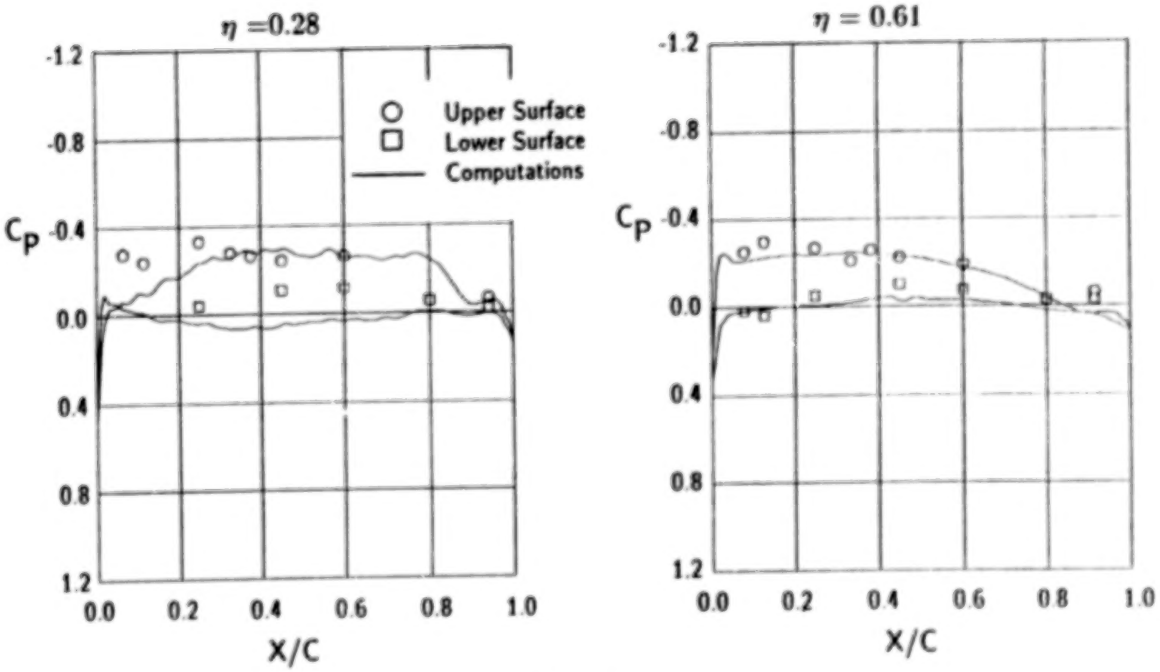

b) Canard

Figure 14 - Comparison of computational results and flight test data - M=0.6, $\alpha = 6.5°$

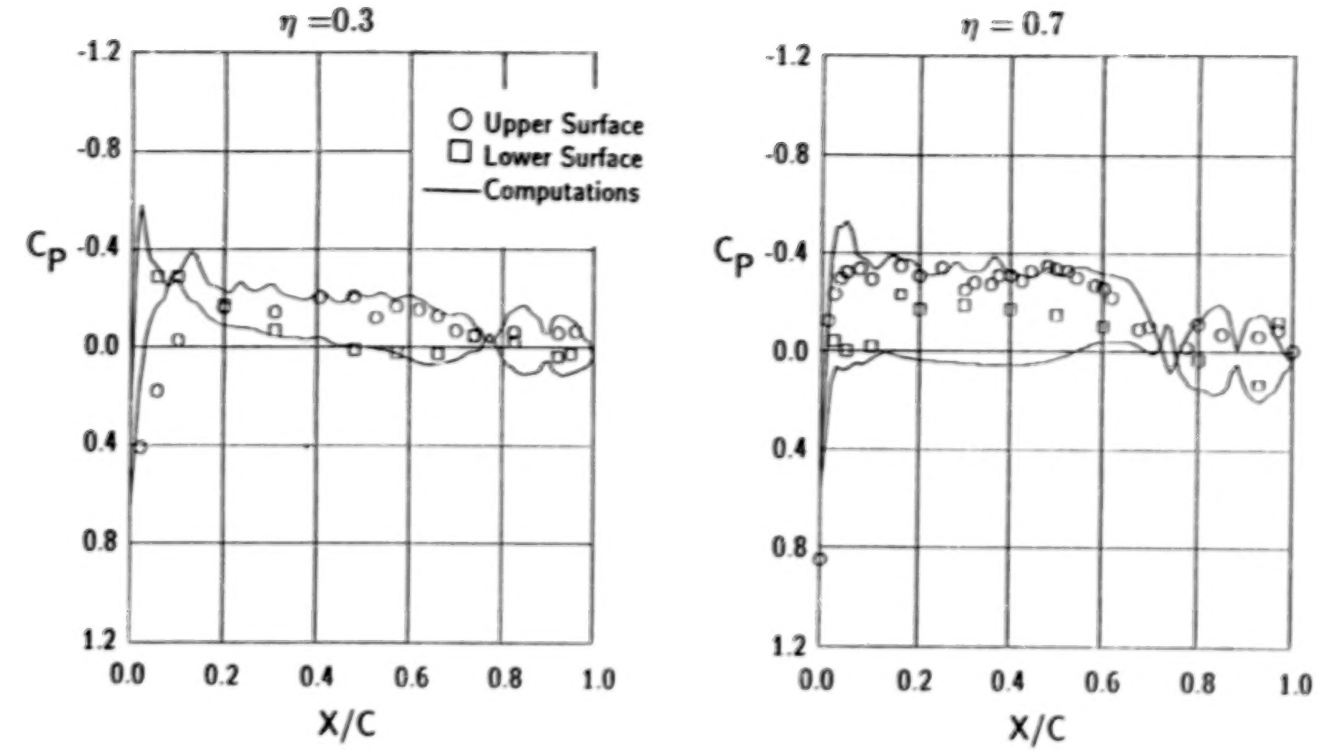

a) Wing

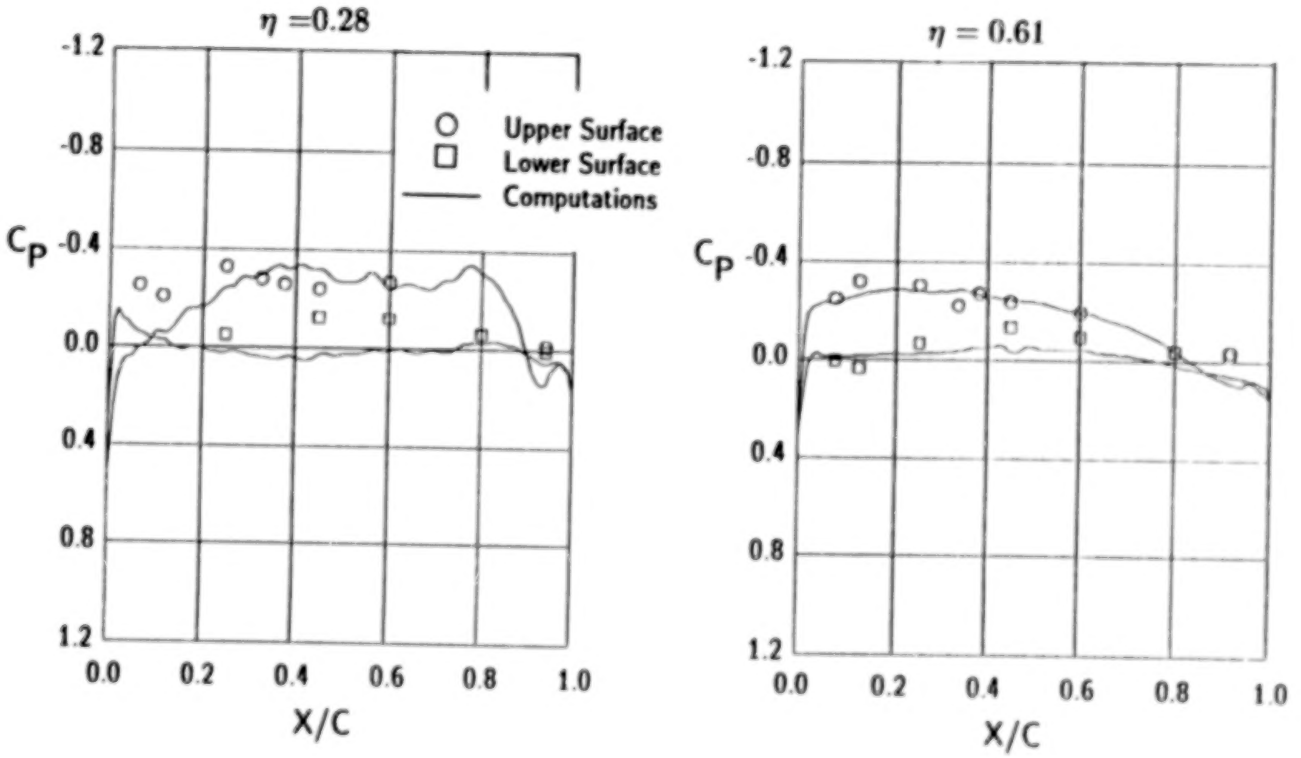

b) Canard

Figure 15 - Comparison of computational results and flight test data - M=0.8, $\alpha = 4.1°$

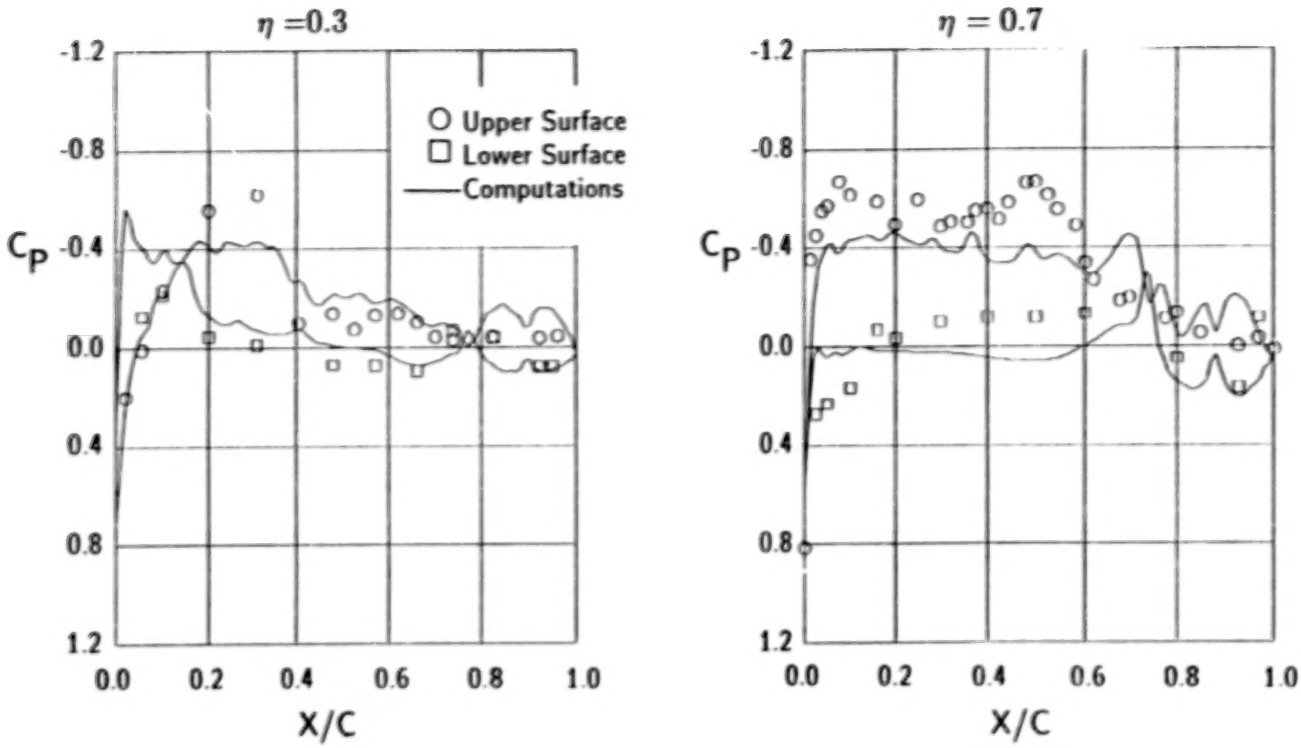

a) Wing

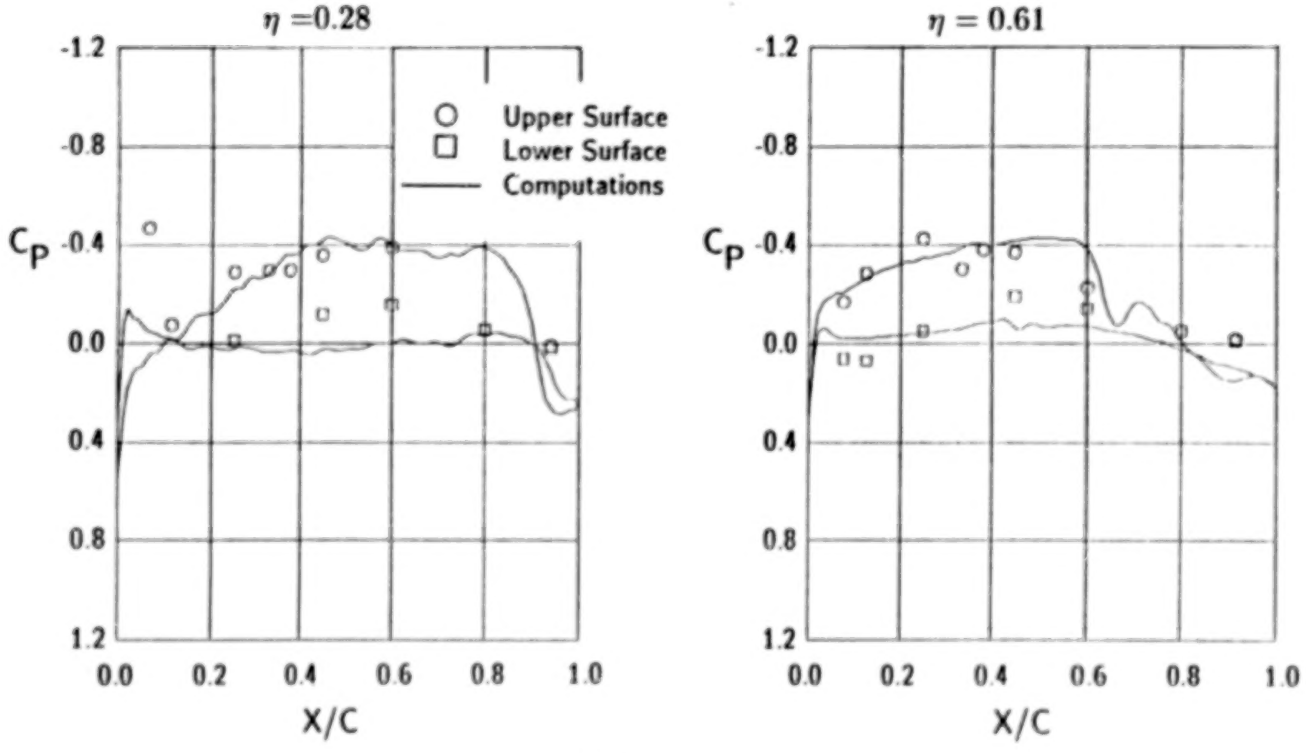

b) Canard

Figure 16 - Comparison of computational results and flight test data - M=0.91, $\alpha = 4.2°$

N91-24138

RESULTS OF CORRELATIONS FOR TRANSITION LOCATION ON A CLEAN-UP GLOVE INSTALLED ON AN F-14 AIRCRAFT AND DESIGN STUDIES FOR A LAMINAR GLOVE FOR THE X-29 AIRCRAFT ACCOUNTING FOR SPANWISE PRESSURE GRADIENT

S. H. Goradia
Vigyan Research Incorporated
Hampton, Virginia

and

P. J. Bobbitt; H. L. Morgan; J. C. Ferris; and W. D. Harvey
NASA Langley Research Center
Hampton, Virginia

SUMMARY

Results of correlative and design studies for transition location, laminar and turbulent boundary-layer parameters, and wake drag for forward swept and aft swept wings are presented in this paper. These studies were performed with the use of newly developed, improved integral-type boundary-layer and transition-prediction methods. Theoretical predictions were compared with flight measurements at subsonic and transonic flow conditions for the variable aft swept wing F-14 aircraft for which experimental pressure distributions, transition locations, and turbulent boundary-layer velocity profiles have been measured. Flight data were available at three spanwise stations for several values of sweep, freestream unit Reynolds number, Mach numbers, and lift coefficients. Theory/experiment correlations indicate excellent agreement for both transition location and turbulent boundary-layer parameters. The results of parametric studies carried out during the design of a laminar glove for the forward swept wing X-29 aircraft are also presented. These studies included the effects of a spanwise pressure gradient on transition location and wake drag for several values of freestream Reynolds numbers at a freestream Mach number of 0.9.

INTRODUCTION

The rise in jet fuel prices during the last decade, and uncertainties of the fuel costs for the future have been the cause of continued worldwide interest in improving military and commercial aircraft fuel efficiency. Additionally, improvements in the range of military aircraft are additional factors for achieving aircraft fuel efficiency and drag reductions. The most promising aerodynamic means of achieving significant gains in aircraft fuel efficiency is to design wings that provide extensive regions of laminar flow (refs. 1 and 2). Laminarization of the boundary layer on the surface of an

aircraft wing can be accomplished by the use of concepts such as Natural Laminar Flow (NLF), Laminar Flow Control (LFC), and a combination of NLF and LFC which is referred to as Hybrid Laminar Flow Control (HLFC).

Extensive regions of laminar flow can be maintained on a wing surface with the NLF concept by suitably tailoring the spanwise and chordwise pressure gradients to limit the amplification of disturbances that trigger the transition of the laminar boundary layer to a turbulent one. Flight tests at the Dryden Flight Research Facility on a variable sweep TACT F-111 Fighter aircraft (ref. 3) with an NLF wing glove have demonstrated that natural laminar flow can be maintained over significant areas at transonic speeds. Recent flight tests of a laminar clean-up glove (a thin, smooth fiberglass coating) on an F-14 aircraft with a variable-sweep wing (ref. 4), equipped with instrumentation for the accurate determination of transition, also revealed similar phenomena. Correlative studies were performed during the present study for the F-14 aircraft laminar wing, clean-up glove using the methods of references 5 and 6 extended to account for spanwise pressure gradient effects. Results of these studies are presented in this paper in the form of theory/experiment correlations for transition location and turbulent boundary-layer parameters. In addition, comparisons of the hot-film experimental data on the F-14 aircraft's wing glove with theoretical predictions are described.

The design of either forward- or aft-swept laminar flow wings at subsonic, transonic, or supersonic speeds, using NLF, HLFC, or LFC concepts requires the use of reliable theoretical computational methods. A number of finite-difference boundary-layer methods, stability methods, and full Navier-Stokes equation solvers are available; however, these methods are not well suited for the large number of calculations required for parametric wing design and optimization studies. Several new theoretical integral-boundary-layer methods (references 5, 6, 7, and 8) have small computer execution times and are very simple to use. These codes have the capability of predicting the laminar, transitional, and separating turbulent boundary layers for applications at subsonic, transonic, and supersonic Mach numbers.

The design studies reported in this paper involve the design of an NLF glove for the forward swept X-29 wing. The methods of references 5, 6, 7, and 8 have been modified for the present theoretical investigations to allow consideration of the effects of spanwise pressure gradient. Results are presented utilizing these modified codes for various spanwise pressure gradients and a prescribed streamwise pressure distribution to determine the extent of laminar flow on the corresponding X-29 wing glove. The wing sections' upper-surface geometrical changes required to obtain the prescribed pressure distribution are also given. Furthermore, the present design-optimization studies show qualitatively the procedure for optimizing values of spanwise gradients so as to minimize the wake drag with due consideration of the effect of imbedded shocks on the boundary layer. Finally a comparison of the extent of laminar flow on "equivalent" forward-swept and aft-swept wing configurations is made.

NOMENCLATURE

AR	aspect ratio
ASW	aft swept wing
c	chord
C_{D_i}	induced drag coefficient = $\frac{C_L^2}{\pi\ AR\ e}$
$C_{D_{wake}}$	wake drag coefficient
C_p	pressure coefficient or specific heat of air at constant pressure
$C_{p_{sonic}}$	pressure coefficient corresponding to local Mach number of 1.0
ΔC_{p_l} or ΔC_{p_c}	defined in figure 18
C_{1_i}	indicator of either growth or decay of disturbance for U component of velocity in transformed plane
C_{1_r}	downstream rate of propagation of disturbance for U component of velocity in transformed plane
C_{2_i}	indicator of either growth or decay of disturbance for W component of velocity in transformed plane
C_{2_r}	spanwise rate of propagation of disturbance of W component of velocity in the transformed plane
e	wing efficiency factor for induced drag
FSW	forward swept wing
H	form factor = $\frac{\delta^*}{\theta}$
L, M, N K, λ	groups of dimensionless parameters in transformed planes presenting the effects of suction, pressure gradient and curvature of velocity profiles. Each symbol defined in text.
L.E.	leading edge
M	Mach number (used only with subscripts)
N.F.	transition or instability due to normal flow
P	static pressure
P_r	Prandtl number

q — dynamic head

Q_x or Q_z — dimensionless parameter representing effects of suction and pressure gradient on the shape of velocity profile in transformed plane

$$Q_x = \frac{\delta^2_{T,s}}{\nu_o}\frac{dU_e}{dX} + \frac{V_s\delta_{T,s}}{\nu_o} \; ; \; Q_z = \frac{\delta^2_{T,z}}{\nu_o}\frac{dW_e}{dZ} + \frac{V_s\delta_{T,z}}{\nu_o}$$

R_∞ — freestream Reynolds number based on chord $= \dfrac{U_\infty c}{\nu_\infty}$

$R_{T,n}$ — $= \dfrac{\begin{pmatrix} Ue \\ or \\ We \end{pmatrix}\delta^{**}_{T,n}}{\nu_m}$

R_{inst} — value of $R_{T,n}$ at neutral point

R_{tran} — value of $R_{T,n}$ at transition

s,ξ,z — curvilinear coordinates in physical plane; s is normal to local sweep lines on wing surface, ξ normal to wing surface, and z normal to s-ξ plane in spanwise direction

S.F. — transition or instability due to spanwise flow

T — temperature, ^oR

T.E. — trailing edge

u,v,w — velocity components in physical planes in s, ξ and z directions, respectively

U,V,W — velocity components in transformed planes in X, Y, and Z directions, respectively

x,y — wing section coordinates in streamwise direction

X, Y — Stewartson's transformed coordinates

$$X = \int_o^s a\,\frac{a_e}{a_o}\,\frac{\rho_e}{\rho_o}\,ds; \qquad Y = \frac{a_e}{a_o}\,\frac{\rho_e}{\rho_o}\int_o^\xi \frac{T_e}{T}\,d\xi$$

Ψ_1 — disturbance stream function for transformed plane X-Y

Ψ_2 — disturbance stream function for transformed plane Z-Y

$\phi_{1(y)}$ — disturbance amplitude function for X direction in transformed plane

$\phi_{2_{(y)}}$ disturbance amplitude function for Z direction in transformed plane

α_1 2π/(wavelength of disturbance in transformed plane in X-direction)

α_2 2π/(wavelength of disturbance in transformed plane in Z-direction)

μ dynamic viscosity

α proportionality constant for viscosity-temperature relationship

ν kinematic viscosity

θ momentum thickness in physical s, ξ plane for 2-D or 3-D

normal direction $\theta = \int_0^\infty \frac{\rho u}{\rho_e u_e}\left(1 - \frac{u}{u_e}\right)d\xi$

$\theta_{T,\ X}$ momentum thickness in transformed X, Y plane for 2-D or 3-D

$= \int_0^\infty \frac{U}{U_e}\left(1 - \frac{U}{U_e}\right)dY$

$\theta_{T,Z}$ momentum thickness in transformed Z, Y plane

$= \int_0^\infty \frac{W}{W_e}\left(1 - \frac{W}{W_e}\right)dY$

$\theta_{p,s}$ $\int_0^{\delta_{p,s}} \frac{\rho u}{\rho_e u_e}\left(1 - \frac{u}{u_e}\right)d\xi$

$\theta_{p,z}$ $\int_0^{\delta_{p,z}} \frac{\rho w}{\rho_e w_e}\left(1 - \frac{w}{w_e}\right)d\xi$

$\theta_{p,n}$ $\int_0^{\delta_{p,n}} \frac{\rho u}{\rho_e u_e}\left(1 - \frac{w}{w_e}\right)d\xi$

$\delta_{p,n}$ greater of $\delta_{p,s}$ or $\delta_{p,z}$

δ	boundary-layer thickness in physical plane
δ^*	$= \int_0^{\delta} (1 - \frac{\rho u}{\rho_e u_e}) d\xi$
δ_T	boundary-layer thickness in transformed plane
$\delta^*_{T,X}$	displacement thickness in transformed X, Y plane for 2-D or 3-D $\int_0^{\infty} (1 - \frac{U}{U_e}) dY$
$\delta^*_{T,Z}$	displacement thickness thickness in transformed Z, Y plane $= \int_0^{\infty} (1 - \frac{W}{W_e}) dY$
$\delta^{**}_{T,X}$	$\int_0^{\delta_{T,n}} (1 - \frac{U}{U_e}) \frac{T_e}{T} dY$
$\delta^{**}_{T,Z}$	$\int_0^{\delta_{T,n}} (1 - \frac{W}{W_e}) \frac{T_e}{T} dY$
	$\delta_{T,n}$ greater of $\delta_{T,X}$ or $\delta_{T,Z}$
Λ	local sweep angle in degree
γ	ratio of specific heats for air
η	$= 2y/b$

Subscripts

o	stagnation condition
e,s	edge of boundary layer in s-direction
e,z	edge of boundary layer in z-direction
aw	adiabatic wall condition
m	mean or average value over boundary-layer thickness
N	normal section
p	physical plane

p,s	physical plane in s-direction
p,z	physical plane in z-direction
p,n	either p,s or p,z
s	direction normal to local sweep lines
T	transformed plane
T,X	transformed plane X-direction
T,Z	transformed plane in Z-direction
w	conditions at wall
X	transformed X-direction
Z	transformed Z-direction
L.E.	conditions at leading edge
T.E.	conditions at trailing edge
δ	parameter based on boundary-layer thickness
θ	parameter based on momentum thickness
∞	freestream value
S	measured in streamwise direction

In addition to the above list of symbols and subscripts, symbols and subscripts are also defined at appropriate places in the text.

DESCRIPTION OF THEORY

A description of the theory for the integral methods used to compute the laminar boundary layer, transition, and the turbulent boundary layer on a swept wing is given in references 5, 7, and 8. These theoretical methods were developed for infinite-span swept wings at subsonic and transonic speeds, and for two-dimensional airfoils and bodies of revolution at supersonic speeds. However, they did not include the effects of spanwise pressure gradient and the resulting effects on the location of transition. The boundary-layer "wash-out" phenomena are present on finite aft swept wing configurations with a given taper and twist, whereas the boundary-layer "wash-in" phenomena are present on configurations with forward sweep. The above theoretical methods of references

5, 6, and 7 have been extended in the present paper to account for the effects of spanwise pressure gradients on laminar boundary-layer transition. At the present time, the effects of suction on the extended method are not considered.

The theoretical programs, which have been developed and used in the present theoretical investigations of the wing glove of the F-14 aircraft and for the parametric design studies of the forward swept wing of the X-29 aircraft with a laminar flow glove, are classified and enumerated as follows:

1. Potential/Viscous Design and Analysis

   a. Perturbation Method of Characteristics for inverse design at transonic Mach numbers.

   b. Bauer-Garabedian-Korn Program for transonic analysis.

   c. NASA-Lockheed Multi-component Airfoil Program for subsonic analysis.

2. Boundary-Layer Analysis

   a. Integral Compressible Laminar Boundary-Layer Method with arbitrary chordwise pressure distribution and spanwise pressure gradient, sweep and suction at subsonic through high supersonic speeds.

   b. Short bubble and reattachment criteria.

   c. Instability and transition prediction due to leading-edge-normal and spanwise flow including the effects of spanwise pressure gradient.

   d. Separating turbulent boundary-layer method from subsonic to transonic speeds.

3. Method for computing $C_{D_{wake}}$ for an infinitely swept wing from subsonic through supersonic speeds.

4. Modified strip method to account for the effects of taper, sweep, and twist on wing-section characteristics.

The theoretical development of the laminar boundary-layer method for an infinitely swept wing will be briefly described. In addition, the methodology for determining the effects of spanwise pressure gradients on laminar boundary-layer growth and on transition location will be outlined.

Governing Equations

The usual governing equations for a compressible hydrodynamic boundary layer on an infinitely swept wing for the coordinate axis system shown in figure 1 are the continuity, streamwise momentum in s-direction, and momentum

in the ξ and z directions. The coordinate axis of figure 1 is chosen for the purpose of facilitating the application of the present theory to the design of the wing sections for an arbitrary wing planform. Moreover, the determination of the effect of the spanwise pressure gradient on the extent of laminar flow on swept wings by the present methods is greatly facilitated by the use of the coordinate axis system selected. Thus,

$$\frac{\partial(\rho u)}{\partial s} + \frac{\partial(\rho v)}{\partial \xi} = 0 \qquad \text{Continuity} \qquad (1a)$$

$$\rho u \frac{\partial u}{\partial s} + \rho v \frac{\partial u}{\partial \xi} = - \frac{\partial P}{\partial s} + \frac{\partial}{\partial \xi}\left(\mu \frac{\partial u}{\partial \xi}\right) + \text{(s-direction momentum)} \qquad (1b)$$

$$\frac{\partial P}{\partial \xi} = 0 \qquad \text{(Normal Momentum)} \qquad (1c)$$

$$\rho u \frac{\partial w}{\partial s} + \rho v \frac{\partial w}{\partial \xi} = + \frac{\partial}{\partial \xi}\left(\mu \frac{\partial w}{\partial \xi}\right) . \qquad \text{(z-direction spanwise momentum)} \qquad (1d)$$

The above equations (1) contain the terms consisting of variable physical properties, such as density ρ and dynamic viscosity μ. Variations of these properties across the boundary layer as well as along the flow direction are not negligible for laminar boundary-layer flow at transonic speeds and are accounted for. At supersonic speeds, variations in the physical properties are very large which means that there is a strong coupling between solutions of the hydrodynamic and thermal boundary-layer equations.

In order to simplify the governing equations (1) for solution by integral techniques while maintaining realistic computational results for the hydrodynamic and thermal boundary layers, the use of the following Stewartson's transformation is made:

$$X = \int_0^s \alpha \frac{a_e}{a_0} \frac{p_e}{p_0} ds \qquad (2)$$

$$Y = \frac{a_e}{a_0} \frac{\rho_e}{\rho_0} \int_0^\xi \frac{T_e}{T} d\xi$$

where α is the proportionally constant for the viscosity-temperature relationship, namely

$$\frac{\mu}{\mu_o} = \alpha \frac{T}{T_o} \tag{3a}$$

$$\alpha = \left(\frac{T_{aw}}{T_o}\right)^{1/2} \frac{T_o + 198.6}{T_{aw} + 198.6} \tag{3b}$$

$$\frac{T_{aw}}{T_o} = \frac{(1 + \sqrt{Pr}\,\frac{\gamma-1}{2} M_e^2)}{(1 + \frac{\gamma-1}{2} M_e^2)} \tag{3c}$$

Furthermore, if it is assumed that the viscous flow on the wing can be divided into a finite number of suitably oriented strips on its surface, and that each infinitesimal control volume of the strip is a portion of an infinite-span swept wing, then the governing equations of motion in the physical and transformed planes can be further simplified. The transformed boundary-layer equations using Stewartson's transformations, for infinite-span swept wing conditions, which can be derived from equations (1) with adiabatic wall temperature, are written as,

$$\frac{\partial U}{\partial X} + \frac{\partial V}{\partial Y} = 0 \tag{4a}$$

$$U \frac{\partial U}{\partial X} + V \frac{\partial U}{\partial Y} = U_e \frac{dU_e}{dX} + \nu_o \frac{\partial^2 U}{\partial Y^2} \tag{4b}$$

$$U \frac{\partial W}{\partial X} + V \frac{\partial W}{\partial Y} = \nu_o \frac{\partial^2 W}{\partial Y^2} . \tag{4c}$$

The relationships between the velocities within the boundary layer and the pressure gradients in the physical and transformed planes can be written ($Pr \approx 1$) as

$$U = \frac{a_o}{a_e} u; \quad V = \frac{a_o}{a_e} v \quad \text{(for adiabatic wall)}; \quad W = w \tag{5a}$$

$$\frac{dU_e}{dX} = \frac{1}{\alpha} a_o \frac{dM_e}{ds} (1 + \frac{\gamma-1}{2} M_e^2)^4 \tag{5b}$$

C-3

while the applicable boundary conditions in the transformed planes are given by,

$$@\ Y = 0 \rightarrow U = W = 0, \qquad V = V_s = -\frac{a_o}{a_e} v_w \tag{6a}$$

$$@\ Y = \delta_{T,X} \rightarrow U = U_e = a_o M_e, \quad \frac{\partial U}{\partial Y} = \frac{\partial^2 U}{\partial Y^2} = 0 \tag{6b}$$

and

$$@\ Y = \delta_{T,Z} \rightarrow W = W_e = w_e, \quad \frac{\partial W}{\partial Y} = \frac{\partial^2 W}{\partial Y^2} = 0 \tag{6c}$$

The compatibility conditions at the surface of the wing in the transformed planes can be written as,

$$@\ Y = 0 \rightarrow -V_s\left(\frac{\partial U}{\partial Y}\right)_w = U_e \frac{dU_e}{dX} + \nu_o\left(\frac{\partial^2 U}{\partial Y^2}\right)_w \tag{7a}$$

$$@\ Y = 0 \rightarrow -V_s\left(\frac{\partial^2 U}{\partial Y^2}\right)_w = \nu_o\left(\frac{\partial^3 U}{\partial Y^3}\right)_w \tag{7b}$$

and in the absence of suction for flows with spanwise pressure gradients,

$$\frac{1}{\rho}\frac{\partial P}{\partial z}\bigg|_{Y=0} = \frac{a_e}{a_o}\nu_o \frac{\partial^2 W}{\partial Y^2}\bigg|_{Y=0}. \tag{7c}$$

The integral equations in the transformed planes in the leading-edge normal direction X and in the spanwise direction Z can be derived by making use of equations (4), boundary conditions (6), and wall compatibility conditions equations (7), and by use of Leibnitz's rule.

Momentum Integral Equation in X-Direction, Infinite Swept Wing Conditions

$$U_e \frac{d}{dX}\left(\frac{K}{dU_e/dX}\right) = 2\left[L - K(H_{T,s} + 2) - S_{\theta_X}\right] \tag{8}$$

Momentum Integral Equation in Z-Direction, Infinite Swept Wing Conditions

$$\frac{d}{dX}\left[U_e W_e \int_0^{\delta_{T,n}} \frac{U}{U_e}\left(1 - \frac{W}{W_e}\right)dY\right] = \nu_o\left(\frac{\partial W}{\partial Y}\right)_{Y=0} - V_s W_e \qquad (9)$$

where $\delta_{T,n}$ is greater of $\delta_{T,Z}$ or $\delta_{T,X}$.

The symbols L, K, and S_θ appearing in the above equation (8) are defined in equation (20) for transformed X and Z coordinates.

The velocity profile assumptions for the flow in the X- and Z-directions in the transformed planes are given by the following equations,

$$\frac{U}{U_e} = A_1 \eta_X + A_2 \eta_X^2 + A_3 \eta_X^3 + A_4 \eta_X^4 \qquad (10a)$$

where

$$\eta_X = \frac{Y}{\delta_{T,X}},$$

and

$$A_1 = 2 + Q_X/6; \qquad A_2 = -0.5Q_X;$$
$$A_3 = -2 - A_2; \qquad A_4 = 3 - A_1 \qquad (10b)$$

$$\frac{W}{W_e} = 2\eta_Z - 2\eta_Z^3 + \eta_Z^4 \qquad (11)$$

where, $\eta_Z = \frac{Y}{\delta_{T,Z}}$,

The numerical solutions of equations (8) and (9) are performed by the Euler method with repeated iterations. These solutions give the shape of velocity profiles $\frac{U}{U_e}$ and $\frac{W}{W_e}$ in the transformed planes under the assumption of infinite-span swept-wing conditions.

EFFECTS OF BOUNDARY-LAYER WASH-IN/WASH-OUT DUE TO SPANWISE PRESSURE GRADIENTS ON TRANSITION ON FINITE, SWEPT, TAPERED, AND TWISTED WING

The results of theory/experiment correlations for several wings using both wind tunnel and flight-test data have indicated that for sweeps greater than approximately 25^{o}, and freestream Reynolds numbers greater than 20 million transition is triggered by spanwise flow in the z direction. Thus, for the purpose of designing laminar-flow wings and gloves at transonic and supersonic speeds at Reynolds numbers and sweeps of practical interest, it is necessary to consider the effects of boundary-layer wash-in/wash-out due to spanwise pressure gradients. This is especially important for wings of supersonic aircraft where the sweep of the leading edge is usually in excess of 45^{o}. In order to account for the effects of boundary-layer wash-in/wash-out on finite swept wings the approach shown schematically in figure 2 is used. This figure shows the infinitesimal control volume composed of surfaces of a trapezoid. The coordinate system is the orthogonal s, ξ and z axes where the s coordinate is normal to the local sweep line, z-coordinate is normal to s in the plane of wing, and the ξ-coordinate is normal to the s-z plane. A_1B_1 and C_1D_1 are constant s/c lines where c is the local chord in s-direction and A_1D_1 and B_1C_1 are parallel to s-direction.

The momentum theorem is applied in the z-direction, which states that the algebraic sum of the forces acting on the control volume ABCD - $A_1B_1C_1D_1$ in the z-direction is equal to the rate of change of momentum in control volume plus the net flux of momentum in the z-direction across the control surfaces of the control volume. For steady mean flow conditions an equation can be derived for the boundary-layer wash-in/wash-out due to spanwise pressure gradient effects on velocity profile $\frac{w}{w_e}$ in the z-direction. This equation in the physical coordinate system for transformed boundary-layer quantities can be written as:

$$\frac{1}{2}(\theta_{T,z})_N \frac{dC_p}{dz} = \left\{ \frac{\partial}{\partial z} \left[(\theta_{T,Z})_o \frac{W_e^2}{U_\infty^2} (1 + 0.2 M_{e,z}^2)^{0.5} \right] \right.$$

$$+ \frac{W_e}{U_\infty} \frac{u_e}{U_\infty} (1 + 0.2 M_{e,s}^2)^{0.5} \left[\frac{1}{M_{e,s}} \frac{d M_{e,s}}{ds} (\delta_{T,X})_o (0.7 + 0.00833 \Lambda_X) \right.$$

$$\left. + (0.7 + 0.00833 \Lambda_X) \frac{d}{ds} (\delta_{T,X})_o + 0.00833 (\delta_{T,X})_o \frac{d\Lambda_X}{ds} \right]$$

$$\left. - \frac{\mu_w}{\mu_o} \cdot \nu_o \cdot \frac{W_e}{U_\infty} \cdot \frac{1}{U_\infty} \frac{1}{(\theta_{T,z})_o} \cdot 0.235 \frac{(1 + 0.2 M_{e,s}^2)^{-3}}{(1 + 0.171 M_{e,s}^2)} \right\}$$

$$\cdot (1 + 0.2 M_{e,z}^2)^{-3} (1 + 0.2 M_\infty^2)^{2.5} / (8.547 + 0.711 M_{e,z}^2) \qquad (12)$$

where

$(\theta_{T,Z})_N$ = Transformed momentum thickness in Z-direction which is modified by the boundary-layer wash-in/ wash-out phenomena due to spanwise pressure gradients on finite-swept and tapered wing.

$(\theta_{T,Z})_o$ = Transformed momentum thickness in Z-direction for infinitely swept wing assumption conditions.

$\Lambda_X = (\delta^2_{T,X})_o \frac{1}{\nu_o} \frac{dU_e}{dX}$ = Dimensionless pressure gradient parameter in X-direction in transformed plane for infinite-span, swept-wing assumption conditions.

$(\delta_{T,X})_o$ = Transformed boundary-layer thickness in X-direction for infinite-span swept-wing assumption condition.

$\frac{\mu_w}{\mu_o} = \left(\frac{T_{aw}}{T_o}\right)^{1.5} \frac{T_o + 198.6}{T_{aw} + 198.6}$ due to Sutherland theory of viscosity.

The following approach is used for the purpose of calculating $(\delta_{T,Z})_N$ and the velocity profiles in the transformed plane in the spanwise direction in order to account for the boundary-layer wash-in or wash-out phenomena.

Define the quantities,

$$\Lambda_{Z_N} = (\delta^2_{T,Z})_N \left(\frac{1}{\nu_o} \frac{dW_e}{dZ}\right)$$

and, (13)

$$\beta_{Z_N} = (\theta^2_{T,Z})_N \left(\frac{1}{\nu_o} \frac{dW_e}{dZ}\right)$$

where:

$(\delta_{T,Z})_N$ = Transformed boundary-layer thickness in Z direction which is modified by the boundary-layer wash-in/wash-out phenoena due to spanwise pressure gradients on finite-swept and tapered wing.

If a fourth order velocity profile is assumed in the spanwise Z direction in the transformed plane, then the relation between Λ_{Z_N} and β_{Z_N} can be derived as the following polynominal:

$$\Lambda_{Z_N} = P_1 + P_2\beta_{Z_N} + P_3\beta^2_{Z_N} + P_4\beta^3_{Z_N} + P_5\beta^4_{Z_N} + P_6\beta^5_{Z_N}$$

where,

$P_1 = 0.032015$

$P_2 = 73.156$

$P_3 = 10.587$

$P_4 = -129.6$

$P_5 = 4669.6$

$P_6 = 43865.0$

thus, $(\delta_{T,Z})_N$ can be written as, $(\delta_{T,Z})_N = (\theta_{T,Z})_N / (\beta_{Z_N} / \Lambda_{Z_N})^{1/2}$.

The velocity profile $\frac{W}{W_e}$ in the transformed plane can therefore be calculated from the following assumed fourth order polynomial given by:

$$\frac{W}{W_e} = B_1\eta_Z + B_2\eta^2_Z + B_3\eta^3_Z + B_4\eta^4_Z$$

where,

$$\eta_Z = \frac{Y}{(\delta_{T,Z})_N} \quad \text{and } B_1 = 2 + \frac{\Lambda_{Z_N}}{6};\ B_2 = -\frac{1}{2}\Lambda_{Z_N}$$
$$B_3 = -2 - B_2;\ B_4 = 3 - B_1$$

THERMAL BOUNDARY-LAYER SOLUTION

Temperature variations within the boundary layer at subsonic speeds are small, hence the effects of temperature variations within the boundary layer on instability and transition at subsonic speeds are neglected. However, at high transonic and supersonic speeds, the heat generated by friction and adiabatic compression is quite significant. These phenomena give rise to large temperature variations across the boundary layer, and it has been found from computational experiments that these large temperature variations affect the following equations for computing temperature profiles; they can be derived using the procedures described earlier.

$$\frac{T - T_w}{T_{e_{Y=\delta_{T,X}}}} = \frac{T_w - T_{aw}}{T_{e_{Y=\delta_{T,X}}}} \left(\frac{U}{U_e}\right) - \sqrt{Pr}\,\frac{U_e^2}{2gC_pT_o}\left(\frac{U}{U_e}\right)^2 \qquad (14a)$$

$$\frac{T - T_w}{T_{e_{Y=\delta_{T,Z}}}} = \frac{T_w - T_{aw}}{T_{e_{Y=\delta_{T,Z}}}} \left(\frac{W}{W_e}\right) - \sqrt{Pr}\,\frac{W_e^2}{2gC_pT_o}\left(\frac{W}{W_e}\right)^2 \qquad (14b)$$

For determining the temperature profile at a given location on the wing use is made of either equations (14a) or (14b) depending upon whether $\delta_{T,X}$ is larger than $\delta_{T,Z}$ or vice versa. The velocity profiles $\frac{U}{U_e}$ or $\frac{W}{W_e}$ in the transformed planes in X or Z direction, which are required in equations (14a) or (14b), are dependent on local pressure gradients in the leading edge normal-s or spanwise-z directions due to use of equations (9) or (11), respectively. Thus, the effect of pressure gradient and suction is implicitly accounted for in the determination of temperature profiles by the present method.

Criteria for Determining Locations of Neutral Instabilities for Velocity Profiles in s and z Directions

The Orr-Sommerfeld equations in transformed planes for X and Z directions can be written as follows: For the transformed coordinate in the X-direction,

$$(U - C_1)(\phi_1'' - \alpha_1^2\phi_1) - U_{YY}\phi_1 = \frac{i}{\alpha_1 R_{\theta_{T,X}}}\left[\phi_1'''' - 2\alpha_1^2\phi_1'' + \alpha_1^4\phi_1\right] \qquad (15)$$

and for the transformed coordinate in the Z-direction,

$$(W - C_2)(\phi_2'' - \alpha_2^2\phi_2) - W_{YY}\phi_2 = \frac{i}{\alpha_2 R_{\theta_{T,X}}}\left[\phi_2'''' - 2\alpha_2^2\phi_2'' + \alpha_2^4\phi_2\right] \qquad (16)$$

The disturbance stream functions for the transformed X and Z directions are assumed, as for the physical plane, as the following types:

$$\Psi_1' = \phi_{1(Y)}e^{i\alpha_1(X - C_1t)} \quad \text{+ X-direction} \qquad (17a)$$

$$\Psi_2' = \phi_{2(Y)}e^{i\alpha_2(Z - C_2t)} \quad \text{+ Z-direction} \qquad (17b)$$

where,

$\phi_{1(Y)}$ and $\phi_{2(Y)}$ = disturbance amplitude function for X and Z direction, respectively in transformed planes

α_1 and α_2 = 2π/(disturbance wavelength in transformed planes in X- and Z-direction, respectively)

X = transformed coordinate for s-direction

Z = transformed coordinate for z-direction

$C_1 = C_{1_r} + iC_{1_i}$

$C_2 = C_{2_r} + iC_{2_i}$

complex in general

C_{1_i} or C_{2_i} = 0 corresponds to neutral instability

> 0 corresponds to amplification of disturbance

< 0 corresponds to decay of disturbance

The generalized solution between the dimensionless pressure gradient parameters and "equivalent" Reynolds number based on momentum thickness for the neutral stability of laminar boundary layers in either s or z direction is shown in figure 3. The curve shown in this figure is derived from solutions of the Orr-Sommerfeld equations, equations (15) and (16), in the transformed X-Y plane or Z-Y plane for appropriate fourth-order polynomial velocity profiles. The effects of pressure gradient in the s-direction or z-direction, local Mach number, temperature profile, and suction have been accounted for in the derivation of this curve. The abscissa of figure 3 is given as the zero suction ($S_\theta = 0$) version of

$$a_o \frac{1}{\alpha}\frac{1}{\nu}\left\{\begin{array}{c}\dfrac{\theta_{p,s}\, dM_{e,s}}{ds} \\ \text{or} \\ \dfrac{\theta_{p,z}\, dM_{e,z}}{dz}\end{array}\right\} \frac{1}{\left(1 + 0.2\left\{\begin{array}{c}M_{e,s}^2 \\ \text{or} \\ M_{e,z}^2\end{array}\right\}\right)^2} \cdot \left[1 - \frac{S_\theta}{\left(M + S_\theta \left\{\begin{array}{c}L_x \\ \text{or} \\ L_z\end{array}\right\}\right)}\right] \qquad (18)$$

where

$$\nu_m = \frac{1}{\delta_n} \int_0^{\delta_n} \nu d\xi$$

δ_n = greater of $\delta_{p,s}$ or $\delta_{p,z}$

$$\nu = \nu_o \left(1 + \frac{\gamma-1}{2} \begin{Bmatrix} M^2_{e,s} \\ \text{or} \\ M^2_{e,z} \end{Bmatrix}\right)^{1.5} \cdot \frac{T}{\begin{matrix} T_{e,s} \\ \text{or} \\ T_{e,z} \end{matrix}} \qquad (19)$$

In equation (19), the term $(\frac{T}{T_{e,s}})$ or $(\frac{T}{T_{e,z}})$ for temperature profile are substituted from equations (14a) or (14b).

It should be noted that because of the choice of the coordinate axis systems shown in figures 1 and 2, it is possible to use the same criteria shown in figure 3 for determining the neutral stability point for disturbances in both the normal and spanwise directions.

Boundary-Layer Transition Criteria

The criteria used in the present method for determining the transition location due to the amplification of disturbances either in the normal or spanwise directions are shown in figure 4. The parametric curves of figure 4 are valid for arbitrary specified pressure gradients - both in the normal as well as spanwise directions. The independent and dependent variables shown in this figure contain groups of several hydrodynamic and thermal boundary-layer parameters which are significant during the transition process. In deriving the curve for low values of freestream turbulence (less than .05 percent), the use of experimental data obtained in flight or low-turbulence wind tunnels is made and this information is put in the transformed planes. The dimensionless parameters shown in figure 4 have been derived from dimensional analyses and by making use of the laws of dynamic similarity. These physical dimensionless parameters consist of the following:

$$K_X = \frac{\theta^2_{T,X}}{\nu_o} \frac{dU_e}{dx} \; ; \quad K_Z = \frac{\theta^2_{T,Z}}{\nu_o} \frac{dW_e}{dZ}$$

$$L_X = \frac{\theta_{T,X}}{U_e} \left(\frac{\partial U}{\partial Y}\right)_{Y=0} \; ; \qquad L_Z = \frac{\theta_{T,Z}}{W_e} \left(\frac{\partial W}{\partial Y}\right)_{Y=0}$$

$$M_X = \frac{\theta_{T,X}^2}{U_e}\left(\frac{\partial^2 U}{\partial Y^2}\right)_{Y=0} \quad ; \qquad M_Z = \frac{\theta_{T,Z}^2}{W_e}\left(\frac{\partial^2 W}{\partial Y^2}\right)_{Y=0}$$

$$S_{\theta_X} = \frac{\theta_{T,X} V_s}{\nu_o} \quad ; \qquad S_{\theta_Z} = \frac{\theta_{T,Z} V_s}{\nu_o}$$

$$R_{N_X} = \frac{U_e \delta_n^{**}}{\nu_m} \quad ; \qquad R_{N_Z} = \frac{W_e \delta_n^{**}}{\nu_m}$$

$$\delta_{n_X}^{**} = \int_0^\infty \left(1 - \frac{U}{U_e}\right)\left(\frac{T_e}{T}\right) dn_X ; \qquad \delta_{n_Z}^{**} = \int_0^\infty \left(1 - \frac{W}{W_e}\right)\left(\frac{T_e}{T}\right) dn_Z$$

$$n_X = \frac{Y}{\delta_{T,X}} \quad ; \qquad n_Z = \frac{Y}{\delta_{T,Z}}$$

$$\frac{T}{T_e} = \begin{matrix}\text{Temperature} \\ \text{Profile}\end{matrix} = F\left(\frac{U}{U_e}, \frac{W}{W_e}, Pr, M_L, \begin{matrix}\text{pressure} \\ \text{gradient}\end{matrix}\right) \qquad (20)$$

In deriving the curves for several higher values of freestream turbulence greater than 0.05% shown in figure 4, use has been made of information presented in figure 5 for a zero pressure gradient and for values of Mach number from low subsonic to high supersonic (up to $M_\infty = 4.0$). It has been hypothesized in constructing the curves of figure 4 for values of freestream turbulence greater than 0.05 percent, that the effect of pressure gradient for freestream turbulence greater than 0.05 is similar to low values of freestream turbulence of 0.05. Curves for freestream turbulence higher than 0.05 percent, shown in figure 4, have been constructed by making use of information in figure 5 and using the above hypothesis.

It needs to be pointed out here that the curves of figure 5 can also be used for other types of disturbances, e.g., noise generated due to the turbulent boundary layer on the walls of the test section of supersonic wind tunnels. This objective can be accomplished after the application of appropriate calibration procedures.

Turbulent Boundary Layer

It has been known from experimental data on sections of NLF wings that if turbulent separation is present upstream of $x/c \approx 0.95$, then the design pressure distribution necessary to maintain laminar flow is degraded. Additionally, the wake drag will be quite high due to presence of the separated flow region. In the present paper turbulent boundary-layer separation is

accounted for by the method developed in reference 8. This turbulent boundary-layer method has already been successfully applied in the design of NLF and HLFC wing sections and for the prediction of wake drag.

To compute the turbulent boundary layer from the location of transition at various spanwise stations to the wing trailing edge, the method of reference 8 was modified to account for effect of spanwise flow assuming infinite swept wing conditions. The important objectives for the computations of the turbulent boundary layer are: (1) to see if turbulent separation is present downstream of the transition location, and (2) to determine the turbulent boundary-layer quantities at the wing trailing edge.

The theoretical method of reference 8 has been developed by analyzing the mean and fluctuating components of velocity profile data obtained by the use of a laser velocimeter for several airfoils with trailing-edge seperation. These experimental data indicated that as the turbulent boundary layer approached the separation location, the fluctuating velocity components become of the same order of magnitude as the mean velocity components within the turbulent boundary layer. This observation suggested the retention of the fluctuating-velocity components in the governing equations of motions as was done in reference 8. This method has been found to be extremely reliable in predicting turbulent boundary-layer quantities, including separation, on wing sections with thickness ratios in the range of $0.09 < t/c < 0.22$ and Reynolds numbers from 2 to 30 million.

Computations of $C_{D_{wake}}$ for Wing Sections

The derivation of the expression for $C_{D_{wake}}$ for an infinitely swept wing is given in Appendix A. This expression, which is valid from subsonic to supersonic speeds, is given as

$$C_{D_{wake}} = \frac{2}{c}\left[(\theta_{uu})_{T.E.}\left(\frac{\rho_e}{\rho_\infty}\right)_{T.E.}\left(\frac{u_e}{u_\infty}\right)^p \cos^2\Lambda_{T.E.} + (\theta_{uw})_{T.E.}\left(\frac{\rho_e}{\rho_\infty}\right)_{T.E.}\left(\frac{w_{e_{T.E.}}}{w_\infty}\right)\sin^2\Lambda_{T.E.}\right]$$

where the exponent p is given by

$$p = [H_{T.E.} + 5 + (\gamma-1)\overline{M_e^2}]/2.0 \qquad (21)$$

The $C_{D_{wake}}$ for a finite tapered swept wing can be computed from equation (21) and by making use of modified strip theory.

APPLICATIONS OF THE PRESENT THEORETICAL METHODS

The theoretical methods described in previous sections are utilized to perform two tasks in the following section, namely:

(i) The predition of transition location and turbulent boundary-layer parameters on the "clean-up" glove of the F-14 aircraft and correlation with experimental data.

(ii) Performing parametric studies for the design of a laminar glove for the forward swept wing of X-29 aircraft.

Correlation with Experimental Data on the Glove of F-14 Aircraft

The planform and instrumentation for the gloved F-14 wing with 20° sweep is shown in figure 6. With the "clean-up" glove installed, the sweep of the wing leading edge was varied from $\Lambda_{L.E.} = 20^{o}$ to $\Lambda_{L.E.} = 35^{o}$, and the flaps and slats were locked in the up position. As shown in figure 6, the three rows of surface pressure orifices are located at spanwise stations $\eta = 0.515$, 0.67, and 0.83, respectively, and were oriented in a direction parallel to freestream for the wing leading edge sweep $\Lambda_{L.E.} = 20^{o}$. In order to avoid interference between hot-film gauges, they were placed at an angle of 30^{o} to rows of surface pressure orifices as shown in this figure. The boundary-layer rakes were installed at two spanwise locations at $x/c = 0.55$ in order to measure the turbulent boundary-layer velocity profiles. Transition and turbulent boundary-layer data were obtained for freestream Mach numbers from 0.6 to 0.8, wing leading edge sweeps from 20^{o} to 35^{o}, and a Reynolds number range of 8×10^{6} to 25×10^{6}. Pressure distributions for the aforementioned three spanwise locations were also measured for these Mach numbers and sweeps. These pressure distributions constituted the boundary conditions for computing both the laminar and turbulent boundary layers and the transition location on the F-14 glove.

Figure 7(a) shows the pressure distributions on the upper surface of the glove at three spanwise locations and hot film traces at station 2 ($\eta = 0.67$) for the wing leading edge sweep of 20^{o}, $M_{\infty} = 0.7$ and a freestream Reynolds number based on chord of 13 million. In addition to using the pressure distributions as boundary conditions, they are used to evaluate the effect of spanwise pressure gradient on the development of the laminar boundary layer and transition location at station 2. Since the experimental pressure data only extended back to $x/c = 0.6$ theoretically computed pressures distributions were used from $x/c = 0.6$ to trailing edge in order to compute the growth of turbulent boundary layers from the transition location to the trailing edge. Figure 7(b) shows the computed results for chordwise transition and instability location due to normal flow (N.F.) and spanwise flow (S.F.) phenomena. The results are plotted in this figure as x/c of instability and transition versus freestream Reynolds number. These results indicate that at a Reynolds number of 13 million, the computed transition

location is due to N.F. phenomena and occurs at x/c = 0.33. The hot film trace shown in figure 7(a) shows that the experimental transition location at station 2 is between $0.3 < x/c < 0.4$. Thus, good agreement is obtained between the theoretically computed transition location and the hot-film-measured transition location. Figure 7(c) shows the results of computations for displacement thickness, δ^*/c, momentum thickness, θ/c, and form factor H, plotted against x/c for station 2. Freestream Mach number, Reynolds number, and leading edge sweep for the results shown in figure 7(c) are the same as for figures 7(a) and 7(b). Experimental data for δ^*/c, θ/c, and H at x/c = 0.55 for station 2 in the turbulent boundary-layer region are also plotted in figure 7(c). These results indicate that present theoretical computations for the turbulent boundary-layer parameters agree quite well with the experimentally measured quantities. Furthermore, these results indicate that the location of transition predicted by the present theory must be in close agreement with experimentally determined transition. It is also interesting to notice from figure 7(c) that the slope of θ/c versus x/c in the laminar flow region is smaller than that in the turbulent region. This large slope of θ/c versus x/c in the turbulent boundary-layer region will lead, of course, to large values of θ/c at the wing trailing edge. The wake drag coefficient, $C_{D_{wake}}$, is directly proportional to the momentum thickness, θ/c, at the trailing edge.

Figures 8(a) and 8(b) show plots of experimental pressure distributions and hot film traces for $M_\infty = 0.801$, a leading edge sweep of 20^0 and freestream Reynolds numbers of 11 million and 23 million, respectively. As can be seen from the comparison of pressure distributions in figures 8(a) and 8(b), there is not any noticeable difference in pressure distributions between Reynolds numbers of 11 and 23 million, and hence, the same pressure distributions at three spanwise stations were used for computations of transition and instability results for the range of Reynolds number shown in figure 8(c). These pressure distributions indicate that the shock strength is high, and for this reason, there seems to be some discrepancy in computed and measured turbulent boundary-layer parameters at x/c = 0.55, as shown in figure 8(e), even though the transition location is predicted quite accurately. The present shock boundary-layer model is being refined in order to provide better initial conditions for turbulent boundary-layer computations downstream of a strong shock.

As seen from figure 8(c), the computed transition location for a freestream Reynolds number of 11 million is at $x/c \approx 0.5$ and caused by N.F. phenomena, however, at a freestream Reynolds number of 23 million the computed results indicate that transition is caused by S.F. phenomena and occurs at x/c = 0.41. Experimental data from the hot film sensor shown in figure 8(a) indicate that at a Reynolds number of 11 million, transition occurs at $x/c \approx 0.5$. Hot film traces at a Reynolds number of 23 million, which are shown in figure 8(b), indicate that transition is occurring, for this freestream condition, at $x/c \approx 0.4$. Thus, as seen from comparisons of

computed results, shown in figure 8(c), with hot film traces of figures 8(a) and 8(b), the present theory reliably predicts both the location of transition as well as its mode, i.e., due to N.F. or S.F. phenomena. Figure 8(d) shows a plot of computed $C_{D_{wake}}$ as a function of freestream Reynolds number. As seen from this figure, $C_{D_{wake}}$ decreases as the freestream Reynolds number increases from 8 to 20 million and above the Reynolds number of 20 million $C_{D_{wake}}$ increase with Reynolds number. The Reynolds number of 20 million, where the computed $C_{D_{wake}}$ becomes minimum, corresponds to the initial triggering of transition due to spanwise flow. This is an important phenomena and one that can be used to advantage as seen in the design of a proposed laminar glove for X-29 aircraft discussed subsequently in this paper. Finally, figure 8(e) shows the plots of computed values of δ^*/c, θ/c and H versus x/c for a Reynolds number of 12.4×10^6.

Figure 9(a) shows the experimental pressure distributions and hot film traces for a wing-glove leading-edge sweep of 25^o, a freestream Mach number of 0.706 and a Reynolds number of 11 million. By using the experimental pressure distributions as boundary conditions (see figure 9(a)), the transition and instability locations are computed and the results are shown plotted in figure 9(b) as a function of freestream Reynolds number. Experimental data for transition obtained from hot film traces, shown in figure 9(a), indicate that transition for a wing glove leading edge sweep of 25.3^o, Reynolds number of 11 million, and $M_\infty = 0.706$ takes place for $0.4 < x/c < 0.5$. Theoretical results for these same conditions shown in figure 9(b) also show that transition should occur at an x/c between 0.4 to 0.5.

Now, it is generally believed that if the freestream Mach number is kept constant, that increasing wing sweep reduces the extent of laminar flow. However, experimental data and calculations for the wing-glove leading-edge sweep of 20^o and $M_\infty = 0.7$, (figures 7(a) and 7(b)) when compared to results for a sweep of 25^o, figures 9(a) and 9(b), show that transition is located closer to the leading edge for the lower sweep. Furthermore, comparison of the calculated results of figure 9(b) with those of figure 7(b) indicates the same phenomena. This is an unusual result and shows the ability of the present methods to optimize wing section geometries and planforms for extensive laminar flow regions at specified freestream conditions.

Figure 9(c) shows the results of theoretical computations for the laminar and turbulent boundary-layer parameters δ^*/c, θ/c and H plotted versus x/c for a leading-edge sweep of 25^o, M_∞ of 0.704 and a Reynolds number of approximately 11 million. For this case, strong shocks are not present at any spanwise station, as can be seen from figure 9(a). The computed boundary-layer parameters agree quite well in the turbulent boundary-layer region at $x/c = 0.55$. This agreement of computations with experiment in the turbulent boundary-layer region is an indication that the computed transition location

is fairly close to the experimental transition location. Moreover, these results indicate the reliability of the present theoretical turbulent boundary-layer method.

Figure 10(a) shows the experimental pressure distributions and hot film traces for a leading-edge sweep of 29.7^{o}, M_{∞} = 0.704, and a Reynolds number of 9.5 million. The corresponding experimental data for a Reynolds number of 19.2 million and leading edge sweep of 31.4^{o} are shown in figure 10(b). Figure 10(c) shows theoretical results for instability and transition locations for a leading-edge sweep of 30^{o} and M_{∞} = 0.704. These results show that for a Reynolds number of 9 million transition takes place at x/c = 0.34 and is caused by S.F. instability phenomena. Experimental data obtained by hot-film sensors, shown in figure 10(a), for a Reynolds number of 9 million indicate similar results, namely transition takes place at an x/c between 0.3 to 0.4. At a Reynolds number of 19.2 million (figure 10(c)), transition due to S.F. takes place at x/c $\approx$ 0.175; experimental hot film trace data for the same freestream conditions, shown in figure 10(b), also indicate that transition occurs between x/c of 0.1 to 0.2.

Design and Parametric Studies for Laminar Glove of X-29 Aircraft

It has been observed from theoretical studies and experimental data that wing sweep have a pronounced effect on transition location when the freestream Mach number and Reynolds number are held constant. It is also believed by many, from a conceptual view point, that it is easier to achieve large laminar-boundary-layer-flow regions on a forward swept wing (FSW) than on an aft swept wing (ASW). This is so because for FSW the local values of sweep are lower near the leading edge and the local sweep angle increases from the leading edge to the trailing edge; whereas, for ASW, sweep angle is the largest near the leading edge and decreases progressively toward the trailing edge. Figure 11(a) shows schematically a comparison of planforms for "equivalent" FSW and ASW. The word "equivalent" implies that for both FSW and ASW, wing area, aspect ratio, taper ratio, and shock locations are identical. Figure 11(b) shows the plots of local sweep angle versus x/c for FSW and ASW of aspect ratio of 4 and taper ratio of 0.4. The planform and variation of sweep angle with x/c shown in figures 11(a) and 11(b) are a rough approximation of the X-29 aircraft wing. The point C in figure 11(b), which is at the intersection of local sweep versus x/c curves for the "equivalent" FSW and ASW, indicates that the local sweep angles for these "equivalent" wings become equal at x/c $\approx$ 0.5. Thus the possibilities of maintaining laminar flow for x/c < 0.5 on an NLF glove for the FSW of X-29 aircraft are much greater than they would be for an "equivalent" ASW with a laminar glove.

It is possible to realize an additional advantage from forward swept wings and this stems from the lower shock-wave drag. If the NLF design pressure distribution is such that the minimum C_p on the upper surface occurs aft of x/c $\approx$ 0.5, then the local Mach number at the shock location for FSW

will be lower than that ahead of the shock on an "equivalent" ASW for the same value of the freestream Mach number. This is so because the local sweep angle for FSW is higher than that for an equivalent ASW downstream of point C ($x/c \simeq 0.5$) as can be seen from figure 11(b). These phenomena would result in lower shock wave drag for FSW for the NLF design glove of X-29 aircraft, and moreover, the susceptibility of the NLF design for FSW to turbulent separation is also diminished. This is because the initial turbulent boundary-layer thickness at the shock location would be lower for the FSW than for the equivalent ASW.

The above discussion suggests that better prospects exist for overall lower total drag for an NLF concept with FSW than one with an equivalent ASW. The superior drag peformance due to application of NLF (or HLFC) concepts to a FSW arise due to the possibility of achieving larger chordwise runs of laminar boundary-layer flow, lower shock wave drag, and less susceptibility to turbulent separation drag.

Figure 12 shows the planform of the X-29 aircraft. The canard and wing are in the same plane. The wing has a leading-edge sweep of approximately 29^{o} and the trailing-edge sweep is 45^{o}. The chord of the first flap extends from $x/c = 0.75$ to $x/c = 0.9$ and that of the second flap extends from $x/c = 0.9$ to $x/c = 1.0$. The wing leading-edge break is at $\eta = 0.25$, and the tip of the canard is at $\eta = 0.49$. Experimental pressure distributions on the canard suggest that boundary-layer flow separation exists on the canard and the possibility exist that the separated wake of the canard may prohibit the achievement of laminar flow on the wing between the wing root and the midspan location. The forward swept wing has associated with it the boundary-layer wash-in phenomenon, and for this reason it is believed that a laminar glove can be designed so as to obtain extensive laminar flow on the outboard wing from $\eta = 0.55$ to $\eta = 0.95$.

Simple-sweep methods or modified simple-sweep methods are frequently used in the design of airfoil sections for aft swept wings. Different forms of modified simple-sweep methods are employed but they give essentially the same results. The present modified simple sweep approach for ASW is illustrated in figure 13. The geometry of the normal section is arrived at from the geometry of the streamwise section by the following expression:

$$(z/c)_{\text{Normal section}} = \frac{(z/c)_{\text{streamwise section}}}{\cos \Lambda_L}$$

where,

$$\Lambda_L = \text{local value of sweep}$$

$$= \Lambda_{LE} + (\Lambda_{TE} - \Lambda_{LE}) \cdot (x/c)$$

The pressure distribution is computed for the normal section by airfoil programs, such as, Bauer, Garabedian, and Korn program (ref. 9) or Lockheed-NASA multi-Component airfoil program (ref. 10). The computations for the normal section Mach number and lift coefficient are made using

$$M_{\infty_N} = M_{\infty_S} \cdot \mathrm{Cos}\Lambda_{effective}$$

where,

M_{∞_N} = effective component of freesteram Mach number for normal section

M_{∞_S} = streamwise freestream Mach number

and, $\Lambda_{effective}$ = Λ @ x/c = 0.25 for subsonic and transonic freestream

Mach numbers

and

$$C_{L_N} = C_{L_S} / \mathrm{Cos}^2\Lambda_{effective}$$

where,

C_{L_N} = lift coefficient for normal section

C_{L_S} = lift coefficient for streamwise section

The thickness of the normal section for the aft wing section is thus greater than that of the streamwise section by the factor of $1/\mathrm{Cos}\Lambda_L$. The pressure distribution computed for this normal section (with $M_{\infty_N} = M_{\infty_S} \mathrm{Cos}\Lambda_{eff}$ and $C_{L_N} = C_{L_S} / \mathrm{Cos}^2\Lambda_{eff}$) is related to the pressure distribution for the streamwise section by,

$$C_{P_{Streamwise}} = C_{P_{Normal}} \cdot \mathrm{Cos}^2\Lambda_L$$

The application of the above-mentioned modified sweep approach to the computation of the pressure distribution for the forward swept wing of the X-29 at $\eta = 0.7$, $M_\infty = 0.91$ and $C_N = 0.351$ is shown in figure 14. It is apparent from this figure that the theoretical pressure distribution computed by the above-mentioned modified simple sweep method for aft swept wings does not agree with the experimental data for the FSW of X-29 aircraft. Consequently a new modified simple sweep approach was developed for the computation of pressure distributions for forward swept wings. In this approach, the ordinates of the upper surface of the normal section are kept

the same as for the streamwise section but the thickness distribution for the normal section is increased by the cosine of the local sweep angle and is given by

$$(t/c)_{\substack{\text{Local}\\\text{Normal}\\\text{Streamwise}}} = (t/c)_{\substack{\text{Local}\\\text{Streamwise}\\\text{Section}}} / \cos\Lambda_L$$

The remaining steps for the computation of the streamwise pressure distribution are the same as for the aft swept wing. Both procedures are illustrated in figure 13. The results of computations of the streamwise pressure distributions, using the new modified simple sweep method, for the X-29 aircraft for $\eta = 0.7$, $M_\infty = 0.91$ and $C_L = 0.351$ are shown in figure 14. As seen in this figure, the agreement between the theoretical upper surface pressure distribution computed by the new modified simple sweep method and experimental data is reasonably good. Hence, the parametric studies for the design of the outboard laminar-glove sections are conducted using this approach.

In order to enlarge the extent of laminar flow for the X-29 wing, by the installation of a wing glove, it is first necessary to determine the extent of laminar flow on the existing X-29 wing. Theoretical computations for instability and transition locations on the existing X-29 wing at $\eta = 0.7$ are plotted in figure 15(a) as a function of freestream Reynolds number. Experimental pressure distributions are used for boundary conditions in this calculation. The computed wake drag coefficient for the existing wing section at $\eta = 0.7$ is plotted as a function of freestream Reynolds number in figure 15(b). The results shown in figures 15(a) and 15(b) illustrate that the extent of laminar flow on the existing X-29 wing is quite limited and, consequently, the wake drag is high for Reynolds numbers in the range of 8 to 30 million.

A number of pressure distributions and corresponding glove geometries have been theoretically investigated in the present studies, under the assumption of infinite-span swept-wing conditions. It is necessary that the glove geometry be compatible with original X-29 wing such that the glove wraps the wing surface with continuous first and second derivatives, and that there be a smooth merging of the glove with the original wing surface. From these considerations, the glove with the geometrical shape designated as XTM2P3K, and shown in figure 16 for spanwise station $\eta = 0.7$ was developed. The geometry of the baseline X-29 for the spanwise station of $\eta = 0.7$ is also shown in figure 16 for comparison purposes. Figure 17(a) shows the computed streamwise pressure distribution for this glove at $\eta = 0.7$ for $M_\infty = 0.905$, $C_{L_S} = 0.435$ and a leading-edge sweep of 30^0. The computed pressure distribution for $C_{L_S} = 0.351$ for the baseline section is also shown in figure 17(a) for comparison. It is important to note the shape of $C_{p_{sonic}}$ in figure

17(a). For the forward swept tapered wing, the $C_{p_{sonic}}$ line has an upward slope, whereas for the "equivalent" ASW the $C_{p_{sonic}}$ line will have a downward slope. These phenomena suggest, for the specified freestream Mach number and value of C_p just upstream of the shock, that the FSW will have a smaller value of shock wave drag than the ASW.

The streamwise pressure distribution computed for the glove with a L.E. sweep of 25^o, and $C_{L_s} = 0.43$ is shown in figure 17(b); since the sweep is lower, the design freestream Mach number was lowered to a value of 0.865 (as compared to an M_∞ of 0.905 for sweep of 30^o). The reason that the Mach number was lowered was to keep the leading-edge normal Mach numbers constant. The theoretical transition characteristics for the X-29 glove for leading-edge sweeps of 30^o and 25^o and zero spanwise pressure gradients are shown in figure 17(c). As seen from figure 17(c), the S.F. instability triggers the transition at a Reynolds number of 12 million for a leading edge sweep of 30^o, and at a Reynolds number of 15 million for a leading edge sweep of 25^o.

Figure 17(d) shows a comparison of the wake drag characteristics for the X-29 glove for leading edge sweeps of 30^o and 25^o. Also plotted in figure 17(d) is the wake drag of the baseline section for a leading-edge sweep of 30^o. These comparisons indicate the following phenomena, first, the wake drag of the glove is lower than the basic X-29 wing section by as much as 17 to 18 counts at a Reynolds number of 10.5 million, and second, when the leading-edge sweep is reduced from 30^o to 25^o, the freestream Reynolds number at which $C_{D_{wake}}$ becomes minimum is increased from 10.5 million to 16 million. However, it may not be possible to reduce the wing glove leading-edge sweep to 25^o because of stability and control considerations.

As stated previously in the theoretical section, the methods of references 5, 6, and 7 have been extended in the present studies to take into account the effects of boundary-layer wash-in/wash-out and spanwise pressure gradients on the development of the laminar boundary layer as well as instability and transition locations. Thus, it was possible to conduct parametric studies on the effects of boundary-layer wash-in phenomena and spanwise pressure gradients on the triggering of transition due to S.F. phenomena. Proper use of spanwise gradients can delay transition to higher Reynolds numbers and result in a wake drag reduction at the cruise Reynolds number. Figures 18(a) and 18(b) show the two types of spanwise pressure gradients which have been utilized to study the effect of spanwise pressure gradients on transition. In figure 18(a), constant spanwise pressure gradients are assumed on the upper surface from $0 < x/c < 0.6$; computations have been performed for spanwise gradients, ΔC_{p_c}, of 0.05, 0.1 and 0.15. For the linearly varying spanwise pressure gradients depicted in figure 18(b), the spanwise pressure gradient is a maximum near the leading edge and it decreases

linearly to zero at x/c = 0.6. Computational results are presented for ΔC_{P_1} values of 0.05, 0.1, and 0.15. Instabilities and transition characteristics due to N.F. and S.F. and wake drag characteristics for the various spanwise pressure gradients shown in figures 18(a) and 18(b) have been determined. A few representative results are shown in figures 19 and 20. Figure 19 shows the plots of N.F. and S.F. transition characteristics for a constant spanwise pressure gradient corresponding to $\Delta C_{P_c} = 0.15$. Also plotted in figure 19 for comparison are the results for N.F. and S.F. transition characteristics on the laminar-flow glove for a spanwise pressure gradient of zero. It can be seen from these results that the Reynolds number at which S.F. triggers transition increases from 12 to 20 million as the spanwise pressure gradient is changed from zero to $\Delta C_{P_c} = 0.15$ (see figure 18(a)). Furthermore, notice the change in N.F. transition characteristics for these two cases. Calculations indicate that turbulent separation does not occur in either of the cases shown in figure 19.

Figure 20 shows the plots of $C_{D_{wake}}$ versus freestream Reynolds number for the various constant spanwise gradients, including zero, considered in the present study. Thus, the results shown in figure 20 illustrate the ability of the present theory for increasing the design Reynolds number for minimum wake drag by controlling spanwise pressure gradients. It is necessary to point out here that constant spanwise pressure gradient increases the shock strength of the inboard spanwise location, $\eta = 0.49$ and decreases it at the outboard station, $\eta = 0.91$. It is likely that these shock strengths (figure 18(a)) will yield different pressure recoveries than that assumed.

Another way to obtain a spanwise gradient is to fix the shock strength and vary the pressure levels near the leading edge. Figure 21 shows the computational results for transition due to N.F. and S.F. phenomena for such a pressure distribution i.e., the linearly varying spanwise pressure gradient, shown in figure 18(b) ($\Delta C_{P_1} = 0.15$) . Also shown in figure 21 are the theoretical transition characteristics for an X-29 glove when the spanwise pressure gradient is assumed to be zero (infinite-span swept wing conditions). Results of figure 21 illustrate that the triggering of transition due to S.F. is delayed from a Reynolds number of 12 million to 16 million due to the effect of spanwise pressure gradient. In addition, the shock strength remains constant along the span when the linearly varying spanwise pressure gradient is assumed. Thus, when the linearly varying spanwise pressure gradient is specified, the shock wave drag remains the same as for a zero spanwise pressure gradient, and also the adverse effect of increased shock strength on the laminar glove design is eliminated.

Figure 22 shows the plots of computed $C_{D_{wake}}$ versus freestream Reynolds number for linearly varying spanwise pressure gradients for several values of ΔC_{P_1}. Also shown are computations for a spanwise pressure gradient of zero for comparison purposes. The results shown in figure 22 further illustrate how the present theory can be used for delaying transition Reynolds number due to triggering of S.F. instabilities by approximately 6 million above the zero spanwise-pressure gradient value by the use linearly varying spanwise pressure gradients. Neither induced drag, C_{D_i}, or shock wave drag are adversely affected.

Comparison Between Equivalent Forward and Aft Swept Wing Concepts for Laminar Flow

A comparison of planforms and local sweep variations for FSW and ASW with an aspect ratio of 4 and a taper ratio of 0.4 is shown in figure 11. The pressure distribution and spanwise pressure gradient selected for making a comparison of laminar flow regions on equivalent FSW and ASW is a linearly varying spanwise pressure gradients with $\Delta C_{P_1} = 0.15$. This spanwise pressure gradient corresponds approximately to that provied by an elliptical spanwise load distribution for both FSW and equivalent ASW. The results of computations for transition locations as a function of the freestream Reynolds number for these "equivalent" wings are shown in figure 23(a) and calculations of $C_{D_{wake}}$ versus freestream Reynolds number are shown in figure 23(b). Figure 23(a) shows that extent of laminar flow for FSW is 15 to 35 percent more than the equivalent ASW for Reynolds numbers from 8 to 30 million. The wake drag for FSW at freestream Reynolds number of 16 million, which corresponds to flight condition for the X-29 aircraft at $M_\infty = 0.905$ and $C_L = 0.435$, is lower by 21 counts than the equivalent ASW.

The comparison shown in figures 23(c) and 23(d) assumes a favorable spanwise pressure gradient that provides a spanwise flow that is opposite to that normally obtained on ASW; this provides a spanload that deviates from the elliptical and causes an increase in C_{D_i} for ASW. Results of computations of the extent of laminar flow, shown in figure 23(c), indicate the extent of laminar flow for FSW is still larger by 7 to 20 percent over the "equivalent" ASW. A comparison of $C_{D_{wake}}$ values under this assumption, as shown in figure 23(d), indicates that for ASW the minimum value of $C_{D_{wake}}$ occurs at a Reynolds number of 11.5 million, whereas for FSW, $C_{D_{wake}}$ becomes a minimum at a freestream Reynolds number of 16.5 million. Moreover, values of $C_{D_{wake}}$ for the range of Reynolds number from 8 to 30 million are lower for FSW than the equivalent ASW.

It is necessary to point out that even though the FSW concept, in general, is better for a laminar-flow wing than the equivalent ASW, it is possible to determine other pressure distributions and spanwise pressure gradients for ASW that yield larger extents of laminar flow than shown in figure 23. The insight for obtaining the conditions for large laminar flow regions for highly swept ASW, especially for supersonic flow conditions, can be obtained by going through an optimizaiton process for chordwise pressure distribution and spanwise pressure gradients as has been done for FSW of X-29 aircraft in the present studies.

CONCLUDING REMARKS

(1) The present integral methods for computing laminar boundary-layer properties and transition have been extended to take into account boundary-layer wash-in/wash-out phenomena and the effects of spanwise pressure gradient on transition for the purpose of delaying transition due to S.F. instabilities.

(2) The above method has been applied to predict transition phenomena on the clean-up glove of the F-14 aircraft. Good agreement has been obtained between the predicted location of transition and experimental data as a function of Reynolds number, Mach number, and wing leading edge sweep. The results of the present studies for the F-14 aircraft wing glove, as well as those of references 5, 6, and 7, indicate that once transition occurs due to S.F., the transition location moves upstream very fast with even slight increase in freestream Reynolds number. Thus, by the use of the present method the wing-section geometry can be designed and spanwise pressure gradient specified in such a manner that transition due to S.F. pheonomena can be substantially delayed. This facilitates obtaining larger laminar-flow regions and making the wing performance less susceptible to minor changes in Reynolds number and Mach number.

(3) Comparisons of the computed displacement thicknesses, momentum thicknesses, and form factors in turbulent boundary-layer regions on the glove of a F-14 aircraft by the present turbulent boundary-layer method with experimental data for several freestream conditions and wing sweeps indicated good agreement. This implies that not only is the present turbulent boundary-layer theory quite reliable, but the transition location prediction is accurate as well.

(4) The extent of laminar flow computed for the F-14 wing glove for a leading-edge sweep of 25^{0} and $M_{\infty} = 0.7$ was larger than that computed for the smaller sweep value of 20^{0}. The experimental data obtained from hot film traces also revealed this unusual pheonomena. This provides additional evidence of the ability of the present method to optimize wing sections as well as the planforms for obtaining large extents of laminar flow.

(5) The effective sweep procedure which is normally used for ASW, when used to compute the streamwise pressure distribution on the FSW of the X-29 aircraft, did not yield good correlation with experimental results. The new effective sweep procedure established during the present study for FSW gives reasonable predictions of streamwise pressure distributions when compared to experimental data for the X-29 wing.

(6) By the use of the method of characteristics, in conjunction with the effective sweep procedure established for FSW, section geometries were established for the outboard glove for the wing of the X-29 so as to obtain the desired chordwise pressure distributions for leading-edge sweeps of 30^{o} and 25^{o}. The computed transition and wake drag characteristics were also computed and compared for these sweeps. The methods were also used to compute transition and wake drag for the basic outboard wing section. This was done for assumed "infinite-span swept-wing" conditions. The wake drag for the investigated glove section was quite superior to the basic section, and the glove with a leading-edge sweep of 25^{o} had a minimum value of $C_{D_{wake}}$ at freestream Reynolds number of 16 million as compared to 10.5 million for a sweep of 30^{o}.

(7) Several spanwise pressure gradients, both constant and linearly varying, for $x/c = 0$ to $x/c = 0.6$ on the upper surface gloves, were investigated for their ability to delay the transition due to S.F. phenomena at $M_{\infty} = 0.905$. It was concluded from these parametric studies that both linearly varying and constant-increment spanwise pressure gradients provided beneficial effects on skin friction drag at the flight condition considered.

(8) Computational experiments were performed to determine the extent of laminar flow on FSW and "equivalent" ASW for identical chordwise pressure distributions and spanwise pressure gradients. This comparison indicated that the FSW concept is superior for achieving large regions of laminar flow and lower wake drag than an "equivalent" ASW concept.

APPENDIX A

Expression for Wake Drag for Infinitely Swept Wing

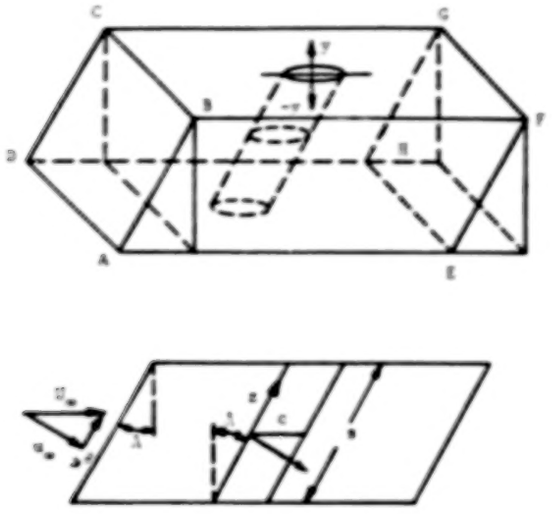

Figure A1. - Coordinate system used for wake drag derivations.

Consider control volume ABCD-EFGH as shown in figure A1 above for a wing with sweep angle Λ. The x-coordinate is perpendicular to the leading edge, the z-coordinate is parallel to leading edge, the y-coordinate is perpendicular to the wing surface, S is equal to wing span as shown, and c is the chord of wing in the direction of flow.

$$\text{Net mass balance across the control volume} = \int_{-\infty}^{\infty} \rho_\infty U_\infty S \cos \Lambda \, dy - \int_{-\infty}^{\infty} \rho u S \, dy = 0 \qquad (A1)$$

Drag = Net momentum flux across control volume

$$= \int_{-\infty}^{\infty} \rho U_\infty^2 S \cos \Lambda \, dy - \int_{-\infty}^{\infty} \rho u S (u \cos \Lambda + w \sin \Lambda) dy \qquad (A2)$$

Multiply equation (A1) by U_∞ and subtract from (A2)

$$\text{Drag} = \int_{-\infty}^{\infty} \rho U_\infty u S(\cos^2 \Lambda + \sin^2 \Lambda)dy - \int_{-\infty}^{\infty} \rho u S(u \cos \Lambda + w \sin \Lambda)dy$$

$$= S \cos \Lambda \, \rho_\infty u_\infty^2 \int_{-\infty}^{\infty} \frac{\rho u}{\rho_\infty u_\infty}\left(1 - \frac{u}{u_\infty}\right)dy$$

$$+ S \sin \Lambda \, \rho_\infty u_\infty w_\infty \int_{-\infty}^{\infty} \frac{\rho u}{\rho_\infty u_\infty}\left(1 - \frac{w}{w_\infty}\right)dy \qquad \text{(A3)}$$

or

$$C_{D_{wake}} = \frac{\text{Drag}}{\frac{1}{2}\rho_\infty U_\infty^2 \, S{\cdot}c \cos \Lambda}$$

$$= \frac{\text{Drag}}{\frac{1}{2}\rho_\infty u_\infty^2 \sec^2 \Lambda{\cdot}S{\cdot}c \cos \Lambda}$$

$$= 2\left\{\frac{\theta_{uu_\infty}}{c}\cos^2 \Lambda + \frac{\theta_{uw_\infty}}{c}\sin^2 \Lambda\right\} \qquad \text{(A4)}$$

where

$$\theta_{uu_\infty} = \int_{-\infty}^{\infty} \frac{\rho u}{\rho_\infty u_\infty}\left(1 - \frac{u}{u_\infty}\right)dy$$

$$\theta_{uw_\infty} = \int_{-\infty}^{\infty} \frac{\rho u}{\rho_\infty u_\infty}\left(1 - \frac{w}{w_\infty}\right)dy$$

For swept wings as well as bodies of revolution the boundary-layer parameters at the trailing edge can be calculated by the theoretical methods described in the main body of this paper. Equation (A4) gives $C_{D_{wake}}$ in terms of conditions downstream at infinity. The following derivations show how boundary-layer parameters at the trailing edge are related to viscous flow quantities at infinity.

The momentum integral equation in the wake in the streamwise direction, either for swept wing or for body of revolution can be written as

$$\frac{d\theta_x}{dx} + \frac{\theta_x}{u_e}\frac{du_e}{dx}\left(2 + \frac{\delta^*_x}{\theta_x}\right) + \frac{1}{\rho_e}\frac{d\rho_e}{dx}\theta_x = 0 \qquad \text{(A5)}$$

where

$$\theta_x = \theta_{uu} \text{ of equation (A4)}$$

By integrating equation (A5) in the wake from the trailing edge to downstream infinity, and after algebraic manipulations the following equation is obtained

$$\left[\ln\left\{\theta_x \rho_e \left(\frac{u_e}{u_\infty}\right)^{(H_x+2)}\right\}\right]_{T.E.}^{\infty} = \int_{T.E.}^{\infty} \ln\left(\frac{u_e}{u_\infty}\right) dH \qquad \text{(A6)}$$

The hypothesis is made that in the wake the following relationship is valid.

$$\ln \frac{U_{e_T}}{U_{\infty_T}} = \ln \frac{U_{e_T}}{U_{\infty_{T.E.}}} \cdot \frac{H_{x_T}-1}{H_{x_{T_{T.E.}}} - 1} \qquad \text{(A7)}$$

The following equation can be derived by making use of Stewartson's transformation for a Prandtl number equal to one.

$$H_x = H_{T_x} \left(1 + \frac{\gamma-1}{2} M_e^2\right) + \frac{\gamma-1}{2} M_e^2 \qquad \text{(A8)}$$

H_x = streamwise form factor in physical plane

H_{x_T} = streamwise form factor in transformed plane

Substitution of equations (A7) and (A8) into (A5) and simplification results in the following equation

$$\theta_{uu_{(\infty)}} = \theta_{uu_{T.E.}} \cdot \frac{\left(1 + \frac{\gamma-1}{2} M_{e,s}^2\right)_{T.E.}^{-2.5}}{\left(1 + \frac{\gamma-1}{2} M_\infty^2\right)^{-2.5}} \cdot \left(\frac{u_{e_{T.E.}}}{u_\infty}\right)^p \qquad \text{(A9)}$$

where,

$$p = \{H_{T.E.} + 5 + (\gamma-1)\overline{M_e^2}\}/2$$

$\sqrt{\overline{M_e^2}}$ Root mean square Mach number in the wake from trailing edge to infinity downstream

Equation (A4) for $C_{D_{wake}}$ for a swept wing contains the crossflow momentum thickness term, θ_{uw_∞}. In order to evaluate this crossflow component of momentum thickness, use is made of the momentum equation in the spanwise direction for an infinite-span swept wing. Thus,

$$\rho u \frac{\partial w}{\partial x} + \rho v \frac{\partial w}{\partial y} + \rho w \frac{\partial w}{\partial z} = - \frac{\partial p}{\partial z} + \frac{\partial}{\partial y} \left(\mu \frac{\partial w}{\partial y} \right) \tag{A10}$$

The infinite-span swept-wing assumption implies

$$\frac{\partial}{\partial z} (\ ) = 0 \tag{A11}$$

and the continuity equation under the same assumption yields,

$$\rho v = - \int_0^y \frac{\partial}{\partial x} (\rho u) dy \tag{A12}$$

Along the locus of minimum velocity in the wake $\frac{\partial w}{\partial y} = 0$. Substituting (A11) and (A12) into (A10) and integrating with respect to y in the wake from 0 to δ_z, the following form of momentum integral equation in the wake can be derived.

$$\frac{d}{dx} \left[\rho_e u_e w_e \int_0^{\delta_z} \frac{\rho u}{\rho_e u_e} \left(1 - \frac{w}{w_e}\right) dy \right] = 0$$

$$\frac{d}{dx} \left[\rho_e u_e w_e \, \theta_{uw} \right] = 0$$

$$\theta_{uw_\infty} = \left(\frac{\rho_{e_{T.E.}}}{\rho_\infty}\right)\left(\frac{u_{e_{T.E.}}}{u_\infty}\right)\left(\frac{w_{e_{T.E.}}}{w_\infty}\right)(\theta_{uw})_{T.E.} \tag{A13}$$

Thus, $C_{D_{wake}}$ can be written from equations (A4), (A9), and (A13) as:

$$C_{D_{wake}} = \frac{2}{c} \left[(\theta_{uu})_{T.E.} \left(\frac{\rho_e}{\rho_\infty}\right)_{T.E.} \left(\frac{u_e}{u_\infty}\right)^p \cos^2 A_{T.E.} \right.$$

$$\left. + (\theta_{uw})_{T.E.} \left(\frac{\rho_e}{\rho_\infty}\right)_{T.E.} \left(\frac{w_{e_{T.E.}}}{w_\infty}\right) \sin^2 A_{T.E.} \right] \tag{A14}$$

Equation (A14) contain terms evaluated at the trailing edge, such as $(\theta_{uw})_{T.E.}$, $(\theta_{uu})_{T.E.}$, $(\rho_e)_{T.E.}$, and $(u_e)_{T.E.}$. These values are computed in the framework of computer programs for boundary-layer methods, (refs. 5, 6, 7, and 8) and pressure-distribution prediction methods such as those of references 9 and 10.

REFERENCES

1. Harvey, William D.; Harris, Charles D.,; Brooks, Cyler W., Jr., Bobbitt Percy, J.; and Stack, John P.: Design and Experimental Evaluation of Swept Supercritical LFC Airfoil. NASA CP-2398, Vol. I, Langley Symposium on Aerodynamics, April 23-25, 1985.

2. Bobbitt, P. J.; Waggoner, E. G.; Harvey, W. D.; and Dagenhart, J. R.: A Faster "Transition" to Laminar Flow. SAE Paper 851855, October 14-17, 1985.

3. Meyer, R. R.; and Jennett, L. A.: In Flight Surface Oil Flow Photographs with Comparison to Pressure Distribution on Boundary-Layer Data. NASA TP 2393, April 1985.

4. Meyer, R. R.; Trujillo, B. M.; and Bartlett, D. W.: F-14 VSTEF and Results of the Cleanup Flight Test Program. NLF and LFC Research Symposium, NASA Langley Research Center, March 16-19, 1987.

5. Goradia, Suresh H.; and Morgan, Harry L.: Theoretical Methods and Design Studies for NLF and HLFC Swept Wings at Subsonic and Transonic Speeds. Natural Laminar Flow and Laminar Flow Control Symposium, NASA Langley Research Center, Hampton, VA, March 16-19, 1987.

6. Goradia, S. H.; Bobbitt, P. J.; Ferris, J. C.; and Harvey, W. D.: Theoretical Investigations and Correlative Studies for NLF, HLFC, and LFC Swept Wings at Subsonic, Transonic and Supersonic Speeds. SAE Technical Paper 871861, presented at the Aerospace Technology Conference and Exposition, Long Beach, CA, October 5-8, 1987.

7. Goradia, S. H.; Bobbitt, P. J.; and Ferris, J. C.: Correlative and Design Studies for NLF and HLFC Swept Wings at Subcritical and Supercritical Mach Numbers. Paper presented at the 1986 SAE Aerospace Technology Conference and Exposition, Long Beach, CA, October 13-16, 1986.

8. Goradia, S. H.; and Morgan H. L.: A New, Improved Method for Separating Turbulent Boundary Layer for Aerodynamic Performance Prediction of Trailing-Edge Stall Airfoils. Paper presented at AIAA 4th Applied Aerodynamics Conference, June 9-11, 1986, San Diego, CA.

9. Bauer, F.; Garabedian, P.; and Korn, D.: A Theory of Supercritical Wing Sections with Computer Programs and Examples, Vol. 66, Lecture Notes in Economics and Mathematical Systems, Springer-Verlag, 1972.

10. Stevens, W. A.; Goradia, S.; and Braden, J. A.: Mathematical Model for Two-Dimensional Multi-Component Airfoils in Viscous Flow. NASA CR-1843, 1971.

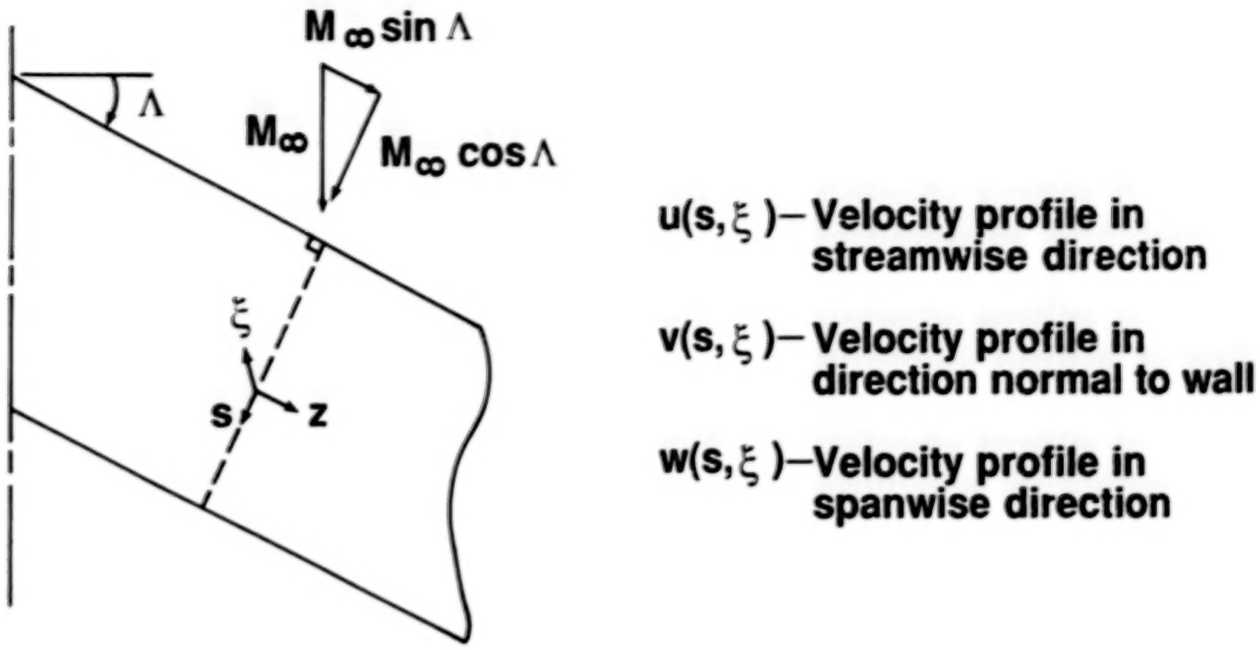

Figure 1. - Definition of coordinate axis system.

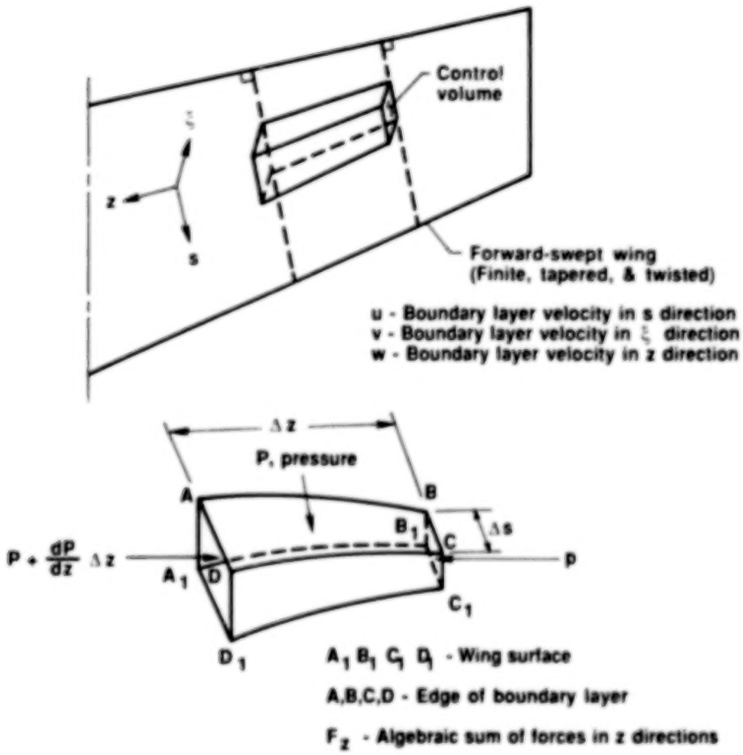

Figure 2. - Schematic of control volume used to account for boundary-layer wash-in/wash-out phenomena.

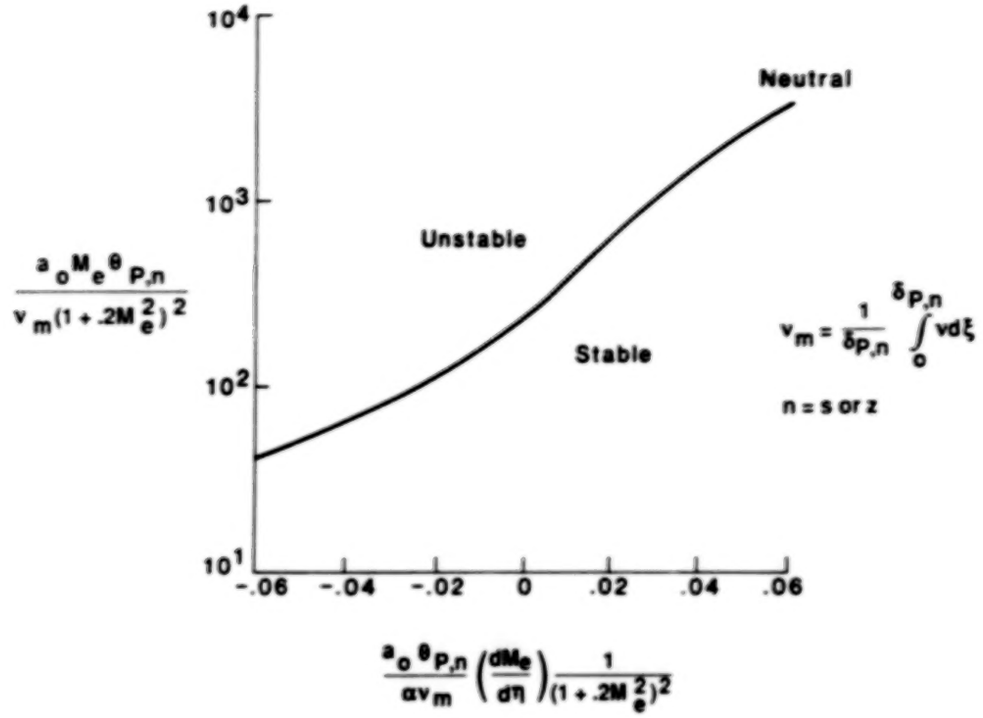

Figure 3. - Criteria for determining laminar boundary-layer neutral instability.

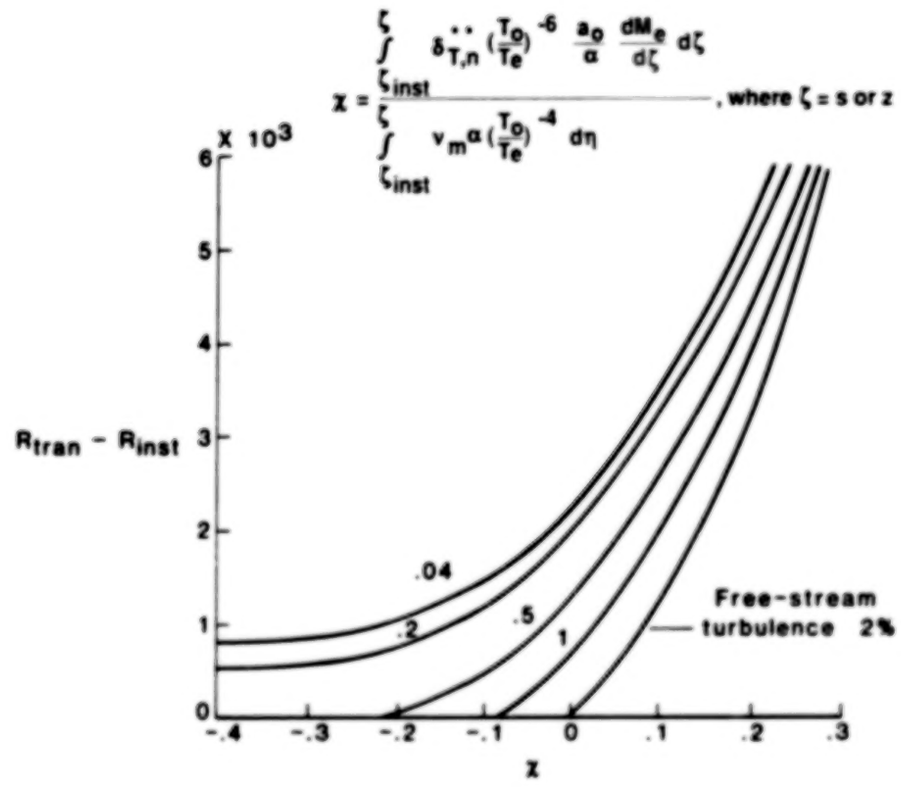

Figure 4. - Criteria for determining laminar boundary-layer transition.

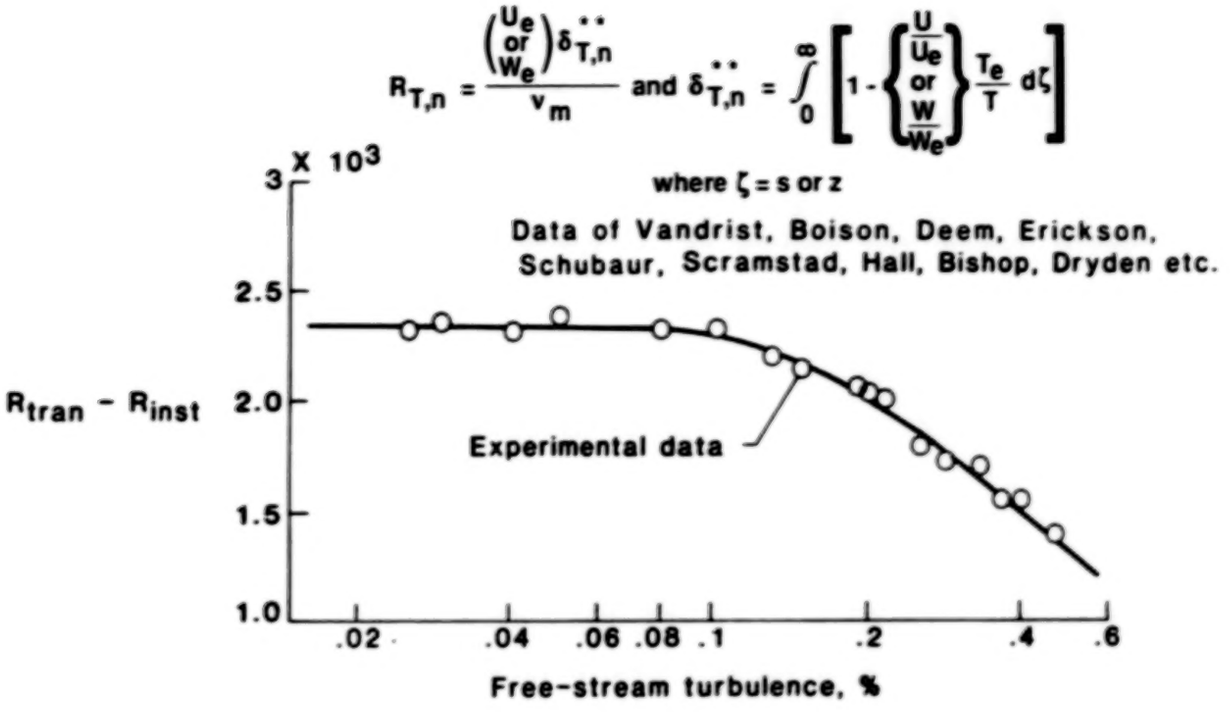

Figure 5. - Effect of free-stream turbulence on the difference of transition and instability Reynolds numbers.

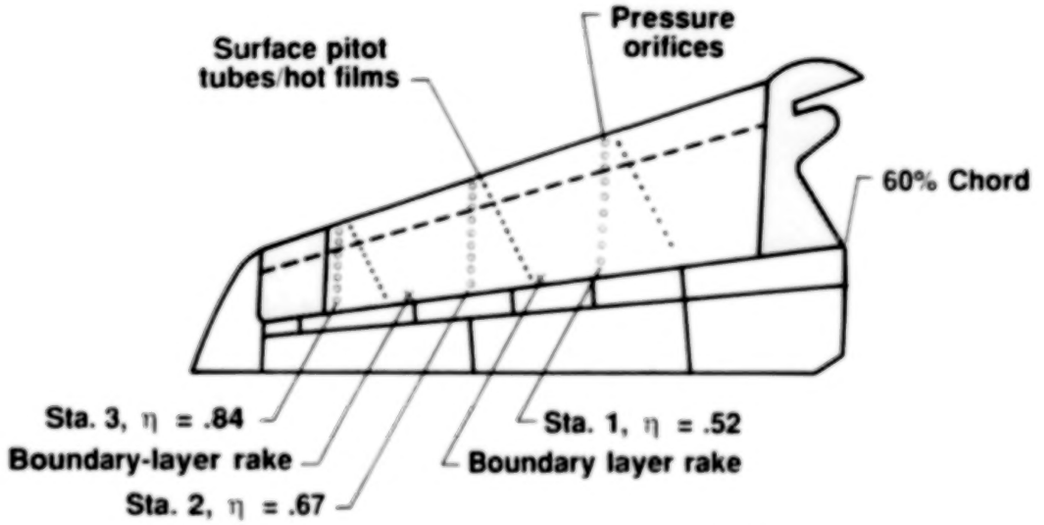

- Three rows of flush static pressure orifices
- Three rows of surface pitot tubes
- Five hot-film gauges
- Two boundary-layer rakes

Figure 6. - Planform of an instrumentation on the gloved F-14 wing.

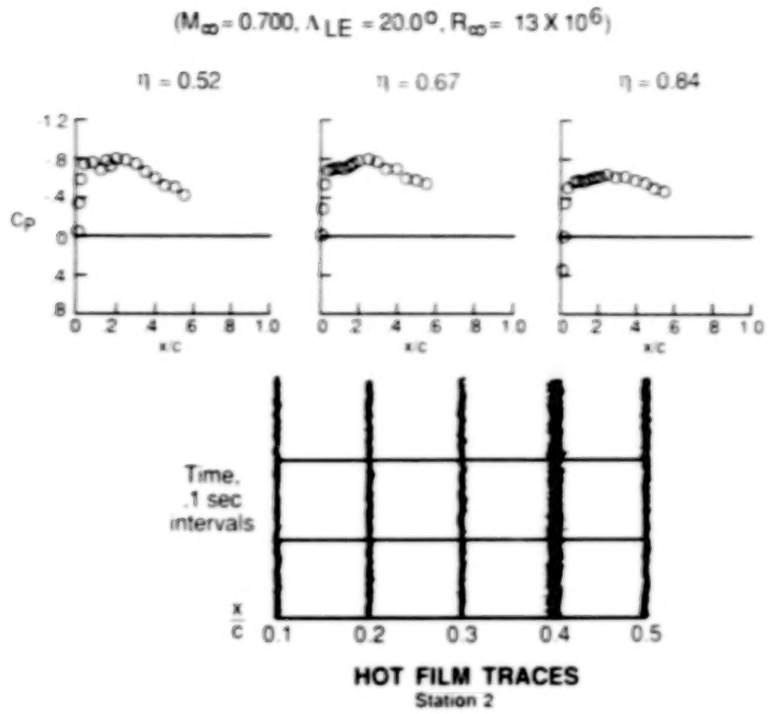

(a) Experimental pressure distributions and hot-film traces.

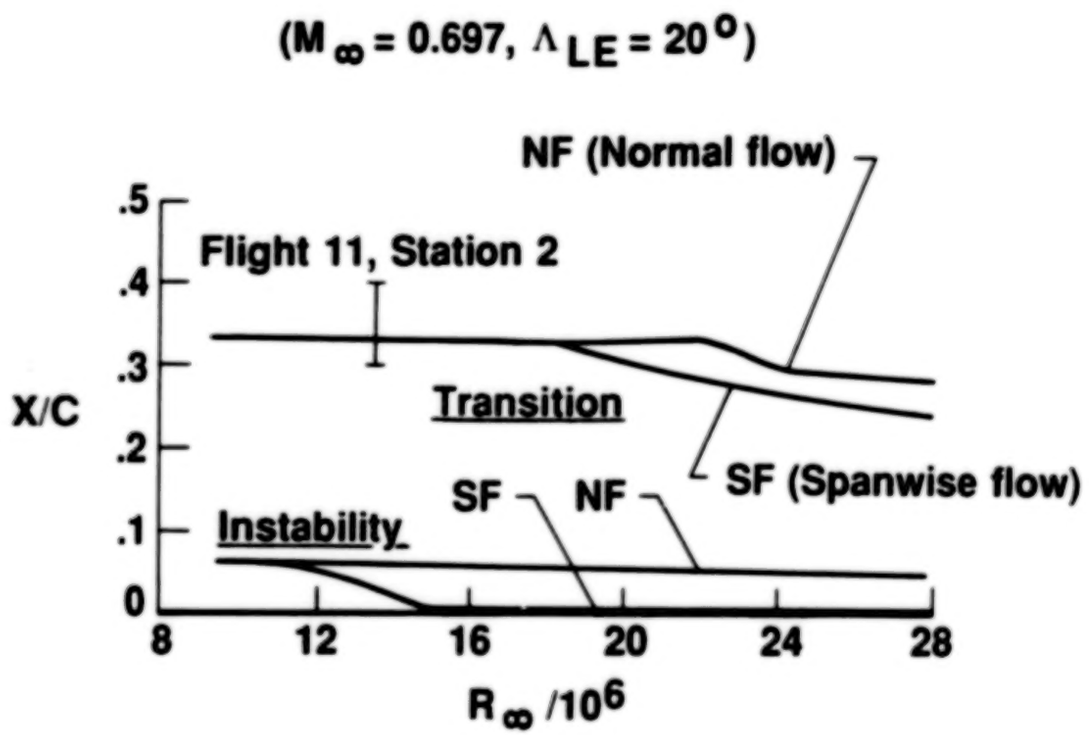

(b) Computed transition locations as a function of free-stream chord Reynolds number.

Figure 7. - Results for the F-14 "clean-up" gloved wing for a leading- edge sweep of 20° and M_∞ of 0.7.

$(M_\infty = 0.697,\ \Lambda_{LE} = 20^o,\ R_\infty = 13.6 \times 10^6)$

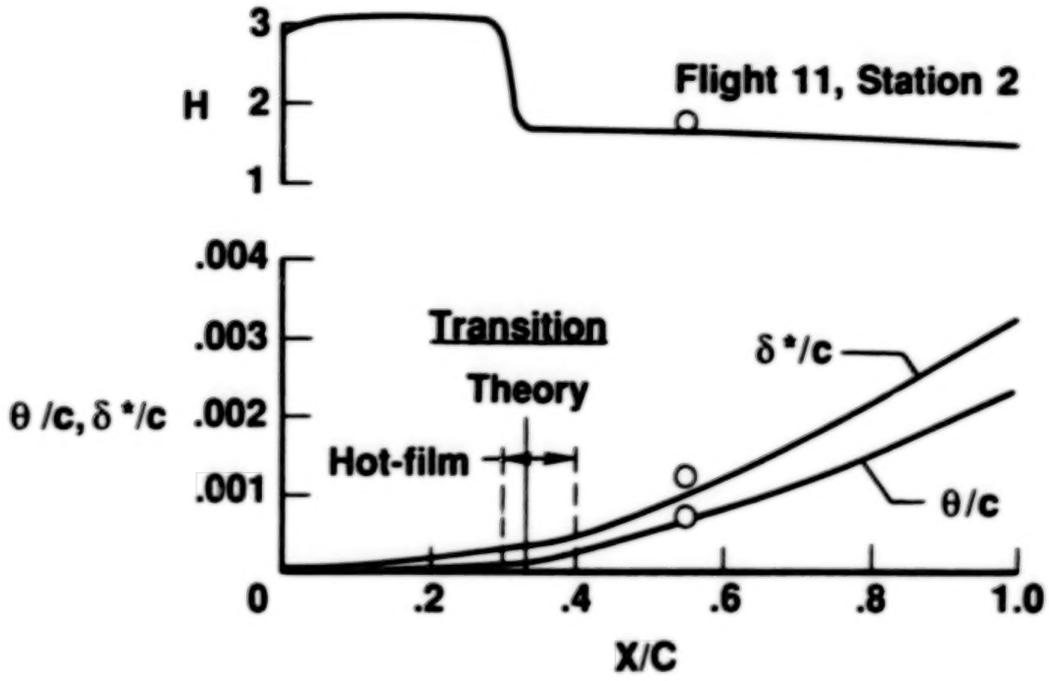

(c) Comparison between computed and flight boundary-layer parameters for $R_\infty = 13 \times 10^6$.

Figure 7. - Concluded.

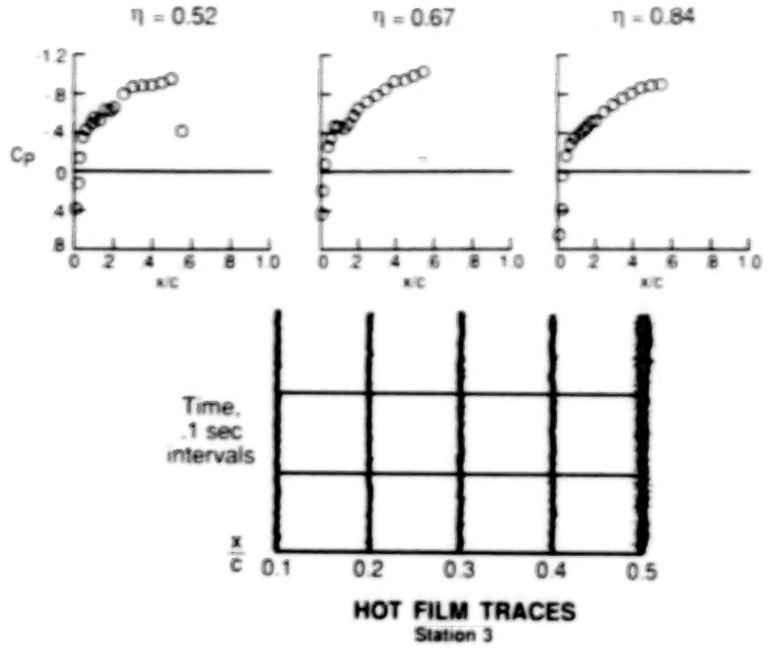

(a) Experimental pressure distributions and hot-film traces for $R_\infty = 11 \times 10^6$.

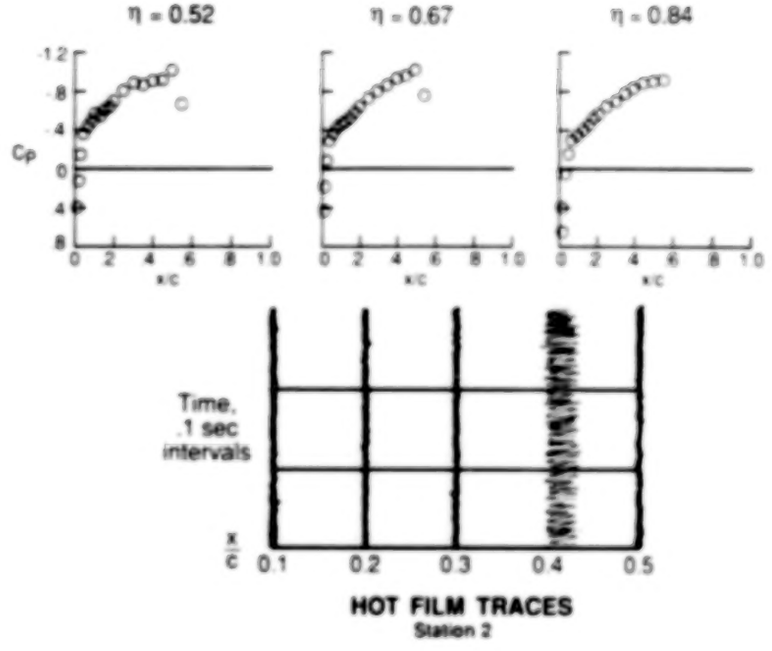

(b) Experimental pressure distributions and hot-film traces for $R_\infty = 23 \times 10^6$.

Figure 8. - Results for the F-14 "clean-up" gloved wing for a leading-edge sweep of 20° and M_∞ of 0.8.

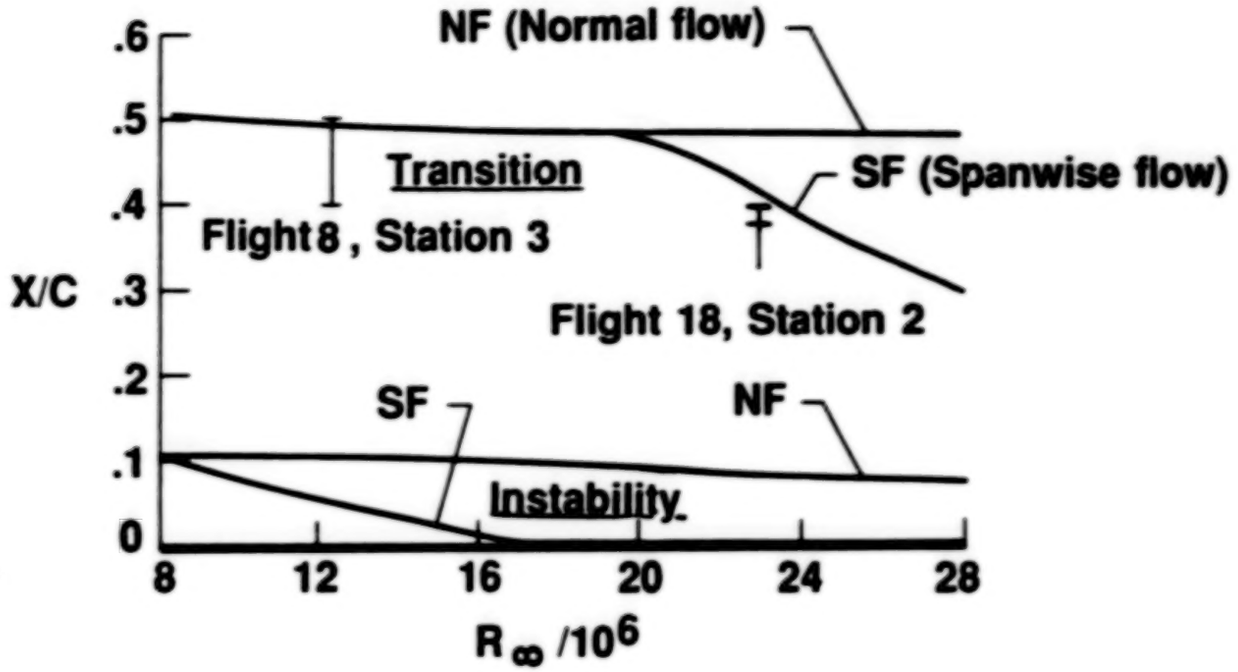

(c) Computed transition and instability locations versus free-stream Reynolds number.

$(\Lambda_{LE} = 20^o$, Station 3)

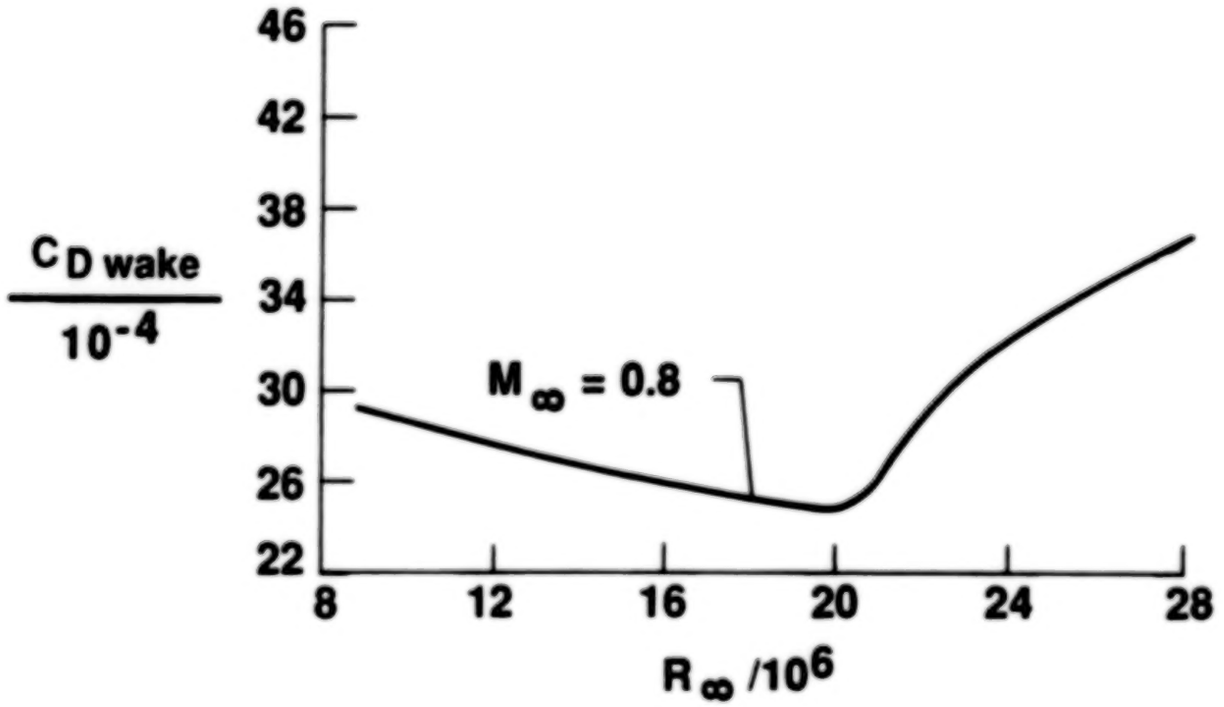

(d) Computed $C_{D_{wake}}$ versus free-stream chord Reynolds number.

Figure 8. - Continued.

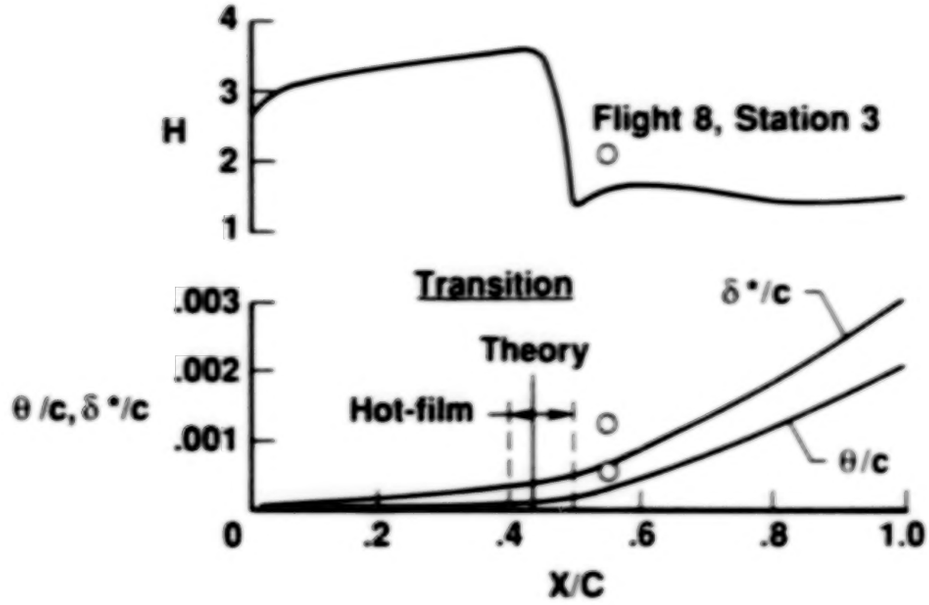

(e) Comparison between computed and flight boundary-layer parameters for $R_\infty = 12.4 \times 10^6$.

Figure 8. - Concluded.

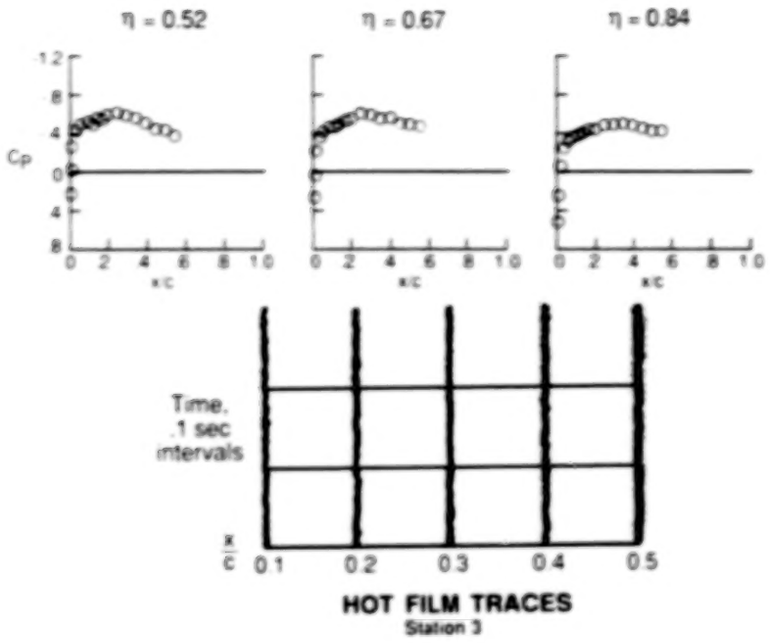

(a) Experimental pressure distributions and hot-film traces.

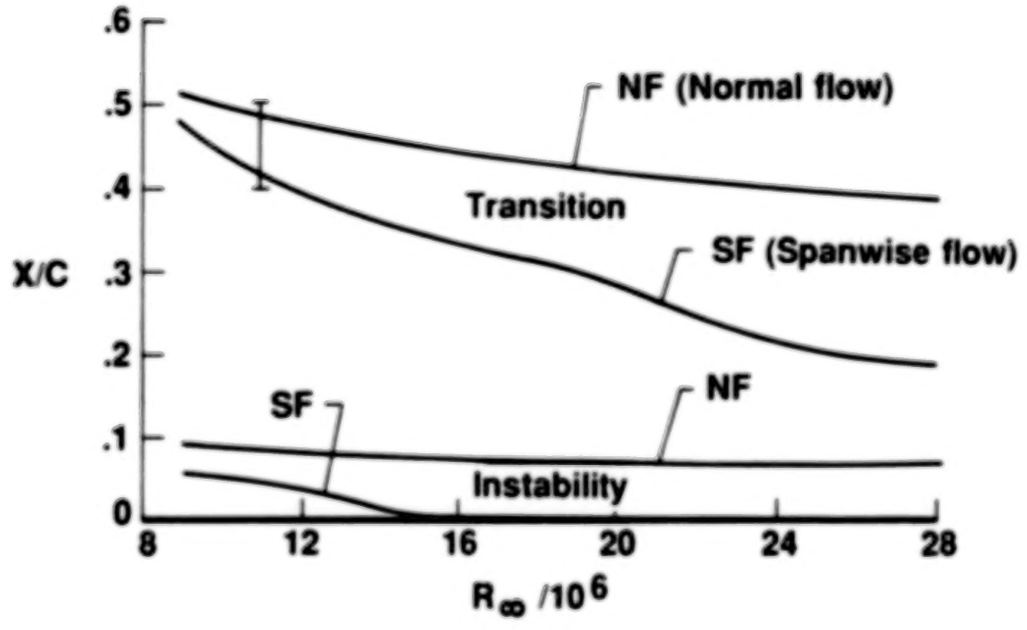

(b) Computed transition locations as a function of free-stream chord Reynolds number.

Figure 9. - Results for the F-14 "clean-up" gloved wing for a leading-edge sweep of 25° and M_∞ of 0.7.

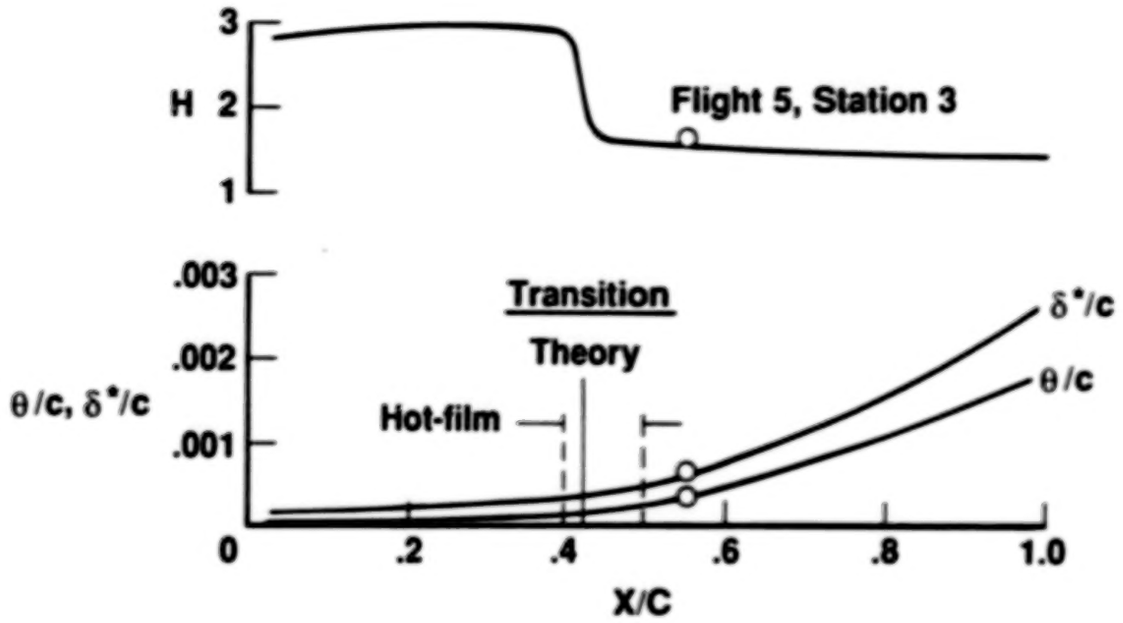

(c) Comparison between computed and flight boundary-layer parameters for $R_\infty = 10.8 \times 10^6$.

Figure 9. - Concluded.

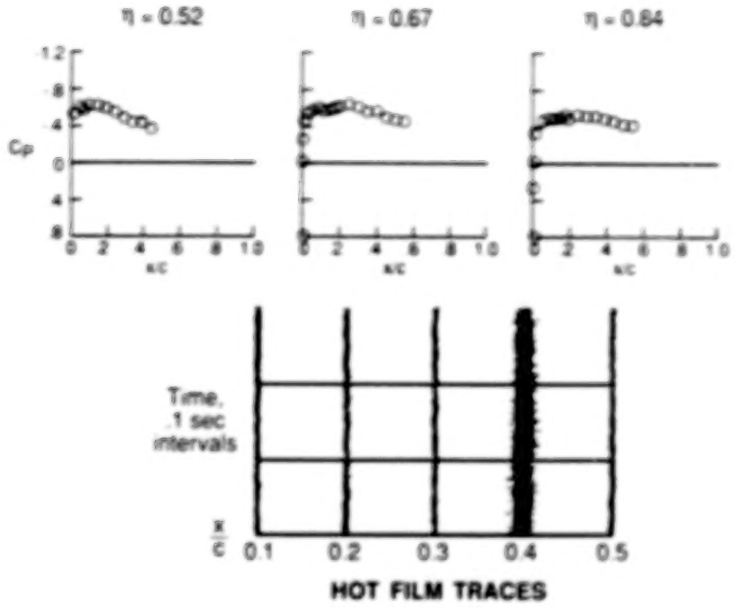

(a) Experimental pressure distributions and hot-film traces for $R_\infty = 9.5 \times 10^6$.

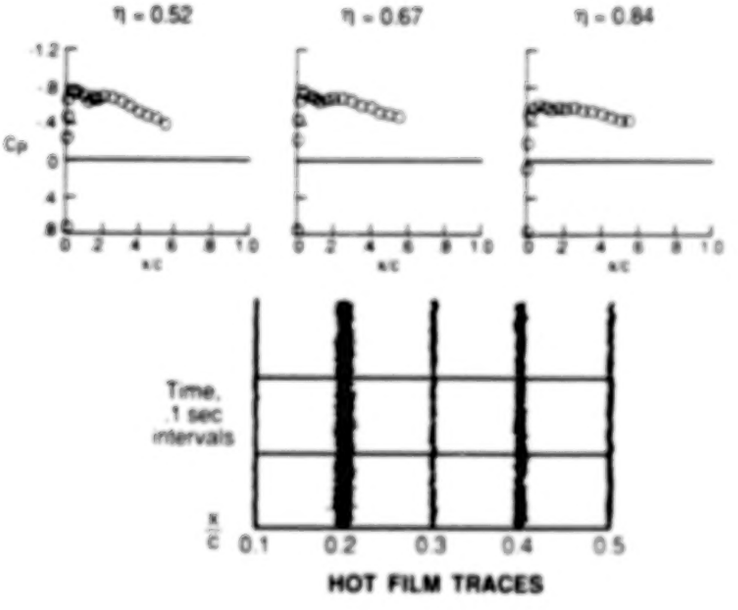

(b) Experimental pressure distributions and hot-film traces for $R_\infty = 19.2 \times 10^6$.

Figure 10. - Results for the F-14 "clean-up" gloved wing for a leading-edge sweep of 30° and M_∞ of 0.7.

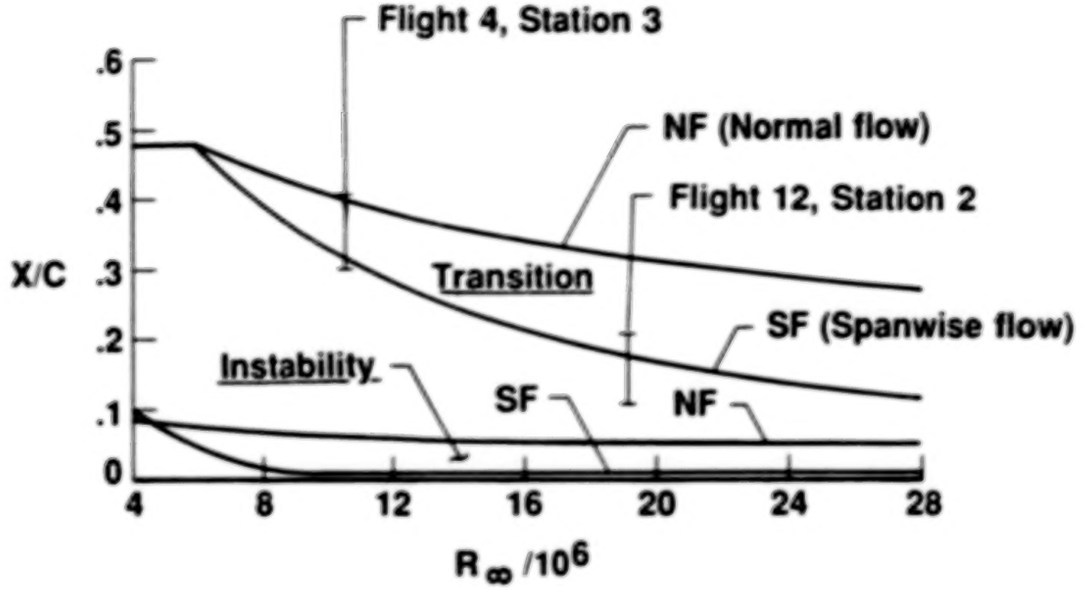

(c) Computed transition and instability locations versus free-stream Reynolds number.

Figure 10. - Concluded.

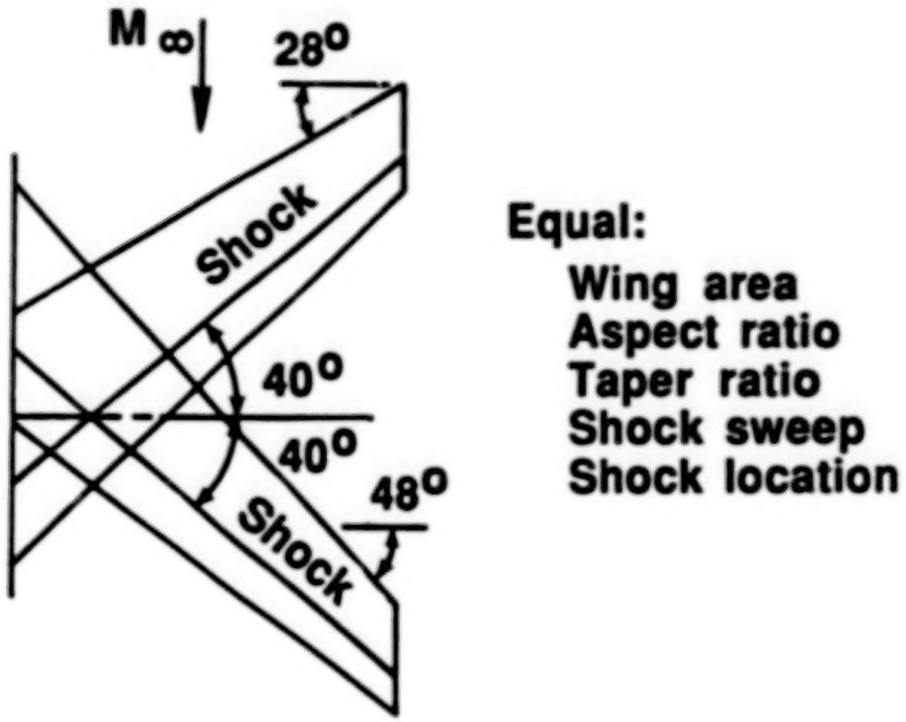

(a) Planforms.

(AR = .4, Taper ratio = .4)

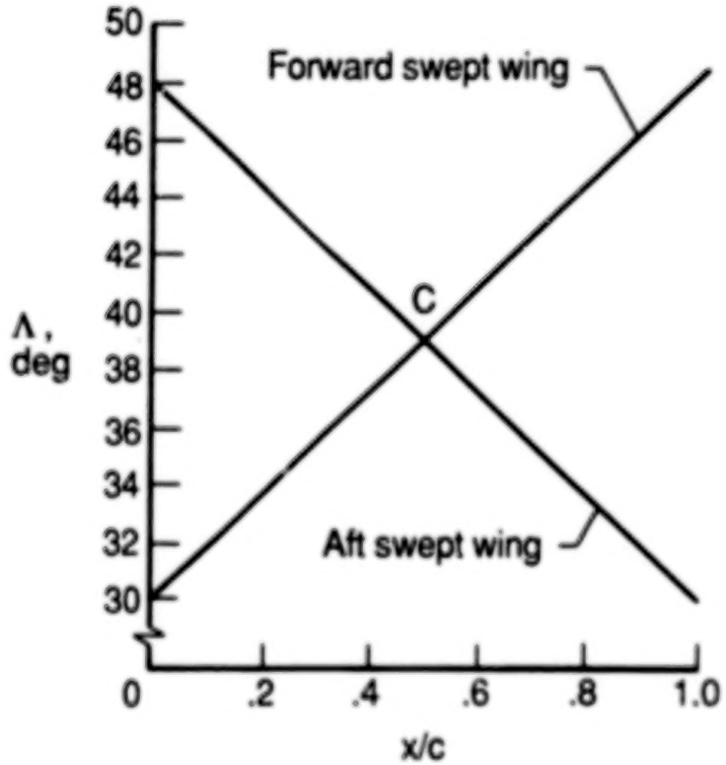

(b) Local sweep variations with respect to x/c.

Figure 11. - Comparison between "equivalent" forward and aft swept wings.

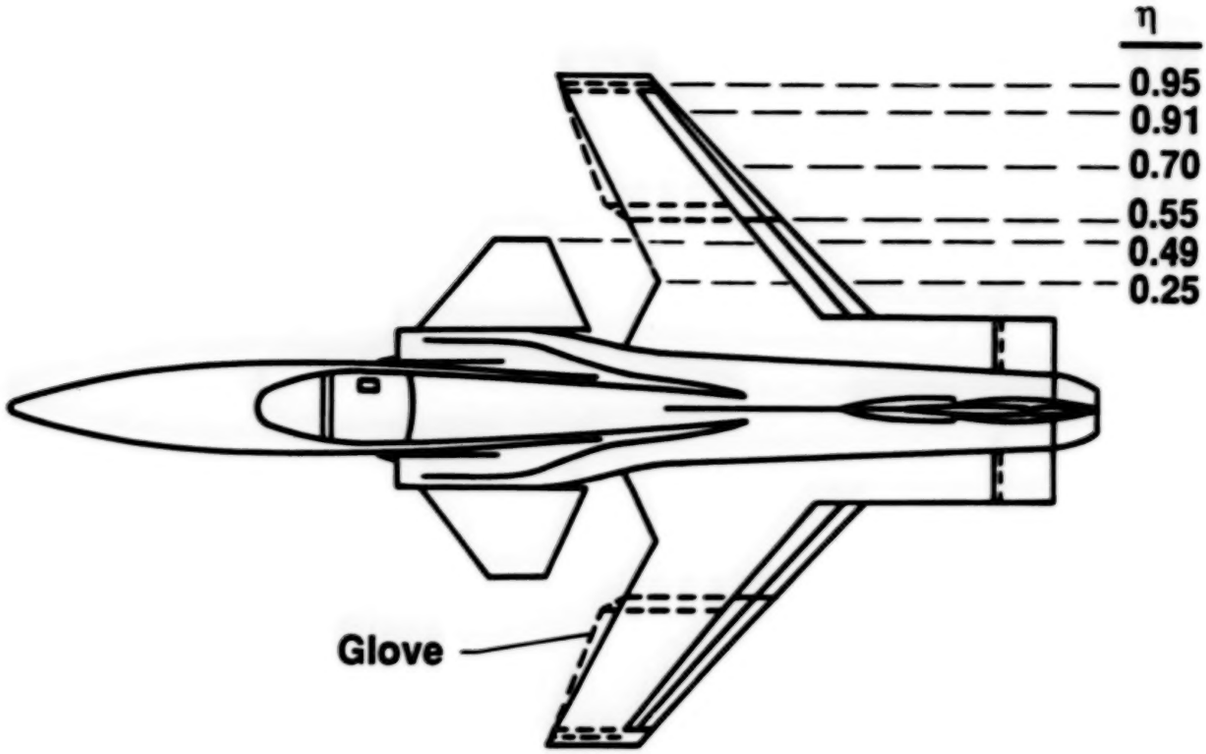

Figure 12. - Planform of X-29 aircraft.

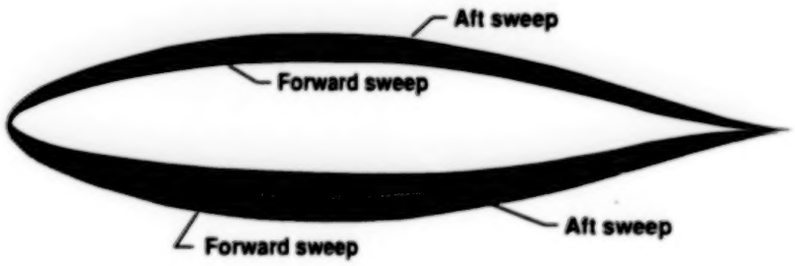

$(Z/C)_N = (Z/C)_S / \cos \Lambda$ upper and lower for Aft Sweep (N = normal, S = streamwise)

$(Z/C)_{N,upper} = (Z/C)_{S,upper}$

$(Z/C)_{N,lower} = (Z/C)_{S,upper} \cdot [1/\cos\Lambda - 1] + (Z/C)_{S,lower} \cdot [1/\cos \Lambda]$

} Forward Sweep

$(M_L)_N = (M_L)_S \cdot \cos \Lambda_{X/C=0.25}$

$(C_p)_{streamwise} = (C_p)_N \cdot \cos^2 \Lambda$ where $\Lambda = \Lambda_{LE} + (\Lambda_{TE} - \Lambda_{LE}) \cdot (X/C)$

$(C_L)_{2\text{-}D} = (C_L)_S / \cos^2 \Lambda_{X/C=0.25}$

} Forward and Aft Sweep

Figure 13. - Sweep procedure for forward- and aft-swept wings.

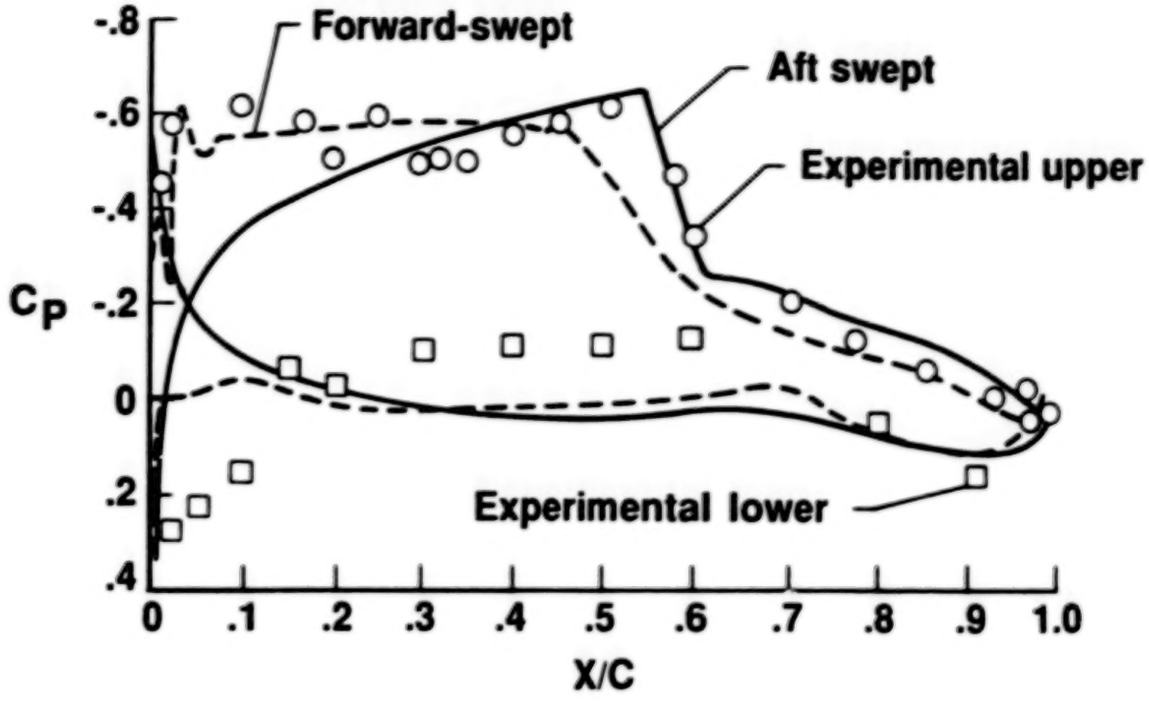

Figure 14. - Computational results for the pressure distributions on the X-29 wing section situated on both forward and aft wings. (M_∞ = 0.91, η = 0.70, Λ_{LE} = 30°)

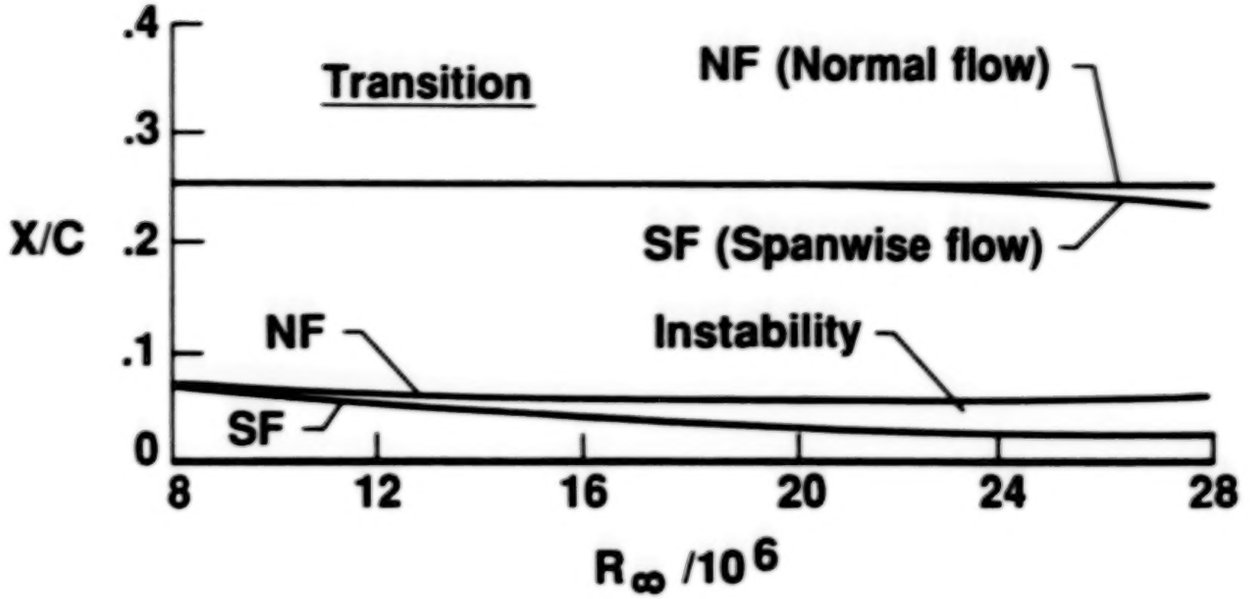

(a) Transition location versus R_∞.

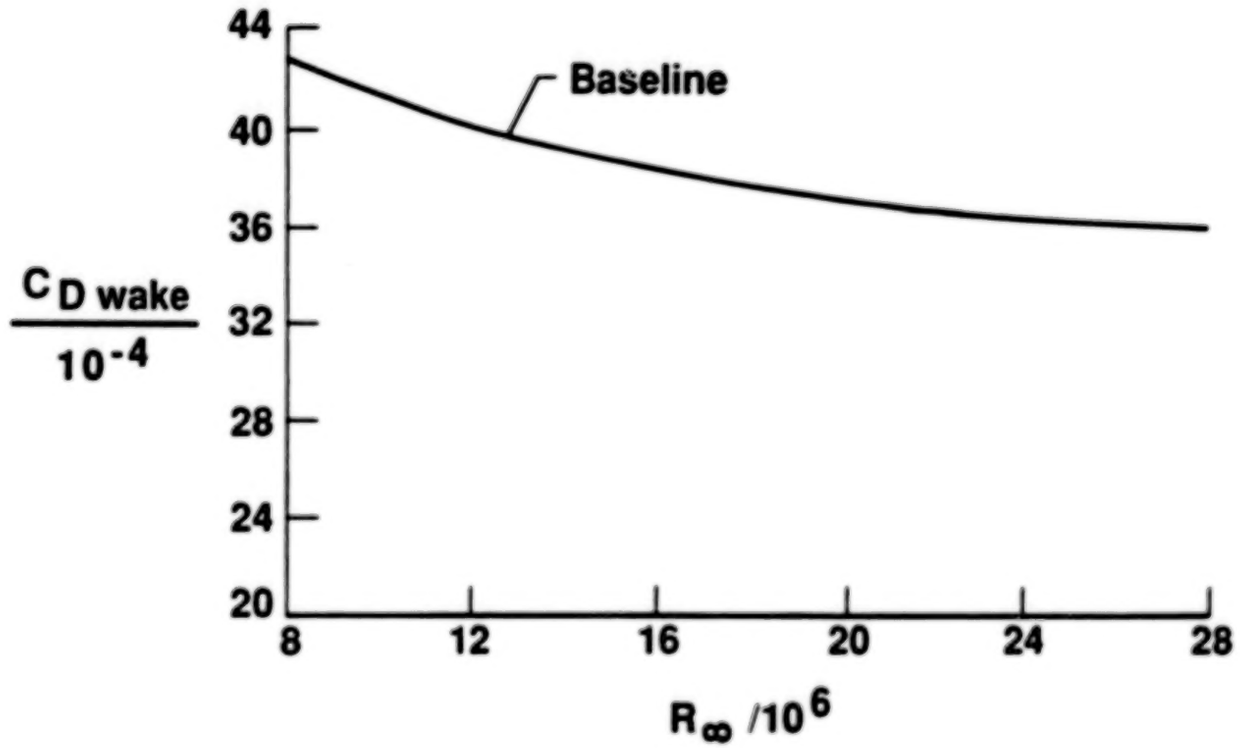

(b) $C_{D_{wake}}$ for baseline versus R_∞ and comparison with NLF-Glove.

Figure 15. - Computed results for X-29 baseline section for $\eta = 0.7$, $M_\infty = 0.91$.

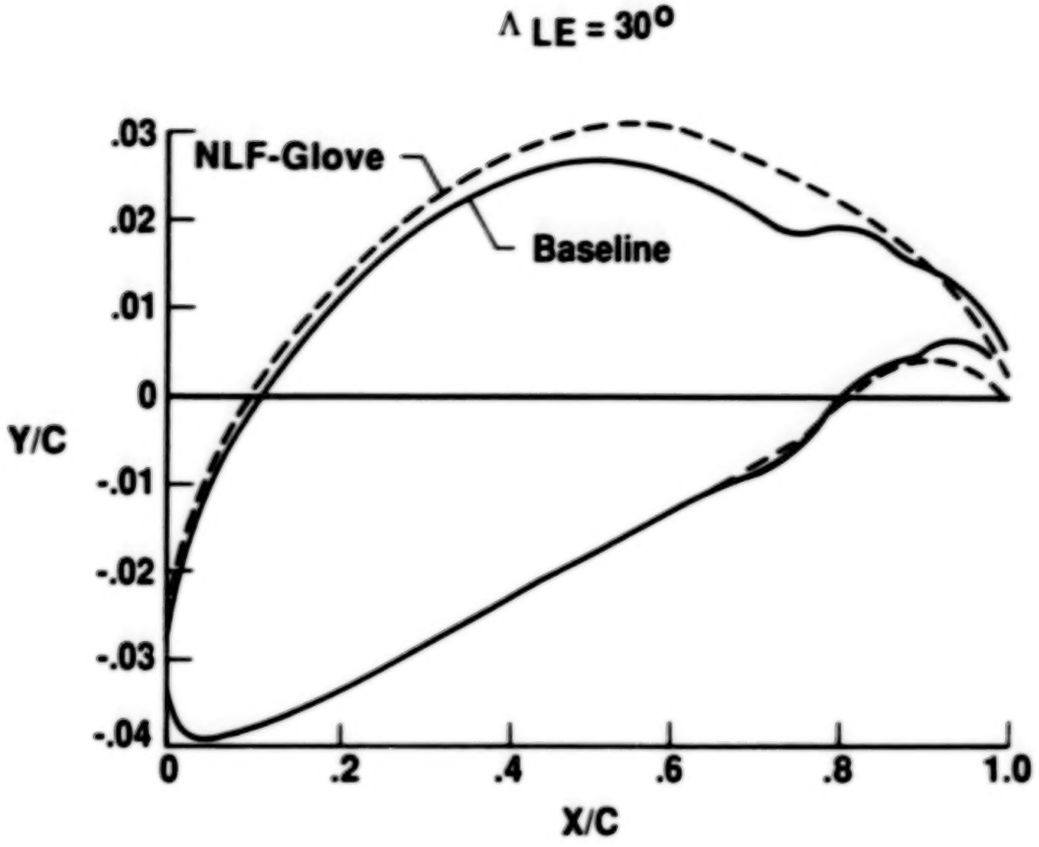

Figure 16. - Comparison between baseline geometry and NLF-Glove for X-29 wing for η = 0.7.

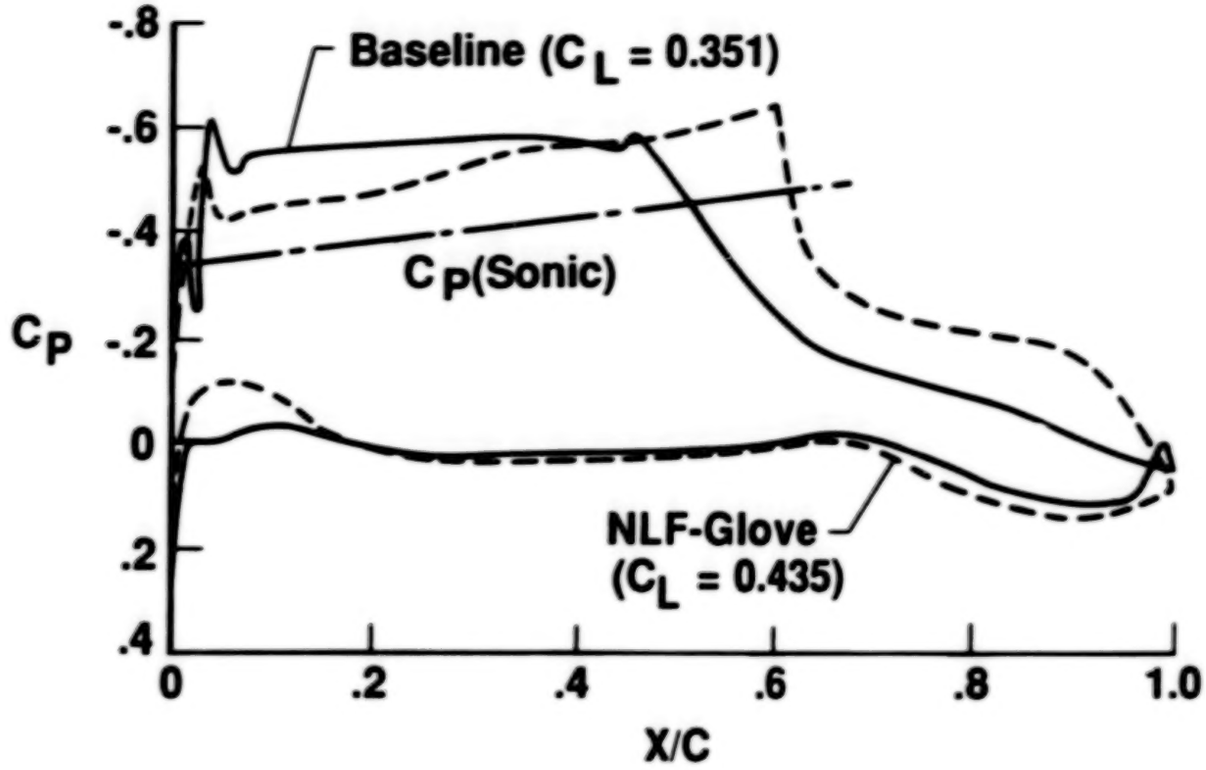

(a) Comparison between baseline and NLF-Glove for M_∞ = 0.905 and leading-edge sweep of 30°.

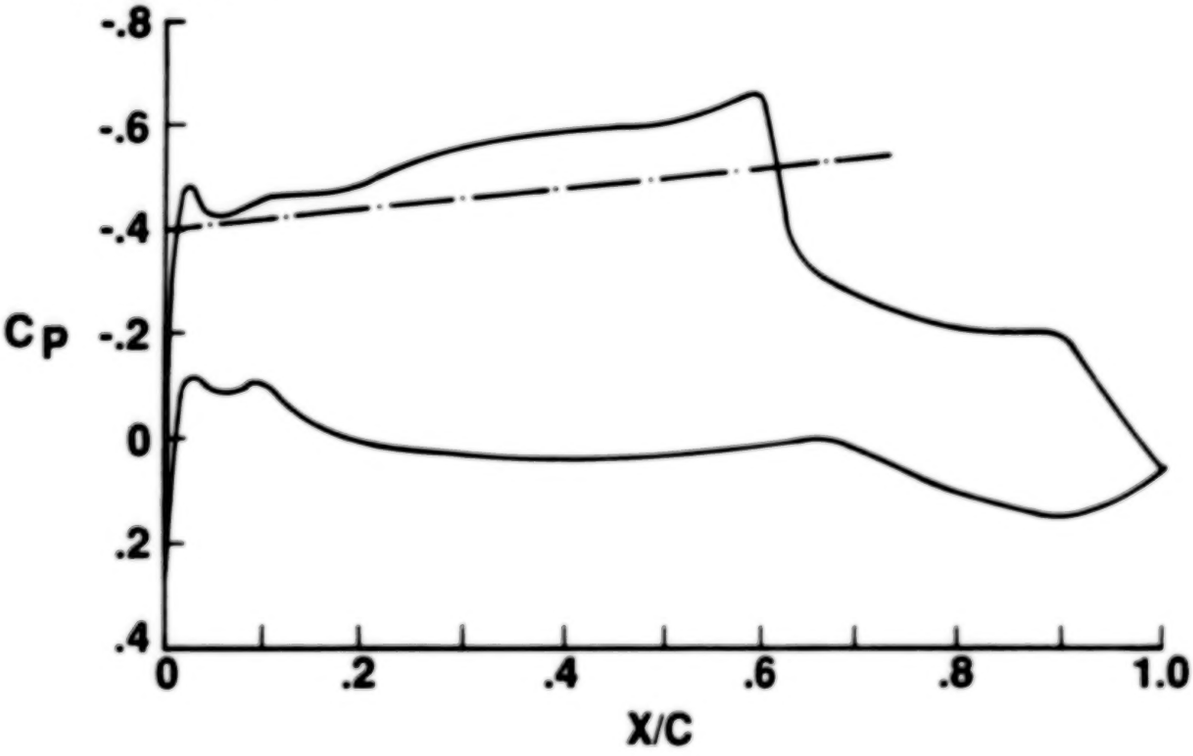

(b) Pressure distribution for M_∞ = 0.865 and leading-edge sweep of 25°.

Figure 17. - Chordwise pressure distributions for X-29 wing section for η = 0.7 and transition location computations.

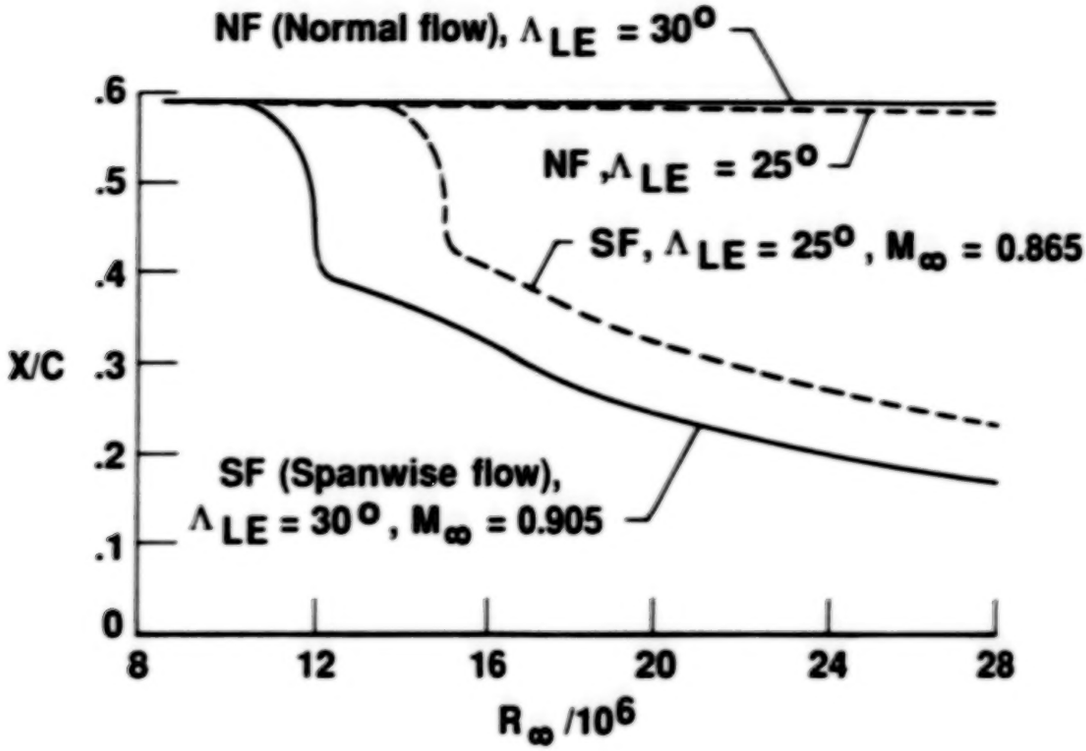

(c) Transition characteristics for leading-edge sweeps of 30° and 25°.

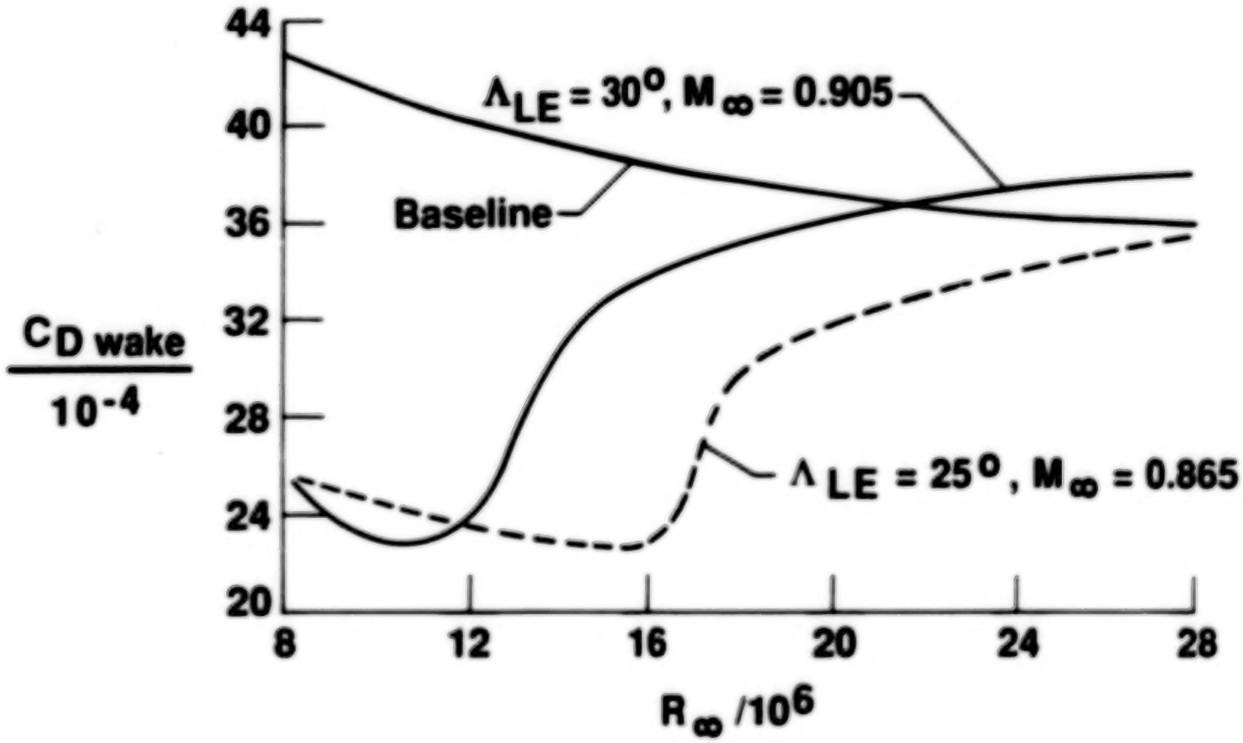

(d) Effect of Reynolds number and leading-edge sweep on $C_{D_{wake}}$.

Figure 17. - Concluded.

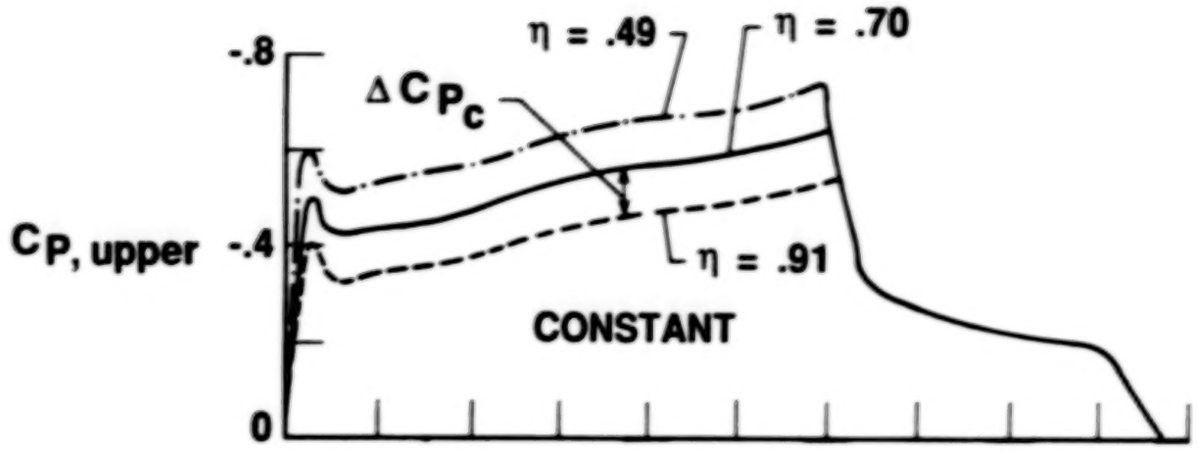

(a) Constant spanwise pressure gradient.

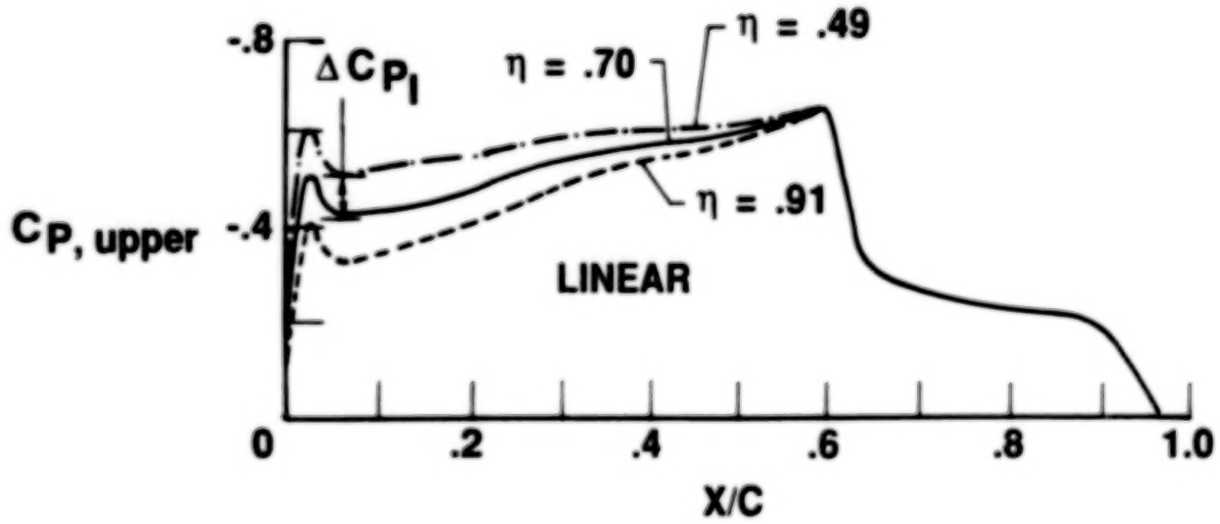

(b) Linearly varying spanwise pressure gradient.

Figure 18. - Schematics showing types of spanwise pressure gradients studied.

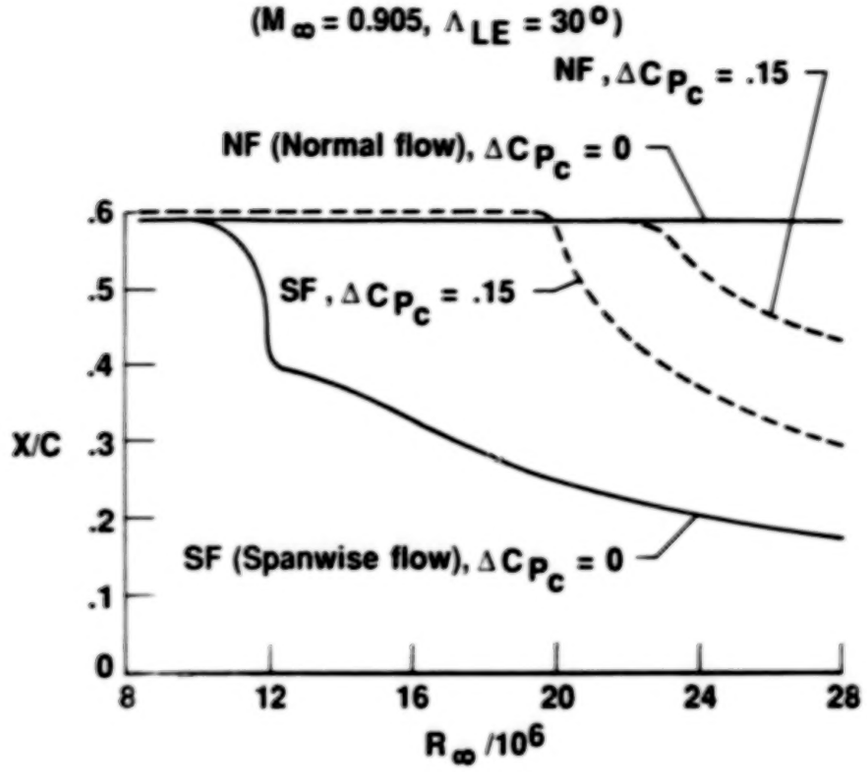

Figure 19. - Comparison of the effect of a constant spanwise pressure gradient of $\Delta C_{P_c} = 0.15$ on transition with that for zero spanwise gradient, i.e., with $\Delta C_{P_c} = 0$.

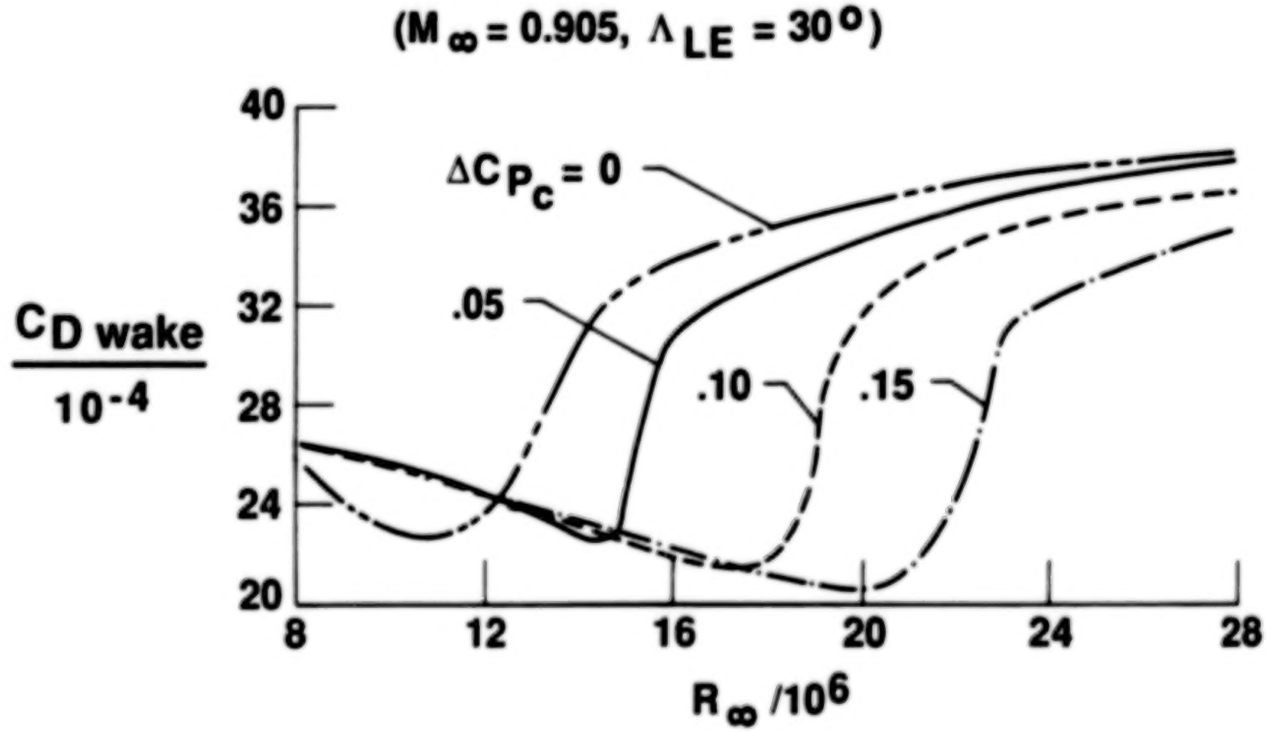

Figure 20. - $C_{D_{wake}}$ versus R_∞ with ΔC_{P_c} as parameter for X-29 glove.

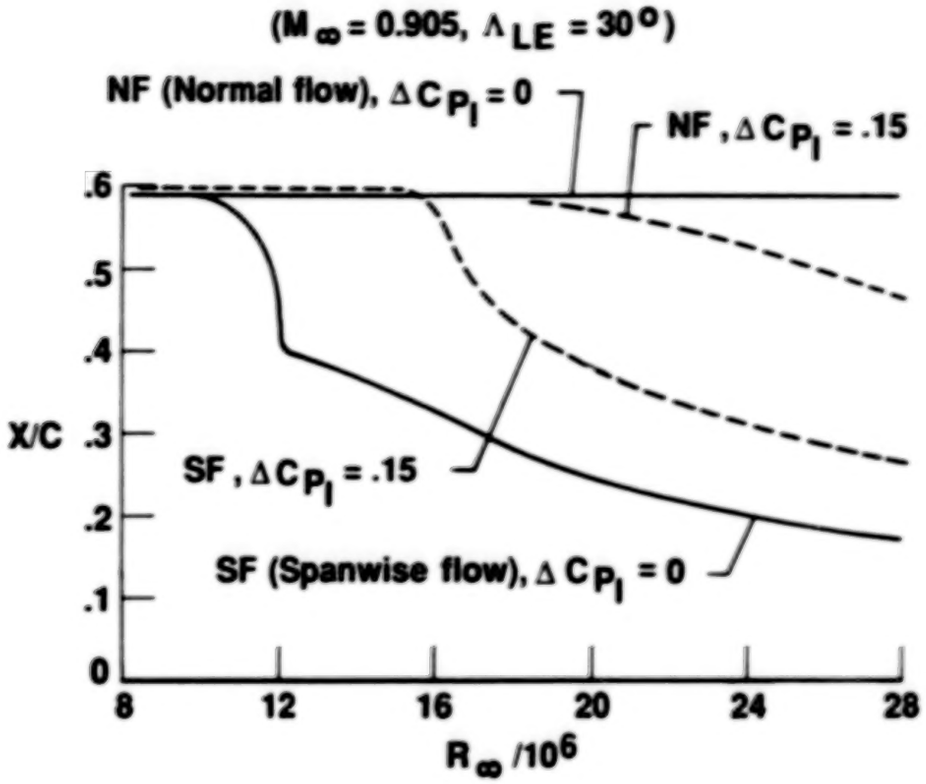

Figure 21. - Effect of linear spanwise pressure gradient of $\Delta C_{P_l} = 0.15$ on transition characteristics of X-29 glove and comparison with $\Delta C_{P_l} = 0$.

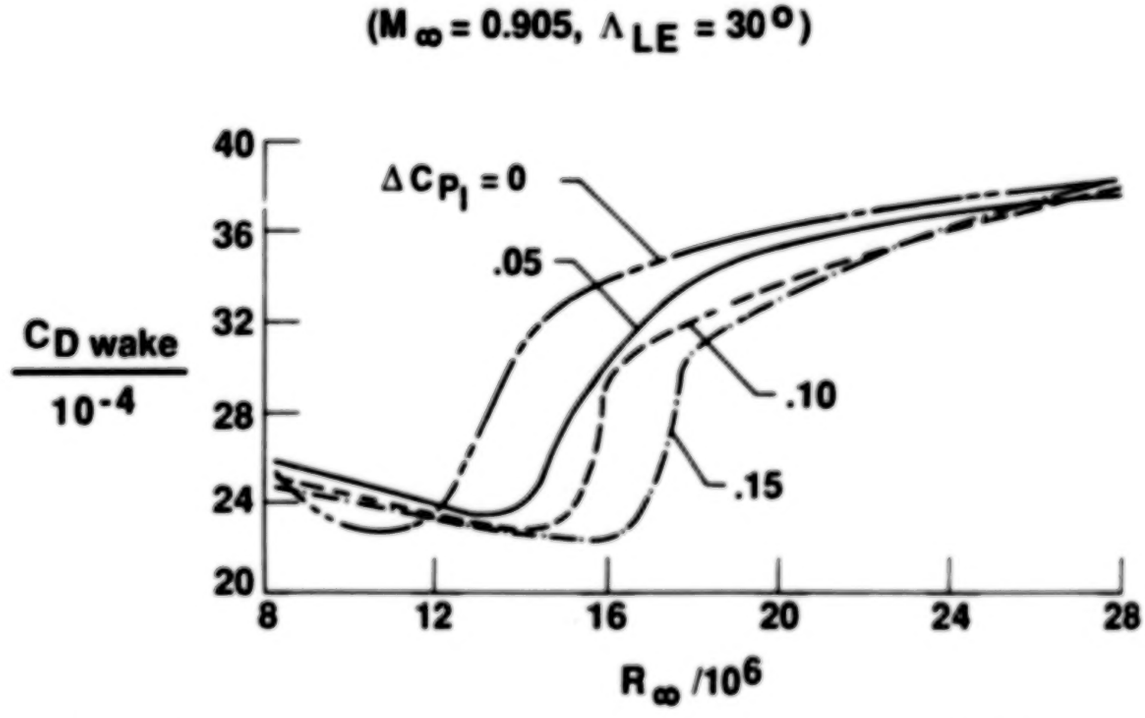

Figure 22. - $C_{D_{wake}}$ versus R_∞ with ΔC_{P_l} as parameter for X-29 glove.

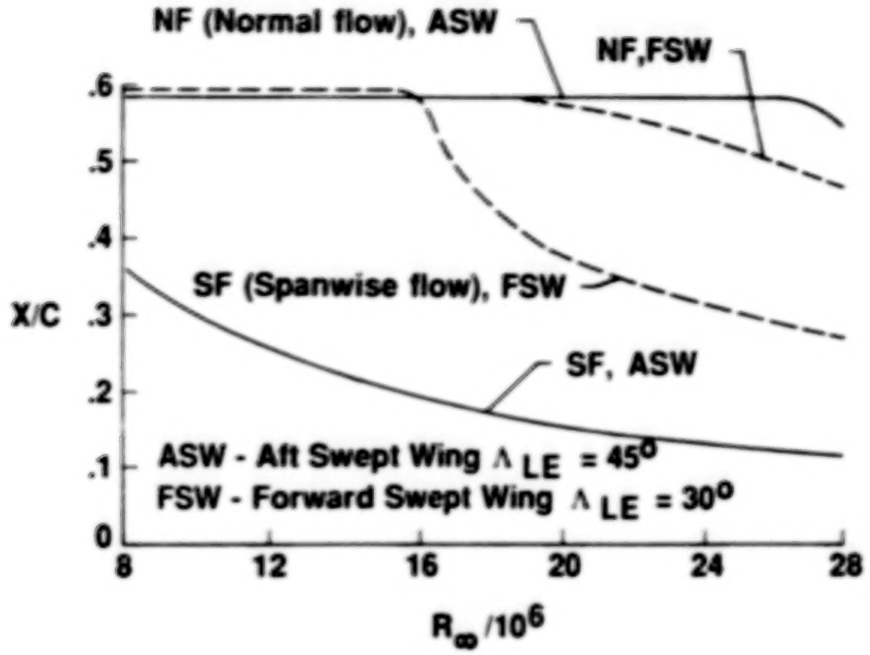

(a) Transition Location versus R_∞ for $\Delta C_{p_1} = 0.15$.

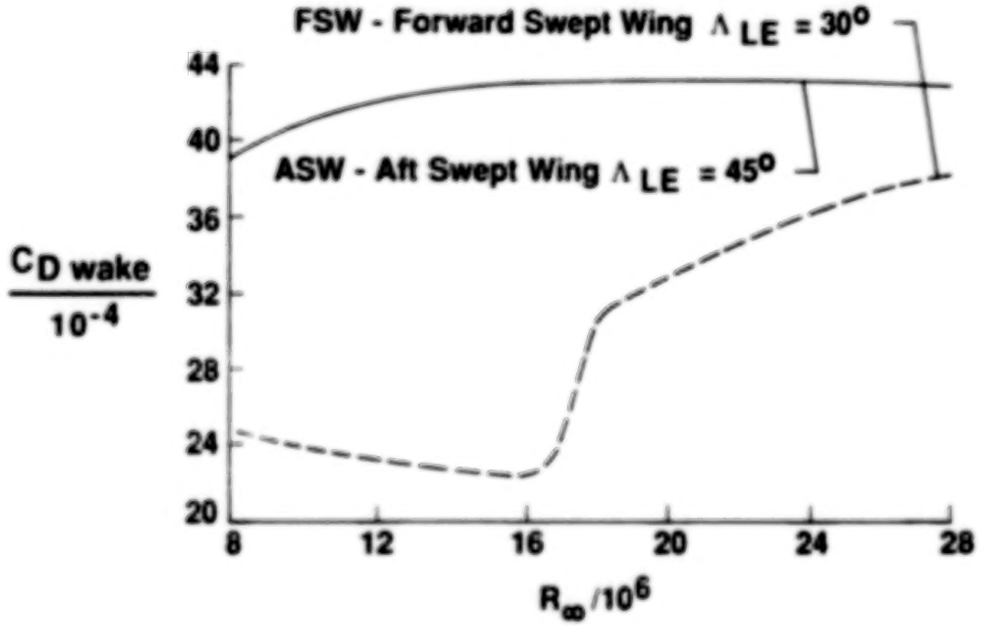

(b) $C_{D_{wake}}$ versus R_∞ for $\Delta C_{p_1} = 0.15$.

Figure 23. - Comparison between FSW and "equivalent" ASW for $M_\infty = 0.905$ and $C_L = 0.435$.

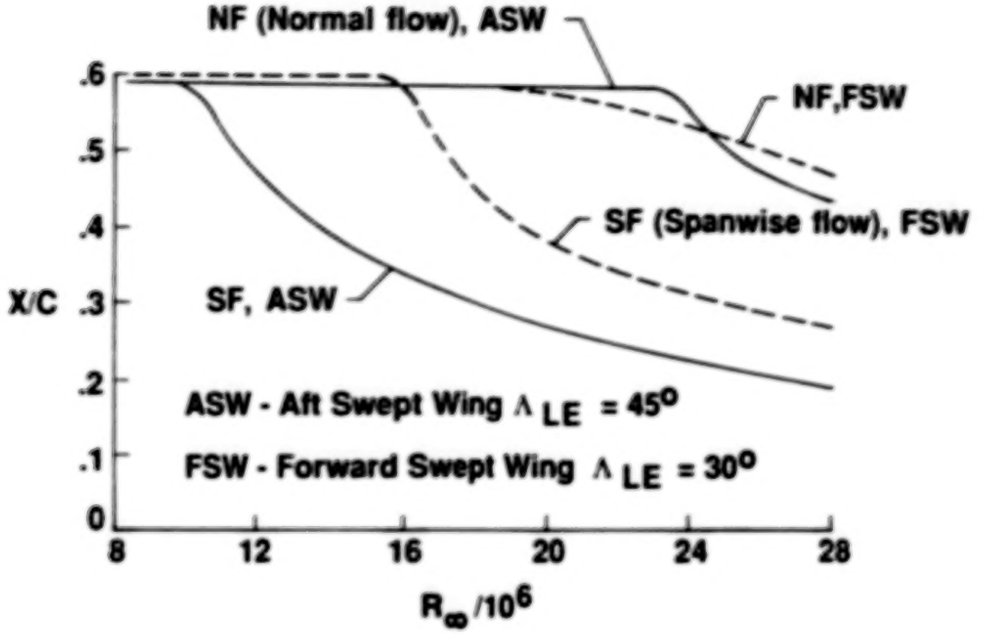

(c) Transition location versus R_∞ for $\Delta C_{P_1} = -0.15$.

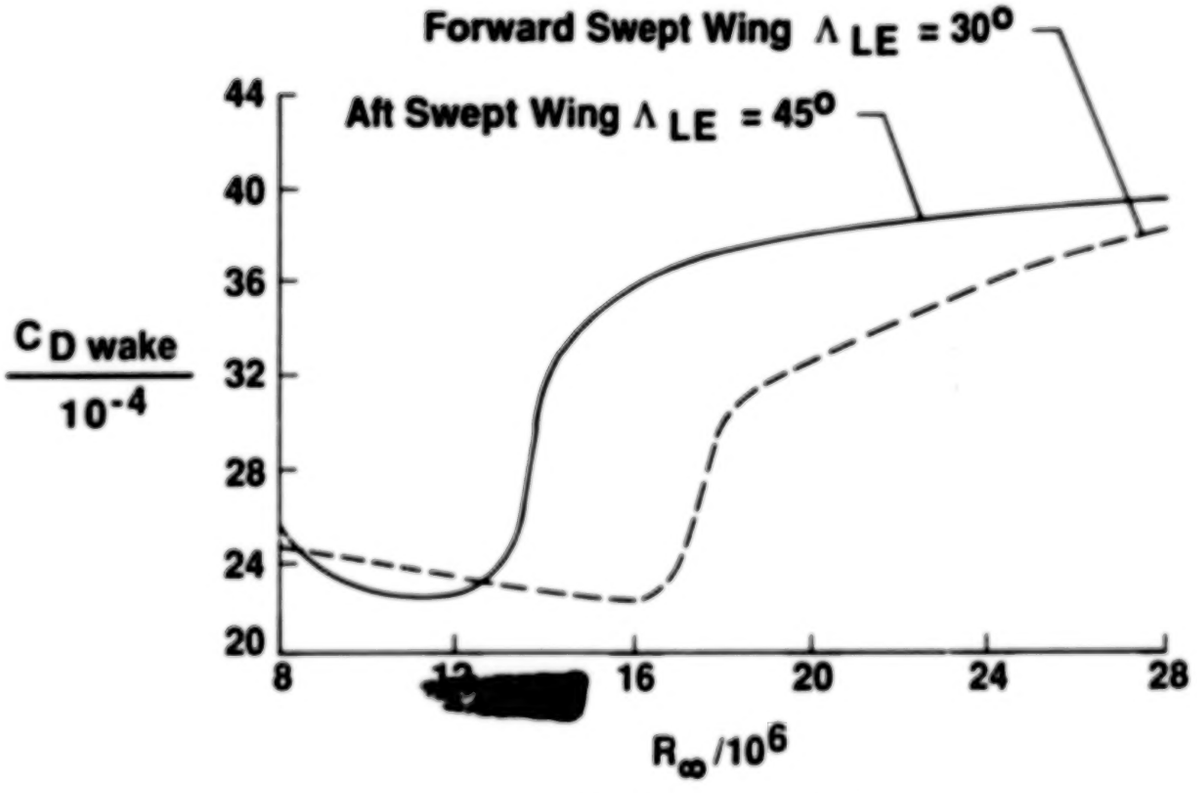

(d) $C_{D_{wake}}$ versus R_∞ for $\Delta C_{P_1} = -0.15$.

Figure 23. - Concluded.

Report Documentation Page

1. Report No.	2. Government Accession No.	3. Recipient's Catalog No.
NASA CP-3020, Vol. II		

4. Title and Subtitle	5. Report Date
Transonic Symposium: Theory, Application, and Experiment	April 1989
	6. Performing Organization Code

7. Author(s)	8. Performing Organization Report No.
Jerome T. Foughner, Jr., Compiler	L-16502
	10. Work Unit No.
	505-60-11-01

9. Performing Organization Name and Address	11. Contract or Grant No.
NASA Langley Research Center Hampton, VA 23665-5225	
	13. Type of Report and Period Covered
12. Sponsoring Agency Name and Address	Conference Publication
National Aeronautics and Space Administration Washington, DC 20546-0001	14. Sponsoring Agency Code

15. Supplementary Notes

16. Abstract

In order to assess the state of the art in transonic flow disciplines and to glimpse at future directions, the NASA Langley Research Center held a Transonic Symposium on April 19-21, 1988. Emphasis was placed on steady, three-dimensional external, transonic flow and its simulation, both numerically and experimentally.

Papers were presented by researchers from NASA, industry, and universities. The symposium included technical sessions on wind tunnel and flight experiments; computational fluid dynamics applications (industry overviews and configuration analysis design); inviscid methods and grid generation; viscous methods and boundary-layer stability; and wind tunnel techniques and wall interference.

The proceedings are published in two volumes as follows because of the range of classifications: Volume I, Unclassified (Parts 1 and 2); and Volume II, Unclassified, FEDD Restricted.

17. Key Words (Suggested by Author(s))	18. Distribution Statement
Aerodynamics External transonic flow Numerical simulation Experimental simulation	[redacted] Subject Category 02

19. Security Classif. (of this report)	20. Security Classif. (of this page)	21. No. of pages	22. Price
Unclassified	Unclassified	242	

NASA FORM 1626 OCT 86

NASA-Langley, 1989

END

DATE

FILMED

JUL 25 1991